Characterization of the stellar variability in CoRoT fields with BEST telescopes

vorgelegt von
Diplom-Physiker
Petr Kabáth
Brno

Von der Fakultät II - Mathematik und Naturwissenschaften
der Technischen Universität Berlin
zur Erlangung des akademischen Grades
Doktor der Naturwissenschaften
Dr.rer.nat.

genehmigte Dissertation

Promotionsausschuss:

Vorsitzender: Prof. Dr. rer. nat. Mario Dähne
Berichter/Gutachter: Prof. Dr. rer. nat. Heike Rauer
Berichter/Gutachter: Prof. Dr. rer. nat. Erwin Sedlmayr

Tag der wissenschaftlichen Aussprache: 01.09.2009

Berlin 2009

D 83

Angefertigt am Institut für Planetenforschung des Deutschen Zentrums für Luft- und Raumfahrt (DLR), e. V., Berlin-Adlershof

Abstract

The first extrasolar planet 51 Peg b around the *G*-type star has been reported in 1995. The planet with few Jupiter masses orbiting its star very closely was detected by measurement of the oscillation in the radial velocity of the host star. In 1999 the first transit, when the planet is eclipsing the host star, of the extrasolar planet HD209458 b was observed with a small ground based photometric telescope. Ever since, new planets in distant systems are continuously being detected with new high precision instruments from the ground and from space.

The department of Extrasolar Planets and Atmospheres at Deutsches Zentrum für Luft- und Raumfahrt, Berlin (DLR) is involved in the detection and characterization of extrasolar planets, through participation in the CoRoT space mission. Furthermore, two ground based photometric telescope systems are operated as a ground based support for the space mission CoRoT, dedicated to asteroseismology and to extrasolar planet search with the help of the transit method.

The BEST project consists of two small aperture wide field-of-view photometric telescopes devoted to the search for transiting Jupiter-sized extrasolar planets and to the characterization of variable stars in CoRoT target fields. The BEST telescope is located at Observatoire de Haute Provence, France and the BEST II telescope is located in the Atacama desert, Chile.

The aim of the thesis is to present the results obtained from BEST project with a particular focus on the BEST II system. Part of the project presented in this thesis concentrated on the setup, laboratory tests and preparation for the operations of the BEST II system in its initial phase in Chile. In particular, technical aspects of the BEST II system, implementation of the robotic mode and the operations were the topic of the second phase of the thesis work presented here. In the final phase, the robotic observational campaign on LRa02 CoRoT target field was successfully carried out and results will be summarized in the second half of this thesis. Essential part describing the results on LRa02 campaign includes the results of work on the data reduction process with determination of the quality of photometric calibration and the estimation of photometric precision of the system. In addition, the comparison of the duty cycles of BEST and BEST II is made. Finally, general implications for the transit search from BEST project are also presented.

The thesis summarizes the scientific results obtained and based on the observations of CoRoT long and intial run fields in the period 2005 to 2009. The data were collected in order to support the CoRoT's follow-up team in the confirmation process of planetary candidates. BEST telescopes can in some cases reject the false positive identification of the planetary candidate which can be due to a background object mimicking the transit event. Additionally, since BEST telescopes observed the CoRoT fields approximately one year ahead the CoRoT the archive data can extend the ephemerids of objects detected with CoRoT.

As a result of observations data on the CoRoT IRa01, LRa01, LRc01, LRc02, LRa02 target fields were collected with both telescopes. Typical campaign length was about three months. The data contain observations from 128 nights (672 hrs.). The whole light curve archive contains information on more than 250000 stars from which about 22423 are marked as potentially variable objects which were further investigated in order to detect new periodic variable stars and planetary transits.

Also a direct contribution to the CoRoT follow-up team which includes an investigation of BEST light curves corresponding to 160 CoRoT candidates will be presented in this thesis. Furthermore, presented work contains an identification of transit events of confirmed planets CoRoT 1b and CoRoT 2b in the BEST data sets after being reported by CoRoT team.

The results on new periodic variable stars contain more than 900 new detections and about 31 reconfirmations of previously detected variable stars which were already listed in catalogs. The result of the transit survey is an identification of two high quality candidates for extrasolar planets in LRa02 data set.

Zusammenfassung

Der erste extrasolare Planet um einen sonnenähnlichen Stern, 51 Peg b, wurde im Jahr 1995 entdeckt. Er ist um ein Vielfaches größer als Jupiter, umkreist seinen Stern in einem sehr nahen Orbit und wurde durch Oszillationen in der Radialgeschwindigkeit des Zentralsterns nachgewiesen. Im Jahr 1999 konnte mit einem kleinen bodengebundenen photometrischen Teleskop zum ersten Mal ein Transit eines extrasolaren Planeten (HD209458 b) beobachtet werden. Seitdem werden fortlaufend neue Planeten in weit entfernten Systemen sowohl vom Boden als auch vom Weltraum aus detektiert.

Die Abteilung "Extrasolare Planeten und Atmosphären" am Deutschen Zentrum für Luft- und Raumfahrt (DLR) in Berlin ist durch die Weltraummission "COnvection, ROtation and planetary Transits" (CoRoT) an der Entdeckung und Charakterisierung extrasolarer Planeten beteiligt. CoRoT ist der asteroseismologischen Untersuchung entfernter Sterne sowie der Suche nach extrasolaren Planeten mithilfe der Transitmethode gewidmet. Darüberhinaus werden vom DLR mit dem BEST-Projekt ("Berlin Exoplanet Search Telescope") bodengebundene Unterstützungsbeobachtungen für die CoRoT-Mission durchgeführt.

Das BEST-Projekt besteht aus zwei Teleskopen mit kleiner Öffnung und groem Gesichtsfeld, die jeweils der Suche nach extrasolaren, jupiterähnlichen Transitplaneten sowie der Charakterisierung von variablen Sternen in CoRoT-Feldern gewidmet sind. BEST befindet sich am Observatoire de Haute Provence in Frankreich, BEST II in der chilenischen Atacamawste.

Das Ziel dieser Doktorarbeit ist die Präsentation des BEST-Projekts, wobei der Schwerpunkt auf BEST II liegt. Dabei sind Aufbau, Test und Inbetriebnahme des BEST II Teleskops in Chile Teil der Arbeit. Besondere technische Aspekte des BEST II-Systems, wie z.B. die Implementierung und Funktion des robotischen Beobachtungsmodus, werden vorgestellt.

In der letzten Phase der Arbeit wurde die robotische Beobachtungskampagne des CoRoT-Feldes LRa02 erfolgreich durchgeführt; die Ergebnisse werden im zweiten Teil präsentiert. Dies beinhaltet die Datenauswertung und Ergebnisse der Beobachtungen, Bestimmung der Qualität der photometrischen Kalibrierung, Abschätzung der resultierenden photometrischen Genaugkeit des Systems und einen Vergleich von Beobachtungszeiten von BEST und BEST II bzw. die Folgerungen daraus für die Transitsuche.

Beobachtungsdaten der CoRoT-Felder IRa01, LRa01, LRc01, LRc02 und LRa02 wurden mit beiden Teleskopen gesammelt. Die typische Kampagnenlänge betrug drei Monate. Die Datensätze beinhalten Beobachtungen von insgesamt 128 Nächten (672 Beobachtungsstunden). Das gesamte Lichtkurvenarchiv beinhaltet mehr als 250.000 Sternen, von denen 22.423 als potentiell variabel markiert und weiter auf Periodizität untersucht wurden. Dabei konnten mehr als 900 Sterne als neue Variable identifiziert und in einem Katalog präsentiert werden, sowie 31 bekannte variable Sterne bestätigt werden. Desweiteren wird in dieser Arbeit ein direkter Beitrag zu den Nachfolgebeobachtungen von 160 CoRoT-Planetenkandidaten vorgestellt und die Entdeckung der Transitplaneten CoRoT 1b and CoRoT 2b in BEST-Lichtkurven diskutiert. Nicht zuletzt konnten im LRa02-Datensatz zwei Transitkandidaten identifiziert werden, die ebenfalls vorgestellt werden.

Shrnutí

První extrasolární planeta 51 Peg b u hvězdy typu G byla ohlášena v roce 1995. Tato planeta o hmotnosti několika násobků hmotností Jupitera obíhající velice blízko své hvězdy, byla objevena pomocí měření změn radiálních rychlostí. V roce 1999 byl pozorován první transit extrasolární planety HD 209458 b přes disk své mateřské hvězdy malým fotometrickým dalkohledem z povrchu Země. Další planety ve vzdálených slunečních soustavách jsou objevovány překotným tempem ze Země i z vesmíru.

Oddělení Extrasolárních planet a atmosfér v rámci istitutu Deutsches Zentrum für Luft- und Raumfahrt, v Berlíně (DLR) se zabývá objevováním a popisem extrasolaárních planet. V rámci programu hledání planet je členem týmu vesmírné mise CoRoT, která má za cíl sledovaní asteroseismologie vybraných hvězd a hledání tranzitujících extrasolárních planet. Oddělení navíc ještě provozuje dva pozemní dalekohledy sloužící jako pozemní podpora pro CoRoT.

Projekt BEST sestává ze dvou malých fotometrických dalkohledů s velkým zorným polem, které jsou určeny k hledání Jupiteru podobných tranzitujících planet a proměnných hvězd v zorném poli mise CoRoT. Dalkohled BEST je umístěn na Observatoire de Haute Provence ve Francii a BEST II se nachází v poušti Atakama v Chile.

Cílem této práce je prezentace výsledků obdržených z projektu BEST s těžištěm na popis a dokumentaci veškerých aspektů BEST II dalekohledu. Ve své první fázi se tento doktorandský projekt zaměřil nejprve na laboratorní testy a přípravu pro fungování dalekohledu BEST II. Ve druhé fázi byly řešeny obzvláště technické detaily projektu a implementace robotického způsobu provozu. V poslední fazi byla uspěšně provedena robotická pozorování hvězdného pole CoRoT LRa02 a výsledky jsou shrnuty ve druhé části této práce. Popis výsledků z pozorování pole LRa02 zahrnuje celý proces zpracování dat a určení kvality kalibračního procesu a fotometrických dat a odhad celkové kvality dat a diskuzi pozorovacího cyklu který obecně ovlivňuje projekty hledající extrasolaární planety.

Výsledky obdržené z analýzy dat z pozorování hvězdných polí IRa01, LRa01, LRc01, LRc02, LRa02 jsou základem této práce. Tato data byla napozorována během 128 nocí, což odpovídá celkem 672 hodinám pozorování. Celý archiv světelných křivek obsahuje informace o 250000 hvězd, ze kterých bylo 22438 označeno jako pravděpodobně proměnné a byly dále analyzovány. Z těchto hvězd byl sestaven katalog čítající více jak 900 nově objevených periodických proměnných hvězd a 31 již dříve známých proměnných hvězd.

Vedle zmíňených výsledků bude popsán přínos BEST II pro určování pravé povahy kadidátů nalezených v rámci mise CoRoT. Dále také budou prezentovány transity planet CoRoT 1b a CoRoT 2b nalezené v archivních datech projektu BEST poté co byly oznámeny týmem CoRoT. Představeny budou také dva nově objevené objekty, které jsou možnými kandidáty na extrasolarní planety.

Contents

Chapter 1

Introduction

Astronomy is one of the oldest science disciplines mainly describing the processes and events related to celestial bodies. In principle, astronomical observations already served to measure time in ancient era. As early as 2400 BC, the Sumerians, populating Mesopotamia, (currently known as Iraq) compiled a calendar with 360 days (1) which was later adopted by the Babylonians and other cultures in the region.

Astronomical observations were used to select the most suitable times for the sowing of spring crops and autumn harvests. Besides, astronomy became significant for practicing religion amongst various cultures. Observations of unanticipated and astonishing events such as Solar eclipses and arrivals of comets have been viewed as an occurrence of special importance since the beginning of time. The first documented total Solar eclipse was probably observed on 3rd of May 1374 BC in Mesopotamian area (2). Some Solar eclipses have even shaped history, for example when influencing the decision of Medean and Lydian rulers during the total eclipse on 28th of May 584 BC, as reported by Herodotus and presumably predicted by Thales. This particular event happened, according to Herodotos (1) during the war between Lydian and Medes, who then subsequently signed a peace treaty. Astronomical observations together with the interpretation of processes in the celestial sphere remained highly significant over the coming centuries.

By the end of the ancient era, the astronomical knowledge and observational techniques were further developed by Arabian astronomers. However, the natural phenomena in the sky were also observed in Europe during the medieval ages. The real break through for astronomy as a scientific discipline followed later with the invention of improved methods for the time determination[1] and with the invention of a telescope at the end of the middle ages. Since then, the development of astronomy has increased at a phenomenal rate.

Nowadays, astronomy offers many exciting possibilities for unveiling the mysteries of the Universe in which we are living. In particular, the introduction of photographic plates and additional developments of large telescope facilities and the following invention of CCD detectors unprecedentedly shifted the scope of potential research topics.

The new research field on extrasolar planets has opened up in the last 50 years.

[1] The first astronomical clock in Europe was constructed in the 13th Century.

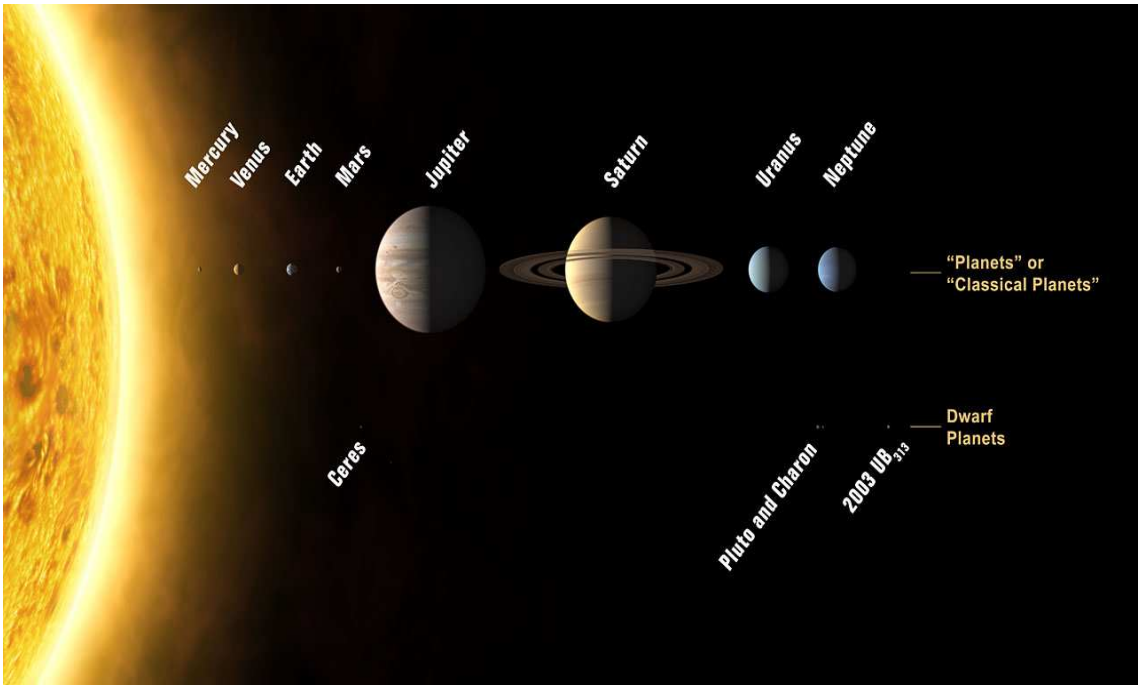

Figure 1.1: *Definition of a planet in the Solar System. Image by IAU (3).*

Fundamental ideas of the planetary astronomy have been proposed and revised over the centuries but only in the late 20^{th} Century this discipline has undergone a new impulse through the first detections of planets orbiting distant stars. The following questions are significantly shaping exoplanetary science.

- Is there life in the Universe on other planets as we know it and if so, under which physical conditions?
- How can we detect extrasolar planets?
- How can we characterize planetary systems and their host stars in general?

A planet within the Solar System is defined according to the IAU 2006 General Assembly agreement as (4):

"a celestial body that

- is in orbit around the Sun,
- has sufficient mass for its self-gravity to overcome rigid body forces so that it assumes a hydrostatic equilibrium (nearly round) shape, and
- has cleared the neighborhood around its orbit."

This definition can be extended to any planet outside the Solar system according to G. Marcy (5) as:

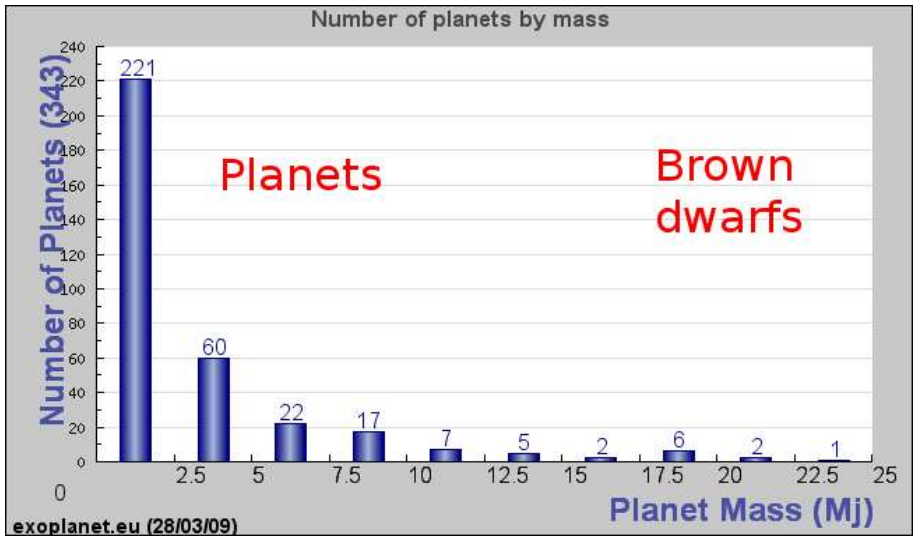

Figure 1.2: *Planet-mass distribution. One clear peak can be seen for planets with* $M < 3M_{Jupiter}$*. The distribution is broken about planetary mass of* $M \approx 13M_{Jupiter}$ *which is the theoretical limit for thermonuclear synthesis of Deuterium. Indication for a second peak can be seen about* $M \approx 17.5M_{Jupiter}$ *corresponding to brown dwarf objects. From Encyclopedia of Extrasolar planets maintained by Jean Schneider (6).*

"an object that has a mass between that of Pluto and the Deuterium-burning threshold ($< 13M_{Jupiter}$ - see Figure 1.2) and that forms in orbit around an object that can generate energy by nuclear reactions."

Objects less massive than $13M_{Jupiter}$ never burn Deuterium nor generate significant energy from any nuclear reactions. Fortuitously, this Deuterium-burning limit at $13M_{Jupiter}$ resides near the upper-end of the observed planet mass distribution (see Chapter 3). Thus, 13 Jupiter masses constitutes an arbitrary but doubtly motivated limit.

In the following sections a brief historical and scientific introduction will be followed by the motivation and the purpose of this thesis.

1.1 Extrasolar planets

Is there life in the Universe as we know it?

The question if there is life in the Universe and whether we are the most unique and only species in the whole Universe had been asked by mankind throughout the centuries. First theories about the extraterrestrial life originated from ancient Greece. The famous Demokritos and Anaximandros described alongside the atomic theory, also the theory claiming the existence of other worlds. The concept of life in the Universe was not very popular during the middle ages since the Ptolemaian geocentric theory was officially favored by the authorities. Claudius Ptolemaios (about 100 - 178) claimed that the Earth is in the center of the Universe and all the celestial bodies are moving within the spheres.

The theory of Ptolemy was met with increasing scepticism at the end of middle

ages in Europe. The idea suggesting the existence of other worlds and life on other planets was first presented by Giordano Bruno (1548 - 1600) and Galileo Galilei (1564 - 1642). Both were at that time persecuted for their revolutionary ideas (7). The situation was different in Holland where the famous dutch scientist Christian Huygens (1629 - 1695) presented a theory about life in different worlds in the Universe. Since the beginning of the Modern Era, the idea of an extraterrestrial life was gaining on importance. A brief summary of the current state of the art of this topic will be given in Chapter 3.

How can we detect planets?

In the Renaissance the Ptolemaian geocentric theory was replaced by Copernicus's heliocentric theory claiming that Earth orbits the Sun. Further development came with Kepler's laws of planetary motion. Also observational astronomy gained in importance. The first documented modern scientific observations of planets in our Solar System were performed by Galileo Galilei. He discovered the Jupiter's Shepherd's Moons and described the results in Siderius Nuncius 1610. One century later, Immanuel Kant (1724 - 1804) describes in his theoretical work (8) from year 1755, the creation of planetary systems and also discusses the possibility of extraterrestrial life. Thirty years later, Sir William Herschel (1738 - 1822) discovered the planet Uranus (9). He also observed changing seasons on Mars (10) and confirmed the existence of an atmosphere on Venus (11). Since then, the research on our Solar System has been continuously expanding and new instruments were paving the way for a new era in planetary research.

These new concepts led necessarily to theories supporting the idea that there are also planet-like bodies orbiting distant stars, i. e. extrasolar planets. In the year 1952 Otto Struve proposed methods for the detection of planet-like bodies (12). He claimed that a Jupiter-sized planet would be detectable around a solar type star simply by measuring the radial velocity oscillation of the star-planet system by obtaining the spectra of such a system. He estimated the oscillation in radial velocity of a star with a planet companion with the mass ten times of Jupiter to be 2 km/s assuming the inclination of 90°. The radial velocity method will be discussed in Section 3.5.4.

Difficulties for the detection of such Jupiter-like planet arise due to fact that planetary orbits can be oriented randomly to the observers line of sight. Also the orbital period of Jupiter, which is 12 years, makes the detection further more difficult because a potential planet must be observed for at least 12 years in order to get a full phase coverage. In addition, Struve proposed to setup the new spectroscopic survey on the binary stars in order to investigate the nature of the bodies in the system.

Struve also suggested a photometric method which is based on the fact that a Jupiter-sized planet will introduce a decrease in intensity of the stellar light when transiting in front of the stellar disc. He estimated the decrease of the intensity to be slightly less than 2% for the Jupiter-sized planet orbiting a Sun like star. Such a decrease was also possible to be measured with the photometric devices of that time. The transit method will be discussed in Section 3.5.1.

Though, the first discoveries of planets orbiting the pulsar stars have been reported in the 1990′s (13). The existence of such planets was more interesting from the planet formation aspect rather then from the aspect of hosting life on its surface.

Therefore, the search focus was thus put on the stars which are inhabiting the main sequence of F, G, K, M stellar types, and especially on the sun-like stars among them (F,G,K).

The discovery of the first extrasolar planet orbiting the main sequence star 51 Peg was reported more than ten years later by Swiss astronomers Mayor and Queloz (14). The planet had been detected by means of radial velocity oscillations measurements (RV) exactly 53 years after Struve's proposal. The oscillation amplitude of Doppler shifted absorption lines in the stellar spectra due to planet was about 59 m/s (14). The planet 51 Peg b is orbiting a G type star with a period of 4.23 days having the minimum mass of $1.2 M_{Jupiter}$ (14). That detection was a major breakthrough and the programs searching for the extrasolar planets by radial velocity measurements have been rapidly developing eversince.

Contemporary operational telescopes are equipped with modern spectrographs like ELODIE(15), SOPHIE (16) and HARPS(17) which allow to obtain a high resolution spectra with a detection limit of a few m/s. RV planet searches have since the first detection found most of the currently known planets.

The second Struve's suggestion also turned out to be correct. In 2000 Charbonneau et al. (2000) (18) reported a first detection of the transit of a known Jupiter-sized extrasolar planet around the star HD 209458. The measured decrease in intensity was as small as 1.3 millimagnitude. This opened the door to projects designed as small photometric surveys operating from the ground. Since a photometric precision of a few percents of magnitude is easily achieved with the help of small-aperture telescopes equipped with modern CCD-detectors.

Observational restrictions due to atmospheric refraction present for the ground based surveys can be avoided with a space mission such as CoRoT (19). The CoRoT mission is implemented by the French Space Agency (CNES) in collaboration with ESA and the National Space Agencies of Austria, Belgium, Brazil, Germany and Spain. The main scientific program is divided into two main parts, astroseismology and photometric search for transits of extrasolar planets. They are complemented by additional scientific topics like characteristics of variable stars. The advantage of the space mission compared to the ground based survey is a high duty cycle and a better photometric quality. CoRoT has been launched successfully on 27 December 2006. The mission will be discussed in greater detail in Chapter 3. The successor of CoRoT, NASA's Kepler space mission[2] searching for Earth-sized planets was launched in March 2009.

Characterization of systems with extrasolar planets

An important aspect of exoplanetary science is a physical description of the detected system. Here, the proper physical characteristics of the host star is essential and might help to full characterization of the reason for the observed variability. Indeed, the observed transit event might be caused due to physical stellar variability (see Chapter 2 and Chapter 3) or due to stellar companion and not necessarily by a planet.

Characteristics of planetary host stars

The ever increasing number of confirmed planets are reported around spectral types

[2]http://www.kepler.arc.nasa.gov/

F,G,K and M (excluding planets orbiting pulsar stars). These stars usually populate the main sequence in the Hertzsprungs-Russel diagram (see Figure 1.3). In this diagram the absolute magnitude against spectral type of planetary host star is plotted and the region of host stars is marked with the corresponding luminosity and temperature included. Currently, no confirmed planets orbiting stars of other spectral types then the above mentioned are known. One potentially interesting low mass object orbiting β-Pictoris (spectral type A) in 10 AU distance has been reported by Lagrange et al. (20) but further observations are needed to determine the proper nature of the β-Pictoris system.

Practical example how important is the proper physical characterization of the host star are obvious from the correlation between the metallicity of the star and the presence of the planet. Fischer et al. (2005) (21) claimed that the stars which are metal rich have a higher probability to harbor a planet. Therefore, radial velocity surveys have been selecting their target stars among the metal rich stars. Most recently, the characteristics of additional stellar hosts detected with different methods (radial velocity and transit methods) are available and, Rauer et al. (2009c) (22) among others claim that the previous planet metallicity correlation might be caused due to observational bias of the surveyed stars.

Currently, typical targets for extrasolar planets surveys are Sun-like stars. But also surveys on M-dwarfs and on giant stars may bring more light into planet system formation processes (23; 24).

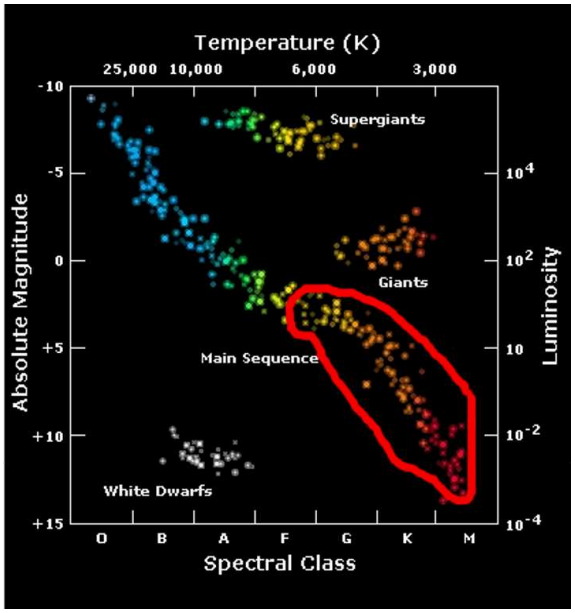

Figure 1.3: *Hertzsprung-Russel diagram. Absolute magnitude of selected star is plotted against their spectral type. Host stars for the confirmed planets can be typically found in the region of dwarf stars marked red in the diagram. Image by ESA (25).*

Characteristics of planetary systems

Figure 1.4 illustrates the development on the research field of extrasolar planet detection. Before 1995, just a few planets orbiting pulsars were known and only since the discovery of the 51 Peg b with RV method in that year, the detection rate has been rapidly increasing. The detection of the transiting planet HD209458

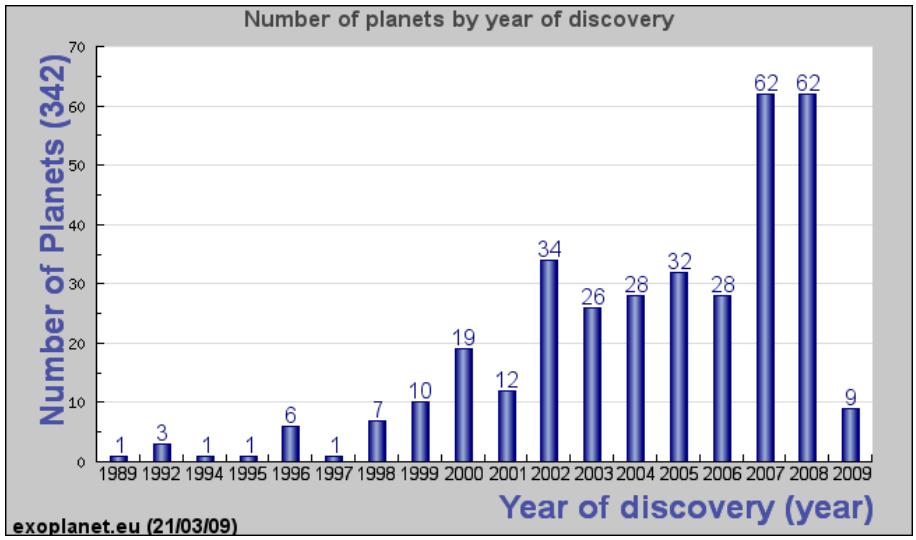

Figure 1.4: *Overview of discovered extrasolar planets since 1989. The histogram also includes pulsar planets. The first exrasolar planet around a Sun-like star was reported in 1995. Graph from Encyclopedia of Extrasolar planets (6).*

b (18) gave a positive impulse for ground based transit surveys. Few years later, towards the end of 2005 as the work on this thesis started only 9 transiting planets were known. However, only one transiting planet from that 9 was discovered with a transit survey (26). The remaining ones of discovered planets in 2005 was 176 with 5 additional pulsar planets. All 176 planets around Sun-like stars were discovered with RV method.

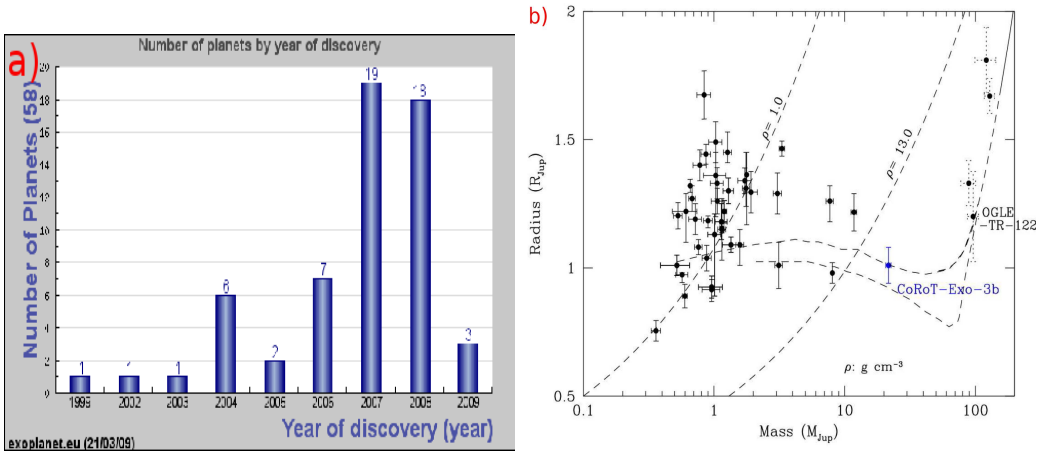

Figure 1.5: *The plot a) shows the development of planetary discoveries with the transit method. The graph b) illustrates the current mass-radius relation of transiting extrasolar planets nowadays. The graph a) is taken from the Encyclopedia of Extrasolar planets, maintained by Jean Schneider (6) and the plot b) from (27).*

A breakthrough came in 2006 and 2007 when new planets discovered by transit surveys have been reported (see Chapter 4). Up to date (5.6.2009), 59 transiting extrasolar planets are known and the distribution of the discoveries is demonstrated in the left panel of Figure 1.5. A radius vs. mass diagram of currently known transiting extrasolar planets is presented in the right panel of Figure 1.5. A gen-

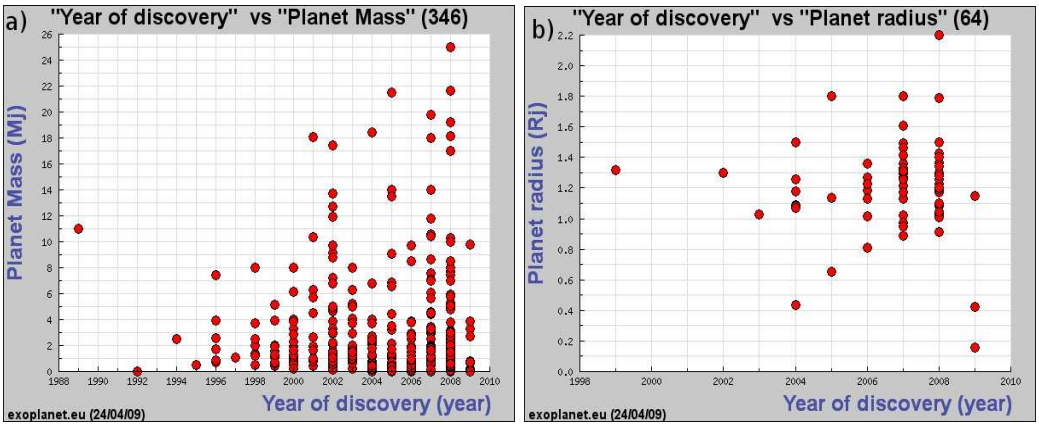

Figure 1.6: *The graph a) shows how the mass (logarithmic scale) of detected planets decreased on annual basis, due to improved sensitivity of the instruments used for the detection. Graph b) demonstrates a clear trend for the radius of detected planets. Excluding the first four planets detected around pulsars before* 1995 *the instrumentation development allowed for detections of increasingly smaller planets, the last one being the CoRoT-7b with* $1.75R_{Earth}$*. Graph taken from the Encyclopedia of Extrasolar planets maintained by Jean Schneider (6).*

eral trend of decreasing size of the detected planets over the years can be seen in Figure 1.6. The first planet around a Sun-like star 51 Peg b is about the size of Jupiter (14). The detection of the first Neptune mass planet Gl 581 b has been reported in 2005 (28). Most recently, a planet CoRoT-7b with an upper mass limit of $11M_{Earth}$ and a radius of $1.75R_{Earth}$ has been reported in (29).

1.2 Context and purpose of this work

Extrasolar planets and atmospheres at DLR

The department of "Extrasolar planets and atmospheres" of the Deutsches Zentrum für Luft- und Raumfahrt (DLR) studies extrasolar planets and investigates primitive bodies of the Solar System. In more detail the topics of interest are [3]:

- "the investigation of the icy components of comets by observations and modeling of the cometary comae"
- "the investigation of extrasolar planet atmospheres and atmospheres of Solar System bodies by numerical modeling"
- "the search and basic characterization of extrasolar planetary systems by photometric observations from space and ground"

In particular, large effort is also put into the detection and characterization process of extrasolar planets since part of the department participate in the CoRoT space

[3] www.dlr.de/caesp

mission. The CoRoT space mission is monitoring 10000 - 12000 stars per observed target field. High precision light curves can be obtained for stars in the magnitude range between 12 - 16 mag. The DLR group contributes in particular to the exoplanetary science team of the CoRoT mission with transit detection algorithms and with modeling and characterization of detected planetary systems. In addition, two medium aperture wide field-of-view (FOV) telescopes, Berlin Exoplanet Search Telescope (BEST) and Berlin Exoplanet Search Telescope II (BEST II), are operated within the BEST project. Both telescopes are used as a ground based photometric support to the CoRoT space mission.

Ground based surveys BEST, BEST II

The BEST telescopes BEST and BEST II have been designed to search for the stellar variability in the selected target fields of CoRoT space mission usually one year ahead the CoRoT's observations.

The BEST telescope monitors a 3.1° square FOV with an angular resolution of 5.5"/pixel. Millimagnitude precision can be reached for stars in magnitude range of 10 - 14 mag. The telescope is operated at Observatoire de Haute Provence (OHP) in remote mode from Berlin. Part of the results presented in this thesis are based on the observations with BEST.

The second survey telescope system BEST II monitors 1.7° square FOV with angular resolution of 1.5 arcsecond/pixel and the millimagnitude precision is reached for stars in magnitude range of 12 - 15 mag. BEST II is located at Cerro Armazones observatory (OCA), Chile, and operated from Berlin. The significant advantage of the OCA is the high number of photometric nights during the year.

Scientific justification of the project

In order to detect a transit of an extrasolar planet a high duty cycle and high precision measurement is required. These conditions are already fulfilled for the CoRoT space mission. However, observed target fields are densely populated with stars and therefore the effect of stellar crowding constraints the detection. The confirmation of the detected planetary transit event is not possible without follow-up observations. Especially, ground based photometric systems with high angular resolution such as BEST II can contribute to the confirmation of the Jupiter-sized candidates by resolving of potential background binary stars mimicking transits. Both BEST ground based surveys can monitor the target stars with high precision in the similar magnitude range as CoRoT. In addition, archived data obtained with BEST telescopes ahead of the CoRoT observations can extend the CoRoT light curves of planetary candidates. This allows to perform the investigation of e.g. transit timing variations.

BEST observations of the CoRoT target fields also provide new detections of variable stars which are interesting for the CoRoT's additional science programmes. From the extended light curves the effects of stellar spots or stellar pulsations can be investigated over longer time scales.

The high duty cycle and a high photometric quality of the data make the BEST surveys suitable for the stellar variability characterization and own transit detection programme.

Purpose of this thesis

The aim of the thesis is to describe the technical setup of the BEST and BEST II telescopes and their contribution to the CoRoT space mission and exoplanetary science. The factors influencing the ground based detection of Jupiter-sized planets will be discussed and the conclusions based on results from BEST & BEST II telescopes leading to optimization of data acquisition process will be presented.

In the scientific part, the purpose of the thesis is to present a catalog of newly detected periodic variable stars and describe the outcome from the BEST II transit survey and the BEST and BEST II contribution to follow-up observations of CoRoT's planets and planetary candidates.

1.3 Structure of the thesis

The structure of the thesis, is as follows:

Chapter 2: Variable stars

In the second Chapter the scientific background of variable stars research in respect to the BEST/BEST II observational campaigns is presented. Specifically, a variable star classification based on investigations of changes in the stellar photometric light curves are presented.

Chapter 3: Extrasolar planets and methods for their detection

In the third Chapter, the previously known extrasolar planets (hot-Jupiter and Super Earths) are described. The abundance of such system in the Universe based on observations of various survey projects and theoretical models are discussed.

In the second part of the chapter, the methods to detect extrasolar planets are discussed with a focus on the transit method and the radial velocity measurement method.

The last part of this chapter deals with the characterization of extrasolar planets. Here, the radial velocity method and transit method is compared and their complementarity nature in terms of physical characterization of the system is discussed. An essential component of the characterization of the detected candidate is the follow-up observation. Therefore the strategy of follow-up campaigns is discussed here also.

Chapter 4: Extrasolar planets surveys

Chapter 4 will provide the present status of extrasolar planets surveys both from the space and ground. The final part of the chapter is dedicated to ground based radial velocity and transit surveys searching for extrasolar planets.

Chapter 5: Theoretical background - photometric measurement

The chapter begins with an introduction to the functionality of the optical systems and detectors. The principle of CCD devices used for astronomic observations will be introduced and measurable quantities with the detectors will be defined.

In the second part of the chapter the influence of various factors on the quality of the measured quantities will be discussed. Effects influencing the uncertainty of the photometric measurement will be presented.

Chapter 6: Berlin Exoplanet Search Telescope project

In the first part of the chapter, the BEST project is described and the OHP site is introduced in terms of observation conditions. BEST technical details and operational scheme will be introduced.

In the second part of the chapter, focus is given on the BEST II robotic telescope system. A detailed description of the Observatorio Cerro Armazones site and the BEST II system is given. The operational scheme extended about technical details of BEST II is described and explained.

Chapter 7: BEST Observations and the acquired data sets

The observational strategy and the data sets on all CoRoT's target fields obtained with BEST and BEST II are presented in this chapter. The duty cycle of BEST II is compared with the BEST duty cycle. The theoretical and real detection probability of transits of extrasolar planets of BEST and BEST II telescopes is discussed and a brief comparison to a typical observational campaign of the OGLE survey is presented.

Chapter 8: Data reduction

Firstly, the data reduction process is described from acquired images to final stellar light curves. The data quality in terms of measurement uncertainties are discussed and demonstrated on BEST II observations. A more detailed analysis on correlated *red noise* is also provided.

Chapter 9: Results of BEST surveys

In this chapter the scientific results obtained with BEST and BEST II telescopes are presented. They include:

- prediscovery observations of CoRoT-1b and CoRoT-2b with BEST
- BEST II follow-up contribution to the CoRoT space mission
- a catalog of newly discovered periodic variable stars with BEST and BEST II
- transiting planetary candidates from BEST II LRa02 observations
- estimation of completeness of observational data set performed on detected variable stars
- the assumed and observed frequency of the transit detection with the used system.

Chapter 10: Summary

The last chapter presents a discussion and a summary of main results obtained with BEST and BEST II surveys.

Appendix - presents a complete catalog of newly detected periodic variable stars and description of all BEST project target fields from the nominal phase of CoRoT space mission.

Chapter 2

Variable stars

The first scientific observations of stellar variability are reported already from the years 1054, 1572 and 1604. In these particular cases supernovae were observed which showed quite large amplitude of the intensity variation. Therefore these objects could be observed by naked eyes. However, a new branch of astronomy related to variable stars gained on importance primarily in the $19th$ Century and began expanding continuously at the beginning of $20th$ Century. Observations of variable stars were supported with introducing of photography into astronomy. Illustrating the situation before the invention of photographic observations Table 2.1 summarizes 17 stars showing variability known in 1844 as presented by Argelander (30). In 1912 Annie J. Cannon mentions in her introduction to English translation of Argelander's text about variable stars that about 4000 such stars are known. That rapid increase in the number of known variable stars was due to systematic searches on photographic plates. In particular 1890 the Harvard College Observatory began with the photographic search from Massachussetts, USA and from its southern observatory in Arequipa, Peru (31). Consequently, also southern sky with its extensive Milky way regions and Magellan Clouds could be explored. Furthermore in, first models explaining stellar variations were introduced by Shapley (32) and Eddington (33) at the same time.

Currently, thousands of variable stars of various types are known and the detection rate is increasing with new monitoring space and ground based surveys. In addition, new models can precisely describe physical processes leading to observed variability. With parameters obtained from the light curve, the observed stellar system can be modeled. In combination with a spectroscopic data the nature of the stars and stellar systems can be determined. In this chapter, types of stellar variability not caused by planetary companions will be introduced.

Every star which shows changes in intensity which are not due to atmospheric or any other artificial effects is classified as a variable[1]. Different mechanisms are responsible for the intensity variation of the stellar light curve. Stars may show periodic or irregular variation. Periods may be strictly regular with span from few minutes to years or semi regular. Also random variations in the light curve are typical for some type of variable stars. However, in this thesis the focus will be on periodic variable stars.

[1]Based on definition by AAVSO - American Association of Variable Star Observers

Table 2.1: *Variable stars known in* 1844 *and a present state. Overview from (30) and (34).*

Star	Discovered by	Year
o Ceti (Mira)	Holwarda	1639
β Persei (Algol)	Monanari	1669
κ Cygni	Kirch	1687
R Hydrae	Maraldi	1704
R Leonis	Koch	1782
ν Aquilae	Pigott	1784
β Lyrae	Goodricke	1784
δ Cephei	Goodricke	1784
α Herculis	W. Herschel	1795
R Coronae Borealis	Pigott	1795
R Scuti	Pigott	1795
R Virginis	Harding	1809
R Aquari	Harding	1810
R Serpentis	Harding	1826
S Serpentis	Harding	1828
R Cancri	Schwerd	1829
α Orionis	J. Herschel	1836
4000	Cannon (30)	1912
41483	Kazarovets (34)	2008

The luminosity vs. spectral type is displayed in the Hertzsprung-Russel (HR) diagram (Figure 2.1), in addition, the effective temperature and the luminosity in solar units is shown. In the diagram, different evolutionary stages of the stars can be seen. Different stars representing prototypes for stellar variability types are shown separately in the HR. Additionally, the instability strip important for pulsating stars is marked in the central part of the diagram. Physical characteristics of the various types of variable stars can be directly derived from the HR diagram. In the following section the different types of variability will be discussed in more detail.

Conclusively, the observations of variable stars provide the information about stellar evolution. The monitoring of stellar pulsations (asteroseismology) provides the observational data for the confirmation of models of stellar atmospheres. Additionally, a stellar activity can be monitored over the long time scales. As already mentioned in particular pulsating stars can be used as candles for the determination of distances in the Universe due to their period luminosity relation (36). Binary stars on the other hand provide better understanding of N-body systems. Binary stars are also very often in close or contact systems with accretion discs. The observations of such systems may provide the better characteristics of the accretion discs, mass transfer and binary system evolution (37). Finding new variable stars enhance the knowledge about various topics of physics and astronomy.

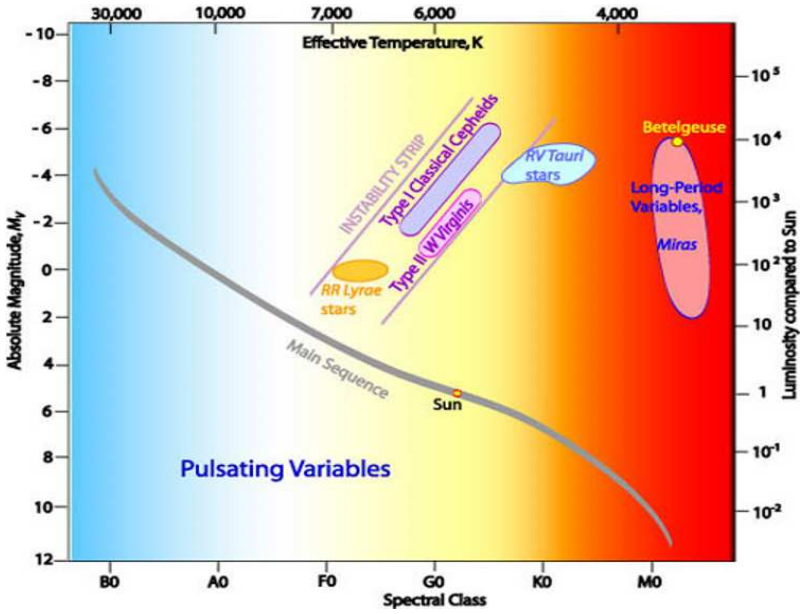

Figure 2.1: *Hertzsprung-Russel diagram with pulsating variable stars in their typical regions. Additionally, the instability strip is marked. Image taken from (35).*

2.1 Intrinsic variability

Intrinsic variable stars are showing changes in the light curve due to physical processes in the star driven by pulsations and processes in the stellar atmosphere, outbursts or in general stellar activity. Typical classes of pulsating stars are described by their prototype systems. Here a brief summary on the different types detected in BEST data sets will be presented. A more detailed description of observational characteristics of variable stars will be given in Chapter 9. The prototypes of intrinsic variable systems are:

- **δ Cephei stars**

This type of stars is represented by high luminosity pulsating stars of at maximum F spectral class, and G to K at minimum. Periods of Cepheids depend on the spectral type and their range spans from 1 to 70 days. The variation shows amplitudes between 0.1 to 2.0 mag. Typical light curve is shown in Figure 2.2. The Cepheids gained in importance after discovery by Henrietta Leavitt (1868 - 1921), who compiled a catalog of about 1700 variable stars in Small (SMC) and Large Magellanic Cloud (LMC). Assuming that the Cepheids in SMC and LMC have approximately the same distance, she found that this type of variables show a proportionality of pulsation period to apparent brightness. Therefore, the distance can be determined from the period intensity

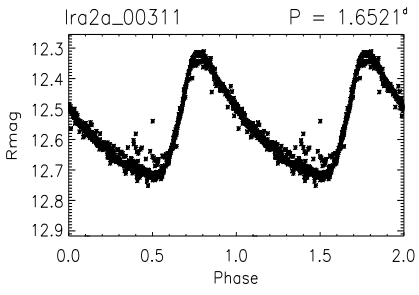

Figure 2.2: *Typical light curve of δ Cep type stars. BEST II light curve.*

relation (36) which makes Cepheids the standard candles for the measurement of distances in the Universe.

- **RR Lyrae stars**

RR Lyr stars are pulsating white giant stars of typically spectral type A. RR Lyr stars are normally less massive and older than Cepheids. Periods range from 0.2 to 1.0 day and typical amplitude variations span from 0.2 to 2.0 mag. RR Lyr show also a strict period-luminosity relation. A typical light curve is shown in Figure 2.3.

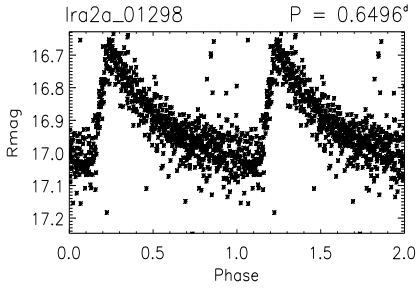

Figure 2.3: *Typical light curve of RR Lyr type stars. BEST II light curve.*

- **δ Scuti stars**

These stars are residing in Hertzsprung-Russel diagram near the crossing of instability strip with main sequence. Typical spectral types of δ Scuti stars are between F8 to A2. Luminosity classes range from dwarfs (V) to sub-giants (III). Periods values are in the range of 0.03 to 0.3 day. Typical amplitude values are below 0.1 mag. Typical light curve is shown in Figure 2.4.

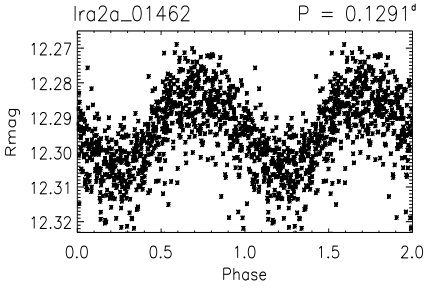

Figure 2.4: *Typical light curve of δ Sct type star. BEST II light curve.*

- **Mira stars**

These stars with long periods from 80 to 100 days are cool stars of M, C and S spectral types. The amplitude variation shown are from typical 2.5 to 5.0 mag. Furthermore, Mira type stars can be resolved due to their typical emission lines pattern in their spectra. A typical light curve shape is shown in Figure 2.5.

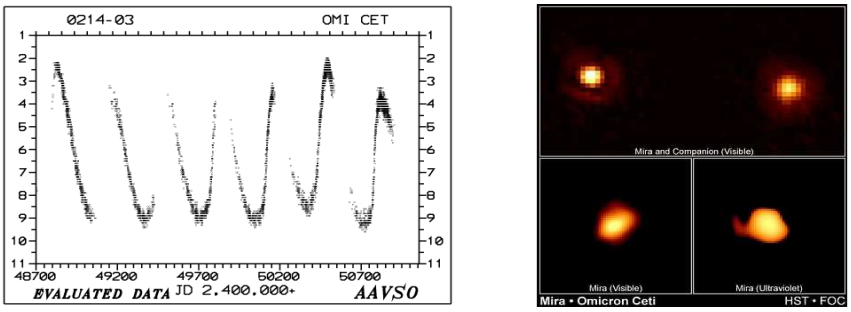

Figure 2.5: *Typical light curve of a o Ceti star (Mira) and its resolved direct image. Figures by AAVSO (38) and HST (39).*

2.2 Extrinsic variable stars

Extrinsic variability is caused by an eclipse of a companion or by spots on the stellar surface. Eclipsing systems consist of two or more stars gravitationally bounded. If the inclination of the orbital plane is favorable for the observation of eclipses from Earth, regular minimums in the light curves are present. Prototype systems are:

- **Algol stars - β Persei prototype**

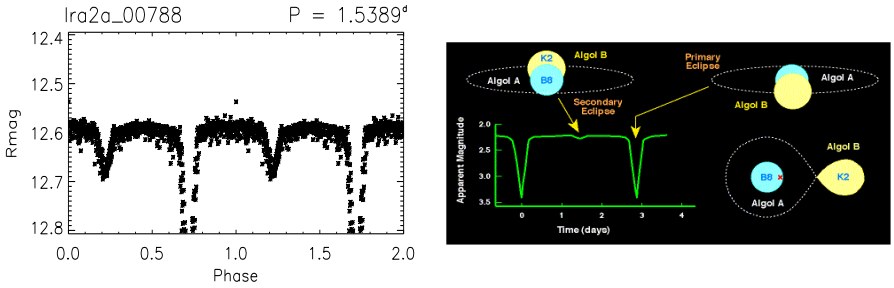

Figure 2.6: *Typical light curve and geometry of an Algol type system. BEST II light curve and image by (40).*

The first observations of these stars were made in 18^{th} Century by J. Goodrick who explained the nature of the light curve variation in 1784 (41). These stars are usually forming close binary systems which orbit each other. Therefore, period ranges are from a few hours to a few days with some exceptions as ϵAur (42). Amplitudes may be as high as one magnitude. A typical light curve and a geometry of the Algol-type system is shown in Figure 2.6.

- **β Lyrae stars**

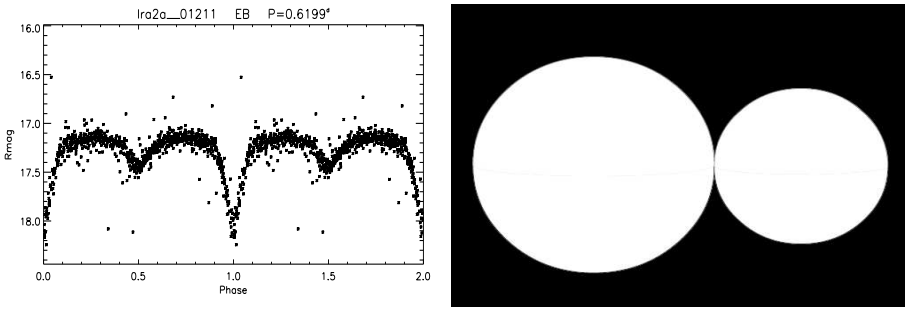

Figure 2.7: *Typical light curve and geometry of β Lyr type stars. Image by BEST II and (43).*

These stars are forming very close and hot binary systems with deformed stellar shapes due to gravity interaction. Orbital periods are within a few days, however with some exceptions. Amplitude variations are typically below 1 mag. Typical light curve and the system configuration is shown in Figure 2.7.

- **W UMa stars**

They are binary systems with components of equal spectral type usually main sequence (W UMa consists of two F type stars). However, the components may posses different masses. These stars are contact systems with shared envelopes. Typical periods are shorter than 1 day and longer than 0.2 day. Amplitude variations range from tenths of mag up to 1 mag. Due to equivalent spectral types of both stars the primary and secondary minimum are of approximately same depth. The typical light curve is shown in Figure 2.8.

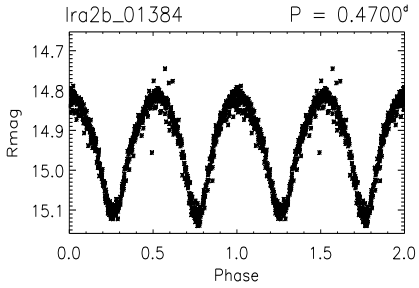

Figure 2.8: *Typical light curve of a W UMa system. The difference to β Lyr stars is due to different spectral type and therefore temperature of stars. Figure from BEST archive.*

- **Rotating and ellipsoidal stars**

These types of stars show small changes in their light curves due to stellar spots on their surfaces. Often these stars can be found in binary systems. Rotating stars form a subgroup of the eclipsing systems. Typical light curve of a spotted star is displayed in Figure 2.9. An introduction into modeling of the spotted stellar surfaces can be found in (44).

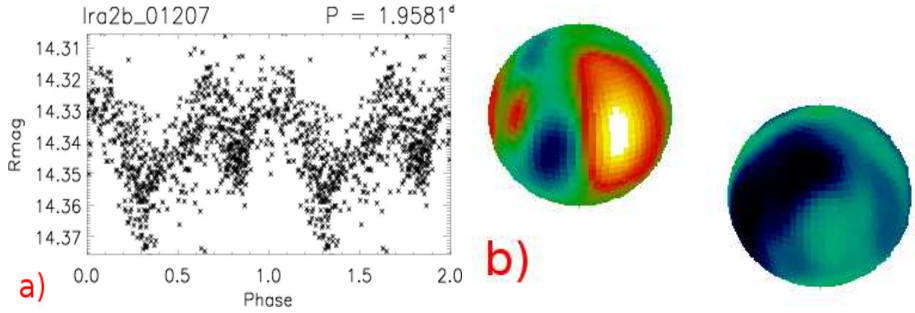

Figure 2.9: *Typical light curve of a spotted star is shown in Figure a). A model of a spot displayed in Figure b). Figure a) was taken from BEST II data archive and Figure b) is by (44).*

Additional special types of stars are irregular, semi-regular, eruptive, symbiotic and cataclysmic stars with disks. The latter star types are in particular supernovae and novae or dwarf novae binary systems with an accretion disk. The variations in the light curves of such stars may be very irregular and random. The phases of outbursts can take just few months and then the star enters the quiescence phase or outbursts can repeat depending on the nature of the system. These stars are also contained in the data sets of BEST and BEST II surveys, however, they are out of the scope of this thesis since only periodic variable stars will be presented.

2.3 Implications for stellar characterization and transit surveys

The correct characterization of stellar variability type is essential also for detections of extrasolar planets. In principle, the system showing an eclipse of a star by a planetary companion can be also classified as variable. Indeed, the star HD209458 with its transiting planetary companion can be found in the General Catalog of Variable Stars (GCVS) (45) as variable $V376Peg$.

Low amplitude background variable stars may be contaminant sources for the transiting planetary candidates. The light curve of a candidate can contain the variability from the close variable star and therefore lead to false identification (false positive). Potential source of difficulties due to variable stars will be discussed in more detail in Chapter 3. Additionally, more detailed discussion of sub stellar eclipsing objects with low amplitudes will be presented in the same chapter.

Chapter 3

Extrasolar planets and methods for their detection

Planets are in comparison to their host star small and hard to detect. The largest planet in our Solar System, Jupiter, has a radius of 10% of R_{Sun}, but due to long orbital period of about 12 years it would not be easily detectable from large distances. The first detections of extrasolar planets showed surprisingly that also Jupiter-sized planets with close-in (< 0.05 AU) orbits exist. Nowadays, more than 300 planets have been discovered. Before a detailed description of the detection methods, an overview on curently known types of extrasolar planets will be given in this chapter. In the second half of this chapter, detection methods will be discussed and compared with focus on photometric transit detection method, since this thesis work was concentrated on photometric ground based surveys with BEST and BEST II telescopes. The last Section of this chapter is dedicated to characterization of extrasolar planets, in particular the measurement of the thermal radiation from a planet.

3.1 Low mass stellar and substellar objects

The important parameter which distinguishes between stars, substellar objects and planets is the mass. Figure 3.1 summarizes the masses and surface temperatures of the object types from a sun-like star to a planetary companion.

Low massive star or substellar object?

Red dwarfs are very cold main sequence stars which are very common in the solar vicinity (46). Low masses, ongoing hydrogen fusion and spectral types of late K or M (see Figure 1.3) are their main characteristics. The minimum mass limit of these main sequence stars is given by $75M_{Jupiter}$ (47). Below this mass, hydrogen fusion reactions in the core of a main sequence star with a solar composition can not occur. A slightly different mass limit is the case for objects with zero metallicity which would have the limiting mass for hydrogen fusion about $90M_{Jupiter}$ (47).

Brown dwarfs

Brown dwarfs are very cold substellar objects with masses less than approximately $90M_{Jupiter} - 75M_{Jupiter}$ (47). The lower mass limit for brown dwarfs is approximately $13M_{Jupiter}$ which is the limiting mass for the fusion of Deuterium (48). Less massive

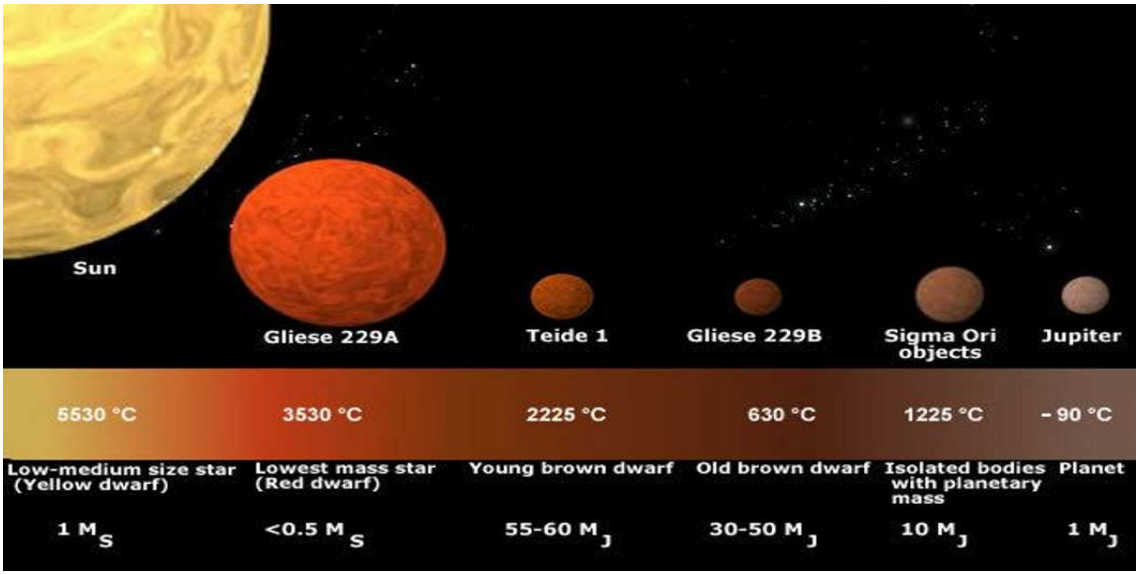

Figure 3.1: *The difference between Solar type stars, M-dwarf stars, brown dwarfs and planets is demonstrated in the Figure. Typical temperatures of Sun likes stars are approx.* 6000 *K, on the other hand brown dwarfs are very cold with temperatures down to a few hundred K. Image by ESA from courtesy of R. Rebolo, IAC, Spain (25).*

objects are known as planets (see IAU definition in Chapter 1) but the border line between brown dwarfs and planets is not clearly defined. In addition to usual spectral classes, a new spectral class L has been established for brown dwarfs with effective temperatures from 2000 K to 1400 K (49). Very cool dwarfs with effective temperatures below 1400K are classified separately as T-dwarfs or Methane dwarfs firstly presented by Nakajima et al. (1995) (50).

The first brown dwarf, in the Pleiades cluster has been reported by Rebolo et al. 1995 (51). Martín et al. 1999 (52) reported the discovery of small separation brown dwarf pair with HST. Several similar systems have been discovered by Koerner et al. (1999) (53). A very interesting brown dwarf was detected by the CoRoT space mission as reported by Delueil et al. (2008) (27).

Further observations of these intriguing objects are needed in order to fully understand the differences in formation of brown dwarfs and planets.

3.2 Hot Jupiters

The first planet of this type is 51 Peg b (14). It is a planet with orbital period of 4.23 days and a diameter of $R_{Jupiter}$ orbiting a solar type star on almost circular orbit. The minimum mass was estimated to be $0.468 M_{Jupiter}$ and the proximity to its host star indicates a high surface temperature about 1300 K. Many similar planets of this type have been discovered since the initial detection (54; 55; 56) and their characteristics can be summarized as follows. A hot-Jupiter like planet has a mass similar or larger than Jupiter ($M_J = 1.8 \times 10^{27}$kg) and orbits its host star usually at a close distances $\ll 1AU$ in a few days. Jupiter sized planets with close-in orbits are the most common detected exoplanets because of their easy detectability with

various methods from the ground. On the other hand, some exceptional cases are known among Jupiter-like planets. They are on very eccentric orbits such as 70 Vir and 16 Cyg B with eccentricities $e = 0.4$ and $e = 0.687$, respectively (57). Interesting is also the system 47 UMa with its orbital period of 3 years and an eccentricity of $e = 0.09$. Thereby very similar to Jupiter but, with a smaller semimajor axis (2.1 AU) and slightly higher mass ($2.4 M_{Jupiter}$ - all parameters from Butler&Marcy 1996 (58)). No other planets were found in the system of 51 Peg but we already know a few systems consisting of more than one planet such as 47 UMa or Gl 581 (59; 60; 61).

Following the first planetary detections many ambitious plans attempting to characterize the planetary atmospheres have been presented. Typical surface temperatures on a hot-Jupiter type planet can reach more than $1000K$ (62). The estimated densities imply a gaseous state or at least an atmosphere which is similar to that of the gas giants in our Solar System. Indications for the composition of the atmosphere were obtained mainly by spectroscopic measurement during the transit event, showing signatures of Hydrogen (63). Additionally, with the development of spectroscopic observational techniques elements like Carbon, Oxygen (64) and water (65) have been recently reported. Due to the proximity to the host-star, tidal forces deforming the planetary atmosphere are expected (66) and the probable effect is also the evaporation of the atmosphere as it is in the case for HD 209458 b (67) and as described in general in (68; 69).

Nowadays, the smallest known hot-Jupiter (hot-Neptune) GJ 436 b has a radius of about $0.438 R_{Jupiter}$ and actually possesses a mass of $1.2 M_{Neptune}$ (70). From the present statistics it is clear that hot-Jupiters are quite common in the Universe (see Section 3.4). But what happened to the smaller planets?

3.3 Towards the Earth's twin - Super Earth planets

Small planets of terrestrial type differ from the giant gas planets by their size, mass and composition. Planets with masses of 1 up to $10 M_E$ are called super Earths (71; 72) and Valencia et al (2007) (71) puts constraints on the radii of super Earths which should be maximal 12200 km ($\approx 1.9 R_{Earth}$) for a 10 M_{Earth} planet. These small planets should consists primarily of rocks, iron and planetary ice (72) and are very interesting with respect to potential extraterrestrial life as we know it from Earth.

How can we determine whether the detected planet might be habitable? The easiest way is to search for the environments which may contain liquid water. Liquid water is on Earth one of the main elements necessary for life how we know it. The presence of water (H_2O) is obvious in the Earth's spectra (see Figure 3.2 b) as observed from the space.

An indication for the presence of life is so called biomarker, providing the signature of biological activity such as living organisms. The most important biomarkers are methane (CH_4) or oxygen (O_2) and ozone (O_3). The boundaries for a planet which

may possess water in liquid state are practically given by the orbital parameters and by the spectral type of the host star. The zone where H_2O is liquid is called a habitable zone (73). In Figure 3.2a) habitable zone is demonstrated in dependence on the spectral type of the host star. The first step to a discovery of a habitable planet is to find an Earth twin in terms of size and mass. The second step would be to identify such a planet in a habitable zone. The ultimate confirmation of whether a life form may be present on the planet would be the spectrum of the atmosphere (see Figure 3.2 b) identifying above mentioned biomarkers.

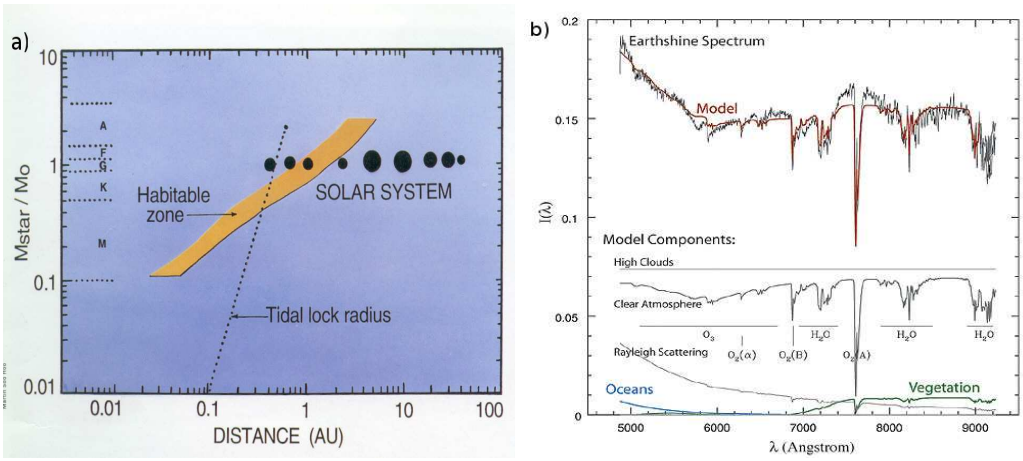

Figure 3.2: *Figure a) presents the distance of the habitable zone dependent on spectral type of the main sequence host star (Kasting et al. (1993) (73). Figure b) presents a modeled spectrum of Earth compared with measured spectrum. Main contributors to the shape of the spectra can be seen. Figure was taken from Woolf et al. (2002) (74).*

Recalling from Chapter 1, the currently smallest planet in terms of radius was detected by the CoRoT space mission reported in February 2009. The planet CoRoT 7b has a radius of $1.75R_{Earth}$ and the upper mass limit of $11M_{Earth}$ (29). Before CoRoT 7b, the smallest planet in terms of radius with $5.5R_{Earth}$ was found by Beaulieu et al. (75). This planet is a rocky planet orbiting a M-dwarf $0.22M_{Sun}$ star at a distance of 2.6 AU. Orbital distance and spectral type of the star implies that the planet is not located within a habitable zone. Small planets in terms of planetary mass were reported most recently by Mayor et al. (2009) (61). The authors report on the detection of 3 super-Earths with minimum masses of 4.2, 6.9 and 9.2 M_{Earth} orbiting the K2V star HD 40307. The same team reported two planets, with a minimum mass $5.03M_{Earth}$ and $8M_{earth}$ respectively, orbiting the star Gl 581 in 2007 already. The system contains a previously detected Neptune-mass planet (28). Additionally, one of the both small planets was believed to be located at the edge of the habitable zone (60). Precise examination of the planetary environment however excluded the previous assumptions of habitability (76). Currently, it is believed that both small planets are located close to the habitable zone but outside of it (77).

Undoubtedly, the search for a small planet located in the habitable zone is one of the main science goals in the near future.

3.4 How many stars harbor planets?

How typical is a sun-like star (F,G,K) harboring a hot-Jupiter planet (semimajor axis (a_{planet}) < 0.1)? A single-team search (Marcy et al. (2005)) (78) reported a $16/1330 = 1.2\%$ frequency which is close to a frequency of $22/850 = 2.6\%$ obtained from the uniform data set reported by Fischer & Valenti (2005) (21). The numerator in both expressions represents the number of detected hot Jupiters and the denominator represents the number of surveyed stars. These numbers are discussed by Greaves et al. (2007) (79) and are in fair agreement with their model prediction of 1% frequency for hot Jupiters. For other Jupiter mass planets in distances > 0.1 AU from their host stars the frequency of $76/850 = 8.9\%$ has been reported by Fischer & Valenti (2005) (21). Extending the orbital distance, Marcy et al. (2005) (78) found a range from $72/1330 = 5.4\%$ within 5 AU up to an extrapolation of 11% within 20 AU. This is consistent with Lineweaver & Grether (2003) who estimated the number of sun-like stars hosting Jupiter-sized planets ($M \sin i > 0.1 M_{Jupiter}$ and $P < 60$ years) to reach up to 22% (80).

Recently, a statistics on small sized planets was presented by Mayor et al. (2009) (61). The authors report the first estimates of the detection frequency of Neptune or rocky planets around G and K dwarfs based on HARPS data. They propose frequency of $30 \pm 10\%$ in narrow range of periods shorter than 50 days.

The main limitation for a statistically correct prediction of frequencies of stars harboring planets is based on the low number of detected systems. Especially, statistics of small-size planets (Super Earths) is lacking. Therefore, the frequencies derived from the observations and subsequent models need to be considered as preliminary. Nevertheless, the abundance of hot-Jupiters (approximately 1%) is of special importance for transit surveys, since these type of planets is most easily detectable from the ground.

3.5 Methods of detecting extrasolar planets

In this section the methods to detect extrasolar planets will be introduced and discussed. Currently, almost all methods are based on either gravitation interaction of a planet-star (dynamical effects) system, or a decrease in the stellar brightness due to an eclipse event caused by the planet. On the other hand, direct imaging of extrasolar planets is gaining on importance due to the development of adaptive optics instruments. A summary of the methods and their success in terms of planet detections is presented in Figure 3.3 (81). In the figure three main branches of planetary detection methods are present:

- Photometric measurements
- Dynamical effects
- Gravitational microlensing

The first two points include transit and radial velocity method (RV). These particular methods are in the focus of this thesis, because the results from ground based

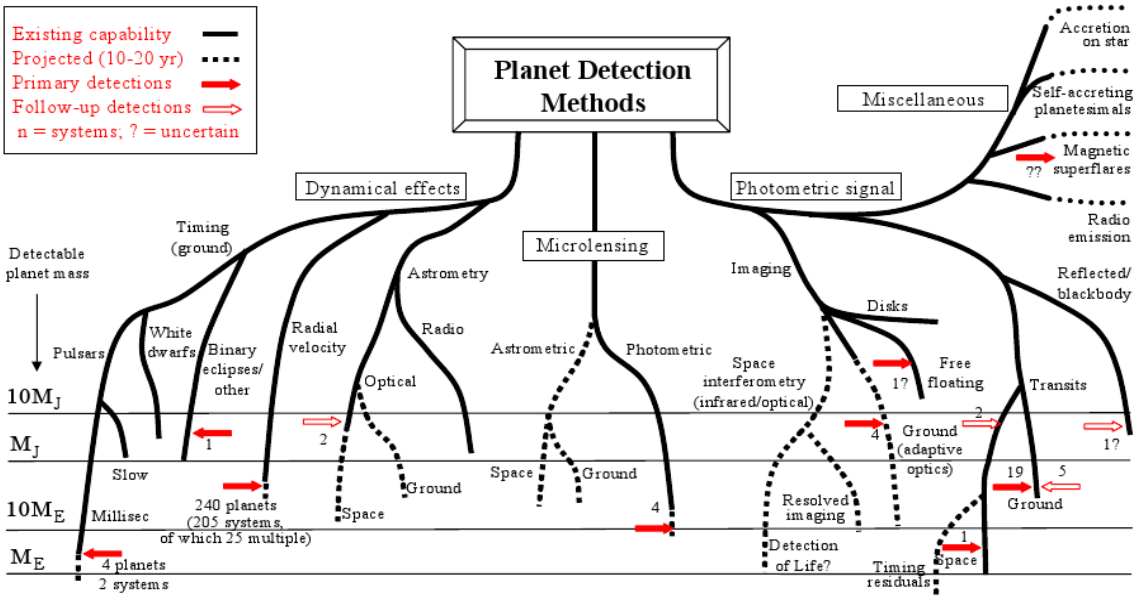

Figure 3.3: *Comparison of the methods of exoplanet detections presents the numbers of detected planets with these methods. Future methods are represented with a dashed line. Figure taken from (81).*

survey telescope BEST and BEST II will be presented. The RV method is complementary to transit detection and can help to fully characterize the planetary system (see Section 3.6.1). In Section 3.5.3 some other detection methods will be discussed briefly.

3.5.1 Transit method (TR)

The first suggestions about this method were raised by Struve (1952) (12). The basic idea is that if the host star possesses a planetary companion that can move in front of the stellar disc, this eclipse will introduce a decrease of the stellar intensity for the duration of the passage which can be observed from great distances. The first transit of an extrasolar planet HD 209458 b was observed by Charbonneau et al. (2000) (18) and is shown in Figure 3.4.

When can we observe a transit?

Assuming that the system contains a planet (see Section 3.4), the orientation with respect to an observer is the important factor for the successful detection expressed by the geometric probability (ψ_{geom}). The geometric probability of a planetary transit in front of a star is determinated by the semi-major axis (a_{pl}), eccentricity (e), radius of the planet (R_{planet}), longitude of periastron (ω) and by the radius of the host star (R_{star}) as (82):

$$\psi_{geom} = 0.0045 \left(\frac{1AU}{a_{pl}}\right) \left(\frac{R_{star} + R_{planet}}{R_{Sun}}\right) \left[\frac{1 + e\cos\omega}{1 - e^2}\right] \tag{3.1}$$

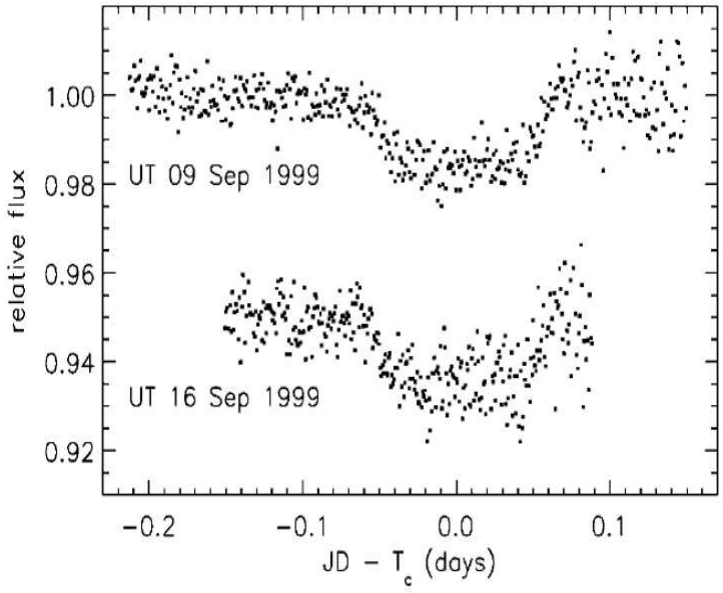

Figure 3.4: *The light curve of the first observed transit of an extrasolar planet around sun-like star HD 209458. Image taken from Charbonneau et al. (2000) (18).*

For the simplified case of a circular orbit ($e = 0$) and $R_{star} \gg R_{planet}$ the geometric probability becomes:

$$\psi_{geom}^{circular} = \frac{R_{star}}{a_{pl}}. \tag{3.2}$$

It is clear from (3.2) that the geometric probability for finding a planet increases with decreasing semi-major axis thus favoring the detection of hot Jupiters on close-in orbits. In Figure 3.5 geometric probability of a transit of a planet at a circular orbit is explained schematically. In general, ψ_{geom} expresses the fact that the transit can be observed only if the planet is projected on the stellar disc as seen by an observer.

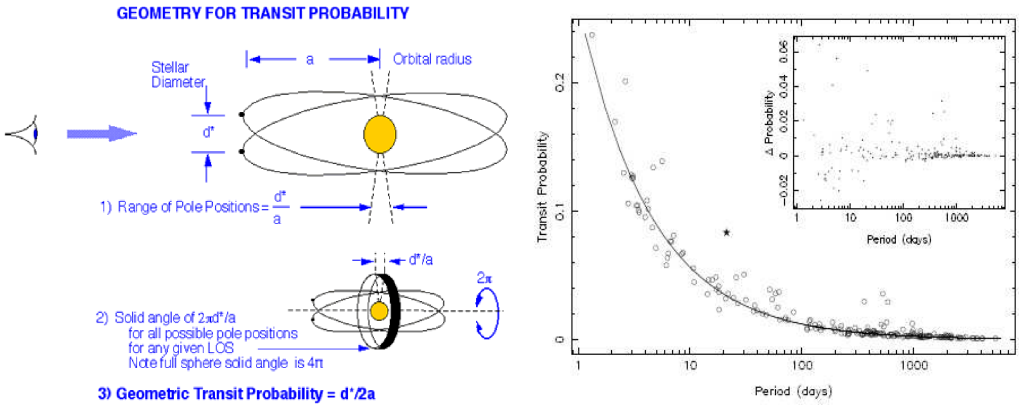

Figure 3.5: *Figure on the left provides an explanation of the geometrical probability ψ of a planetary transit. Image by NASA. Figure on the right presents the geometric probability for* 200 *planets detected with RV method. Image taken from Kane & von Braun (2008) (83).*

The geometric probability puts constraints on detection limits of the transit method what is illustrated with a right panel of Figure 3.5). The geometric probability ψ_{geom} decreases with the orbital period of the planet. A transit of a giant hot-Jupiter planet like 51 Peg b has about 10% geometric probability. If 1% of all stars in the Galaxy would harbor a similar giant planet then we would need to observe at least 1000 stars in order to be able to detect a transit. The Earth would cause a decrease in intensity of the Sun of approximatelly 8.5×10^{-3}% an the transit would take 13 hrs (see Table 3.1). Currently, such measurement precision can be reached only with space missions such as CoRoT or Kepler. On the other hand the detection of hot-Jupiter sized planet is now easier with CCD detectors, having a large field-of-view which can observe several thousands of stars at once with a high duty cycle. Therefore, the detection of the transit event is more likely with such instruments, including wide field-of-view ground based surveys observing from locations with excellent weather conditions. A geometric probability for the planets in the Solar System is summarized in Table 3.1.

Table 3.1: *Transit depth, transit duration and geometrical probability of planets in our Solar system. Values by NASA.*

Planet	P (yrs)	R_{planet} (km)	a_{pl} (AU)	ψ_{geom}	δ	Δt (hrs)
Mercury	0.241	2439.7	0.39	1.19	1.2×10^{-5}	8.1
Venus	0.615	6051.8	0.72	0.65	7.6^{-5}	11.0
Earth	1.000	6378.1	1.00	0.47	8.4×10^{-5}	13.0
Mars	1.880	3397	1.52	0.31	2.4×10^{-5}	16.0
Jupiter	11.86	71492	5.20	0.089	0.0101	29.6
Saturn	29.5	60268	9.5	0.049	0.0075	40.1
Uranus	84.0	25559	19.2	0.024	0.00135	57.0
Neptune	164.8	24764	30.1	0.015	0.00127	71.3

Observable parameters

Parameters of the transiting system can be derived from the observed light curve. A typical light curve during the transit event is illustrated in Figure 3.6. The derivables from the light curve are:

- **Ingress and egress** - events are described in Figure 3.6 by times $t_{ingress} = t(c) - t(b)$ and $t_{egress} = t(f) - t(e)$. The shape and duration of the ingress and egress part depends on the projected latitude on the stellar disc described by inclination angle (i).
- **Transit depth (δ)** - is described by the intensity decrease of the stellar flux due to planet. The amplitude during the eclipse phase in the flat part is expressed as:

$$\delta \propto \Delta I = \frac{I_{out} - I_{transit}}{I_{out}} \propto \frac{R^2_{planet}}{R^2_{star}} \tag{3.3}$$

  where R_{planet} and R_{star} are the radii of a planet and a host star, respectively. This formula is an approximation assuming that the luminosity of the stellar disc is uniform without stellar spots and limb darkening.

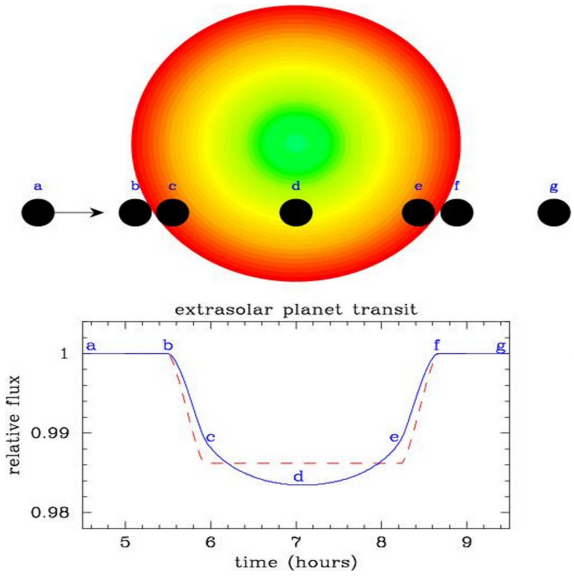

Figure 3.6: *Characteristic shape of the light curve during the transit event. Transit begins with ingress phase when the projected planet disc touches the stellar disc at time $t(b)$. Flat phase of transit begins when the projected planetary disc moves to phase $t(c)$. Transit event ends with egress $t(e)$ and last contact of the projected planetary disc with the stellar disc $t(f)$. The dashed line represents uniform intensity distribution of the stellar disc. Solid line displays the observed shape of the light curve due to limb darkening effect. In this particular case the transit of HD 209458 b is presented. Image by Sullivan & Sullivan (2003) (84).*

- **Transit shape** - during the eclipse phase the shape of the transit is given by (85):

$$I(p,z) = 1 - L(p,z) \tag{3.4}$$

where

$$L(p,z) = \begin{cases} 0 & 1+p < z \\ \frac{1}{\pi}\left[p^2\kappa_0 + \kappa_1 - \sqrt{\frac{4z^2-(1+z^2-p^2)^2}{4}}\right] & |1-p| <\leq |1+p| \\ p^2 & z \leq 1-p \\ 1 & z \leq p-1 \end{cases} \tag{3.5}$$

d is the distance of the centers of mass of star and planet, z is defined as d/R_{star} and $p = R_{planet}/R_{star}$. The second case corresponds to the ingress and egress part of the eclipse whereas the third case in Equation (3.5.1) corresponds to the flat part of the transit (see Equation (3.3)). Coefficients in Equation (3.5.1) are given by:

$$\kappa_0 = \cos^{-1}\left[(p^2+z^2-1)/2pz\right]; \kappa_1 = \cos^{-1}\left[(1-p^2+z^2)/2z\right] \tag{3.6}$$

As for the transit depth ΔI for the transit shape the effects of the limb darkening are neglected in Equation . Usually, the limb darkening need to be taken

into account in particular for high S/N light curves. The effect of limb darkening on the transit shape is demonstrated in Figure 3.7. Theoretical transit depths caused by planets with radius $R_{planet} = 1.3R_{Jupiter}$ (corresponding to HD 209458 b) for different spectral types of the host star are summarized in Table 3.2. It can be seen that the transit depth increases with the spectral type of the host star going from smallest (0.92%) for a F0V stars to the highest (6.63%) for M0V star.

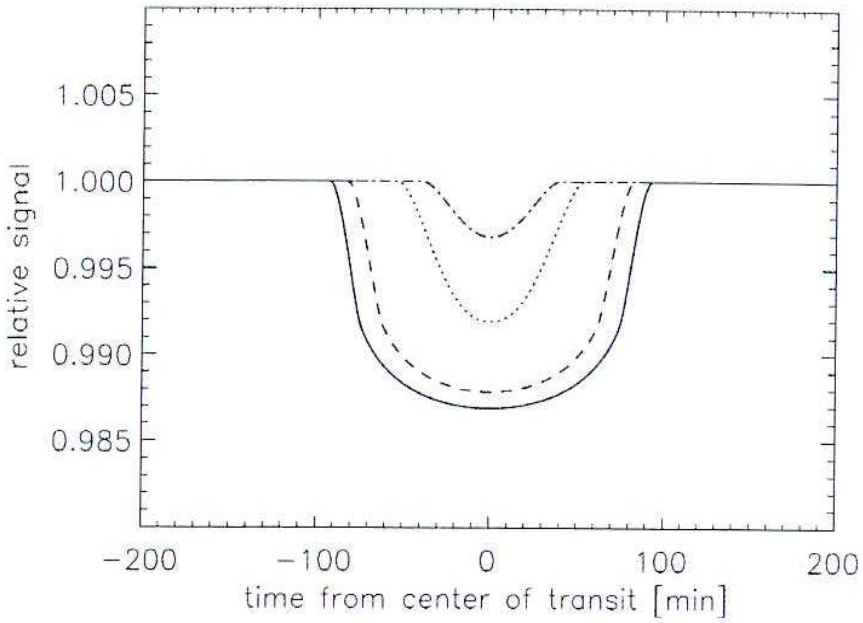

Figure 3.7: *Limb darkening effect for a central transit (solid line) to a grazing eclipse (dashed). Image taken from Voss (2006) (86).*

Table 3.2: *Theoretical transit depth for planet with radius of* $1.3R_{Jupiter}$ *with/without quadratic limb darkening coefficients (87) in R-band filter according to Voss (86). The G2V star corresponds to the Sun.*

Star	δ (%)	δ(%)(limb darkening)
F0V	0.75	0.92
F5V	1.00	1.20
G0V	1.39	1.69
G2V	1.69	2.08
G5V	1.99	2.46
K0V	2.34	2.98
K5V	3.28	4.50
M0V	4.70	6.63

- **Transit duration (Δt)** - is defined as the time between a first and last contact of the projected planet and stellar disc. Therefore it can be defined as $\Delta t = t_4 - t_1$. The exact form of transit duration Δt is derived from the geometry of the star-planet system and given by (88)

$$\Delta t = 2\sqrt{\frac{1-(\rho\cos i)^2}{(R_{star}+R_{planet})^2}}(R_{star}+R_{planet})\frac{\sqrt{1-e^2}}{1+e\cos\Phi}\left(\frac{P}{2\pi GM}\right)^{1/3} \tag{3.7}$$

here, G is the gravitational constant, and ρ is the star-planet distance at the time of transit, corresponding to a phase Φ and e is the eccentricity of the planetary orbit. The approximation of the transit duration for circular orbits has a form

$$\Delta t_{circ} \approx \frac{PR_{star}}{\pi a}\sqrt{\left(1+\frac{R_{planet}}{R_{star}}\right)^2-\left(\frac{a}{R_{star}}\cos i\right)^2} \tag{3.8}$$

where P is the orbital period, a is the orbital radius and R_{star}, R_{planet} are the stellar and planetary radii, respectively.

- **Planetary inclination** i - can be determined from the formula:

$$i = \arccos\left(\frac{R_{Star}k_{min}4\pi^{2/3}}{GM_{StarP^2}^{1/3}}\right) \tag{3.9}$$

where k_{min} is an impact factor defined by (89) and G is the gravitational constant.

3.5.1.1 Transit timing variations (TTV)

Transit timing variations can be used in connection with the transit method to detect additional planets in the planetary system. If a planet circles a star on a Keplerian orbit, then the transit event occurs according to multiples of an orbital period. In case when additional bodies or planetary rings are present in the system the orbit is no longer Keplerian. Small wobbles caused by either:

- a) second (or more) undetected planet
- b) planetary rings
- c) moons orbiting the transiting planet, trojan planets

would cause a difference in transit timing (see Figure 3.8) because the system orbits the common mass center which is not exactly in the center of the host star. Investigating the observed (O) deviations σ_{TTV} of j transit times t_j from the calculated (C) times given by multiples of orbital period (P) characterizes the magnitude of the perturbation. Mathematically is σ_{TTV} defined as

$$\sigma_{TTV} = \frac{1}{N}\left[\sum_j^N (t_j - t_0 - jP)^2\right]^{1/2} \tag{3.10}$$

where P and t_0 are chosen to minimize σ_{TTV}. Here, t_0 is the epoch of the first transit, j is the transit number and N is the number of transits observed. Example

of a plot with observed and calculated times (O-C), from which the σ_{TTV} might be determined, is presented in Figure 3.8. The absolute value of change in timing of a transit due to perturbing object depends on the planetary system characteristics. In particular, the masses of the disturbing and transiting planets, the orbital velocities and the semi major axis will influence the transit timing variations (90; 91; 92). Additionally, if the periods of the planetary system is in resonance the perturbation will be amplified. For resonant planets the differences between transits may reach up to a few minutes over a time span of one year (90) (see Table 3.3).

In Agol (2005) (90) an example of a system consisting of a hot Jupiter with 3 days period is perturbed by a lighter exterior planet at a circular orbit. Periods of planets are in 2 : 1 resonance. Such a system could cause the maximal deviation in the transit timing of about 3 minutes over 5 months. A modeled cycle of a transit timing changes is shown in Figure 3.8. Table 3.3 summarizes the changes in transit timing for different systems. It can clearly be seen that the TTVs are large if the perturbing object is large or if the orbital periods of the system are in resonance.

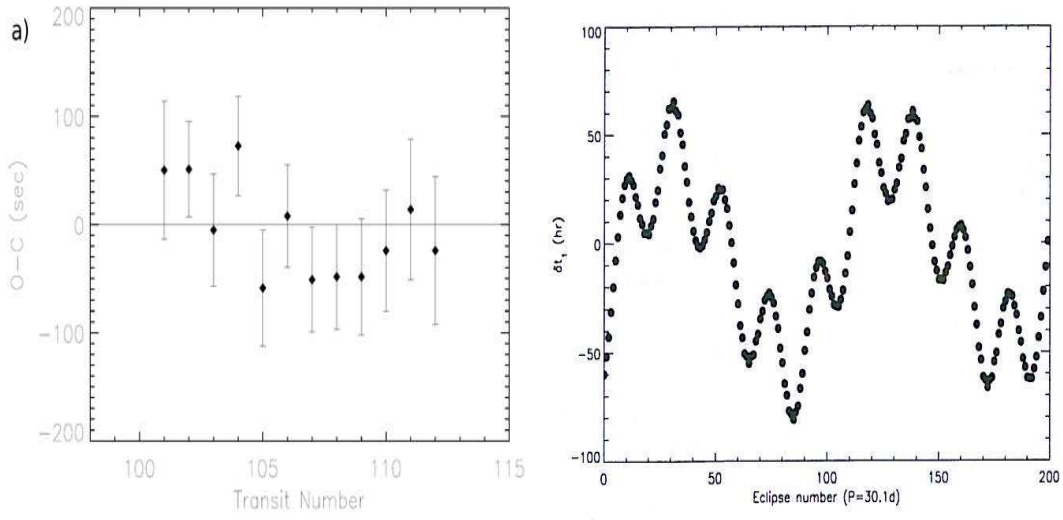

Figure 3.8: *a) O-C diagramm for HD 189733 b (Miller-Ricci et al. (2008) (93)). b) TTVs for Gliese 876c. Image taken from Steffen (2006) (91)*

Table 3.3: *Values for TTVs for different systems according to Kirste (2008) (92)*

System	TTV ($\pm min$)
Jupiter-Earth system	0.5
Earth-Pluto system	10^{-7}
Earth-Venus system	21
Neptune-Pluto system (3:2 resonance)	
transiting Neptune	1175
transiting Pluto	6×10^{7}
Hot-Jupiter with Earth (1:2 resonance)	7×10^{-4}
Sun-Earth-Moon system	15.2

3.5.1.2 Overview on transit method and TTV

The photometric detection of a transit provides information about transiting system. Direct observable is the light curve which shows the decrease of the intensity during the transit event. Parameters of the planetary systems, obtainable with either transit method, TTV or observation of the secondary eclipse (see also Section 3.6.3) are summarized in Table 3.4. First two columns describe the parameter and the third column states how it can be determined. Parameters directly derivable from the light curve or from the fit of the eclipse part of the light curve are marked "light curve fit/folded light curve". Parameters which need an additional information are commented properly. Furthermore, for some parameters additional input obtained from the follow-up observations with different methods is needed. Such parameter is a planetary radius (R_{planet}) for which the information about the star is needed, temperature of the atmosphere (T_{atm}), planetary mass (m_p) and planetary density (ρ_p). Additionally, the parameters obtainable with TTV method are included.

Table 3.4: *Overview on parameters obtainable with transit method, TTV and from secondary eclipse observations.*

Parameter		derived from	Reference
Orbital period	P	folded light curve	
Transit depth	δ	light curve fit	(85; 89)
Transit duration	Δt	light curve fit	(89; 88)
Flux ratio	ΔI	light curve	
Planet to stellar radius ratio	R_{pl}/R_s	from flux ratio	
Planetary radius	R_p	$R_p = R_s\sqrt{\Delta I}$	
Inclination	i	light curve fit, secondary eclipse	(89)
Eccentricity	e	secondary transit	(94)
Planetary mass	m_p	i, $m_p \sin(i)$	
Planetary density	ρ_p	R_p,m_p	
Temperature of the atmosphere	T_{atm}	secondary eclipse, albedo	(94)
Transit timing variation	σ_{TTV}	O-C curve	(90; 92)
Additional planets, moons, rings		transit timing variation	(90; 92)

3.5.2 Radial Velocity method (RV)

The radial velocity (RV) method for planetary detection is based on the dynamic effect caused by the planetary companion. An additional planetary companion causes that the barycenter of the system moves outwards from the center of the star (see Figure 3.9). RV oscillations due to the planet can be determined from the shift of observed stellar spectral lines. However, the shift of spectral lines for star-planet system is much lower than for e.g. a star-star system. The first extrasolar planet around the sun-like star 51 Peg b was discovered with help of this method (14) with measured RV oscillations amplitude of $59m/s$ (14). For the comparison, Jupiter causes an amplitude in the radial velocity of the Sun of about $12.5m/s$ with a period of 11.9 years. Earth on the other hand causes an amplitude of $0.1m/s$. Current operational instruments are able to reach a precision of about $3m/s$ [1]. Moreover, difficulties will arise for the measurements which require a precision better than $1m/s$. Here, the influence from the stellar atmosphere as short period pulsation (96; 97)

[1] HARPS at La Silla, Chile

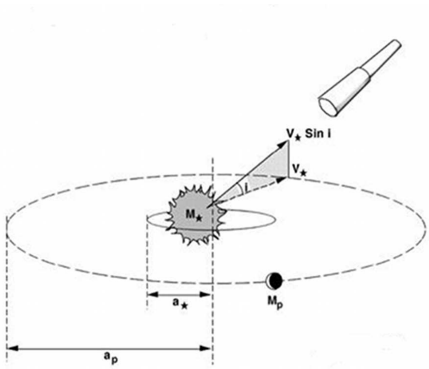

Figure 3.9: *Mass of the hidden planet shifts the barycenter of the system outwards from the center of the star. Star is thus orbiting the new barycenter and its radial velocity can be measured from the ground for the favorable values of inclination angle i. Image by University of Geneva (95).*

begin to influence the RV curve and it is no longer possible to decide whether the RV is caused by the planet or by the stellar atmosphere.

Observable quantities

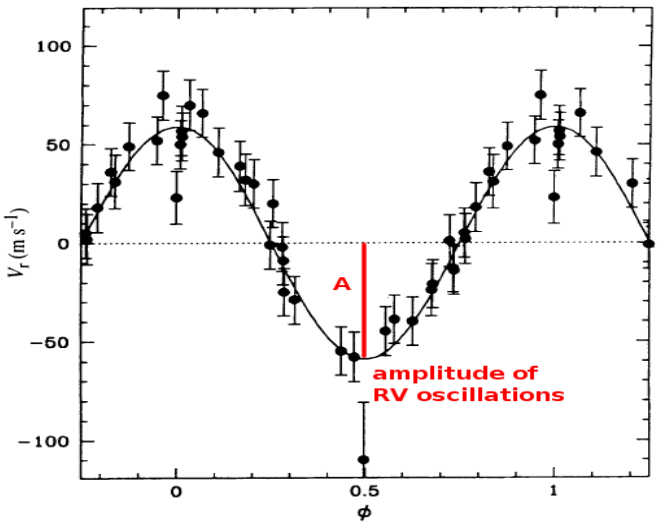

Figure 3.10: *RV curve of 51 Peg b. A N-planet system would show more complex RV curve. Image taken from Mayor & Queloz (1995) (14).*

Direct observable quantity is the radial velocity of the star at different times. The values of the radial velocity are obtained from the stellar spectra taken for each measurement point. The radial velocity oscillations in time are presented in Figure 3.10. The following parameters can be determined directly from the measurements:

- **Orbital period** (P) - can be determined directly from the shape of the RV curve. It is defined as a time difference between two equivalent phases (see Figure 3.10).
- **Amplitude of RV oscillations** (A) - can be directly determined from the RV curve (see Figure 3.10).

Further parameters characterizing the system can be derived from the observables. The amplitude A caused by the planetary companion is given by (98)

$$A = \left(\frac{2\pi G}{P}\right)^{1/3} \frac{M_{planet} \sin i}{(M_{planet} + M_{star})^{2/3}} \frac{1}{\sqrt{1-e^2}} \tag{3.11}$$

where M_{star}, M_{planet}, is the mass of the star and the planet, respectively, P is the orbital period of the planet, e is eccentricity and i is an inclination angle. The period (P) given in years is related to semimajor axis (a_{planet}) by using the Kepler's third law as:

$$P = \left(\frac{a_{planet}}{1AU}\right)^{3/2} \left(\frac{M_{star}}{M_{Sun}}\right)^{-1/2} \tag{3.12}$$

In the simple case of the circular orbit and if $M_{star} \gg M_{planet}$, the equation (3.11) simplifies to:

$$A = \left(\frac{2\pi G}{P}\right)^{1/3} \frac{M_{planet} \sin i}{(M_{star})^{2/3}} \tag{3.13}$$

A main limitation of the RV method is, that the information about the planetary inclination can not be obtained. This makes an absolute mass determination impossible. Only a lower mass limit M_{lower} can be determined as:

$$M_{lower} = M_{planet} \sin(i) \tag{3.14}$$

Another important information obtained from the spectrum is the spectral type of the host star. This has a direct impact on the follow-up observations (see Section 3.6). Properly determined spectral type can put constraints on the nature of the system. All parameters obtainable with the RV method are summarized in Table 3.5.

Table 3.5: *Overview on physical characteristics of planetary systems provided by the RV method.*

Parameter		determined from
Spectral type of host star		stellar spectrum
Amplitude of RV oscillations	A	RV curve
Orbital period	P	RV curve
Minimum mass	M_{lower}	$M_{pl} \sin(i)$
Eccentricity	e	fit of the RV curve

3.5.3 Other methods

In Figure 3.3 it can be seen that other detection methods such as gravitational microlensing and astrometric method make use of dynamical effects. They will be presented here. Furthermore, a method of direct imaging will be presented. This method is gaining more importance with the dynamical progress of adaptive optics to minimize the influence of Earth's atmosphere.

Microlensing method

A signal from a distant star can be magnified due to gravitational lens as described by Einstein (99). The principle of the microlensing method is shown in Figure 3.11. If a star with a planet is eclipsing a background star, the light of the background star is magnified by the star-planet system. However, the probability of a suitable alignment of objects is very small (10^{-6} for the lensing by the galactic halo (100)). This fact can be compensated by observations of very large number of stars. The advantage of the method is that it is sensitive to find planets with very low masses orbiting their host stars at close-in orbits (1-5AU). However, the disadvantage is that the configuration of the star-planet system and of the background star will never repeat itself. Therefore, further observations of the detected systems are not possible with this method. The smallest planet found with help of this method is a rocky planet at $5.5M_{Earth}$ and orbiting a host M-dwarf star at 2.6AU (75).

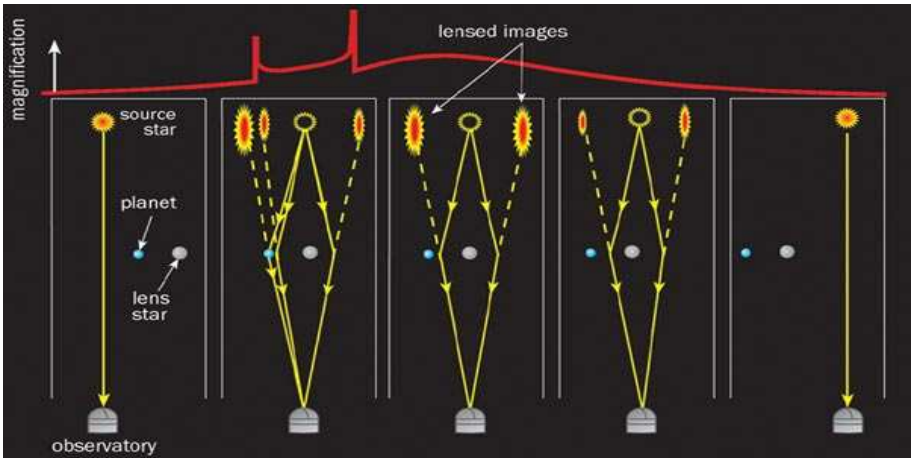

Figure 3.11: *Principle of the planet detection by microlensing method. Image taken from physicsworld.com (101).*

Astrometric measurements

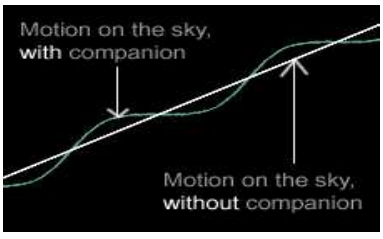

Figure 3.12: *Principle of astrometric method. Image from (81).*

A planet orbiting a star causes a shift of the barycenter outwards from the stellar center. Consequently, projected stellar trajectory on the sky is not a straight line, but instead a sinusoidal curve. This is illustrated in Figure 3.12. The shape of the projected trajectory is given by the mass of the planet M_{planet} and M_{star} star and by the semimajor-axis of the planet. The disadvantage of this method is that the precision of the astrometric measurement of a few miliarcsec must be achieved in order to measure the perturbation of the projected trajectory of a Jupiter seen from 10 pc. On the other hand, this method is sensitive for planets orbiting at a great distance from their host star. However, currently no planet has been confirmed and only one planetary candidate was reported (102). However, the required precision should be reached with GAIA space mission[2] to be launched in 2011 (103).

[2]http://gaia.esa.int/

Direct imaging

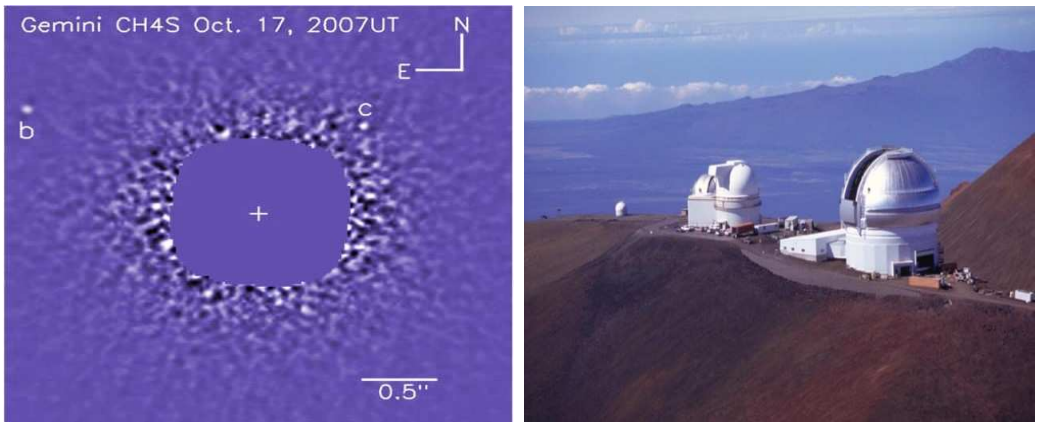

Figure 3.13: *a) Multiple planetary system detected by GEMINI and KECK telescopes. Two detected planets are marked with letters. The third planet is not in field-of-view of the image. b) GEMINI North observatory at Hilo, Hawai. Image by Gemini and Keck observatories.*

Planetary companions are unfortunately much fainter than their host stars. Therefore, a direct image of an extrasolar planet in the light reflected from its host star is a challenging quest. The brightness ratio between a Sun like star and a Jupiter-like planet is about 10^{-9} in the maximum elongation. Therefore, the planet signal is blended by the stellar signal. In addition, planet-star angular separation is normally below the seeing resolution of the ground based observatories. An extensive development of instruments which can correct for the influence of the atmosphere is ongoing (104). Also a coronoghraphy method when the stellar image is subtracted and only planetary signal remains is developing quickly (105). The progress of direct imaging can be illustrated with the discovery in Figure 3.13, presenting the most recently detected multiple planetary system with GEMINI North and KECK instruments equipped with adaptive optics. The system consists of three planets with masses from $7M_{Jupiter}$ to $10M_{Jupiter}$ (106).

3.6 Follow-up observations of candidates and extrasolar planets

3.6.1 Complementarity aspect of RV and transit method

In the previous section the transit method and the radial velocity method for detection of extrasolar planets were described. The observable and derivable parameters from Table 3.6 give an overview of the results which can be obtained with these methods. It can be seen in Table 3.6 that for a full characterization of the detected system, observational data obtained with both methods are needed. This is in particular the case of the determination of accurate planetary mass and planetary radius for which a spectral type and radius of the star is also needed. On the other hand, some particular planetary parameters obtained with transit method can be

confirmed with radial velocity method and vice versa. This can be illustrated with the case of the first transiting planet HD 209458 b found. This system was detected with RV method by (107) who put constraints on the lower mass limit and predicted the transit events but the full characterization of the system was impossible. Later a transit was successfully observed and the exact mass could be determined (18).

Another important aspect of the RV and transit methods is their complementarity during a follow-up observation of candidates. With both methods combined false detections can be identified. The strategy will be discussed in the next section.

Table 3.6: *Planetary parameters derivable with radial velocity (RV) and transit method (TR).*

Parameter	Method	Reference
Orbital period	RV, TR	(88; 81)
Transit depth	TR	(88)
Transit duration	TR	(88)
Planetary radius	TR+RV (spectrum)	
Inclination	TR	
Planetary mass	RV+TR	
Planetary density	RV+TR	
Characteristics of the atmosphere	TR+RV	(94)
Spectral type of the host star	RV (spectrum)	

3.6.2 False positive detections

The cause of the transit event in the light curve does not necessarily need to be due to a planetary companion. Such case of misidentification is called *false positive* detection. Typical cases of false positive detections are exemplified in Figure 3.14. They include

A - Grazing eclipse of an optical binary - two physically separated stars in the line of sight mimicking the transit event
B - Variability of the star - such as stellar spots introducing the transit shape due to stellar rotation
C - Low mass stellar companion or brown dwarfs - see Section 3.1
D - Background eclipsing binaries including triple system - eclipsing star in the background and/or unresolved physical triple system introducing false transit signal to the light curve of a planetary candidate

A good example for the confirmation process of the planetary candidate is the approach used by the CoRoT space mission (19). The detected transit events of candidates are followed-up with photometry, low resolution spectroscopy and high resolution spectroscopy (RV).

The photometric follow-up

The photometric follow-up observations (108; 109; 110) are carried out with instruments having high angular resolution to resolve the effect of the stellar crowding. Stars which are influencing the flux of their close neighbors (in the CoRoT resolution) might produce the transit like shape in the light curve. The higher angular

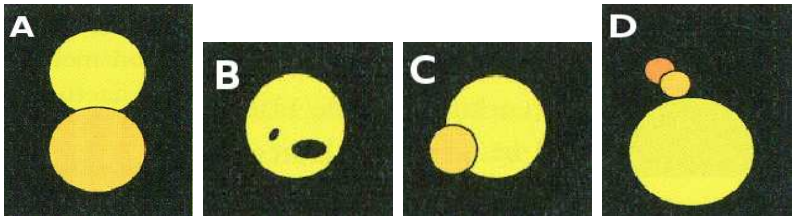

Figure 3.14: *Possible sources of false positive identification: A - Grazing eclipse of an optical binary, B - Variability of the star, C - Low mass stellar companion or brown dwarfs, D - Background eclipsing binaries including triple system. Images by Ruth Titz (DLR).*

resolution separates single components and the star causing the transit like shape of the light curve can be identified.

Photometric method is also capable to distinguish the special case of unresolved triple system which might be composed from the candidate and unresolved background binary mimicking the transit shape. The high angular resolution photometry from the ground separates between the candidate star and the unresolved binary system.

Most efficient photometric technique in both cases is the on-off photometry. The principle is to perform a few observations of the system during the out of transit phase and compare them with observations made during the "in-transit" phase (108). This photometric technique is highly efficient in terms of use of telescope time since more candidates can be observed simultaneously.

Low resolution spectroscopic follow-up

Already one measurement in low resolution mode spectroscopy can rule out the case of a grazing eclipse, since physical binary stars would posses common spectral lines what is not the case for optical binary systems. The nature of the system can be resolved from the spectral characterization of the star and from the knowledge of $v \sin i$ which could indicate a possible synchronization with a massive companion (110). This type of follow-up observations rules out the high-mass components.

As an example, the case of low massive stellar object or brown dwarf can be confirmed from the spectral lines from already two low resolution spectra (110; 109).

High resolution spectroscopic follow-up (RV)

High resolution spectroscopic follow-up is performed with very stable spectrographs like HARPS (17) which can detect the oscillation in radial velocity from few m/s. These measurements can confirm low-massive planetary objects and in some cases rule out the stellar variability (109). The precise RV method was described in Section 3.5.2.

3.6.3 Characterization of the planetary atmospheres - secondary eclipse

The secondary eclipse occurs when the planet is moving behind the stellar disc. Then, the thermal radiation from the planet can be directly measured. The comparison of the total flux, when the planet is out of from the eclipse phase can be

compared with the flux, when the planet is behind the stellar disc. The decrease in the total flux is the thermal radiation of the planet. Since the planetary temperature of hot-Jupiters might reach 10^3 K, therefore their peak of radiation is in infra-red (IR) wavelengths. Therefore, the intensity decrease will be maximal in IR wavelengths and can reach a few millimagnitudes for a hot-Jupiter like planet. On the contrary, the secondary eclipses in the visible light would show the intensity decrease of a few micromagnitudes, which is undetectable from the ground. The typical primary eclipse (planet transiting in the front of the stellar disc) show signal decrease of about 1% for a hot-Jupiter planet. Therefore, the IR range is most suitable for the measurement of thermal radiation from the planet during the secondary eclipse.

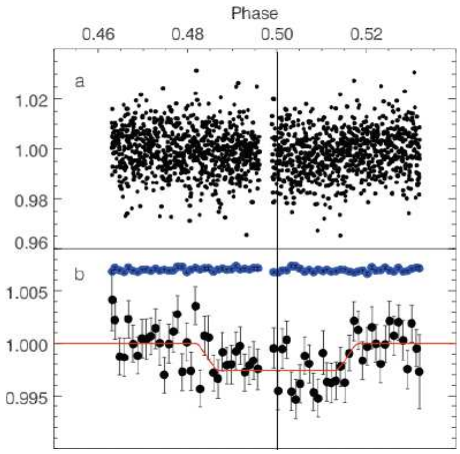

Figure 3.15: *Secondary eclipse of HD209458b observed with Spitzer at 24μm. Deming et al. 2005 (111)*

The first attempt to observe the secondary eclipse has been performed from the space with the Spitzer infrared satellite. The thermal radiation of planets HD 209458 b and *TrES-1* (111; 94) has been successfully measured (see Figure 3.15) at different IR wavelengths. There were also several attempts to measure the intensity decrease during the secondary eclipse from the ground. The first successful detection from the ground has been reported by Sing et al. (2009) (112), Snellen & de Mooij (2009) (113) and Alonso et al. (2009) (114). Based on these observations, further conclusion about the planetary atmosphere can be achieved (111). Furthermore, the eccentricity of the planet can be determined from the timing of the secondary eclipse with a higher accuracy than with RV method (94). Such non-zero eccentricity implies an extra source of excitation such as another planet or tidal forces forming the planetary atmosphere (94; 114) which need to be determined with further spectroscopic follow-up observations.

Chapter 4

Extrasolar Planets Surveys

This chapter gives an overview on the present space and ground based extrasolar planet surveys. Strategies of the surveys will be described and compared. As already mentioned, a proposal of a survey focused on detection of extrasolar planet was raised already in 1952. Nevertheless, the first transit searches started to operate in the very beginning of the 21^{st} Century. Since then, numerous ground and space based projects have been designed and set-up and they will be described in the first part of the chapter which is being dedicated to space missions and in particular to the CoRoT space mission. In the second part the most successful ground based surveys will be described.

4.1 Extrasolar planets from the Space before CoRoT space mission

The Hubble Space Telescope[1] (HST) launched in 1990 consists of a 2.4-m primary mirror. The telescope is equipped with various instruments with Wide Field and Planetary Camera 2 (WFPC2) and Space Telescope Imaging Spectrograph (STIS) being the most important instrument for the extrasolar planets surveys. The host star HD 209458 was observed with STIS in 2000 during the transiting event (115). High precise light curve obtained with HST is presented in Figure 4.1.

In frame of the "Sagittarius Window Eclipsing Extrasolar Planet Search" (SWEEPS) programme a dense stellar field in direction to the center of the Galaxy was observed continuously for 7 days in 2004. The SWEEPS survey detected transit events in 16 from total number of 180000 stellar light curves (116). However, the follow-up observations in order to confirm the nature the detected events are nearly impossible due to stellar crowding and faintness of the objects. Only two out of 16 candidates have been confirmed as a planet with the help of RV follow-up observations (116).

[1] http://hubblesite.org

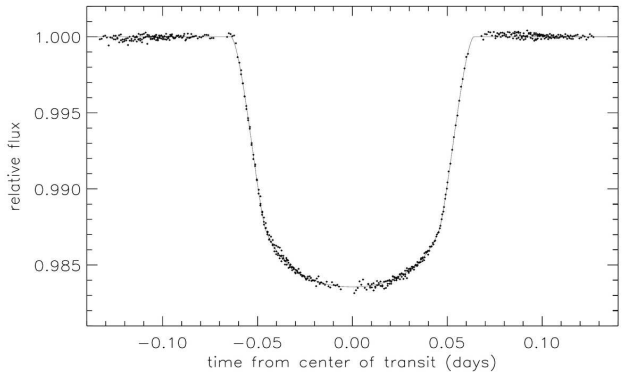

Figure 4.1: *Stellar light curve of the HD 209458 during the planetary transit obtained with STIS HST. Image taken from Brown et al. (2001) (115).*

4.2 The CoRoT space mission

CoRoT (**Co**nvection **Ro**tation and **T**ransit) is an international[2] space satellite mission led by the French space agency CNES (19). The CoRoT mission performs observations of stellar pulsations (asteroseismology) of selected stars and photometric searches for transit events caused by extrasolar planets. In addition, a programme on "additional science" is performed on dedicated objects, including variables, binaries, etc. The mission was launched on the 15th of December 2006.

CoRoT in brief

The CoRoT satellite consists of a 27-cm aperture telescope with the $2.70° \times 3.05°$ field-of-view (FOV). A high duty cycle of almost 90% and a photometric precision of 7×10^{-4} micromagnitudes (117) makes CoRoT suitable to search for low amplitude variations in stellar light curves. Half of the total FOV is dedicated to asteroseismology and the other half is dedicated to the exoplanetary science.

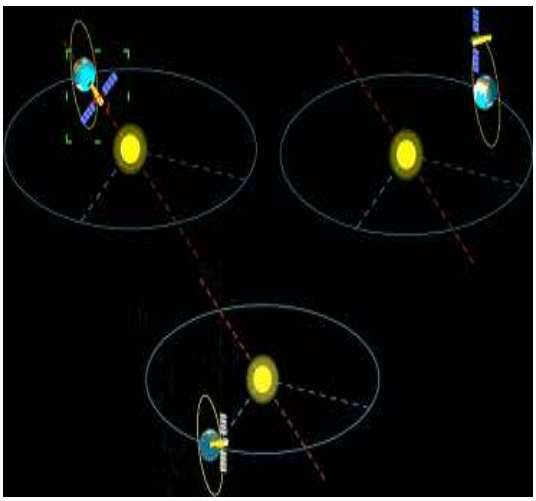

Figure 4.2: *Pointing of the CoRoT satellite. Image by CNES.*

The CoRoT satellite is orbiting the Earth on a polar orbit, which puts constraints on the observation programme. The target field can be observed only for a maximum of 5 months, before the satellite would be blinded by solar light. Therefore, the satellite can observe one field continuously only for a maximum of 150 days. The principle of the satellite pointing is shown in Figure 4.2.

CoRoT in detail

The satellite consists of telescope which is connected to the PROTEUS platform where the equipment is installed. The external cylindrical baffle protects the tele-

[2]ESA, Austria, Belgium, Brazil, Germany, and Spain

scope against the stray light from the Earth. The optical system consists of two parabolic mirrors mounted off axis. A schematic overview of the optical setup is presented in Fig4.3.

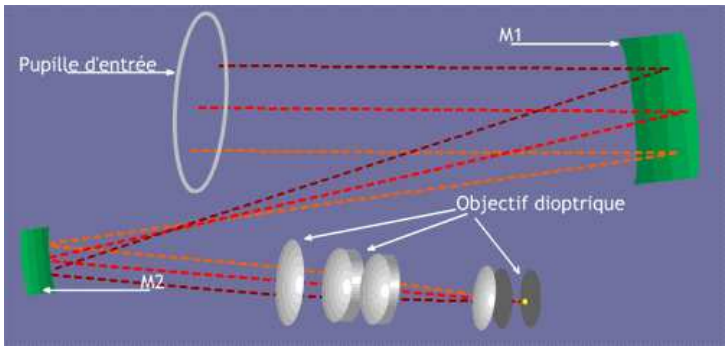

Figure 4.3: *Optical setup of CoRoT instrument. Image by CNES & (118).*

Four 2K×4K CCD segments sensitive in optical wavelengths are used for imaging. One segment containing two CCDs detectors is dedicated to extrasolar planets and the other similar segment is dedicated to asteroseismology. Point spread function (PSF) of a solar type star with 5.7 mag star detected with the asteroseismology CCD part is about 400 pixels due to defocussing and the PSF of exoplanetary CCD is about 70 pixels prisms for a K2 star with 13 mag (119). The light detected with exoplanetary CCD segments is dispersed due to a small prisms mounted in front of the detector. Therefore, the data are obtained in three different color channels (120) which do not have direct correspondence with any standard photometric systems. A frame from an exoplanetary CCDs with three "colors" is shown in left Figure 4.4

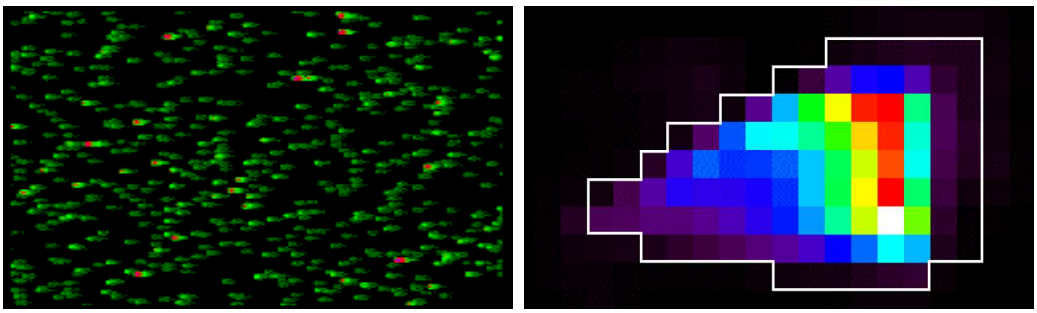

Figure 4.4: *Left Figure shows the signal coming through the prisms. Right image presents an example of a stellar mask. Image by CNES (121) and (118).*

The use of prisms in the exo-channel should prevent false positive alarms caused by the misidentification of the variability type. In some particular cases, a light curve of the observed star can show transit-like patterns which might be the case of stellar spots or when the star is pulsating. The color information should be able to distinguish between these false positives since the variability due to e.g. stellar spots is different in different colors. On the other hand, stellar PSFs are broadened due to prisms and planetary candidates need to be followed-up in order to confirm the true nature of the variability since the unresolved object from the vicinity of the candidate can be mimicking the transit event. Additionally, due to hardware

limitations approx. only $10000 - 12000$ stellar masks were prepared for the observed objects. These masks are divided into groups which are characteristic for different spectral types of observed stars. An example of such mask is presented in right Figure 4.4.

Observations

Due to the mission design, the observations for the nominal phase are organized into 6 long run (LR) targets which are observed for about 150 days, one initial run (IR) observed for 30 days. In addition, a few short runs (SR) are observed for maximum of 60 days. One pair of long run stellar fields is located in the direction to the Galactic center (LRc01, LRc02) and the second pair is located in the anticenter direction (LRa01, LRa02). Two areas from which target fields are selected (the CoRoT-eyes), are displayed in Figure 4.5. Short run fields are observed in the time when the change of the instrument's pointing is prepared. Selected target fields are populated by stars with an optimized dwarfs to giant ratio. In Figure 4.6 an observed field IRa01 is shown on the left and the stellar distribution of the bright stars in the field is on the right. An overview on the observed initial and long run fields is presented in Table 4.1 (short run fields are excluded).

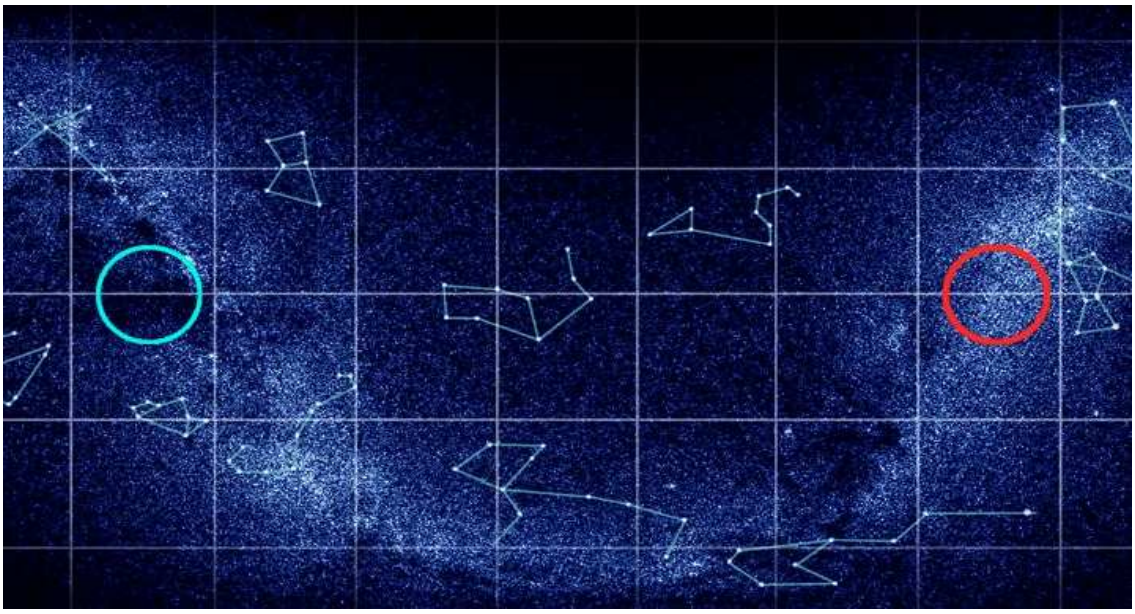

Figure 4.5: *The region of CoRoT eyes. All the CoRoT fields and thus also the BEST/BEST II fields are selected within these two regions. Red circle represents fields marked with "anti-center" and light blue circle represents fields marked as "center". Image by CNES (121).*

Table 4.1: *Initial run and long run fields observed with CoRoT (excluding short runs).*

Field	α	δ	Observed
IRa01	$\alpha = 06^h\ 57^m\ 18^s$	$\delta = -01^\circ\ 42'\ 00"$	2007
LRc01	$\alpha = 19^h\ 23^m\ 33^s$	$\delta = +00^\circ\ 27'\ 36"$	2007
LRa01	$\alpha = 06^h\ 46^m\ 53^s$	$\delta = -00^\circ\ 12'\ 00"$	2007/2008
LRc02	$\alpha = 18^h\ 38^m\ 38^s$	$\delta = -06^\circ\ 24'\ 00"$	2008
LRa02	$\alpha = 06^h\ 54^m\ 14^s$	$\delta = -04^\circ\ 22'\ 48"$	2008/2009

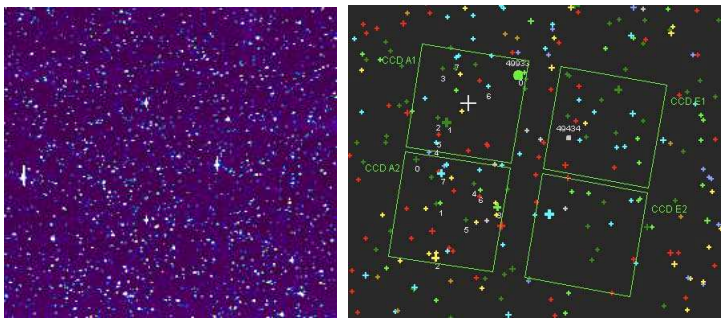

Figure 4.6: *A CoRoT image of a field IRa01 (left). CCD structure of CoRoT with stars in the FOV from a catalog (right). Images by CNES (121).*

Organization of the exoplanetary science activities

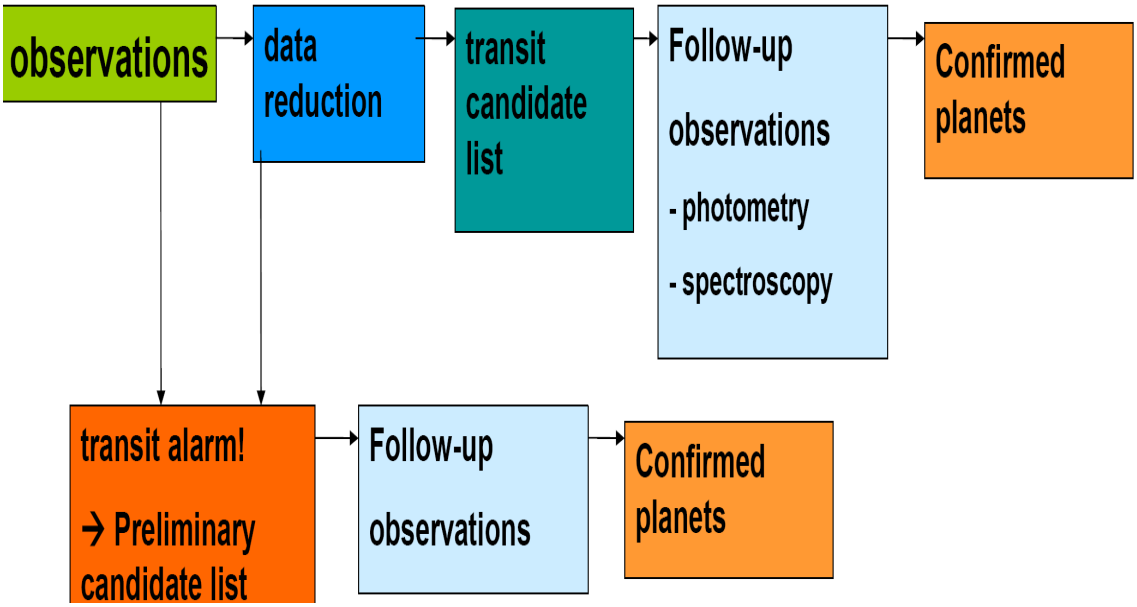

Figure 4.7: *The CoRoT mission organization scheme begins with observation of the selected target fields. The scheme presents the steps from the delivery of the data to co-investigators to confirmation of planets.*

The exoplanetary science activities are conducted by CoRoT Exoplanetary Science Team (CEST) consisting of Co-Investigators from different institutes located in participating countries. Figure 4.7 presents a scheme how the detected candidates are confirmed or rejected. The Co-Investigators obtain the calibrated reduced data in form of stellar light curves on which transit search routines can be directly applied. The outcome is the candidate list contributed from different teams. This candidate list is sent to spectroscopic and photometric follow-up teams which schedule the observations of the candidates. This process can take more than a year because of the observations constraints (observability on sky, brightness, target of opportunity observations...).

In order to speed up the process of planet detection, an alarm mode identifies transiting candidates in not finally processed light-curves with only some weeks of observations. These candidates are provided to the follow-up groups. The planets

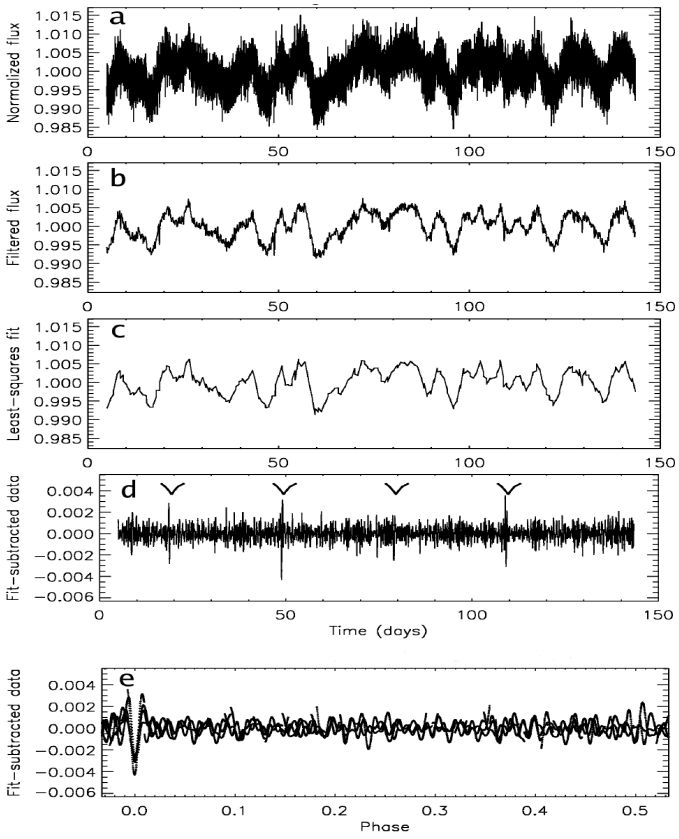

Figure 4.8: *Different steps in the BAST routine written by Renner et al. (2009) (123) and used for the transit detection in the CoRoT data. a) the original light curve, b) low-pass filtered light curve, c) least-square fit on subsets of the light curve models the stellar variability, d) and then is subtracted from the light curve with transits indicated, e) presents the clean light curve folded with the found period.*

confirmed in the alarm mode are typically Jupiter sized because they show deep transit events which are easily detectable, but also the smallest planet CoRoT 7 b was detected in the alarm mode (29).

Transit search

The data delivered to Co-Investigators are searched for the transit events by their own transit search routines usually based on BLS algorithm (122). Here as an example the transit detection routine BAST developed by the Berlin DLR team is presented. In Figure 4.8 different steps in the BAST routine are exemplified. Firstly, noisy data (top panel) are filtered with a low-pass filter (central panel) which eliminates high frequency variations. In the second step, low frequency variations due to stellar variability are subtracted by fitting of a polynomial and then the transit events are searched for the box shaped signals. If present and detected, the transits are marked and the period is determined (123).

The need for the ground based support

The confirmation process of planetary candidates requires photometric (108) and spectroscopic (109) follow-up observations as discussed in Section 3.6.1. In this phase ground based photometric telescopes play an important role by identification of false positive alarms. Especially, ground based telescopes with higher angular resolution

than CoRoT (2.3"/pixel) can identify potential contaminant from the candidate's vicinity mimicking the transit event. Such contaminant can be an eclipsing binary star which is unresolved in the CoRoT mask but with a follow-up instrument it can be properly separated from the candidate (see Section 3.6.1). This is the main justification for the BEST and BEST II telescopes as discussed in Chapter 1.

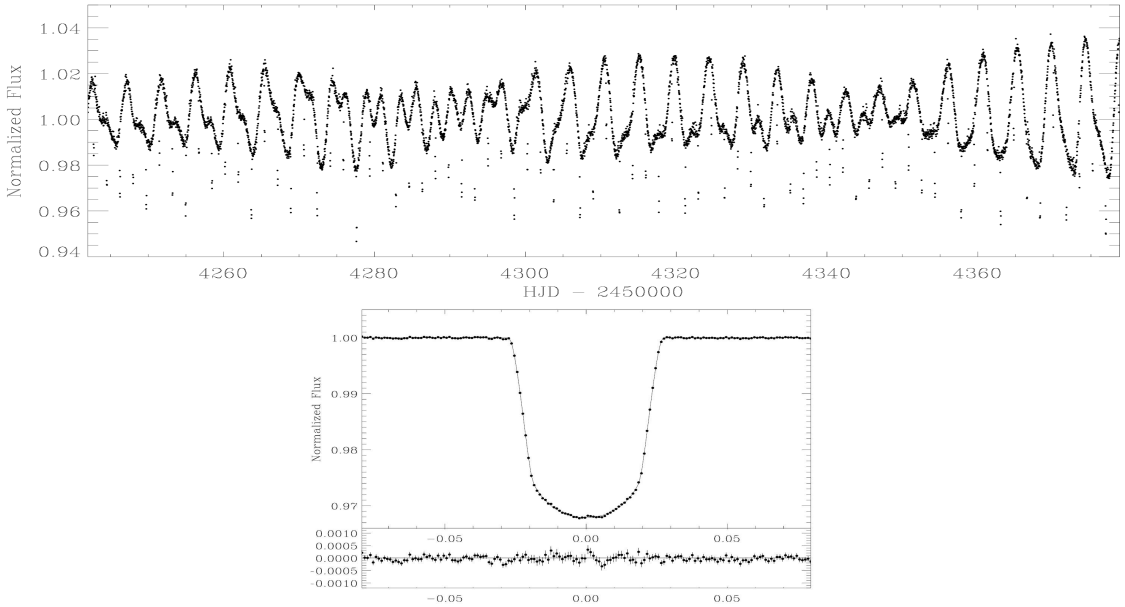

Figure 4.9: *Left panel shows a complete light curve of the host star of CoRoT 2 detected with CoRoT. The variability in the light curve is due to activity of the star. Right panel shows the transit event of CoRoT 2. Both figures taken from (124).*

Detected extrasolar planets

Currently, the CoRoT space mission has detected six extrasolar planets which were confirmed with follow-up observations. The first hot-Jupiter planet CoRoT 1b with orbital period of 1.5 days was detected in the first observational field IRa01 in 2007 (125). The other planets CoRoT 2b (see Figure 4.9 for the light curve and transit event) (LRc01) (124; 114; 126), CoRoT 4 (IRa01) (127; 128), CoRoT 5b (LRa01) (129) and CoRoT 6b (LRc02) (130) are also Jupiter-sized planets on close-in orbits. The most interesting planet detected most recently by CoRoT is CoRoT 7b (LRa01) which is with a radius of 1.75 R_{Earth} (29). This planet is the smallest known extrasolar planet ever detected by transit and radial velocity methods. In addition, the object CoRoT 3b (LRc01) was classified as a very interesting brown dwarf (27).

4.3 Kepler and future space missions

Kepler

The CoRoT space mission was followed with the NASA space mission KEPLER (131), launched in March 2009. Kepler is a 0.95-m equipped with 42 2200 × 1024 pixel CCDs resulting in approximately a 105 deg^2 FOV. The satellite which will perma-

nently observe one field in Cygnus constellation for 3.5 years. In total approximately 100000 main sequence stars in range from 9 to 14 mag will be observed (132). The photometric precision and the duty cycle are designed to discover Earth-sized planets on long periodic orbit in habitable zones of the target stars. In general, data obtained with Kepler should provide more detail on the statistical distribution and the structure of planetary systems.

Future space missions

Future space missions also have ambitious aims, in particular the detection of planets on long distance orbits and planets suitable for life forms. Further important scientific achievement will be the refining of the statistics on the planetary systems distribution in the Universe.

ESA's GAIA space mission (103) will be launched in 2011. The main scientific goal of GAIA is 3D-mapping of the Galaxy. Therefore, astrometric data for more than 1 billion stars will be obtained. This should also provide planetary detections using the astrometric method. Additionally, photometric data on several hundred thousand stars will be searched for the transit events. The estimated number of hot-Jupiter systems is expected to reach several hundreds.

Recently, a concept for the space mission PLAnetary Transits and Oscillations of stars (PLATO) (133) has been presented in the framework of the ESA "Cosmic Vision" program. Continuous high precision photometric observations of a large sample of stars (> 100000) over 5 years period should allow the detection of Earth twins with the transit method. Furthermore, planets with even longer orbital periods should be detectable. The parameters of the space missions presented in the text are summarized in Table 4.2

Table 4.2: *Comparison of space based transit survey projects*

Survey	Apert.(m)	FOV(deg^2)	Range(mag)	Res("pix^{-1})	Since	Nr. stars
SWEEPS (116)	2.4	202"×202"	19-26		7d in 2004	1800000
CoRoT (119; 19)	0.027	8	12-16	2.3	2007	50K
Kepler (131)	1.0	105	9-15	4	2009	100K
GAIA[3]	$2\times1, 45\times0.5$				2011	>1 billion
Plato (133)	1.0	900			>2015	100K

4.4 Ground Based Transit Surveys Overview

In the last decade, many ground based transit surveys have been searching for extrasolar planets. In general, the existing surveys can be divided based on their aperture, angular resolution and FOV. Here the surveys are divided based on their aperture into small (up to 12-cm) with large FOV, medium (up to 40-cm) and large projects ($>$ 40-cm apert.). The surveys presented in this section are only the most successful ones in terms of operations. The technical parameters of additional surveys can be found in Table 4.4. In addition, an overview of detections of planets with different surveys is shown in Table 4.3.

Table 4.3: *Transiting extrasolar planets. Detections are sorted by survey projects.*

Survey	Nr. of planets
SuperWasp	15
HATNet	10
OGLE	8
XO	5
CoRoT	6
TReS	4
Others	8

Small size surveys - (up to 12-cm aperture)

Usually, a small aperture telescope (defined as small in terms of aperture and simple optics) which is able to monitor a vast number of stars is a very powerful instrument for planet search. Precision of about 0.01 mag can be easily reached and the costs of such instrumentation are relatively low. However, the crucial aspect of a successful planetary transit survey is to have a high duty cycle. This demand slightly limits the places suitable for such a transit survey. Desirable is also to be able to observe from more than one location leading to improved coverage of the duty cycle. The surveys which will be described here are located mainly at Hawaii, Chile and Africa and nowadays report new detections of transit candidates on a monthly or yearly basis.

- **Trans-atlantic Exoplanet Survey** - the TrES is a network of three autonomous telescope systems, STARE (Tenerife), SLEUTH (Palomar) and PSST (Arizona). STARE has been mentioned above. SLEUTH is a 100 cm telescope covering $36deg^2$ on the sky. Operational since 2003. PSST has an aperture of 100 cm diameter covering $36deg^2$ on the sky operational since 2004. In addition to the first detection of a transit event with STARE (18) four more transiting planets have been reported up to date.

- **XO** - the XO project consists of two 11 cm telescopes located at Haleakla observatory, Hawaii. Each telescope covers about $51deg^2$ of sky having an angular resolution of 25.4"/pixel. The project is operational since 2003 with five reported transiting planets.

- **SuperWASP** - the SuperWasp is operated by a consortium of UK institutes and IAC, Spain. Two SuperWASP observatories are located at La Palma, Spain and at the Sutherland Station, South Africa. A system of 8 telescope lenses with aperture 11 cm have been set-up at each location. All telescopes are equipped with $2K \times 2K$ CCDs. The field of view for each telescope covers about $64deg^2$ with an angular scale of 13.7"/pixel. The first detection of an exoplanetary transit has been reported in 2006 by (145). With 15 planets found, SuperWASP is the most successful transit survey up to date in terms of detections.

- **Hungarian Automated Telescopes Network** - the HATNet is operated by CfA Harvard in cooperation with the Hungarian Academy of Sciences. In total 6 telescopes are located at Hawaii and at Fred Lawrence Whipple Observatory (FLWO, USA). An additional telescope WHAT (139) is located at Wise

Table 4.4: *Comparison of ground based transit survey projects.*

Survey	Location	Apert.(mm)	CCD	FOV (deg^2)	Range(mag)	Scale(")	Since	Nr. stars	Filters
OGLE[a]	Las Campanas	1300	8K×8K	0.34		0.26	1992	$> 10^6$	UBVRI
APT[b]	Australia	500	2K×2K	6	9.4	10-15	1995		B,V,R,I
Vulcan[c]	Lick Obs.	120	4K×4K	49	< 13		1999	6000	V, R
STARE[d] (TrES)	Tenerife	99	2K×2K	32		10.8	1999	>24000	B,V,R
ASAS-3[e]	Las Campanas	2×71, 250, 50	$2\times2K\times2K$	64, 4.8, 936			2002		V,I
SuperWasp[f]	S. Africa, La Palma	2×8×111	2K×2K	16×61	<13	13.7	2002	$> 100K$	
BEST[g]	OHP	195	$2K\times2K$	9.6	10-14	5.5	2002	100K	clear
XO[h]	Haleakla	2×110	1K×1K	51.84	12	25.4	2003	$> 100K/year$	400-700 nm
WHAT[i]	Wise Obs.	110	2K×2K	67.24	10-14	14	2004	15000	I
HATNet[j]	Hawaii, FLWO	6×110	2K×2K	67	I<14	14	2003	96K	I
VulcanSouth[k]	Antarctic	200	4K×4K				2004-2005		600-700nm
SLEUTH[l](TrES)	Palomar	100	2K×2K	36	< 14		2003	10000	r',g,i,z
PSST[m](TrES)	Arizona	100	2K×2K	36	10-13	10	2004	4000-12000	B,V,R, VR
BEST II[n]	Armazones	250	$4K\times4K$	2.8[o]	10-16	1.5	2007	100K	clear
TEST[p]	Tautenburg	300	$4K\times4K$	4.8	10-15	2	2007	50000	(UBVI)R
ASTEP-South[q]	Antarctic	100	$4K\times4K$				2008		
MEarth[r]	FLWO	2×400	$2K\times2K$	0.18	< 9	0.75	2008	4131	
PANSTARRS[s]	Haleakla	4×1800	1.4bil pix.	49	<24	0.3	ongoing	6000/night	g,r,i,y
VISTA-ROPACS[t]	Paranal	4000	$8K\times8K$			0.339	ongoing		Z,Y,J,H,K_s
ASTEP	Antarctic	400					2010		
PASS[u]	Antarctic	all sky		5.5-10.5				250K	
ICE-T[v]	Antarctic	2×600		65			2012	1.3M	yes
OmegaTrans[w]	Paranal	2600	16K×16K	1	13.5-17.5	0.26		200K	R

[a]Currently OGLE-III - (134)
[b]http://mcba11.phys.unsw.edu.au/ apt
[c] (135)
[d]http://www.hao.ucar.edu/public/research/stare/stare.html - (26)
[e]http://archive.princeton.edu/ asas/
[f]http://www.superwasp.org/
[g]www.dlr.de/caesp - (136),(137)
[h]http://www-int.stsci.edu/ pmcc/xo/ - (138)
[i]http://wise-obs.tau.ac.il/ what/ - (139)
[j]http://www.cfa.harvard.edu/ gbakos/HAT/ (140)
[k]http://www.polartransits.org/about.html
[l] (141)
[m] (142)
[n]http://www.dlr.de/pf/desktopdefault.aspx/tabid-4515/7415_ read-11158/
[o]BEST II alternates between 2 fields then FOV=5.6
[p](143)
[q]http://pleiades.unice.fr/astep/
[r]http://www.ast.cam.ac.uk/\~jmi/talks/iau253_~mearth_~may2008.pdf
[s]http://pan-starrs.ifa.hawaii.edu/public/
[t]http://www.vista.ac.uk/
[u]http://www.iac.es/proyecto/pass/ - (144)
[v]http://www.aip.de/pr/Mitt/PM_AIP-Teleskop_Antarktis_Logo.pdf -in German
[w]http://www.strw.leidenuniv.nl/ snellen/Omegatrans/index.html

observatory, Israel. Each telescope has an aperture of 11 cm and covers about $67 deg^2$ on the sky with an angular resolution of 14"/pixel. The project has been in operation since 2003, when it replaced a single HAT prototype (146) telescope at FLWO. The first extrasolar planet detection within HATNet has been reported in 2007 (147) and to date, 10 planets have been confirmed. HATNet is currently the second most successful transit survey.

Medium and large size surveys - (> 12-cm aperture)

Medium and large aperture telescopes are represented with BEST, TEST, MEarth (148) and OGLE (149) projects. For this surveys smaller field of view compared to previously discussed surveys is compensated with the detection range covering stars between $10 - 19$ magnitudes. Additionally, higher angular resolution of few "/pixel.

- **Tautenburg Exoplanet Search Telescope (TEST)** - TEST is a 30-cm aperture telescope located at Tautenburg Observatory, Germany (143). Observations are performed in a robotic mode in R filter. The telescope has been fully operational since 2007. No planets were detected so far.

- **BEST** - BEST (136) is a 19.5-cm aperture telescope system operated in the remote mode by Deutsches Zentrum für Luft- und Raumfahrt. The telescope is located at Observatoire de Haute Provence, France since 2006. Brief overview on the BEST setup will be presented in Chapter 6 . Additionally, some scientific results as prediscovery observations of CoRoT 1b and CoRoT 2b (137) will be presented in Chapter 9.

- **BEST II** - BEST II (150) is a 25-cm aperture telescope system operated in the robotic mode by Deutsches Zentrum für Luft- und Raumfahrt. The telescope is located at Observatorio Cerro Armazones, Chile. Regular operations began in 2007. The system concept, photometric quality and scientific results will be described in following chapters.

- **MEarth** - last year (2008), the survey MEarth (148) started to operate from Fred Lawrence Whipple Observatory (FLWO). MEarth project consists of two 40-cm aperture robotic telescopes. Both telescopes are monitoring a selected group of M-dwarfs in the solar vicinity. The outcome should be a detection of a rocky planet around M-dwarf star which can be in the habitable zone. Transit depth of a potential planet orbiting an M-dwarf star should be more than 0.01 mag for a planet of a few Earth masses. Furthermore, the habitable zone around M-dwarf stars is closer to the host. Both facts are supporting the relevance of M-dwarf surveys.

- **The Optical Gravitational Lensing Experiment (OGLE)** - the OGLE-III telescope is a large aperture survey with 1.3 m aperture located at Las Campanas, Chile. However, the survey was primarily designed to observe gravitational lensing events in the Galaxy. Since observed targets are in the galactic center, the high density of stars also provides enough targets for transit search. The first successful detection of a transiting planet with OGLE was reported in 2003, being the first discovery achieved through the transit method (151). Currently, 8 transiting planets have been discovered with OGLE survey.

4.5 Future ground based projects

The growing number of planets detected with transit methods clearly demonstrates the significance of transit surveys. Furthermore, the follow-up observations of confirmed planets showed that transit method is also a powerful complementary method to the radial velocity surveys (151; 18). The number of projects based on the use of the transit photometry from the ground and from space is steadily increasing.

A small survey project is the HAT-South telescope network which will be operating in future from three different locations around the globe in the southern hemisphere. The network of telescopes should provide a high duty cycle.

Another ambitious ground based project under construction is Panstarrs which will be searching for several thousands of Jupiter-sized planets, with its sub-project Pan-Planets (152), based in Hawaii. Four 1.8-m telescopes should survey about $6000 deg^2$/night of sky primarily searching for the minor bodies from the Solar System. In addition, the obtained stellar light curves will be searched for the planetary transits. Currently, the prototype Panstarrs-1 is being commissioned at Haleakla observatory, Hawaii.

Equally challenging projects are the proposed surveys from the Arctic Dome-C plateau. Currently, a predecessor of ASTEP telescope, the ASTEP-South (University Nice (153)) is testing the site at Dome-C. The obtained results should support the larger 40-cm telescope ASTEP which will cover $1 deg^2$ of the sky. ASTEP will be commissioned in 2010. Excellent atmospheric conditions (154) together with a continuous three months lasting night should improve the detection rate significantly.

4.6 Radial Velocity planet surveys

Currently, the most successful method for detection of extrasolar planets is the RV method. Since the detection of 51 Peg b, more than 300 planets were detected with RV measurements. The main parameters of projects searching for extrasolar planets are summarized in Table 4.5.

Table 4.5: *Comparison of radial velocity survey projects.*

Survey	Telescope	Instrument	Stars	Sensitivity	Ongoing
California and Carnegie Planet Search	WMKO, 10-m	HIRES Upgrade	1000	1m/s	2004
	Lick Obs., 3-m	Hamilton	300	5m/s	1992
Amglo-Australian Planet Search	AAT, 3.9-m	UCLES	159	3m/s	1998
Geneva Planet Search	OHP, 1.93-m	ELODIE	320	8-12 m/s	1994
	ESO, La Silla 3.6-m	HARPS	1000	1m/s	2003
Kompetenzzentrum für Exo-Planeten, Jena/Tautenburg[4](26)	VLT, 8.2-m	UVES		6 m/s	2001
	TLS, 2-m				

- **Geneva RV survey** - The Geneva extrasolar planet survey uses various telescopes on both southern and northern hemispheres. The ELODIE instrument installed at OHP 1.93-m telescope (15), which detected the first extrasolar

planet 51 Peg b has been replaced by SOPHIE (16). SOPHIE is a high resolution spectrograph with the capability to detect variations in radial velocities down to $3ms^{-1}$. A second instrument HARPS is installed at ESO 3.6-m telescope. HARPS is a spectrograph which is extremely stable and therefore, theoretically a precision of about $1ms^{-1}$ is expected (17). Geneva planet survey confirmed 121 extrasolar planets with masses below $10M_{Jupiter}$ since 1995 (155). The most recent being a planet around star GJ 581 in a multiple system with a minimum mass $1.9M_{Earth}$ and probably located in the habitable zone (61).

- **N2K survey** - The N2K survey searches 2000 not yet by the other programmes surveyed stars for hot Jupiter planets. Within these surveys the Magellan, KECK and Subaru telescopes are used for the high precision radial velocity survey. The first planet with a Saturn mass has been reported in 2005 (156).

- **Anglo Australian Telescope RV survey** - the Anglo Australian Doppler precision survey (157) is performed with a high resolution spectrograph UCLES (R=45000) installed at 3.9-m Anglo Australian Telescope, Siding Springs observatory, Australia. The survey can reach a level of $3ms^{-1}$ for bright stars. Several extrasolar planets have been reported since 1998.

- **Thüringer Landessternwarte Tautenburg** - the observatory located near Jena, Germany is performing a RV survey with the 2-m "Alfred-Jensch-Teleskop". A precision of 6 to 7 m/s with a S/N-ratio of 80 to 100 can be reached down to 8^{th} mag star. The survey reported several planets and one of them around the giant star (23).

4.7 Future RV instruments

The aim of the RV surveys is to reach m/s or even cm/s measurement precision in the radial velocity. Therefore, new instruments are planned for the upcoming decades. A few of them are listed below.

The High Accuracy Radial velocity Planet Searcher/North - HARPS North

HARPS North is a project undertaken jointly by the Harvard-Smithsonian Center for Astrophysics and the Geneva Observatory to detect earth-sized rocky exoplanets(158). The HARPS North will be installed at 4.2-m William Herschel telescope located at La Palma, Spain. The instrument is a fiber fed, cross-disperser echelle spectrograph similar to HARPS South at 3.6-m ESO telescope at La Silla, Chile (17). The precision in RV measurement will reach $1m/s$. The instrument will be operational in 2010 (159).

ESPRESSO - will be a super stable high resolution optical spectrograph using the combined light of the four 8.2-m telescopes of the VLT with a predicted precision of 10 cm/s (160).

NAHUAL - will be a high-resolution multi-purpose near infrared precision spectrograph planned for 10-m telescope at La Palma, Spain (161).

Chapter 5

Theoretical background - photometric measurement

The most powerful scientific instruments since ancient times are our senses. In particular, human eyes have been of great importance for astronomy since centuries. As a receptor of incoming light they can detect the photons and convert them into an image in the human brain. A new era for astronomy began in 19th Century when the photographic plates were invented. The next step took place only in the middle of the 20th Century when the first photomultiplyers were manufactured. However, the photographic plate still lived besides the photomultiplier until the invention of the CCD camera at the end of 20^{th} Century. Since then the CCD camera has became one of the most important receptors in astronomical research. In this chapter, the theoretical background of photometric measurements will be presented. The first sections will describe the telescope and CCD detectors and their characteristics. Additionally, the background for imaging process will be presented. In the second part, the uncertainties due to instrument electronics and atmospheric conditions such as seeing and atmospheric turbulence influencing the measurement will be discussed.

5.1 The telescope

The first telescope was invented in 16^{th} Century already. Since that time the basic principle did not change. The telescopes may consist of an optical lens system, such a telescope is known as a *refractor*. A second group of telescopes is known as *reflector* and consists of a larger primary mirror and a smaller secondary mirror which reflects the incoming beam to the focus. Currently, larger telescopes are provided with mirrors because of better technical feasibility than *refractors*. Various modifications of the basic *reflector* principle resulted in systems of e.g. Cassegrain, Coude, Newton and other types. The basic difference is the consistence and shape of the mirrors in the optical system and the position of focus. Figure 5.1 shows a reflector telescope of Cassegrain type.

Imaging and the focal length

The imaging of the telescope obey exactly the same laws of optics as the imaging with a simple pin hole camera (Camera Obscura) which is a simple hole in the plane

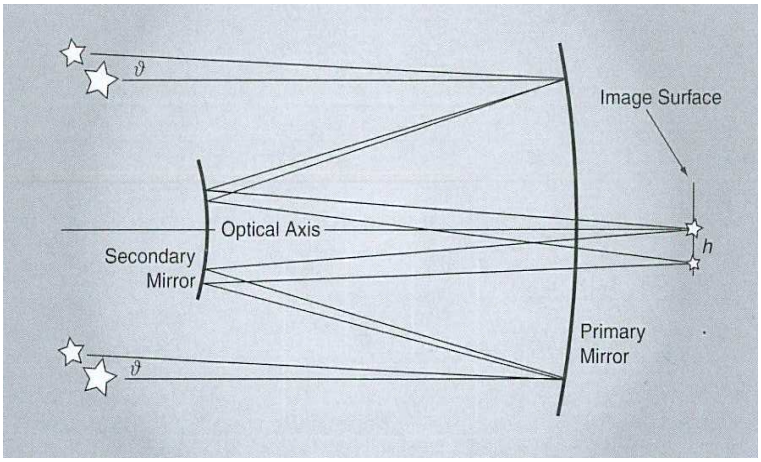

Figure 5.1: *Principle of a reflecting telescope of a Cassegrain type. The incoming light is reflected on the primary mirror and the secondary mirror redirects the beam to the focal plane where the detector is installed. Image from Berry (2006) (162).*

object focusing the beams. However, the only difference is that usually the angle Θ between an object and the optical axis is very small. An image of a distant stars which is located off-axis is reconstructed in the focal plane in a distance $h = f \tan\theta$ from the optical axis with f being the focal length of a telescope.

The field-of-view

Other parameters characterizing the telescope's properties are the aperture d, focal ratio $1/f$ giving the ratio of an aperture and a focal length and the field-of-view (FOV). FOV can be determined in radians by

$$\theta_{FOV} = 2 \arctan \frac{D_{detect}}{2f} \tag{5.1}$$

where D_{detect} is a size of the detector installed in the focal plane. The corresponding value in degrees can be obtained as

$$FOV(deg) = \frac{180}{\pi} \theta_{FOV}. \tag{5.2}$$

5.2 CCD detectors

Light sensitive detectors are installed in the focal plane (see Figure 5.1). One of the most revolutionary detectors used nowadays is the Charge Coupled Device (CCD) introduced in 1969 by Willard S. Boyle and George E. Smith working in the Bell Laboratories[1]. The principle of the photon detection is based on the Einstein's photoelectric effect. CCDs are capable to detect the light over a broad range of wavelengths with high quantum efficiency and can also monitor a relatively large area on the sky.

[1]http://www.alcatel-lucent.com/wps/portal/BellLabs

Typical CCD device consists of hundredths of small micrometer-sized metal oxide semiconductor arrays of capacitors formed on a silicon substrate. Each element of the array (see center Figure 5.2) is called photo detector (pixel). The charge in each photo detector is isolated due to voltage applied through the conductive channels on the surface of silicon (see left Figure 5.2). Photons entering the silicon crystal lattice during the exposures induce the electrons from a low-energy valence-band state to a high-energy conduction-bound state, partially discharging the capacitors. The degree of discharge of each capacitor is proportional to the number of photons incoming during the exposure. The remaining charge in the photo sites after exposure is sequentially shifted to a charge sensing-node, amplified (see right Figure 5.2) and converted to a digital signal which can be displayed as an image on the screen of a computer. In the following sections, properties of the telescope+CCD optical system will be discussed in more detail.

Figure 5.2: *The function of a CCD chip is demonstrated in the left figure. The central figure shows a real CCD matrix consisting of single pixels. The principle of the readout of a CCD is shown in the right panel. Images taken from (163; 164).*

Angular resolution of a pixel

The angular resolution of a photo detector - pixel can be determined similar as the FOV presented in previous section. Therefore, one pixel will have an angular resolution given by

$$\theta_{pixel} = 2 \arctan \frac{D_{pixel}}{2f}. \tag{5.3}$$

For small arguments in arctan function Equation (5.3) can be written in the form

$$\theta_{pixel} \approx \frac{D_{pixel}}{f} \tag{5.4}$$

where D_{pixel} is a pixel size (typically a few microns) and f is the focal length of the optical system. According value in degrees can be obtained from the relation

$$\theta_{pixel(deg)} = \frac{180}{\pi} \theta_{pixel}. \tag{5.5}$$

Imaging - Airy disc

An Airy disc is the bright, diffuse central spot of light formed by an optical system imaging a point source of light. The Airy disc is surrounded by diffraction patterns. The numerically obtained angular diameter of an Airy disc θ_{Airy} is given by

$$\theta_{Airy} = 2.44\frac{\lambda f}{D}(radians) \tag{5.6}$$

where f is the focal length, D is the aperture of the telescope and λ is the wavelength of the incident flux. An Airy disc and the corresponding Full Width in Half Maximum (FWHM) is shown in Figure5.3. The FWHM of the Airy disc is given by (162)

$$FWHM_{Airy} = 1.02\frac{\lambda}{D}(radians) \tag{5.7}$$

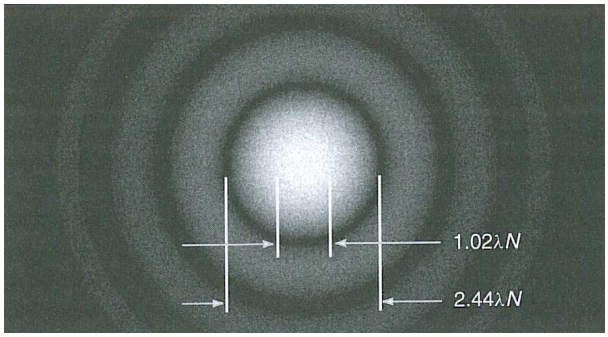

Figure 5.3: *Airy disc as seen in the focal plane. The whole diameter of* $2.44\lambda N$ *corresponds in the ideal case to a point spread function (PSF of an observed object). The inner circle of* $1.02\lambda N$ *corresponds to the FWHM of an ideal observed object. N is the focal ratio. Image taken from (162).*

Point spread function (PSF)

The characteristic of the flux detected in the focal plane is given by the point spread function (PSF - see Figure 5.3) which has in an ideal case the diameter of an airy disc, i.e. $2.44\lambda N$ where N is the focal ratio[2]. But under normal observing conditions the PSF is larger than the FWHM of an Airy disc ($FWHM_{Airy}$) due to defocussing or atmospheric turbulence. The corresponding $FWHM_{PSF}$ of the PSF characterizes the angular resolution of the instrument.

Sampling

The pixel scale (see Equation (5.4)) is related to the FOV of the system as

$$\theta_{pixel} \approx \frac{\theta_{FOV}}{N_{pixels}} \tag{5.8}$$

[2]Focal ratio is defined as $\frac{f}{D}$ where f is the *focal length* and D is the aperture of the optical system.

where θ_{FOV} is the FOV of the system and N_{pixels} is the number of all pixels. In other words, θ_{pixel} expresses how large angle is covered by a single pixel. Typical values are in range of a few arcseconds.

If $\theta_{pixel} \gg FWHM_{PSF}$ the image is undersampled and a part of the information will be lost. According to the Nyquist's theorem the pixel scale must be half of the FWHM of the PSF ($\theta_{pixel} = \frac{1}{2} FWHM_{PSF}$) to be critically sampled (162). In case $\theta_{pixel} \ll FWHM_{PSF}$ the image is oversampled and the whole information about the PSF will be stored. Oversampling allows to detect a larger number of photons before saturation of the CCD detector. It might be most easily reached with the help of defocussing of the system. However, a reasonable undersampling may be a trade-off for the large FOV in which more stars can be observed.

Quantum efficiency

The photon detection rate depends additionally on the wavelength of incoming photons. The *quantum efficiency* of the CCD describes how many incoming photons of different wavelengths can be detected. Typical values of *quantum efficiency* can be as high as 66% for wavelengths about $650nm$ what is the case of BEST II CCD (see Chapter 6).

Analog digital units (ADU)

The principle of the detection and readout is illustrated in Figure 5.2. The incoming signal from the amplifier is digitalized and stored. Values of the intensity are given in ADU. The signal in ADU is proportional to the number of incoming photons as

$$S(ADU) = N_{e^-}/g \tag{5.9}$$

The conversion factor between electrons and ADU is called gain g, given by the manufacturer of the instrument.

Bias

A constant value of voltage is applied to all pixels of the CCD to make certain that the voltage presented to the A/D converter is never negative. This bias signal is distributed by read-out noise. The read-out noise consists of a Gaussian noise caused by the electronics of the CCD and of the computer and is therefore specific for the used devices.

Dark current

The electrons can be also excited thermally. The number of thermally excited electrons depend on the operational temperature of the detector and on the exposure time. The thermally induced current, called dark current, influences the measurement and the subsequent image processing. The contribution to the uncertainty of the measurement will be discussed in the following section.

5.3 Measurable quantities

The number of photons which interact with the CCD detector is proportional to induced electrons. Therefore, the number of collected photons depends on the exposure time. Different sources of noise are affecting the signal. Some noise sources

are given by the CCD characteristics while others are due to calibration process and photon flux structure. The accurate determination and minimization of the uncertainty resulting from the various statistical noise sources is essential for accurate signal detection, e.g. the shallow transits of extrasolar planets.

The signal

The mean number of incoming photons in a unit of time is given by

$$dN = \frac{dE}{h\nu} \tag{5.10}$$

where E is the mean energy, ν is the frequency of the incoming photons and h is the Planck's constant. The total number of incoming photons within an exposure of duration T_{exp} is given by

$$N = \frac{AT_{exp}}{h} \int_0^\infty f_\nu \nu^{-1} d\nu \tag{5.11}$$

where f_ν is the in time constant flux density incoming through an area A. However, as described earlier only part of the photons given by "quantum efficiency" Q can be detected. If the constant photon flux through the area A is assumed and the gain g of the detector is given then the number of detected photons, the signal S in ADU, is given by

$$S(ADU) = \frac{AT_{exp}}{gh} \int_0^\infty Q f_\nu \nu^{-1} d\nu \tag{5.12}$$

The process of photon detections is a stochastic process. Each stochastic process is described by the Poisson distribution. Therefore the resulting detection noise can be expressed by

$$\sigma = \sqrt{S} \tag{5.13}$$

However, also other sources of noise affect the incoming signal. In the following paragraphs different types of measurement uncertainty will be described.

Bias - measured bias counts are represented with S_b The corresponding noise contribution is represented by σ_b (see Section 5.2)

Dark current - measured counts due to the dark current are represented with S_d. The corresponding noise contribution is represented by $\sigma_d^2 = S_d/g$

Flat field

Each pixel within the CCD posses a slightly different response function to incoming photons. The resulting changes in the sensitivity within a frame can be corrected with a flat field image. Such a short exposure image is taken with the telescope pointing to a uniformly illuminated background. E.g. the a sky during the dawn or dusk or a white plate illuminated with a lamp. The change in transmissivity of the pixels is expressed by n_{flat} and it is present in every acquired scientific image. The corresponding noise introduced by a flat field correction is represented by σ_{flat}.

Sky background

The total measured flux S consists of photons from the star S_{star} and photons from

the sky background S_{sky}. Therefore, the measured flux (without contribution of dark current and bias) can be expressed as

$$S = (S_{star} + S_{sky}). \tag{5.14}$$

Therefore, the sky background contribution to the noise can be expressed with

$$\sigma_{sky} = \sqrt{\frac{S_{sky}}{g}} = \sqrt{\frac{S - S_{star}}{g}}. \tag{5.15}$$

where S is the total measured signal and S_{star} is the signal from the object.

Measured signal

The total measured signal S then can be expressed as

$$S = n_{flat}(S_{star} + S_{sky}) + S_b + S_d \tag{5.16}$$

where all the contributions to S are described above.

5.4 How to estimate the stellar flux?

Now taking into account that the stellar image is spread over several pixels it is needed to determine the contribution S_{star} of all such pixels. In order to determine the incoming stellar flux (I_{star}) the signal from pixels containing the stellar image are summed up and the sky background signal is subtracted.

Apparent brightness

In astronomy the relative intensity is defined by the *apparent brightness* in magnitude (m). The flux from the object I_{star} in ADU is converted by

$$m_1 = -2.5 \log \frac{I_{star}}{I_0} + m_2 \tag{5.17}$$

with I_0 being intensity of a reference star. Selecting an arbitrary the value for m_2 according to flux I_0 provides the calibration of the instrumental magnitude system. One can define an unlimited amount of instrumental magnitude systems. Therefore, standard stars which had fluxes measured in exactly defined photometric system (e. g. Johnsons or Cron-Cousins) and which have the extinction corrected magnitude value (to be described in the following section) are used as reference sources (165).

The light curve - The magnitudes of the stars are determined for every observation resulting in a time series $m_k(t_i)$ expressing the change in the stellar flux in time. This time series $m_k(t_i)$ which is the end product of photometric data calibration is called a *light curve*. A more detailed description of the data reduction process adopted for the BEST/BEST II systems will be presented in Chapter 8.

5.5 Influence of the atmosphere

Astronomic observations from the ground are limited due to refraction of the incoming light in Earth's atmosphere. In particular, different atmospheric layers are characterized by different pressure and temperature. Local conditions in each layer might be very variable on scales of milliseconds. These variations are called local turbulence and they directly influence the transparency of the atmosphere for the incoming stellar light. Such small changes are refereed as atmospheric refraction. The parameter describing the atmospheric conditions is in astronomy known as seeing. In particular, in the visible part of spectra the atmospheric turbulence causes a "flickering" of the stellar image known as scintillation and is detectable by the human eye. The above mentioned phenomena and their influence on the photometric error budget will be described in the following sections.

5.5.1 Atmospheric extinction

The thicker the airmass which the beam must pass, the stronger is the effect of the atmospheric refraction. The airmass X is in its simplest form defined as

$$X = \sec(Z) \tag{5.18}$$

where Z is a zenith distance. The formula shows that in the zenith the light has to cross the thinest air mass. Therefore, the beam is only slightly influenced. In contrary, the airmass is growing to infinity near the horizon. Equation (5.18) holds for small airmasses. Which is moving further towards large airmass where a more detailed approximations needs to be applied (162; 166).

The influence of the atmosphere on the measurement of stellar intensity can be expressed by

$$m = m_0 - K_1 X - K_2 X(b - v) \tag{5.19}$$

where K_1 is the first order extinction coefficient describing the transparency of the atmosphere, K_2 is the second order extinction coefficient which is dependent on the color of the star, $b-v$ is the color index of the star and X the air mass of observation. The value of m_0 expresses the apparent brightness which star would have outside the Earth's atmosphere.

5.5.2 Seeing

The seeing gives a direct measure of the changes in the image due to atmospheric conditions. It can be characterized with a FWHM of the stellar PSF. The PSF of the star is changing due to local atmospheric conditions. The variation of the stellar PSF is described by the Fried parameter (r_0) representing the maximum path on which the incoming radiation is still coherent. Therefore r_0 depends on the variance of the refractive index in the atmosphere $C_n^2(h)$ where h represents the altitude. The generally used Kolmogorov model of turbulences gives the following relation

$$r_0 = 0.185\lambda^{6/5}(\cos(Z))^{3/5}\left(\int C_n^2(h)dh\right)^{-3/5} \tag{5.20}$$

where Z is the zenith distance of the observed object and λ is the wavelength of the incoming radiation. Fried parameters typically range from a few centimeters for the locations with very stable atmospheric conditions to a few tenths of centimeters at the sea level (167).

The exact derivation of the time for which the incoming wave is coherent is rather complex see e.g. (168; 169). Small changes of the coherency of the incoming light on the time scales of few milliseconds are averaged for longer exposures, exactly for $T_{exposure} \gg \tau_{coher}$ where τ_{coher} represents a coherence time, for more detail see (168). Therefore, the changes in the coherency are not observable any longer and the shape of the resulting PSF shows a Gaussian form with a FWHM of

$$FWHM_{turb} = 0.98\frac{\lambda}{r_0} \tag{5.21}$$

The typical value for the seeing dependent changes in FWHM are about few arcseconds.

5.5.3 Scintillation

The intensity changes in the incoming flux are described by phenomena known as scintillation. This effect can observed also by naked eye on the bright stars which flicker. The additional intensity changes are a new source of noise contributing to the total error budget. The scintillation noise σ_{sc} is expressed in general by (168)

$$\sigma_{sc}^2 = \int_0^\infty C_n^2(h)W(h)dh \tag{5.22}$$

where W is the weighting function, h is the altitude of the observatory and C_n^2 is the variance of the refractive index. For the scintillation at the zenith hold following equations:

$$\sigma_{sc} = \begin{cases} S_1 & \text{for } D \ll r_F \\ S_2 \cdot D^{-7/6} & \text{for } D \gg r_F \\ S_3 \cdot D^{-2/3} \cdot \Delta t^{-1/2} & \text{for } D \gg r_F,\ \Delta t \gg (\pi D)/v_\perp \end{cases} \tag{5.23}$$

where D is the aperture of the telescope, t is the exposure time, V_{perp} is the speed of turbulence layer and $r_F \approx (\lambda h)^{1/2}$ is the Fresnel radius where h is altitude of the turbulent layer, λ wavelength of the incoming radiation. Usually, Fresnel radius is negligible in comparison to the aperture of the telescope and the exposure time is also much longer in comparison to $\frac{(\pi D)}{V_{perp}}$ for small aperture telescope. Therefore, in case of BEST/BEST II the third equation for σ_{sc} applies. In Figure 5.4 the values of σ_{sc} and S_3 coefficient for different apertures of a telescope located at Paranal observatory are shown. However, it is clear that σ_{sc} limits the observations on scale of few millimagnitudes (< 0.0008 mag - see Figure 5.4).

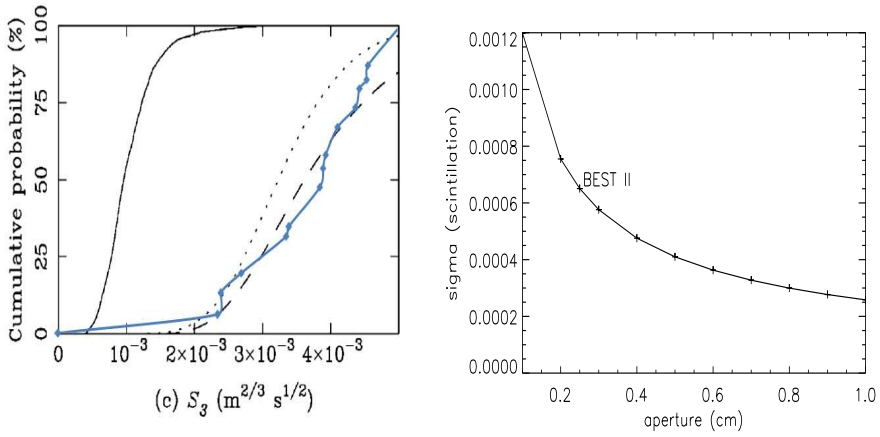

Figure 5.4: *Cumulative probabilities for the S_3 coefficient is shown in the left plot for Paranal (25 km from Observatorio Cerro Armazones) as blue line compared to Cerro Tololo - dashed (Image by ESO (168)). Different σ_{sc} values for different apertures (the values from Paranal were adopted). The relevant value of scintillation noise for BEST II is marked in the plot.*

The resulting scintillation noise can be expressed in magnitudes as (170)

$$\sigma_{sc}(mag) = 2.5 \log(\sigma_{sc} + 1) \tag{5.24}$$

5.6 Total uncertainty of the measurement

Different contributions to the total uncertainty of the measurement introduced by either CCD performance or due to atmospheric influence have been described. Now the total uncertainty σ_{system} of an observational sequence can be expressed as:

$$\sigma_{system} = \sqrt{n_{flat}^2(\sigma_{sky}^2 + \sigma_{star}^2 + \sigma_{sc}^2) + \sigma_b^2 + \sigma_d^2 + \sigma_{flat}^2(S_{star} + S_{sky})^2 + \sigma_{rest}^2} \tag{5.25}$$

where σ_{rest} is the contribution form all other unresolved uncertainties from e.g. the data reduction process. These additional uncertainty will be described in Chapter 8. All the uncertainties are independent from each other i.e. uncorrelated.

Additionally, correlated errors are introduced due to systematic effects such as periodic instrumental failure. These systematic effects are described with the correlated noise component - red noise. Since red noise is a correlated noise the corresponding uncertainty can not be simply added to Equation (5.25). The red noise will be described in more detail with respect to telescope system BEST II in Chapter 8 and it can be estimated from the data sets directly.

Chapter 6

The Berlin Exoplanet Search Telescopes

The Department of Extrasolar Planets and Atmospheres within Deutsches Zentrum für Luft- und Raumfahrt (DLR), Berlin Germany, operates two small aperture wide field-of-view telescopes. The main scientific goal of the telescopes is the search for transiting Jupiter-sized planets and stellar variability characterization in the CoRoT observational fields. The general requirement is the ability to observe several thousands of stars with high photometric precision and a high duty cycle. In this Chapter technical details of the Berlin Exoplanet Search Telescope (BEST) will be briefly introduced and then focus will be given on Berlin Exoplanet Search Telescope II (BEST II) from setup to full operational mode (see Figure 6.1).

Figure 6.1: *The BEST family: BEST and BEST II located on opposite hemispheres.*

6.1 BEST

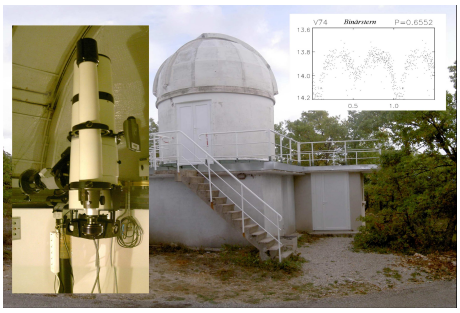

Figure 6.2: *BEST telescope at OHP.*

The Berlin Exoplanet Search Telescope (BEST) is a 19.5-cm aperture Cassegrain system with a FOV of $3° \times 3°$ currently located at Observatoire de Haute Provence (OHP), France. The telescope is equipped with a 2×2K air cooled CCD with a pixel scale of 5.5"/pixel. Observations are performed without filter. A smaller telescope equipped with a ST-4 SBIG CCD is used as a guide telescope with 4.5×4.5 arcminutes FOV. Both telescopes are installed on German equatorial mount. Technical details of BEST are summarized in Table 6.1.

The BEST is operating as a ground based support of the CoRoT space mission. Main goals are photometric follow-up observations of CoRoT's candidates and stellar variability characterization. The specifications of the BEST telescope make the system suitable for simultaneous monitoring of several thousands of stars with millimagnitude photometric precision. This allows to search for transits of Jupiter sized extrasolar planets, since the typical intensity decrease in the stellar light curve is in the order of the BEST's measurements precision (see Chapter 3).

BEST was originally installed at Thüringer Landessternwarte Tautenburg, Germany (TLS) from 2002 to 2004. This phase is described in detail in (136; 86). At TLS high altitude circumpolar target fields with various stellar densities were selected for observations. Transit candidates and variable stars from the TLS period are presented in (86). After the relocation to OHP in 2004, BEST serves fully as a ground based support for the CoRoT space mission, and the first CoRoT's long run and initial run fields have been the main observational targets (171; 172; 173).

6.1.0.1 OHP site

The Observatoire de Haute Provence is located in southern France at: longitude: $\lambda = 5°\ 42'\ 44"$ E , latitude: $l = +43°\ 55'\ 54"$, altitude=650 m. The OHP is hosting 1.93-m and 1.52-m telescopes and some other smaller instruments which profit from about 40% of photometric nights per year and 60% nights which are usually clear (168; 174). An important factor for variability characterization, besides the photometric quality, is a high duty cycle coverage. TLS offered in comparison with OHP less photometric nights (see (86)). Therefore, the relocation of the BEST telescope to Observatoire de Haute Provence, France was initiated in 2004 well before the launch of CoRoT. The first observational campaign in 2005 at OHP showed that the amount of photometric nights doubled in comparison to TLS.

6.1.0.2 BEST system description and operations

The main telescope specifications of the BEST system are summarized in Table 6.1. BEST was operated in observer mode during the TLS period resulting in a rela-

Table 6.1: *BEST telescope specifications.*

Telescope	Cassegrain, Lichtenknecker (Guider telescope)
Instrument	CCD: AP 10 (Thomson THX899M)
Cooling	thermoelectric with air
Aperture	19.5 cm, 9 cm (Guider)
Focal ratio	F/2.7, F/10 (Guider)
CCD size	2048×2048, 192×164 (Guider)
Pixel size	14μm, $13.75 \times 16\mu$m (Guider)
Pixel scale	5.5 arcsec/pixel
Field-of-view	$3.1° \times 3.1°$, 4.5×4.5 arcminutes (Guider)
Mount	M 100B German equatorial
Guiding	FS2 (Astro Electronic)
Tracking	CCD: ST-4 (SBIG)

tively high demand for manpower necessary for the operations. Thanks to remote operational mode, the telescope and the dome are currently controlled by an observer from Berlin who takes calibration frames, points the telescope to the target and starts an automatic observing sequence. When the observing run is finished one more set of calibration frame is taken and the telescope is parked. The typical observational sequence consists of:

calibration frames - bias, dark, flat fields
scientific sequence - 40, 120, 240 sec. exposures with bias and dark frames

In this work data acquired with BEST in the period from 2004 to 2007 on the CoRoT long run fields (LRc01, LRa01) and one initial run field (IRa01) are presented. More detailed description of the performed observations can be found in (171; 172; 173). An overview of the collected data and the campaign characteristics can be found in Table 7.1.

6.1.0.3 Lessons learned from BEST

The lessons learned from the performance of BEST operations can be summarized as follows:

A high duty cycle is needed for the successful transit detection - The OHP site provides compared to the TLS site a doubled number of photometric nights (approximately 40% at OHP). However, no transit events were found due to the low probability of the detection (later discussed in Chapter 7). A clear conclusion was that the duty cycle must be increased in order to find a transit events of Jupiter-sized planets in close-in orbits. Therefore, a site with better observing conditions was needed. The present location of BEST II in Chile can provide a nearly doubled number of photometric nights compared to OHP (73%). This significantly increases the probability of a transit detection.

Better angular resolution - The observed fields had a high stellar crowding re-

sulting in misidentification of transit events (e.g. with a close eclipsing binary). BEST has a pixel scale of 5.5 arcseconds/pixel which is slightly worse than CoRoT's angular resolution of 2.3 arcsecond/pixel. In order to resolve stellar PSFs and to provide an improved support to the CoRoT's follow-up observations, a better angular resolution is needed. Indeed, the BEST II telescope was designed with an angular resolution of 1.5 arcseconds/pixel.

High demand for manpower necessary to operate the telescope - The operations at TLS and OHP were performed in an observer mode thereby requiring an operator on site for periods of two to three weeks. The subsequent operation in remote mode at OHP still needs an operator who is controlling the system from Berlin during the whole night. At TLS we observed 22 nights and at OHP more than 38 nights per campaign. The number of staff to control the telescope is at least two persons over an extended time period. The expected number of nights for an observatory in Chile would be about 70 nights for a campaign which would be impossible to cover in manual mode. Therefore, one of the main lessons learned was the need of the robotic operation mode in order to decrease the number of staff members operating the telescope.

Experience gained from the remote operation mode - The remote mode operations with BEST was the first step towards a fully automatic system. The performed operations provided us with the experience on the autonomous execution sequences and with the necessary safety procedures and control sequences because the BEST observations were run semi-automatic. Therefore the BEST II telescope in Chile was designed for a robotic mode with all experience applied which were gained from the remote observations by the BEST from OHP.

6.2 BEST II

Figure 6.3: *BEST II operational at OCA.*

The plans for the new telescope Berlin Exoplanet Search Telescope II (BEST II) were introduced with the progress of the CoRoT space mission. In particular, the

Table 6.2: *Project schedule for BEST II.*

	Date	Phase
System design	2005	I
Purchase of components	October-February 2005/2006	I
Laboratory tests (DLR)	February-August 2006	I
Transport I. part	September-December 2006	I
Transport II. part	November-February 2006/2007	I
Installation at OCA	February-April 2007	I
First light	15 March, 2007	II
Commissioning phase	April-June 2007	II
First scientific run (observer mode)	2007 July-September	II
First robotic observations	2007/2008 November-March	III
Normal operations, full automatization	2009/2010	IV

BEST II design was based on the acquired experience with the BEST operations at TLS and OHP. A suitable site with excellent weather conditions was found at Observatorio Cerro Armazones (OCA) in the Atacama desert, Chile.

The BEST II design is similar to BEST consisting of a small aperture telescope with a wide field-of-view which can observe several thousands of stars with high photometric precision. Compared to BEST the parameters of the new telescope needed to be adjusted (e.g. size of the CCD chip, resulting angular resolution). The main difference between the two systems is that the operational mode was designed to be fully automatic. This was given due to a limited internet bandwidth at the OCA site and due to a location in a desert on the other part of the globe, making all logistic aspects here different. Therefore, a different degree of autonomy for operations and maintenance was required to decrease manpower needed as mentioned in the previous section.

The plan of the BEST II project was divided into four phases (see Table 6.2). Below the various steps from planning to automatic operations (robotization) are described:

Phase I - this phase included the system design based on BEST experience and the implementation of technical solutions needed for the robotic operations. Main components such as telescope, mount, CCDs, webcams, various sensors (temperature, movement) and control PCs were purchased during this phase. Additionally, as a DLR contribution to the infrastructure of the observatory, batteries, for the storage of solar energy and a diesel generator were purchased.

This thesis work started in 2006 during the ongoing component purchase phase (initiated in early 2005). After the definition and setup of the h/w components the whole system was tested in the laboratory and optical instruments (CCDs) were checked for performance. The installation of the system as well as the control electronics was performed in cooperation with colleagues at DLR[1]. At the same time control s/w for simple operational sequences such as normal and emergency shutdown, and normal operations was tested and optimized. Additionally, the integrated functionality of h/w and s/w was tested during July and August of 2006.

[1]Anders Erikson, Hartmut Korsitzky, Andreas Kotz, Christopher Carl, Pascal Hedelt - all DLR

The successfully tested system was prepared for shipping to Chile in two parts. The first part of the shipment contained the main components such as telescope, mount and control computers. Thus the system could be operated immediately after arrival and installation in Chile. This equipment left DLR in September 2006 and arrived in Antofagasta, Chile in January 2007 after a long transport through the Panama channel. The second part of the equipment including mainly electronics for the robotic operations was shipped in November 2006 and arrived in Chile in February 2007. After the arrival mount and the telescope were installed and aligned. In the second step, the electronic equipment and communication cables were installed and the system was prepared for the fine tuning required for the scientific operations.

This PhD project consisted then of numerous travels to OCA in particular to adjust and test the system and to obtain the first light on March 15 ,2007 (see Figure 6.4). The Phase I was successfully finished after commissioning of the telescope in June 2007.

Figure 6.4: *First light image with BEST II of the Orion Nebula obtained on 15 March, 2007.*

Phase II - The second phase began in July 2007 with the first scientific observations in observer mode from OCA. In parallel, this phase also served to test the functionality of the system and as a preparatory phase for the automatic operation. In particular, the control electronics securing the safe operation in automatic mode were implemented and tested. The first scientific data were taken during observational campaigns in July and August 2007.

During a maintenance trip to OCA in October 2007 a DAVIS instruments weather station was installed to monitor the local conditions. Phase II represents a substantial part of this thesis work in which the telescope was successfully prepared for automatic operations.

Phase III - In this phase from November to March 2007/2008 the science operations were performed automatically. The observer needed just to open the roof from a remote place and then submit an observing plan to the local controlled computer. The weather conditions were checked via he control program and in case of

a strong wind the telescope could be parked and the observations terminated. Due to technical problems beyond our control with the roof, the operator preparing the observations at the beginning of the run was needed. However, the observation and the shutdown sequence were performed automatically. The capability of the system in terms of photometric precision and quality is demonstrated in the thesis on the data set obtained during this period (see Chapter 8).

Phase IV - In this phase, a full robotization of the observations will be achieved. The operations will be run automatically just by submitting a script with observing plan. In addition, the roof and the safety position check of the telescope will be performed automatically without an operator. Furthermore, the data treatment in terms of basic calibration (see Chapter 8) could be performed on site automatically if so desired. Theoretically, longer observational campaigns without any human assistance will be possible when all problems with the roof are solved. This final phase is planned for 2009 - 2010 and partly beyond the time allocated for this work.

6.2.1 Observatorio Cerro Armazones

Figure 6.5: *View at OCA from Armazones mountain.*

The observatory

Observatorio Cerro Armazones is located at 24°35′53” South and 70°11′47” West at an altitude of 2817 m in Atacama desert, Chile (see Figure 6.5). The site is operated by Astronomisches Institut von Ruhr Universität Bochum (AIRUB), Germany in cooperation with Universidad Católica del Norte (UCN), Antofagasta Chile. The DLR contributed to the local infrastructure with batteries and an electricity generator unit for power supply.

In the normal mode the observatory is powered 100% by renewable energy sources. One hundred solar panels (each providing 130 W) are installed on the main observatory building. In additon, two wind energy converters are planned as a reserve power supply. The water is heated with an additional flat-plate solar-thermal col-

lector. The heat produced by computers and servers in the main building is used for the heating of rooms.

The observatory is connected via radio link to the internet but with low bandwidth (512 kBit/s). The bandwidth constraints the potential operation mode and data download via internet. Therefore, large volumes of data can not be downloaded but either need to be transported to Europe or processed on site (as foreseen for phase IV of the BEST II implementation).

The observatory hosts besides the BEST II telescope also the AIRUB operated Hexapod (HPT)[2] 1-m telescope equipped with an Echelle spectrograph BESO ($R = 50.000$). In addition, two telescopes VYSOS 6 a 15-cm refractor, [3] and a smaller VYSOS 16 ca. 40-cm aperture Coudé telescope are operated at OCA. In the near future, the Infra Red Imaging Survey[4] (IRIS) 80-cm telescope equipped with an infrared detector will be installed. The latter telescope will be operated by AIRUB in cooperation with the University of Hawaii.

BEST II building

The BEST II telescope is installed at a separate house on the western side of the main observatory building. The height of BEST II house is about 2-m exactly covering the telescope with a roll-off roof. An anemometer, wind direction measurement device and temperature sensors on a weather station are located on the eastern side of the BEST II house. A view of the house is shown in Figure 6.6.

Figure 6.6: *View at BEST II building.*

General weather conditions at OCA

On average similar weather conditions as for the nearby ESO-Paranal (25 km away) observatory apply to OCA. The seeing and number of photometric nights at Paranal observatory[5] are presented in Figure 6.7. Normally, 73% nights per year are photometric (176). Clear skies without clouds are typical for the Chilean summer period from November to April. On the other hand during May, July and September strong winds ($> 15m/s$) make the observations impossible. The total number of

[2]http://www.astro.ruhr-uni-bochum.de/astro/oca/hpt.html
[3]http://www.astro.ruhr-uni-bochum.de/astro/oca/vysos.html
[4]http://www.astro.ruhr-uni-bochum.de/astro/oca/iris.html
[5]http://www.eso.org/sci/facilities/paranal/site/paranal-figs.html#seeing

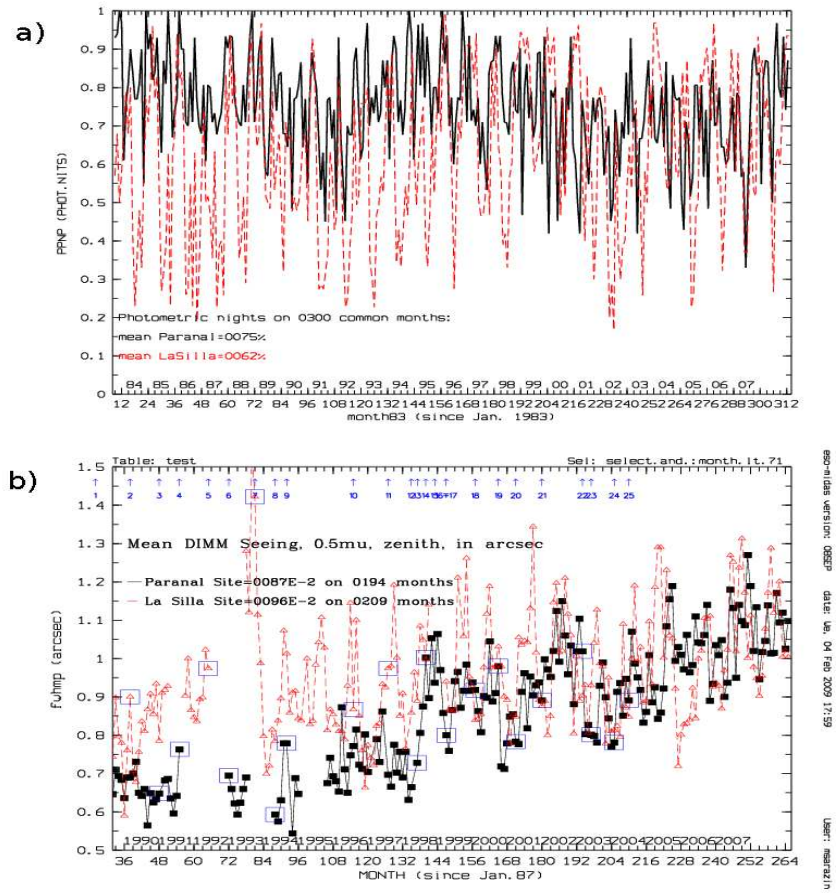

Figure 6.7: *Plot a) shows a statistics on photometric nights over years. Plot b) presents values of seeing for different years. Presented values were determined for ESO-Paranal observatory. Both images are by ESO (175).*

nights with strong wind conditions[6] occur on average during 50 days/year mostly during the above mentioned period.

The temperature over the year ranges from few degrees Celsius below zero in winter - sometimes with a few sudden temperature drops during the nights - to +35° C in the summer. Relative humidity is about a few percent $(5 - 16\%)$ making the atmosphere very transparent. In October 2007 a small *DAVIS Instruments Vantage 2000 Pro* weather station monitoring wind strength, pressure, temperature, wind chill and relative humidity was placed at the housing of DLR telescope[7].

Weather conditions during the 2007 **-** 2008 **period**

The weather for the first observational campaign lasting from July - August 2007 was affected by cloudy periods what is typical for Chilean winter season. In addition, high wind speeds over 15 m/s made the observations impossible on several nights. Unfortunately, weather data could not be collected because the weather station was installed only in October 2007 after the campaign end. Since October 2007 the weather station is monitoring wind speed, indoor and outdoor temperature, humidity, wind direction and atmospheric pressure. The measurements are taken

[6]http://www.eso.org/sci/facilities/paranal/site/paranal.html
[7]http://hpt.dnsalias.com:8080

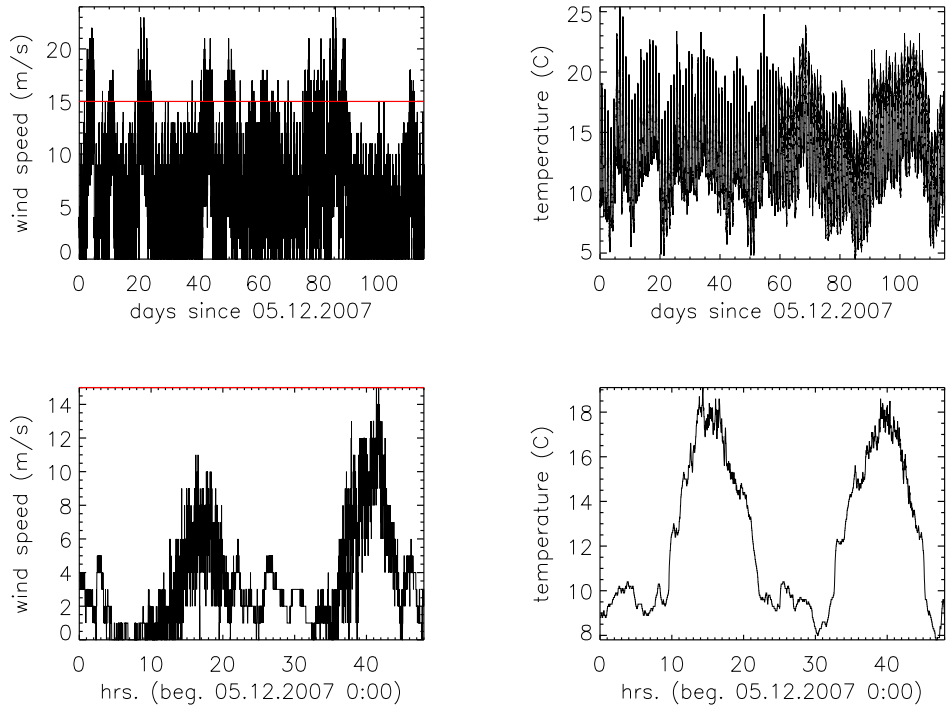

Figure 6.8: *Typical weather conditions at OCA: Plot at top left represents the wind speed during the campaign LRa02 starting in December* 2007*. The red line represents the limiting value of the wind speed for closing down of the observatory. Top right plot shows a temperature profile for LRa02 campaign. In the bottom left and bottom right typical wind speed and temperature profiles on two nights can be seen.*

every minute and stored on the computer. The robotic campaign between November 2007 and March 2008 was performed under mostly excellent weather conditions. Only three nights were affected with thin cirrus clouds and four with strong wind which was mostly active during the day (about 44 days) but slowed down at evenings.

Typical wind speed trends can be seen in two plots on the left in Figure 6.8. The lower diagram presenting the wind speed profile starts at midnight 5 December, 2007 and phase without the wind lasts approximately to 10 am and then the wind speed increases and again slows down at about 8 pm. For clarity data for the following day are also shown. The upper diagram in the same figure presents the wind speed over the complete campaign starting on 5 December 2007 and ending in April 2008.

The diagrams on the right side present the corresponding daily temperature profile with a peak usually during the afternoon lasting to the sunset in the upper panel and the lower panel shows the temperature distribution for two nights (starting on 5 December 2007). In Table 6.3 a detailed statistics for the 2007/2008 campaign based on the weather station data is presented.

The presented weather statistic shows the suitability of the OCA site for survey programs such as BEST II which require high duty cycle and excellent photometric conditions. In principle, no safety measures regarding the rain fall need to be taken since no rain was detected during the complete campaign. The average rain fall is

$<$ 10 mm per year[8] at the site. The only factor which needs to be seriously taken into account is the wind speed because it can reach in same case more than 20 m/s. Therefore, a closing conditions of strong wind were set 15 m/s. Clouds are also very rare but if they occur they influence only the quality of the observations and not the telescope safety.

Table 6.3: *Weather conditions at OCA during* 2007 - 2008.

weather conditions	nights 2007/2008
total no. nights	92
clear nights	89
strong wind during the night ($>$ 15 m/s)	4
strong wind during the day ($>$ 15 m/s)	44 (days)
clouds	3

6.2.2 System description

The main components of the BEST II system are divided into three classes, as can be seen in Figure 6.9. They consist of the telescope and mount (yellow box), control computers, network electronics (router, IP-link - green box) and auxiliary devices such as webcams, a weather station and the roof motors (blue box). The system (including the roof) is controlled via computers connected with the DLR control center in Berlin. The main specifications of the system are provided in Table 6.4. The following sections will describe the system and its operational scheme in more detail.

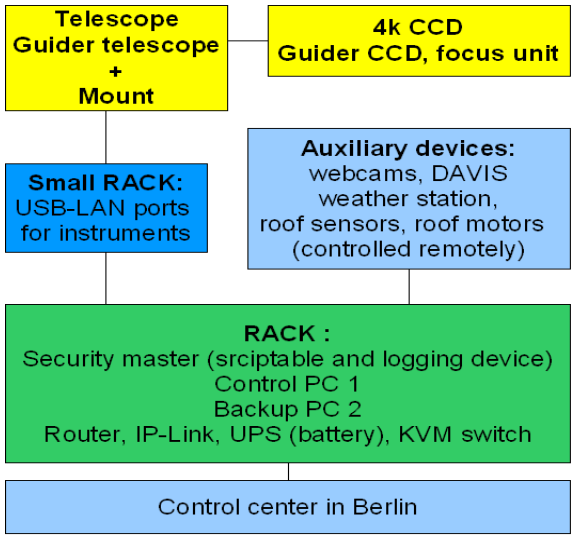

Figure 6.9: *Schematic diagram of the BEST II system consisting of three (four) main components presented with different colors.*

[8]http://www.eso.org/sci/facilities/paranal/site/paranal.html

Table 6.4: *BEST II telescope specifications.*

Telescope	BRC, TEC APO 140 ED (Guider)
Instrument	CCD: FLI KAF16801E2 (Kodak)
Cooling	peltier cooling
Aperture	25-cm, 14-cm (Guider)
Focal ratio	F/5.0, F/7.0 (Guider)
CCD size	4096×4096, 1530×1020 (Guider)
Pixel size	9 μm, 9μm (Guider)
Pixel scale	1.5 arcsec/pixel
Field-of-view	$1.7° \times 1.7°$, $1.6° \times 1.0°$ (Guider)
Mount	GM 4000 (10 Micron) German equatorial
Guiding	CCD: ST-1603 ME (SBIG)

6.2.2.1 Concept of the system setup

BEST II is operated in the robotic mode because of above presented reasons (manpower, internet bandwidth). Therefore, the system must be able to perform observations securely and automatically taking into account changing local conditions. The concept of operations is built around two control computers. The first PC is dedicated to control of telescope operations and the second PC is used for the backup of the obtained data and for the monitoring of weather conditions. In addition, if the control PC1 would experience a failure PC2 can overtake the operation tasks, since the s/w setup is mirrored between the two computers. The operational concept is

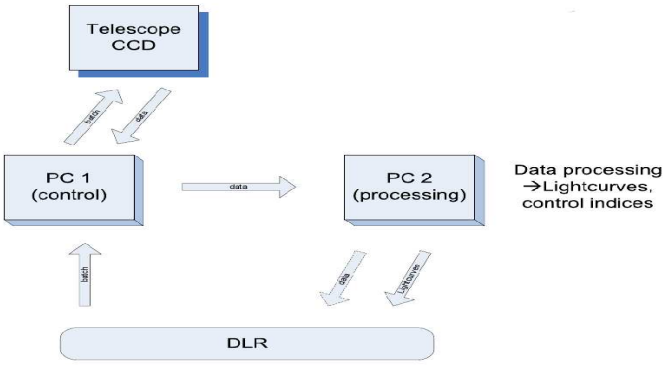

Figure 6.10: *Concept of BEST II operations is based on robotic operations.*

illustrated schematically in Figure 6.10. A file with observational sequence execution commands is submitted to PC1 from the control center in Berlin. PC1 then controls all the functionality of the data acquisition while PC2 stores the data and serves as a backup computer of the system. Furthermore, an image processing pipeline will be installed on PC2 in a near future. In the following paragraphs the main components of the system will be described beginning with main component *RACK*

box equipped with the electronics and ending with the CCD camera mounted at the telescope.

6.2.2.2 RACK

The main control *RACK* is located at eastern wall of the observatory house and contains the control electronics including the *security master*, control PCs, the battery and internet devices controlling the communication with the institute in Berlin. Overheating is prevented by three fan units which are switched on automatically dependent on the temperature in the RACK. Since the environment at the observatory is very dusty, the incoming air is filtered by an exchangeable cotton-like filter which is placed at the bottom of the *RACK* and can be exchanged easily. The overall setup of the *RACK* is presented in Figure 6.11 and the devices in the *RACK* are as follows:

The security master - This is a scriptable device controlling the environmental sensors installed inside the RACK, the status of the power switches for all other devices and the health of the system. The *security master* can be controlled with an interactive interface remotely. In particular, power supplies for the PCs, CCDs, mount, the telescope, webcams and for the lights mounted in the observatory building can be controlled here. In addition, the roof sensors reporting the position of the roof can be controlled with the *security master*. Each process is documented and stored in a log file. All functions described here can be also controlled automatically with a control s/w

PC1 - This is the main computer (CL9-1.6 GHz CPU, 1024 MB RAM) controlling the observational tasks, one 70 Gb hard disc is internal and up to two portable discs (450 Gb each) can be inserted in order to store the data.

PC2 - This is the backup computer with specifications same as *PC1* but only monitoring the weather conditions via DAVIS weather station. The *PC2* is used for the backup of the observational data. The functionality of PC 1 and PC 2 can be switched in case of malfunction of *PC1*.

IP-link & KVM switch - Internet devices.

Router - the internet traffic is controlled with this standard type device.

UPS - This unit consists of a Pinnacle 1500 series UPS from Alpha Technologies equipped with $3 + 6$ (standard UPS and battery extension pack) batteries that can provide the additional power in case of power failure for maximum of 20 minutes to safely shutdown the system. All connected electronic devices are divided into three groups connected to different power circuits with respect to their importance for the operations. E.g. PC1 and the main CCD camera is on a priority circuit which will be powered as long as possible in case of power failure.

Three fan units - used for the cooling of the environment in the *RACK*. The fan

Figure 6.11: *Figure a) presents the RACK with electronics controlling the system operations. 1) is the security master, 2) is PC1, 3) router, 4) PC2, 5) IP-link, 6) KVM-switch 7) battery, 8) fan, 9) interface with cable ports. Figure b) presents an interface for cables (see 9) in Figure a)) connecting the instruments with the control PCs. Ports: GK and POW - power supply ports, 4CC - scientific CCD, GCC - guider CCD, MT - mount, LAN - free port for LAN connection, D1, D2 - Internet ports, FC, MC - free ports.*

starts automatically, when a certainly defined temperature is reached in the *RACK*.

Additionally, the *RACK* is equipped with temperature and movement sensors monitoring the health of the system. All information from the sensors are secured in internal logfiles.

The cables connecting the electronics in the *RACK* with the instruments at telescopes are converted from USB into Local Area Network (LAN) type cables and connected via interface (see Figure 6.11 b)) in the *RACK* to the *Small RACK*.

6.2.2.3 Auxiliary devices

The auxiliary devices include a weather station, webcams, roof motors, temperature and movement sensors and observatory lamps mounted in the BEST II building. Two webcams are directly accessible via internet. One webcam is movable and can monitor the whole BEST II house. The second webcam is fixed at one position and monitors the telescope. The two motors for opening the roof parts (northern and southern) can be controlled remotely.

6.2.2.4 Small RACK

Figure 6.12: *Small RACK.*

The *small RACK* (see Figure 6.12) is located under the telescope on a plate on the side of the pier (see Figure 6.14). The main purpose is to store all important power supplies and cable ports for the instruments (CCD+telescope) at one place. The instruments connected to the *small RACK* can be controlled automatically via *security master* with help of executable scripts from PC1. Figure 6.13 presents the labeling of the cable slots for the different devices.

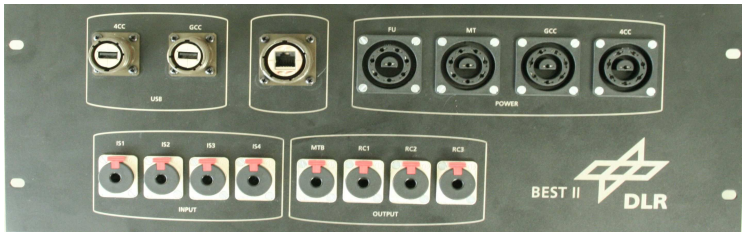

Figure 6.13: *An interface with ports at small RACK. Top row USB:**4CC** - USB cable from the scientific CCD, **GCC** - USB cable from the guider CCD; one slot for future LAN operation mode of the mount; power:**FU** - power supply focusing unit,**MT** - power supply mount,**GCC** - power supply guider CCD,**4CC** - power supply scientific CCD. Bottom row INPUT: all positions free for environment checking sensors; OUTPUT: **MTB** - triggers the mount to switch on/off, **RC1** - free, **RC2, RC3** - ports for the roof opening/closing one for each half.*

6.2.2.5 The mount

Figure 6.14: *The mount with the telescope at OCA. (May* 2007*).*

The mount (see Figure 6.14) was purchased from BAADER Planetarium, Germany. It is a commercial mount of a German Equatorial type fabricated by the Italian company 10 Micron and modified for observations at the southern hemisphere. It is installed on a massive pier fixed on a concrete pedestal in the center of the observatory house (see Figure 6.6). Inside of the mount and pier is a channel for cables from the instruments so that they do not disturb observations (see Figure 6.15 c). The power supply for the mount is installed in the *small RACK*.

The mount communicates with the computer PC1 via a *RS232* cable where a control software (see Section 6.2.2.1) for the operation of the system is installed. The *RS232* (see Figure 6.15 b) is connected to the *small RACK*. Additionally, the mount can be operated by a handpad directly (see Figure 6.15a) or with the s/w *virtual keypad* which has exactly the same interface as the true handpad. The normal communication during observations is performed within the *Astrophysics mount* (AMP) protocol with drivers based on ASCOM platform[9]. If the mount is switched off the last position is stored and after the reboot no synchronization is needed. Internal hardware limits are set in the firmware of the mount, preventing movements which could damage the system. In addition, when these limits are reached the motors will switch off automatically. An internal pointing model, stored in the firmware of the mount, is used for the

Figure 6.15: *a) displays the handpad box which can be used to control the telescope at OCA, b) shows the ports of the mount, c) the channel inside the mount allows the secure routing of cables from instruments.*

centering of scientific frames. A very good pointing accuracy reaches a precision of a few seconds of arc. Therefore, almost all scientific frames are centered at one position on the sky. In addition, systematic tracking errors are also negligible.

[9]http://ascom-standards.org/

6.2.2.6 The Telescope

Figure 6.16: *The telescope tube in the laboratory.*

The Berlin Exoplanet Search Telescope II is a Baker-Ritchi-Chrétien-250 (BRC-250) with a diameter of 25-cm with focal ratio $f/5$ manufactured by Takahashi[10] (see Figure 6.16). The BRC system contains of two non-spherical (hyperbolic) mirrors (primary and secondary) and of two supplementary lenses correcting the spherical abberation, coma and also astigmatism. The BRC-250 is temperature-compensated by using carbon fiber tube which assures precise focus that will not change with temperature fluctuations. Additionally, for future operations a motorized focus unit is mounted but it is currently not in use.

The telescope is equipped with a 4096×4096 pixels front illuminated CCD which is mounted in the focal plane on the adapter installed on the telescope's movable collimator. The resulting FOV of the optical system is $1.7° \times 1.7°$ on the sky with an angular resolution of 1.5 arcseconds/pixel.

6.2.2.7 The guiding system

For the guiding an additional air cooled SBIG CCD[11] camera ST-1603 ME (1530×1020 pixels at 9 micron) is mounted on a smaller TEC APO 140 ED[12] refractor with an aperture of 14-cm and the focal length $f = 980$ mm (F/7 focal ratio). The quite large FOV of approximately $1.7° \times 1.7°$ assures constant availability of suitable star for the guiding corrections to the telescope motors. The selected guiding star is centered on the guider CCD before the scientific exposure and its position is monitored with a series of short exposures. In case, that the guiding star moves from the center a small correction is applied to the mount forcing the guiding star to be centered again.

The guiding telescope is mounted in metal rings placed together with a main telescope on the plate fixed to the mount (see Fig. 6.14). Due to this the focal axis of both telescopes are parallel and the parallax of the system negligible. The process of finding of a suitable star for the guiding and the guiding itself is controlled automatically via observation control software (see below).

[10] http://www.optique-unterlinden.com/takahashi/en/BRC-250.php
[11] http://www.sbig.com/products/1603_new.htm
[12] http://www.baader-planetarium.de/tec/tec_start.htm

6.2.2.8 The BEST II 4k-CCD

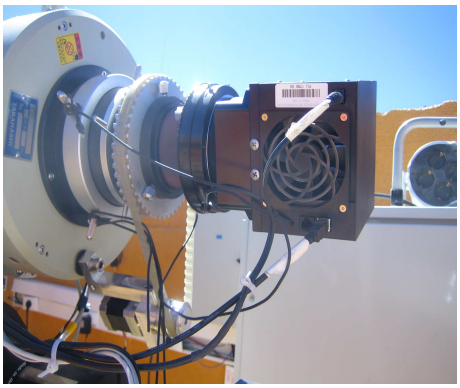

Figure 6.17: 4096 × 4096 *CCD.*

The BEST II CCD was purchased from Finger Lakes Instrumentation. It is a front illuminated 4096 × 4096 pixels CCD with the KAF IMG-16801E1 chip and have a pixel size of $9\mu m$. The digital resolution is 16 bit with a saturation level of $100,000e^-$ corresponding to 65536 ADU. The CCD is cooled thermoelectric cooling and can reach about 30° below ambient. All main specifications of the CCD are summarized in Table 6.5.

Readout time - The readout time of the CCD is around 90 seconds for full frames. This rate of the readout time constraints the sampling of scientific frames and the observational sequence. It is possible to read-out small parts of the CCD which reduces the readout time.

Gain factor - This factor can be determined quickly from the obtained frames using the relation (162)

$$g = \frac{(\overline{S}_{flat1} + \overline{S}_{flat2}) - (\overline{S}_{bias1} + \overline{S}_{bias2})}{\sigma^2_{S_{flat1}-S_{flat2}} - \sigma^2_{S_{bias1}-S_{bias2}}} \tag{6.1}$$

where $\overline{S}_{flat}$ is the mean signal (ADU) in a flat frame and $\overline{S}_{bias}$ is the mean signal in a bias frame. The gain factor was determined from test frames obtained at an operational temperature of −20.3° C to be $g = 1.9e^-$/ADU. This value is in agreement with the value provided by manufacturer[13].

Dark current level - The low dark current level does not exceed the mean value of $50e^-s^{-1}\text{pixel}^{-1}$ at 25°. At an operational temperature of −20° C the mean dark level of the whole image was measured to be about 5 ADU for a 240 seconds exposure. This is less than $9.5e^-s^{-1}$/pixel (see Chapter 8). With an increasing temperature the dark current reaches up to 100 ADU at 10° C but in general, below −10° C the dark current is less than a few ADUs. The temperature dependency measured during tests at OCA are shown in Figure 6.18 a).

Bias level - The mean value of the bias was determined to be $S_B = 4400$ ADU during tests at the OCA site. The variation of the bias level over a whole observation campaign will be discussed in Chapter 8. The readout noise in e^- can be roughly estimated from two test bias frames (taken at −20.3° C) according to method by (162)

$$\sigma_{readout}(e^-) = \frac{g\sigma_{B1-B2}}{\sqrt{2}} \tag{6.2}$$

[13]FLI technical support provided the value of g=1.8-2.0 e^-/pixel

and giving a value of $\sigma_{readout} = 3$ ADU$= 5.7e^{-}$.

The peak quantum efficiency (q) - A value of 66% is reached at wavelengths around 650 nm. The complete response curve of the CCD is shown in Figure 6.18 b). The relevant curve for BEST II CCD in this figure is the upper one corresponding to a Grade 1 chip. The second curve in the same figure corresponds to a Grade 2 CCD chip.

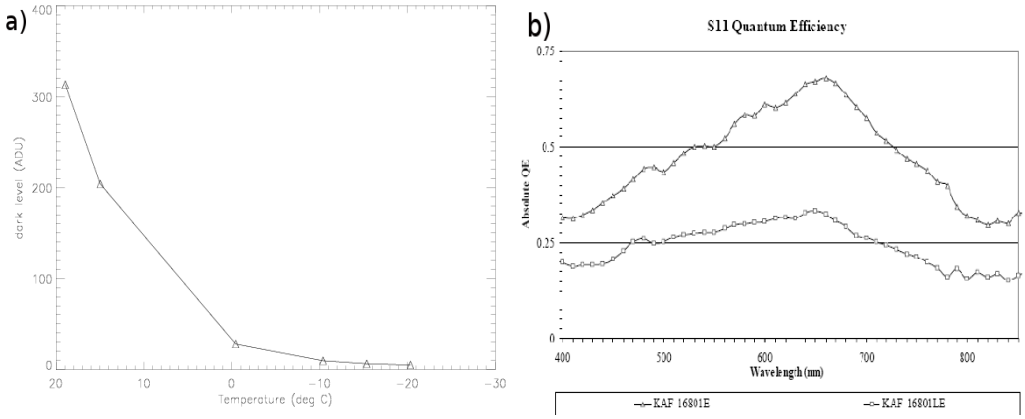

Figure 6.18: *Panel a) presents a temperature dependency of dark current level for various temperatures for* 240 *second exposures. Spectral response of KAF16801E1 CCD chip is shown in the panel b). Image by Kodak.*

Table 6.5: *Finger Lakes Imager CCD specifications.*

Chip	KAF16801 Grade 1
A/D converter (bit)	16
Size	4096×4096
Pixel size	9
Cooling	peltier cooling
Gain (e^{-}/ADU)	1.9 (1.8-2.0)
Well depth (ADU)	65535
Bias level (ADU)	≈ 4200
Readout noise (ADU)	5
Dark current (ADU)	< 6
Readout time	approx.90 sec

6.2.3 BEST II operations

BEST II operations are performed in robotic mode with only slight human interference required. The system described in previous sections allows autonomous operations. The scheme of the overall operational sequence can be seen in Figure 6.19.

The sequence of operations consists of the following basic steps, firstly a script with commands for the system is submitted before observation from Berlin to OCA. Then, the system health is checked and the observatory and the components are prepared for the observational sequence. After sunset calibration frames are taken and followed by the scientific images acquisition. At the end of the observational night

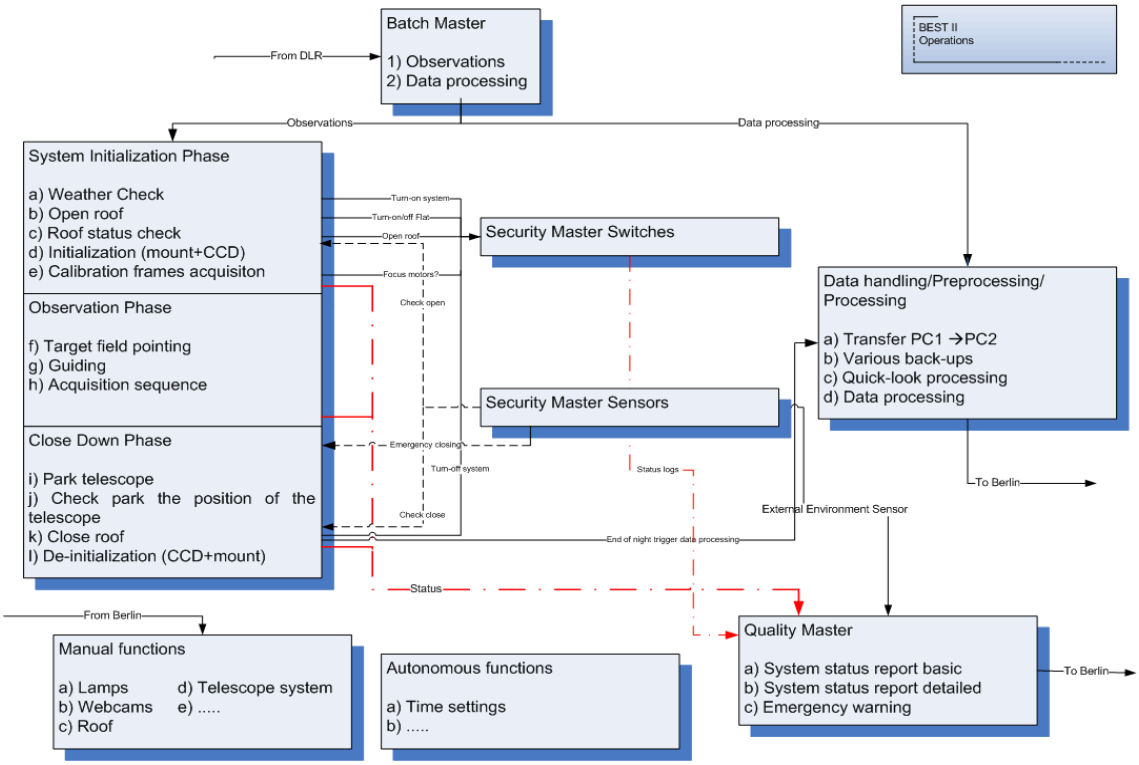

Figure 6.19: *Detailed scheme of BEST II operations with defined safety procedures.*

the system is shut down and acquired data is backed-up. Local weather conditions are monitored continuously with DAVIS Vantage 2000 weather station. In case of bad weather the system is permanently shut down. In more detail, the observation phase can be divided into following steps (see Figure 6.19):

System initialization phase:
Weather check - the weather data from the DAVIS meteorological station are checked and in case of normal conditions (wind speed < 15 m/s) the observation sequence is initiated .
Opening of the roof - The roof is opened by a script via control software ACP. Currently, the roof needs to be opened remotely from DLR.
Checking the status of the roof - The status of the roof is checked by roof sensors reporting, its position. Alternatively, in the roof can be checked with webcams.
Initialization sequence of the telescope and CCDs - This is done automatically automatically with a control software.
Calibration frames at dusk: bias, dark, sky flat field frames - These frames are acquired by an observatory control program.

Observation phase:
Pointing at target, centering.
Guiding - suitable stars is found and the guider CCD is started with a control program.
Scientific frames acquisition sequence.

Close down phase:
Parking the telescope - is automatically performed after finish of the run with a control program.
Checking the telescope position - is checked by a control s/w. Alternatively the position of the telescope can be check by webcams.
Closing of the roof - Roof is closed automatically by a script via the control software. Currently, the roof must be closed remotely from DLR.
Shutdown of the mount and CCDs - is automatically performed with a control program.

Quick look at the data and the data processing:
Due to low bandpass of the Internet connection an automatized quick look routine for the fast data check such as determination of good and bad flat fields and other calibration frames. In a near future, also an auomatized routine performing a basic data calibration is foreseen for OCA. These features will be implemented in 2009/2010.

6.2.3.1 BEST II control software

```
; -------------------------------------------
; This plan was generated by ACP Planner 3.1.3
; -------------------------------------------
;
; For:            admin
; Targets:        2
; Start Imaging: 31-Aug-2008 16:11:03  (local)
; Total Time:     00:10:40
;
; User Comments:
;           this is an observational script for LRc3
; -------------------------------------------
;
;
;
;
; === Target lrc3a ===
;
#sets 5
;
; WARNING: Folder path is not portable.
#dir F:\N080831\lrca    ; Images forced to go into this folder
#count 1
#interval 120
#binning 1
lrc3a   18:33:11.00     -06- 39' 01.0"
:
```

Figure 6.20: *Script file with commands for the observational sequence.*

The telescope and mount operations are performed with help of the Observatory control program (ACP) software[14]. This software controls all phases of operations from the initialization, calibration frames acquisition, telescope pointing, guiding, scientific frames acquisition and safety shutdown.

This robotic mode allows a very easy operation of the full system. The operator needs only to submit an observational script with coordinates of targets and number and times of exposures (see 6.20). All calibration and observation phases are executed in order they are written in the script file. The file can contain constraints in terms of minimum air mass when the observation begin, or simply the date of the start. In principle, long sequences lasting more than one night can be planned and submitted.

Additionally, the hardware limits of the mount are controlled for software limits with ACP, thereby providing a high level of safety. The weather information is continuously updated with help of data incoming from the weather station which

[14] www.dc3.com

are transfered and controlled with ACP Weather Server[15] s/w providing the relevant information to ACP to initiate an emergency shutdown if needed.

The scheme of ACP functionality and structure with respect to other components is shown in Figure 6.21. In the figure four main components of the ACP software are differentiated with color and it is divided into various sub-parts. The main s/w controlls an ACP Weather and telescope drivers in the second, ASCOM driver, level (blue). Yellow boxes present a weather station and a MaxIm Dl software containing the standard drivers. The third level (green) the devices connected and controlled via ACP.

The ACP consists of main program including the support routines which are called during the observation. It needs only the ASCOM platform[16] used as a standard for the communication between hardware (mount, telescope,..) drivers and computers and MaxIm DL[17] which is used for the image acquisition. Numerous objects provide an access to the functions stored in the support libraries. Additionally, self written scripts in VBScript and JScript can be implemented if needed. Therefore, the operator has the flexibility of adding custom routines which are specific for the telescope system such as additional safety checks.

Also some other standard programs as FocusMax[18] for the control of focus, planetarium program such as The Sky[19] and already mentioned ACP Weather Server can be installed. .

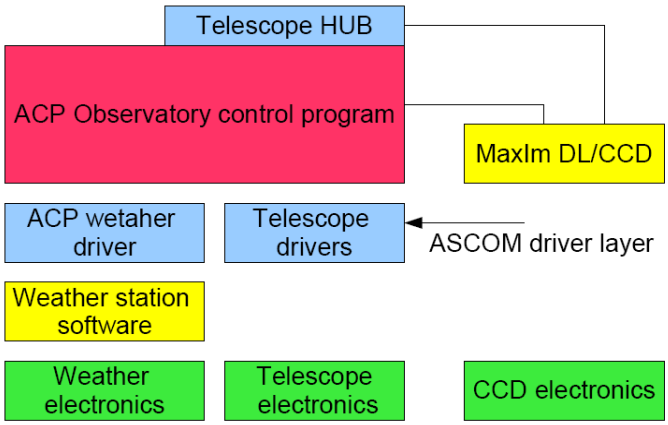

Figure 6.21: *Scheme of functionality of the ACP control software for the BEST II in the present configuration. (More detailed scheme, for ACP functionality can be found in (177).)*

In case of a general of power supply failure at OCA, the UPS provides about 20 minutes of additional operations. In this time the system can be shutdown. In the present state, no check within ACP is performed whether the power supply works normally but this feature is planned for future custom emergency scripts run under ACP control software.

[15] http://www.ccdastro.net/wwi.html
[16] http://ascom-standards.org/
[17] http://www.cyanogen.com/
[18] See web page www.dc3.com
[19] http://www.bisque.com/products/thesky6/

6.2.3.2 Data treatment

An important aspect of the BEST II operation is the data treatment. Since no staff is located at OCA permanently the acquired data need to be securely stored for longer periods of time. For the data storage four 500-Gb portable discs connected to PC1 is used. After each observing sequence a backup of the acquired data is made. In total, the four data discs, two for each PC, are providing 2 Tb of disc space for this purpose. Each CCD frame has a size of approximately 33 Mb. Therefore data collected during one night of observations can reach a total size of $4 - 8$ Gb and monthly data volumes of 150 Gb can be used. Therefore, the available disc capacity (science frames, backup) is provided for a campaign lasting approximately 6 months. Then all data discs are replaced by service staff and transported to DLR.

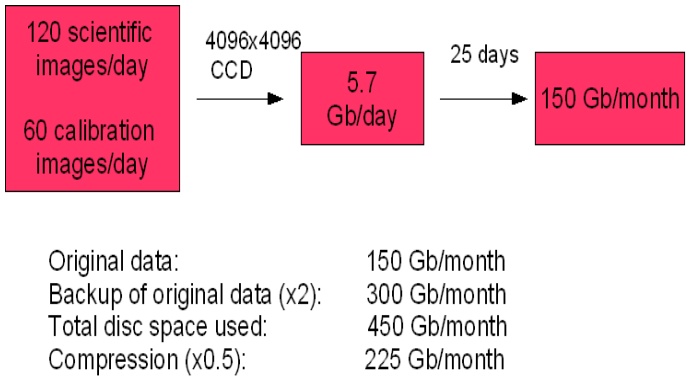

Figure 6.22: *The statistic on disc space needed for data storage and data reduction for a typical BEST II campaign. One day is assumed to have* 10 *hrs.*

An overview on a disc space needed for the data storage is presented in Figure 6.22. Total frame number taken during the night of observation is approximately 180 images resulting in 150 Gb of data. Two backups of the original data will increase the necessary disc space about more 300 Gb leading to a total used disc space of 450 Gb. In case of 50% compression of the data at the end of campaign a total disc space needed will decrease to 225 Gb per month.

Figure 6.23: *Cluster computer system for the data analysis at DLR.*

At DLR a data processing unit is available for the BEST II data treatment. It consists of a 18 nodes *SUN Fire Z20* computer cluster system (see Figure 6.23) used for the data reduction and analysis. This includes the calibration, photometry, and scientific analysis. A more robust long-term data storage scheme is planned to be implemented in a near future.

6.2.4 Lessons learned

A number of lessons have been learned during the installation and first operations with the BEST II system. They include:

- A very important phase was the testing phase at DLR and the simulation of the operations. The experience gained during this phase have made the installation and operations at OCA easier.
- Fully robotic operations can be performed with a relatively simple technical setup based mainly on commercial products.
- The possibility of full remote manual control of the system for a complete shutdown and reboot is a very important feature also after the installation phase. Although, not often used it is of importance to handle unusual technical problems.
- An important part of the system is the safety check of all components and a safety shutdown sequence in case of emergency such as bad weather conditions (already implemented) or failure of the power supply (implemented in a near future).
- Also for a robotic telescope some local support at a basic level is important for unexpected failures.
- It is possible to keep the system on the good observational level with 2-3 maintenance trips per year.

The scientific aspects learned from the comparison of the OHP and OCA sites and the different telescopes with respect to transit detections will be discussed in Chapter 7. For that purpose a quick comparison of the main parameters of both surveys are summarized in Table 6.6.

Table 6.6: *BEST & BEST II a technical comparison.*

	BEST	BEST II
Site	Provence, France	Atacama, Chile
Operations mode	remote from Berlin	robotic
Instrument	CCD: Apogee10	CCD: FLI KAF16801E2 (Kodak)
Aperture	19.5 cm	25 cm
Focal ratio	F/2.7	F/5.0
CCD size	2048×2048	4096×4096
Pixel scale	5.5 arcsec/pixel	1.5 arcsec/pixel
Field-of-view	$3.1^\circ \times 3.1^\circ$	$1.7^\circ \times 1.7^\circ$
photometric nights	40%	73%

Chapter 7

Observations and the data set

The purpose of the BEST project is ground based support of the CoRoT space mission. Therefore CoRoT's initial and long run observational fields were selected for monitoring with BEST and BEST II.

The data acquisition and scientific result for the BEST observational campaigns on the CoRoT's long runs LRa01, LRc01 and on initial run IRa01 were presented in Kabath et al. (2007), Kabath et al. (2008) & Karoff et al. (2007) (172; 173; 171). The results of the CoRoT long runs LRc02 and LRa02 observed with BEST II was described in Kabath et al. (2009) and Kabath et al. (2009b) (178; 179) The centers of CoRoT fields (FOV approx. $2.7^\circ \times 3^\circ$) are located at coordinates:

LRc01: $\alpha = 19^h\ 23^m\ 33^s$ and $\delta = +00^\circ\ 27'\ 36"$
LRa01: $\alpha = 06^h\ 46^m\ 53^s$ and $\delta = -00^\circ\ 12'\ 00"$
IRa01: $\alpha = 06^h\ 57^m\ 18^s$ and $\delta = -01^\circ\ 42'\ 00"$
LRc02: $\alpha = 18^h\ 38^m\ 38^s$ and $\delta = -06^\circ\ 24'\ 00"$
LRa02: $\alpha = 06^h\ 54^m\ 14^s$ and $\delta = -04^\circ\ 22'\ 48"$

These fields are in more densely populated regions of the Milky Way. In addition, the selection process favored the fields with high amount of main sequence dwarf stars in order to increase the probability of transit detection (180).

In this work all the observations on all CoRoT fields observed with BEST and BEST II are presented. An example of one field observed with BEST and the statistics on the acquired data will be discussed in Chapter 8. Information for remaining fields observed with BEST is included as catalog in the Appendix. In case of BEST II observations, the data on LRa02 field, which were taken in the robotic mode from OCA, will be presented in more detail as an example illustrating the potential of the survey. A catalog with all available information on the CoRoT fields observed with BEST/BEST II is presented in Appendix A.2.

The BEST and BEST II surveys can be compared based on their respective duty cycle coverage and some general conclusions can be made concerning the yield. Therefore, the BEST LRa01 and the BEST II LRa02 data sets will be compared. Primarily, since these are comparable campaigns of high photometric quality and therefore reflecting the full capability of the systems.

7.1 Overview of BEST target fields

The CoRoT fields observed with BEST are centered at coordinates:

LRc01 center: $\alpha = 19^h\ 00^m\ 00^s$ and $\delta = +00^\circ\ 01'\ 55$" - FOV $3.1^\circ \times 3.1^\circ$
LRa01 center: $\alpha = 06^h\ 46^m\ 24^s$ and $\delta = -01^\circ\ 54'\ 00$" - FOV $3.1^\circ \times 3.1^\circ$
IRa01 center: $\alpha = 06^h\ 46^m\ 24^s$ and $\delta = -01^\circ\ 54'\ 00$" - FOV $3.1^\circ \times 3.1^\circ$

The pointing of the BEST target field slightly differs from the pointing of CoRoT (see previous page) because the field was selected so that bright stars in CoRoT's astroseismology FOV were avoided during the BEST observations but the CoRoT exoplanetary field could be fully covered. An example of the orientation of BEST target field IRa01 with respect to CoRoT FOV is displayed in Figure 7.1. More details about the observed target fields are summarized in Table 7.1.

Table 7.1: *Details for target fields observed with BEST from OHP.*

Target	LRc01	LRa01	IRa01
Observation phase	Jul. - Aug. 2005	Nov. - Mar. 2005/2006	Dec. 2006
Total duration (days)	98	105	40
Fields	1	1	1
Nights	35	23	12
Hrs. observed	130	140	70
Frames	727	434	300
Calibration frames approx.	1400	920	480
Sampling rate approx. (min)	8	8	8
Exposure time (sec)	240	240	240

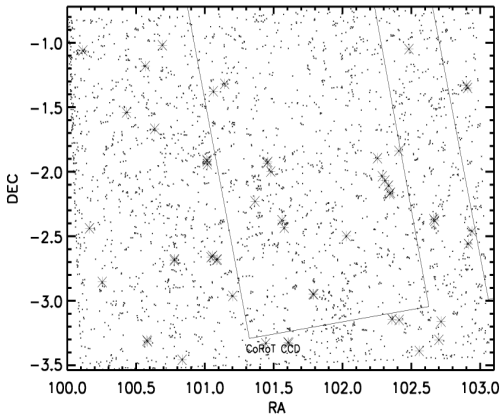

Figure 7.1: *The orientation of BEST IRa01 FOV with respect to CoRoT FOV. Dots representing detected stars and crosses the newly discovered periodic variable stars.*

7.2 Overview of the BEST II target fields

BEST II observed two CoRoT fields LRc02 and LRa02 during the 2007 - 2008 campaigns. The BEST II has a smaller FOV ($1.7^\circ \times 1.7^\circ$) compared to BEST but two subfields for each CoRoT field were observed (LRc02a, LRc02b & LRa02a, LRa02b).

Therefore, the complete FOV similar to FOV of CoRoT exoplanetary channel could be reached. The center coordinates of these BEST II subfields are:

LRc02

LRc02a: $\alpha_a = 18^h\ 41^m\ 02^s$, $\delta_a = +07°\ 12'\ 54"$ - FOV 1.7°.7°
LRc02b: $\alpha_b = 18^h\ 43^m\ 33^s$, $\delta_b = +05°\ 59'\ 53"$ - FOV 1.7°.7°

LRa02

LRa2a: $\alpha = 06^h\ 50^m\ 46.3^s$, $\delta = -03°\ 59'\ 31.0"$ - FOV 1.7°.7°
LRa2b: $\alpha = 06^h\ 51^m\ 13.9^s$, $\delta = -05°\ 26'\ 16.0"$ - FOV 1.7°.7°

The LRa02 field was chosen as an example to be discussed here. The details for the LRc02 target field can be found in Appendix. The orientation of both subfields of LRa02 target field with respect to CoRoT's FOV is shown in Figure 7.2.

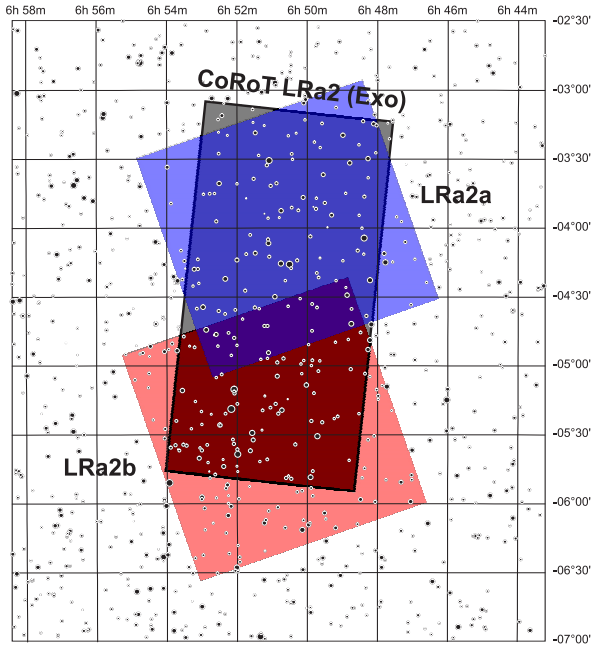

Figure 7.2: *Orientation of LRa02 subfields with respect to CoRoT Exoplanetary field.*

The BEST II data set on the CoRoT's LRa02 field has been obtained during the Chilean winter 2007/2008. We observed in a robotic mode on 39 nights within the total time span of 91 days. Generally, data were not taken during bad weather periods. In particular, we did not observe when the wind velocity reached $> 15m/s$ as well as during partly cloudy nights. Additionally, nights 3 days before and after the full Moon were excluded since the bright sky background affects the photometric quality. Part of the LRa02 data were taken in the first test phase of the robotic mode we also experienced some minor technical problems limiting the acquired volume.

The LRa02 data set contains of up to 836 scientific frames providing in total 231 hours of observations. A typical single observing sequence contains approximately 20 calibration frames including bias, dark and flat fields. The exposure time of flat fields was also fixed to 5 seconds providing approximately $2-4$ frames per night due to long read out time of the CCD. The average number of scientific frames per night per target field was 24. A summary of the observational statistics of frames taken on the LRa02 campaign is shown in Table 7.2 compared to LRc02 data set.

Table 7.2: *Characteristics of the LRc02 and LRa02 data sets.*

Target	LRc02	LRa02
Observed	July - August 2007	November - February 2007/2008
Total duration (days)	36	91
Fields	2 (lrc2a,lrc2b)	2 (lra2a,lra2b)
Nights	20	41
Hrs. observed	120	231
Frames	373 (lrc2a), 232 (lrc2b)	836 (lra2a), 793 (lra2b)
Calibration frames approx.	600	1230
Sampling rate approx. (min)	15	15
Exposure time (sec)	240	240

7.3 A quantitative comparison of the BEST/BEST II data sets

The purpose of a quantitative comparison of the BEST and BEST II systems is to provide an estimate of the potential for such systems in terms of duty cycle. The lessons learned from the comparison of these two systems can be applied for any future projects.

In Table 7.3 a quantitative comparison of all data sets in terms of hours observed is provided. From all the observational campaigns BEST data sets LRc01 and IRa01 was selected to be compared with BEST II LRc02 and LRa02 data sets because they are comparable in terms of campaign duration.

The performance of BEST II system can be compared with other surveys operating under similar observing conditions. The most suitable system for such a comparison is OGLE which is located at Las Campanas observatory, Chile (see Chapter 4). The OGLE surveys the sky regions in the galactic bulge with a high duty cycle. Here not the total yield but only the duty cycle coverage and its implication for the transit detection probability will be discussed. Information of a representative target field from the OGLE survey is provided in the last row of Table 7.3

7.3.1 BEST vs. BEST II

In the following text BEST and BEST II will be compared in terms of total duty cycle and the probability for observation of a transit event of a short periodic planet. The duty cycle is an important factor for the detection of transits and it is determined by the quality of the observing site. Also the technical reliability of the system is a crucial aspect for the high duty cycle.

Table 7.3: *Overview on all data sets taken on CoRoT fields with BEST and BEST II.*

Telescope	Field	Obs. period	Obs. nights/total nights	Obs. hrs.
BEST	LRc01	Jun.-Aug. 2005	35/98	130
BEST	LRa01	Oct.-Apr. 2005/2006	23/105	140
BEST	IRa01	Nov.-Dec. 2006	12/40	70
BEST II	LRc02	Jul.-Aug. 2007	20/36	121
BEST II	LRa02	Nov.-Mar. 2007/2008	38/91	231
OGLE (181)	Eta Carinae	Feb. - May 2002	76/95	≈ 380

Duty cycle coverage

In Figure 7.3 the maximum observational time reachable at OCA is given in black. The selected fields are assumed to be observable if their altitude is at least 30° above the horizon and the minimum observable time is at least 2.5 hrs. Furthermore, three nights before and after full moon were excluded, corresponding to white gaps in the figure. The red stripes in the figure represent the time when observations of the fields with BEST were performed.

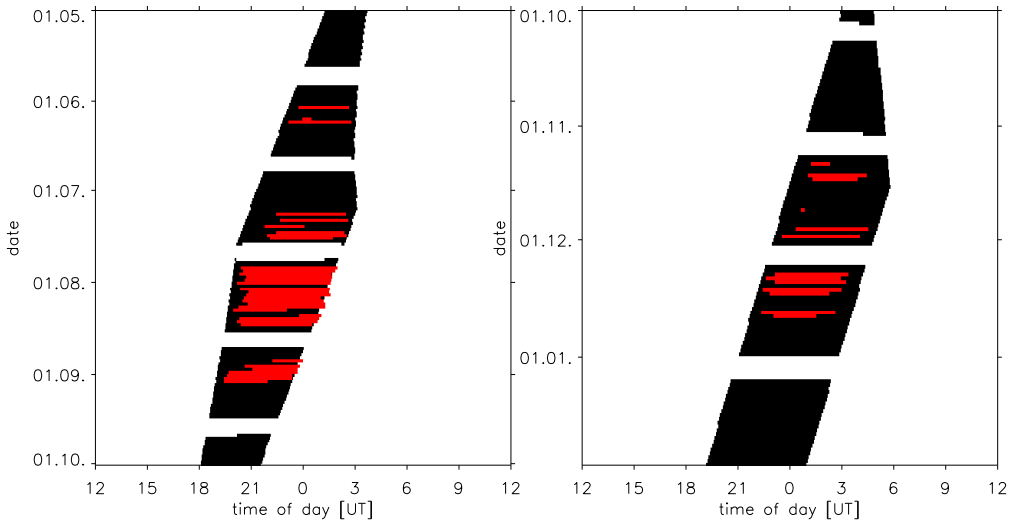

Figure 7.3: *Maximal duty cycle is compared with the real duty cycle for BEST LRc01 (left) and IRa01 (right).*

The IRa01 field was observed on 12 nights (70 hrs.) from a total number of 40 (960 hrs.) potential good nights, resulting in a total duty cycle $C_{IRa01} = \frac{\text{hrs. observed}}{\text{total hrs.}} = 70/960 \approx 7\%$. The LRc01 field was observed on 35 nights (130 hrs.) from the number of 98 potentially good nights (2352 hrs.) resulting in duty cycle coverage C_{LRc01} of $C_{LRc01} = 130/2352 \approx 5.5\%$.

The field LRc02 was observed on 20 nights (120 hrs.) out of 36 potentially good nights (864 hrs.) resulting in a duty cycle coverage of $C_{LRc02} = 120/864 \approx 14\%$. The $LRa02$ was observed on 41 nights (231 hrs.) from a total number of 91 potentialy good nights (2184 hrs.), resulting in $C_{LRa02} = 231/2184 \approx 11\%$. It can be seen that the amount of hours observed for LRa02 is approximately double compared to the amount for LRc02.

The right plot in Figure 7.4 shows that the duty cycle coverage for the LRa02 field is better than for the LRc02 field. In most cases the time gaps without observations

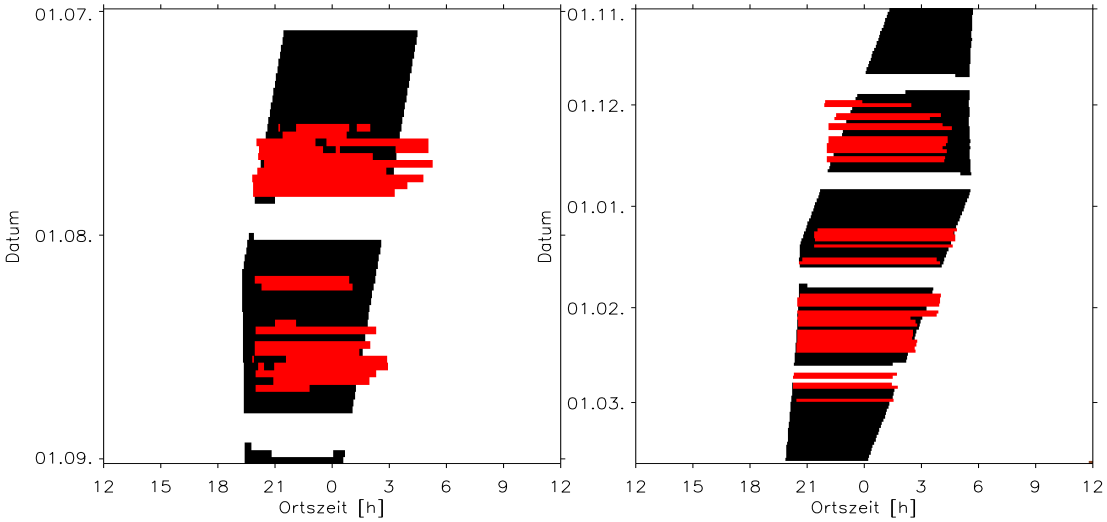

Figure 7.4: *Ideal duty cycle is compared with the real duty cycle for BEST II LRc02 (left) and LRa02 (right). Note that due to technical fine-tuning of the BEST II system the LRc02 campaign was shorter.*

were due to technical problems during the final adjusting of the system. In the case of LRc02 the first week in July was affected by a period of bad weather conditions. In the case of LRa02 the campaign started later due to the final implementation of the robotic mode at the end of November.

Comparison of the plots in Figure 7.3 & Figure 7.4 indicates that BEST II duty cycle is more than doubled compared to the BEST duty cycle in terms of total hours observed. The different campaign lengths were given by the field visibility on the sky and by technical aspects. One should note that for both of the BEST II campaigns technical improvements were performed in parallel and in the future even a higher duty cycle can be expected when the system is operated in the normal mode. The observing mode for ongoing BEST II campaigns is more or less at maximum possible level. Therefore, the OCA site is clearly favored in terms of duty cycle compared to OHP.

Transit detection probability

The knowledge of real duty cycle coverage can be used to determine the probability for detection of a transit event. Usually, observations of at least three transit events are needed in order to confirm the orbital period of a potential planet. Therefore, the probability of observation of three transit events for the ideal ($C_{ideal} = 100\%$) and real duty cycle characterizes the potential yield. The difference between real and ideal duty cycle can be caused due to various circumstances e.g. due to bad weather conditions or technical closure-time.

A transit probability based on number of potentially good nights was simulated according to (168; 182). Then, it was compared with the real duty cycle obtained with our observations of BEST LRc01 and IRa01 and BEST II LRa02 and LRc02 fields. The detection probability of at least three transit events was plotted against the semi-major axis (orbital period) of a planet and compared for BEST and BEST II (see Figure 7.5 and Figure 7.6).

Figure 7.5 presents the probability of transit detection for BEST LRc01 and IRa01

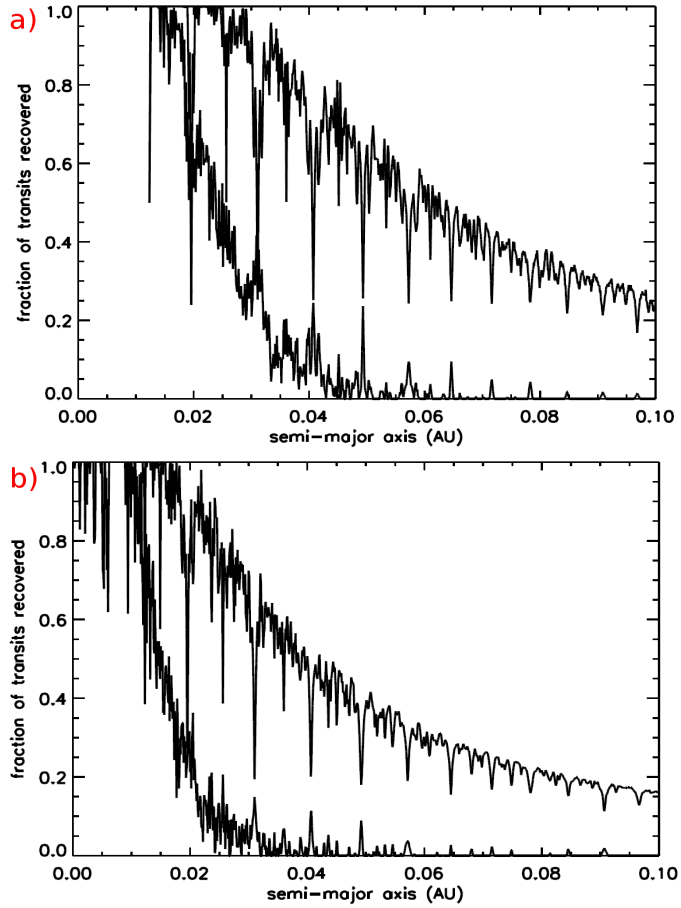

Figure 7.5: *The probability of the detection of at least three transit events of planet is plotted against the length of semimajor axis of the planet. Upper line represents the simulated ideal duty cycle (excluding clouds) and the lower line represents the real observed duty cycle for the BEST LRc01 field (a) and for the BEST IRa01 field (b). Figures were taken from (182).*

target fields. It can be seen that the probability of detection of three transit events is 100% only for semimajor axis below 0.015 AU (equivalent to orbital periods below 1 day) and then reaches 50% for semimajor axis below 0.02 AU (orbital periods around 1.5 days) for LRc01 and 0.015 AU (orbital periods around 1 day) for IRa01. The probability reaches 0% for the semimajor axis larger than 0.045 AU for LRc01 and 0.035 AU for IRa01.

The same type of plots is presented in Figure 7.6 showing the probability of transit detection for BEST II fields LRc02 and LRa02. It can be seen from the figure that the chance to detect at least three transits of a planet with semimajor axis below 0.05 AU ($P \leq 1$ day) is 100%. For semimajor axis larger than 0.05 AU the detection probability begins to decrease reaching 0% for a planet with semimajor axis > 0.1 AU and a period $P > 12$ days.

A comparison of the values for detection of three transits with BEST and BEST II in LRc01 and LRa02 data sets can be made with help of values presented in Table 7.4. In the table the period ranges for transit probability detection of 100%, 50% and 20% compared for BEST and BEST II are shown. The duty cycle of BEST II in principle allows the a good detection probability of planets with orbital periods up

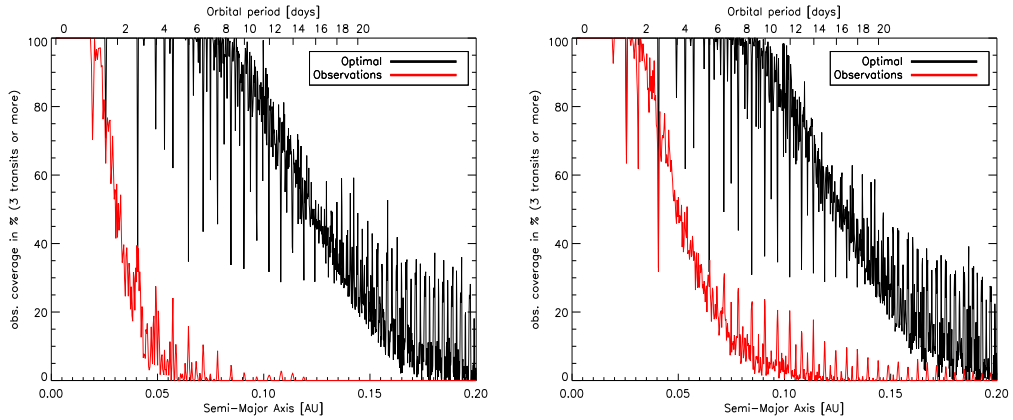

Figure 7.6: *Left plot is for he BEST II LRc02 field and right plot is for the BEST II LRa02 field. The probability of the detection of at least three transit events of planet is plotted against the length of semimajor axis of the planet. Black line represents the ideal duty cycle (excluding clouds) and the red line is the real observed duty cycle.*

to at least 4 days. The same probabilities for the BEST telescope at OHP show that only planets with orbital periods below 2 days can be expected to be detected. The comparison demonstrates the significance of the local observing conditions at the site and that also in this aspect OCA is a factor 2 better compared to OHP.

Table 7.4: *Comparison of detection probability (Ψ_3) to observe three transits against maximum detectable orbital period (P) for an extrasolar planet in the BEST LRc01 and the BEST II LRa02 data sets. Values taken from Figure 7.5 & Figure 7.6.*

Ψ_3 (%)	BEST (LRc01) P (days)	BEST II (LRa02) P (days)
100%	< 1	< 2
50%	< 1.5	< 4
20%	< 2	< 6

7.3.2 BEST II vs. OGLE

The duty cycle of BEST II will be compared with the OGLE survey located at Las Campanas Observatory, Chile (see Chapter 4). The OGLE survey observes under weather conditions slightly worse compared to OCA. In comparison with BEST II the OGLE FOV is about four times smaller but the selected fields contain a higher amount of stars. An OGLE campaign on the Carina target fields in 2002 (181) was selected as a representative campaign for the comparison with BEST II. The season of the year was comparable with the observational period of LRa02 field. Also some other more detailed studies on the potential yield of OGLE were already performed on this target field. In addition, the most of the OGLE transiting planets were detected in this target fields (183).

The OGLE campaign lasted for 95 (2280 hrs.) nights with 75 nights (each night up to 6 hrs.) of observational data resulting in $\approx$ 380 hrs. of observations for the complete campaign. The OGLE survey dos not present the exact number, therefore

we assumed an average number of 5 hrs per night what is typical for this season of the year (see Table 7.3). The duty cycle of OGLE in hours is $C_{OGLE} = \frac{380}{2280} \approx 16\%$. The BEST II LRa02 campaign was carried out with lower duty cycle due to intial test phase of the robotic mode. Preliminary results from the presently observed (November 2008 to March 2009) fields with BEST II during a campaign lasting for ≈ 70 (1680 hrs.) nights illustrate the contemporary potential of BEST II. The observations were performed on about 60 nights during this campaign, resulting in ≈ 350 hrs of observations. This statistic indicates an effective duty cycle $C_{newfield} = \frac{350}{1680} \approx 20\%$. Furthermore, this number is fully comparable and even better than the OGLE survey duty cycle. In addition, the difference is in a good agreement with slightly different observing conditions between the sites of the OGLE and the BEST II survey.

7.3.3 Summary

From the presented comparisons of duty cycles of BEST and BEST II it is clear that BEST II has an advantage of much better observing conditions at OCA than at OHP. These conditions are indicating the high potential for a future BEST II transit survey. In quantitative terms BEST II compared with BEST possesses following improved characteristics:

- better duty cycle coverage with at least factor 2

- a corresponding higher probability to detect transit events

- potential planets with orbital periods up to 4 days can be detected with 50% probability, whereas potential planets up to orbital periods of 6 days can be detected with a probability of 20%. The same numbers for BEST are 1.5 days orbital period for 50% detection probability and 2 days orbital period for 20% detection probability.

- the duty cycle of BEST II is comparable with OGLE typical duty cycle implying the future potential for the transit detection with BEST II

Further improvements of BEST II duty cycle are foreseen as indicated by the preliminary results from ongoing observations. At that point, future optimization of the planet detection probability with BEST II can then only be achieved by the increase of the number of observed stars (see also (168)). This will be further discussed in Chapter 9.

Chapter 8

Data reduction

This Chapter will firstly describe the data reduction process in general terms, I.e. the BEST/BEST II data pipeline. In the second part of the chapter, one of the BEST II target fields will be used as an example to illustrate the functionality. The LRa02 data were obtained with robotic mode operations and possess the highest duty cycle coverage in comparison with all other BEST/BEST II data. Therefore, the LRa02 data are most suitable for the discussion about data reduction and obtained photometric quality. All other fields have been reduced in a similar way as described in (171; 172; 173; 178; 179).

8.1 Description of the data reduction pipeline

The data reduction pipeline consists of three main[1] steps, the basic data calibration, image subtraction performed with the ISIS package (184) and finally aperture photometry before the data are ready for the science analysis. These main steps are accompanied by a few substeps. A more detailed schematic description of the pipeline structure is presented in Figure 8.1.

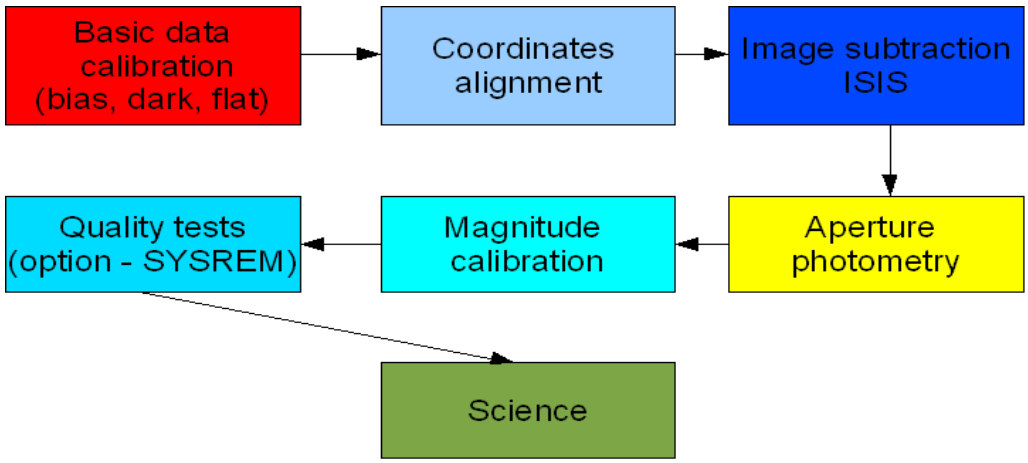

Figure 8.1: *Schematic diagram showing the procedures during the data reduction process from the raw data to final light curves.*

[1]red, dark blue and yellow boxes in Figure 8.1

8.1.1 Data calibration

In the calibration process instrumental effects, cosmic rays, etc. in the raw scientific data are corrected. Such effects contributing to the total uncertainty of the measurement are bias voltage, dark current and sensitivity variation of the pixels as outlined in Chapter 5. The input for this first step is a raw (uncorrected) scientific frame as well as the calibration frames and the final product will be the calibrated frame which can be further reduced and analyzed. In Figure 8.2 the main steps of data calibration are shown. The calibration images are firstly combined into master frames which are then used to correct the above mentioned effects in the same order as presented in the figure and resulting in the corrected image.

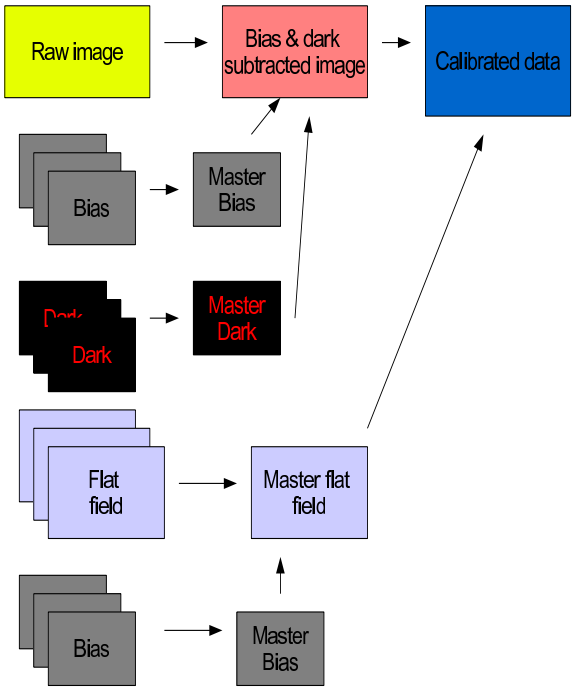

Figure 8.2: *Schematic diagram showing the procedures in the photometric calibration phase.*

The different steps of the calibration process can be summarized quantitatively as:

$$I^{c,i}_{x,y} = \frac{I^{r,i}_{x,y} - MD_{x,y} - nMB_{x,y} \times \overline{OM^{i}_{x0,y0}}}{nMF_{x,y}} \tag{8.1}$$

where $I^{c,i}_{x,y}$ is the calibrated i^{th} scientific frame and $I^{r,i}_{x,y}$ is an i^{th} raw image. The upper index is the image number and the type of image (here r - raw and c - calibrated) and the lower index is related to pixel coordinates of the CCD. The terms in Equation (8.1) representing substeps of the calibration process are described below.

Oversampled margin ($\overline{OM^{i}_{x0,y0}}$) - is a part of the detector $(x0, y0)$ which is used for a reference of the bias level value since it is blocked from the incoming light. The value of OM is determined from the science image and provides the actual value of the bias. Therefore, fluctuations of the bias level on longer time scales can be

corrected more effectively. The area consists usually of a several rows of pixels and the value of $\overline{OM^i_{x0,y0}}$ of i-th image can be obtained as:

$$\overline{OM^i_{x0,y0}} = \text{median}_{x0,y0}(I^i_{x0,y0}) \tag{8.2}$$

Normalized master bias ($nMB(x,y)$) - the normalized master bias consists of j single bias frames $B_i(x,y)$ obtained on the short time scale median. The resulting master bias frame ($MB_{x,y}$) is obtained as a median of corresponding pixel values on every single bias frame. The bias frame is taken with 0 seconds exposure time. The master bias is divided (normalized) with the median value of $MB_{x,y}$ resulting in $nMB_{x,y}$. The whole process of obtaining of $nMB_{x,y}$ can be written as:

$$MB_{x,y} = \text{median}_j(B^j_{x,y}) \tag{8.3}$$

and the required normalized master bias $nMB_{x,y}$ will be finally obtained as:

$$nMB_{x,y} = \frac{MB_{x,y}}{\text{median}_{x,y}(MB_{x,y})} \tag{8.4}$$

Master dark ($MD_{x,y}$) - consists of j dark frames $D_j(x,y)$. The master dark frame is obtained as median of corresponding pixel values on every single dark frame. Dark frames are taken with the same exposure time as the scientific frames. The process of obtaining of master dark can be written as:

$$MD(x,y) = \text{median}_j(D^j_{x,y} - MB_{x,y}) \tag{8.5}$$

Normalized master flat ($nMF_{x,y}$) - consists of k single flat field images $F^k_{x,y}$ which were bias corrected and which is normalized by its median value. The exposure time of flat fields is up to a few seconds. In the real data the dark current is usually not relevant for a few seconds exposure, therefore the dark correction is not performed. Following two step equation describes the process:

$$MF_{x,y} = \text{median}_{x,y}(F^k_{x,y} - MD_{x,y} - \overline{OM^k(F^k_{x0,y0})}nMB_{x,y}) \tag{8.6}$$

and the required normalized master flat can be obtained as:

$$nMF_{x,y} = \frac{MF_{x,y}}{\text{median}(MF_{x,y}} \tag{8.7}$$

After application of this process the data are calibrated properly and can be used for the further reduction.

8.1.2 From calibrated images to light curves

The calibrated data is further reduced in order to obtain the final light curve representing the intensity variation of the observed object in time as defined in Chapter 5. The data reduction process is performed after the basic data calibration with a pipeline consisting of several subroutines. Main parameters are stored in a configuration file with the data.

8.1.2.1 Interpolation of coordinates for every image

The position on the sky of science frames can differ slightly due to small pointing errors. These must be corrected since the image subtraction process used later requires stars to be centered at same pixel on every image. Therefore a reference frame corresponding to the image with most representative part of the sky common for all science images is selected for an image alignment for a common internal CCD coordinate system. The used coordinate transformation is determined for high number of stars with help of SAME_XY (185) routine based on the algorithm by Pal et al. (186). Initially, CCD (x,y) coordinates of stars located on the reference frame are determined with an IDL subroutine FIND called from SAME_XY. Then, a cubic spline convolution function is applied on CCD (x,y) coordinates. In addition, a rotation of the frames with respect to reference frame is determined. The intensity of the rotated pixels is determined with interpolation method applied on intensity profiles of 16 neighboring pixels. Further, the transformation including the rotation is applied on every image. The resulting product are frames with stars centered at the same pixel on every image. Also images which were rotated due to the different position of the mount have the same orientation after the interpolation process. The rotation can be due to fact, that the German equatorial mount needs to flip when observing near the meridian and therefore images after flip are rotated about 180°. Furthermore, the routine can identify frames where no stars could be detected for example due to bad tracking.

Image subtraction with ISIS package

The image subtraction method scales the seeing in all images from the data sets to the seeing of a reference frame. As a result, the image subtraction yields only the residua of variable objects on the final frames and constant stars are eliminated. Later, an aperture photometry can be performed on the resulting frames in order to determine the intensity of the variable objects. In addition, the image subtraction routine has an advantage compared to standard profile fitting photometry (PSF photometry) routines as DAOPHOT (187) that it does not need to find an exact PSF profile for every star. This might be a difficult task especially for crowded stellar fields where the PSFs often overlap.

When all images are aligned an image subtraction routine from the ISIS package (184) is applied. Within the image subtraction routine the images with best seeing are selected as a reference and the seeing on the rest of the images is matched to the reference value with the help of kernel function $K(x, y)$ obtained from:

$$Ref(x, y) \otimes K(x, y) = Im(x, y) + bg(x, y) \tag{8.8}$$

$Ref(x, y)$ being the reference frame, $Im(x, y)$ represents the frame to be subtracted and the $bg(x, y)$ has a polynomial form and represents the sky background. The proper determination of the form for *kernel function* is the key to the successful image subtraction. Alard & Lupton (1998) (188) and (2000) (184) determined the best form of $K(x, y)$ as:

$$K(u, v) = \sum_i a_i \times B(u, v) \tag{8.9}$$

where $B(u, v)$ is Gaussian and a_i are the coefficients of the polynomial form of the third order. When the seeing on all images has been matched to the seeing value on the reference frame, the PSF of every star on every image is subtracted from the PSF of the corresponding star on the selected reference frame. As a result, only stars showing variability will remain on the subtracted image. Within the routine also the effect of the varying sky background is compensated (see (188; 184) for more detail).

8.1.2.2 Aperture photometry

To obtain the magnitudes of stars, an aperture photometry routine based on algorithms written by (171; 185; 168) is applied on the reference frame and on subtracted frames. Firstly, the stars are identified with an IDL routine FIND which determines the centers of stars on the reference image. Stars with PSF differing too much from the Gaussian shape are rejected. A parameter THRESHOLD (T) is to be set in order to constrain the detection of the stars in terms of S/N ratio. Setting a high value of the parameter T will reject those faint stars which can be hardly distinguished from the background noise variations. To estimate the proper value of T another routine PRE_PHOT using an iterative process introduced by Fruth (2008) (168) plots the shape and the structure of the stellar profiles of selected stars with nearly similar flux. The value of the THRESHOLD for which the PSFs of selected stars begin to differ significantly from the Gaussian form is selected for the data reduction. Then the FIND routine is executed with the new parameters. Additionally, stars close to saturation limit are rejected. A typical FWHM of a stellar PSF must be determined in order to select an appropriate apertures r_{in} and r_{out} for the determination of the stellar flux and the contribution of the sky background.

The selected aperture r_{out} is divided into 8 parts. Then, the median values of the sky background in the segments are used for the determination of the total sky background flux S^i_{sky} around the i-th star with an iterative algorithm written by (171). The stellar flux of the i-th star on the reference frame (ref) is determined as

$$S^{ref}_i = S^i_{sky} - S^i_{r_{in}} \tag{8.10}$$

where $S_{r^i_{in}}$ is the signal summed over pixels within the r_{in} aperture. Thereafter, the above described process is applied on n subtracted images and the residual flux of i-th star S^i_{diff} is obtained. Then, the light curve as a time series can be expressed in magnitude m as a function of time t as follows

$$m(t)_{i,n} = 25 - 2.5 \log_{10} \left(S^i_{ref} - (S^i_{diff,n} - S^i_{sky,n}) \right) \tag{8.11}$$

In principle residual flux of the ith star is determined on n frames and then the light curve is obtained as a time series. The value of the zero point m_0 was selected as 25, however the zero point level can be selected randomly, because instrumental magnitudes are later calibrated with a standard stellar catalog. From the light curve an average magnitude can be determined as

$$\langle m_i \rangle = \text{median}(m_i(t_n)) \tag{8.12}$$

with i being star number and t_n the time stamp of measurement acquisition. The photometric error σ^i_{ph} can be expressed by

$$\sigma^i_{ph} = \left(\frac{\sum_n (m_i(t_n) - (\langle m_i \rangle))^2}{(\sum_n 1) - 1} \right)^{\frac{1}{2}} \tag{8.13}$$

The selection process of an aperture is discussed in (171; 172) in more detail for the BEST data. Aperture photometry with parameters applied on BEST II LRa02 data will be presented in Section 8.2.

Extinction correction

It is important to note that with the subtraction of background signal a first atmospheric extinction correction is applied. The changing value of the air mass during the observation influences the stellar signal but also the signal incoming from the sky background in the same frame. Therefore, the information about changing extinction is contained in the values of $S^i_{sky,n}$. In order to test the extinction influence, an amount of 5000 constant stars with the lowest *rms* values are selected from the data set. Then, the sample is checked for the intensity changes with respect to the median value of the magnitude $\langle m \rangle$ on all n frames. The determined differences are used for the correction of the magnitude values of every star on every image. The values are well in millimagnitude level and therefore, we can assume that the extinction correction is already effective within the aperture photometry on subtracted images.

8.1.2.3 Astrometry and absolute magnitude calibration

Firstly, the astronomic coordinates must be assigned to the internal coordinates of the detected objects. Secondly, instrumental magnitudes are converted to a magnitude scale of a standard stellar catalog.

Astrometry

As a final step of data pipeline the astrometry is applied. The coordinates of the detected stars are still in an internal CCD (x,y) coordinate system and now need to be converted into general astronomic coordinate system. The coordinate transformation is determined again for smaller number of reference stars (not all stars detected in the images are present in the catalogs) on the same reference frame as for aperture photometry with help of ASTROMETRY routine based on the algorithm by Pal et al. (2007) (186). As an input reference catalog USNO-A2.0 is used. When the transformation for this group of reference stars is determined, then it is applied on internal coordinates of every detected star on the reference frame. The output are coordinates in the World Coordinate System (WCS - right ascension, declination) stored together with light curves.

Magnitude calibration

After the successful determination of the WCS coordinates for every star the instrumental magnitude scale must be compared with a stellar catalog in order to determine a zero point for the magnitude scale. For this purpose, the UNSO-A2.0 catalog (189) was used as the reference. Constant stars on the reference frame are matched with the equivalent stars in the catalog. In case of successful identification the magnitude difference between the BEST II magnitude system and the magnitude in the catalog is estimated. The mean value of the magnitude differences is then applied to all BEST II stars. As a result the light curves with the magnitude scale referenced to USNO-A2.0 red magnitude (R) is stored.

8.1.2.4 SysRem

SysRem (190) is a detrending algorithm which removes residual systematic noise which can remain in the light curve. The advantage of the SysRem algorithm is that the true nature of the noise affecting the light curves does not need to be known. Only systematic effects which affect large number of light curves are removed. E.g. these systematics can be caused due to second order extinction coefficients as various color effects.

The general idea of the algorithm is based on the problem of finding of the minimum solution firstly for the c_i and then a_j coefficients in equation:

$$S_i^2 = \sum_j \frac{(r_{ij} - c_i a_j)^2}{\sigma_{ij}^2} \tag{8.14}$$

where σ_{ij} is the uncertainty of the measurement of star i in the image j, a_j the air mass of image j, c_i the extinction coefficient of star i and r_{ij} the residual of average subtracted stellar magnitude of star i in image j (190).

In order to correct the above described systematic effects a SysRem (190) based algorithm as implemented by Wiese (2007) (182) was applied on the BEST/BEST II data. The improvement of the photometric quality was minimal. Only a slight improvement in number of high quality photometric light curves was observed compared to data sets without applying SysRem.

On the other hand, the data sets used for the detection of periodic variable stars contained less light curves showing artificial periods due to e.g. diurnal cycle. In addition, no deformation of the light curves due to application of our SysRem based algorithm was detected. Currently, a new version of SysRem based detrending algorithm is tested on archival BEST data sets and will be implemented in a near future.

8.2 Application of the pipeline to BEST II LRa02 data

The functionality of the pipeline function will be demonstrated on the BEST II LRa02 data set beginning with the photometric calibration and ending with the

absolute magnitude calibration and correction of systematic effects.

8.2.1 Basic data calibration of LRa02 data set

Bias

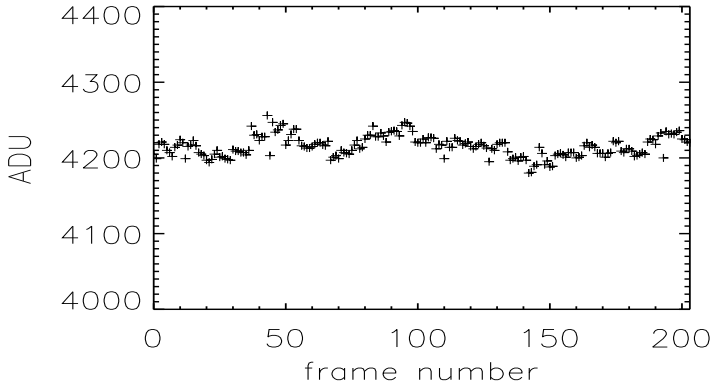

Figure 8.3: *Variation of median value of the bias level in individual frames for the LRa02 campaign over the complete data set. Bias variation are corrected with an oversampled margin level $\overline{OMI_{0,i}}$. Oversampled margin consists of not light sensitive pixels.*

In Figure 8.3 the bias level variation for the FLI CCD during the LRa02 campaign is shown. It can be seen in Figure 8.3 that the maximal bias level variation is about 60 ADU and the median value is $\overline{S_b} = 4215$. This variation of the bias level on long time scales is compensated by using of the *oversampled margin* as described in the previous section. The median value of the bias level is shown in Table 8.1. Usually, up to 10 bias frames acquired in a short time scale were used for the master bias frame per night. Also control frames were acquired during the observing run in order to monitor bias variations on longer time scales.

Dark current

The BEST II CCD is characterized by low level dark noise (see Chapter 6). The operational temperature was $-20°$ C during the complete campaign. In Figure 8.6 median values of a master dark frames for every night for the LRa02 field are shown. The mean value of all dark frames over the complete campaign is $\overline{S_d} = 4.52$ ADU with a standard deviation of 1.74 ADU. Therefore in principle, the dark current variation is negligible in comparison to other noise sources and the dark current level over the complete campaign is stable. Typically, up to 10 dark frames were used for the master dark frame. The median value of dark level is shown in Table 8.1.

Table 8.1: *The bias and dark level median values for the complete campaign.*

field	median bias (ADU)	median dark (ADU)
LRa02	4215.00 ± 13.63	4.52 ± 1.74

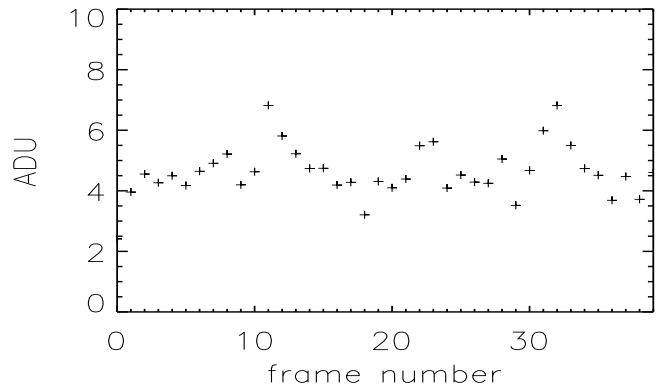

Figure 8.4: *Variation in the median value of master dark frames over the complete campaign for the LRa02 field.*

Flat field

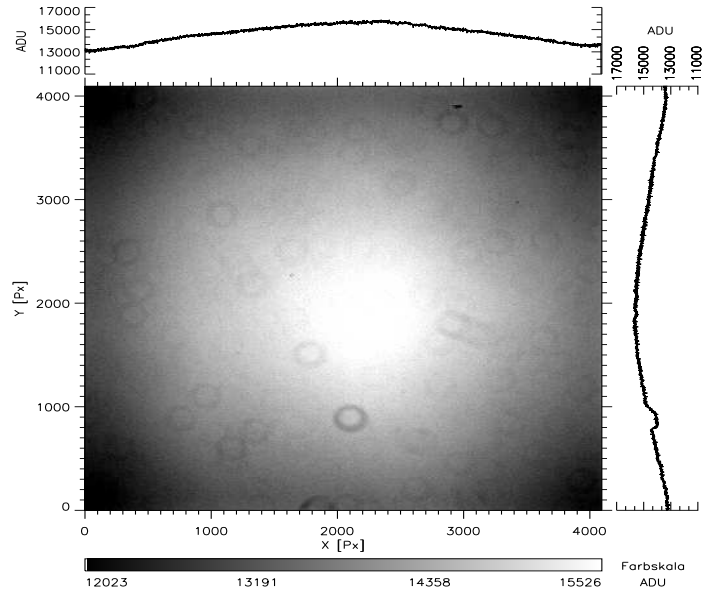

Figure 8.5: *Typical intensity profile of a sky flat field. Ring like patterns due to sand on the optical elements. The rings may possess an outer radius of up to* 50 *pixels.*

The flat fields are taken on the twilight sky. A technical limitation of the BEST II system is the long readout time of the CCD (up to 90 seconds) which constrains the number of obtainable images during the twilight. Therefore, flat fields taken on different nights must be combined. The typical intensity profile of a flat field frame is shown in Figure 8.5. The small rings (maximally 100 pixels wide) are caused by dust particles on the CCD window. This variation of the flat field intensity profile due to dust must be estimated in order to select the maximal time interval in which flat field frames can be combined. In case of LRa02 campaign, flat fields taken maximally within 7 days (typically between 7-14 frames) were combined into a master flat. Images separated by longer than one week are affected with dust grains.

The significance of the dust grains evolution can be determined when flat fields taken at different times are divided. Then the resulting masks can be compared with a pattern in scientific images. The rings due to dust grains which are present on both

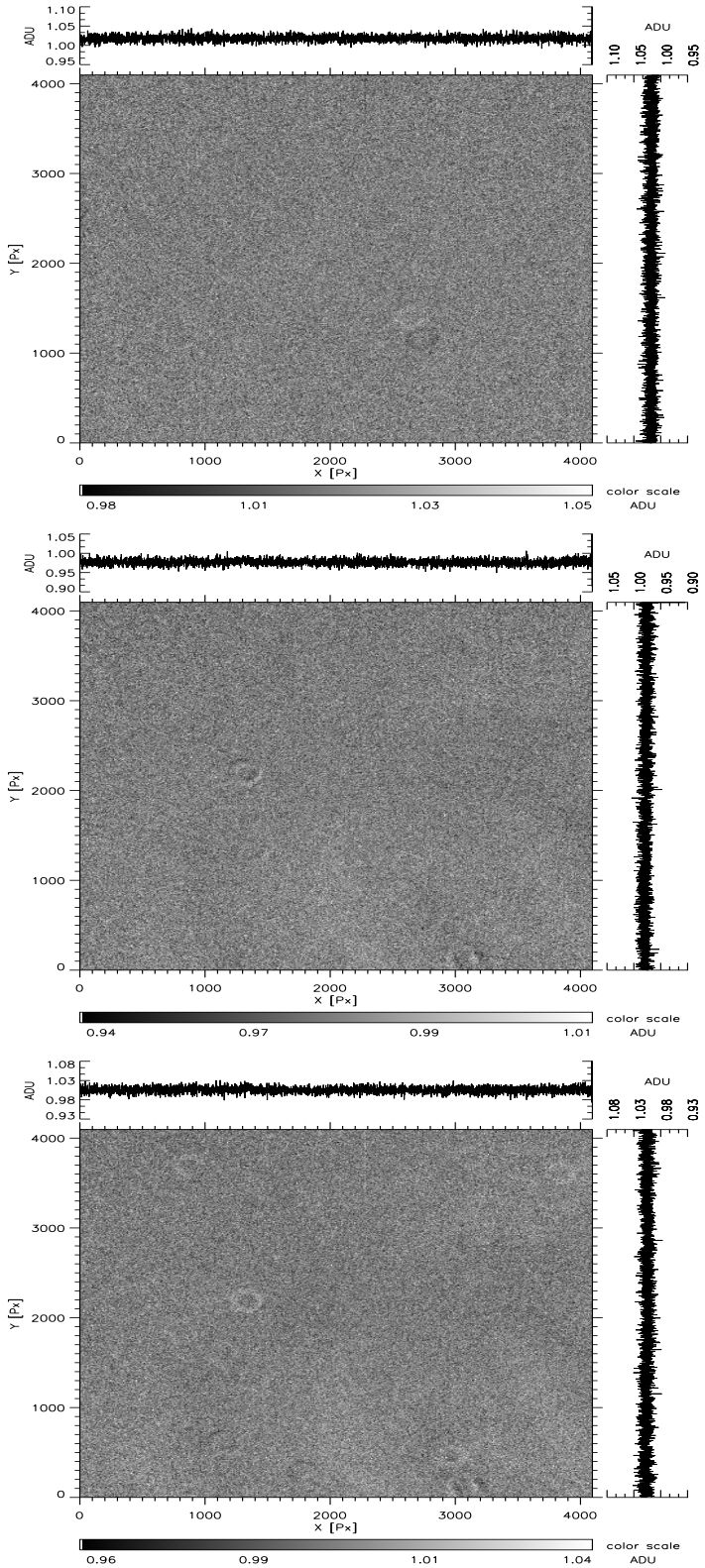

Figure 8.6: *Flat fields taken during different observing runs were divided together. From top to bottom images represent the time difference between two flat fields of* 1, 26, 38 *days.*

frames will disappear due to division and only new rings will remain in the resulting frame. An example of the dust grains evolution during the LRa02 campaign is illustrated in Figure 8.6. There, flat field frames divided by another flat field frames taken 1, 26 and 38 days later are shown respectively. In the upper figure, which is representing the time interval between flat fields of one day, only two new dust grains are present. After 26 and 38 days more 5 or 9 new rings, respectively, can be found (see Figure 8.6). The time interval of 7 days was selected as optimal in order to obtain a reasonable number of flat field frames used for the master frame and at the same time keep a low contamination level of evolving dust grains.

8.2.2 Photometry of the LRa02 data

The calibrated data are further processed with an automatic pipeline performing image subtraction and aperture photometry. Resulting products are light curves of stars which are stored for further analysis. Here, theoretical steps described in Sections 8.1.2 to 8.1.5 will be illustrated on the LRa02 data set.

Frames alignment

The first step in the photometric calibration is to transform all stellar coordinates into a common coordinate system. In Figure 8.7 the output from the routine SAME_XY (see Section 8.1.2) shows the percentage of stars identified in images with respect to reference frame. The frames with percentage less than 50% of successfully identified stars are checked manually. The inspection of several such images showed that the identification of stars did not work properly if less than 50% of the stars were identified. Therefore, this limit was set for the pipeline. However, to avoid the removal of good images with this criterion a visual inspection is necessary and only in the second run the selected frames can be removed. Typical causes for failure of identification of stars are tracking errors moving the stellar image on the CCD chip during exposures or clouds passing the FOV of the telescope.

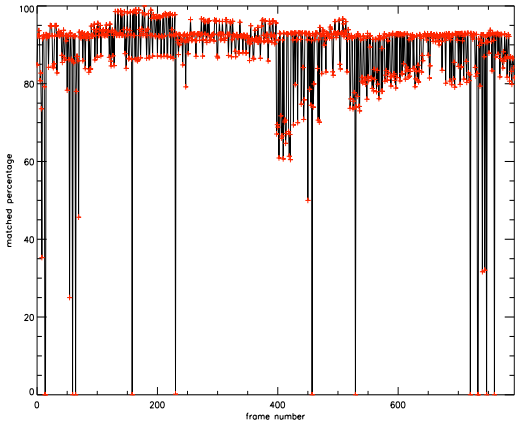

Figure 8.7: *Percentage of stars identified in scientific frames with respect to the reference frame. Images with less than* 50% *of identified stars are checked manually and if they are considered to be inadequate, they will be removed from further data reduction.*

Image subtraction (ISIS) - In order to prepare a reference frame for ISIS 10 images spread over the whole LRa02 campaign with good seeing conditions were

selected. An internal ISIS routine combines the chosen images into a reference frame that was used for the image subtraction. The content of an ISIS parameter file used for the LRa02 data set is presented in Table A.1 in Appendix A.1. Figure 8.8 shows a reference image (left) and a subtracted image (right) illustrating the input and output of the image subtraction process. In the original image before subtraction all stars can be seen. After the image subtraction the constant stars are not present anymore and only residuals of variable objects with respect to the reference frame remain (in figure as black spot).

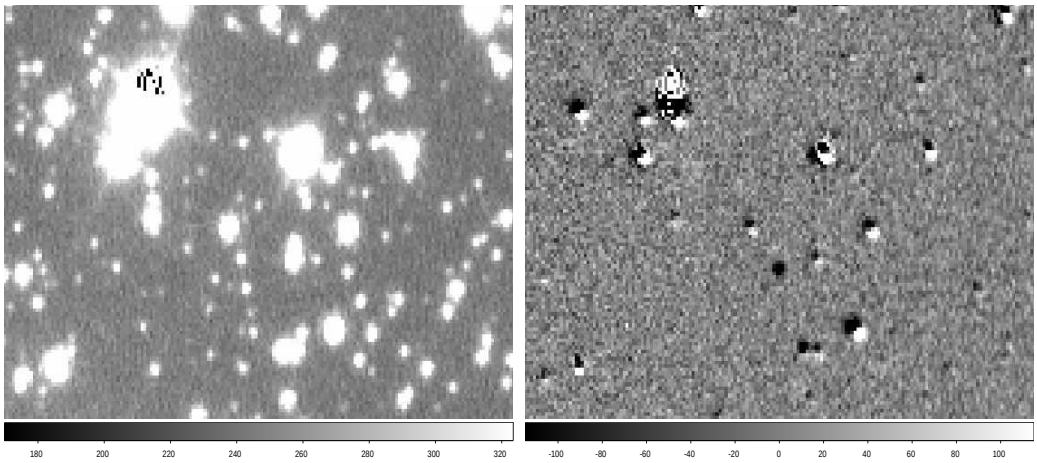

Figure 8.8: *The reference (left) and subtracted image (right) from the BEST II data set. In the subtracted image only residua for variable stars remain.*

Aperture photometry

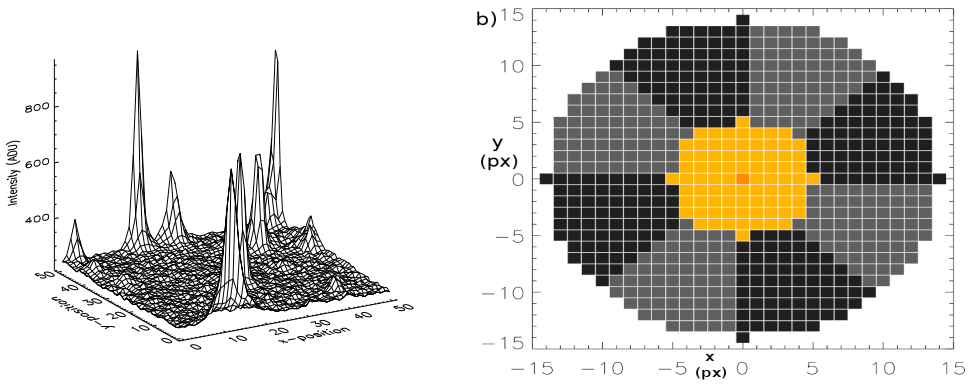

Figure 8.9: *Stellar profiles on the sub area of the reference frame (left). Structure of the photometric aperture used for the data reduction of LRa02 campaign (right). Right figure was taken from (168).*

Before the aperture photometry is applied, all stars with flux levels > 48000 ADU were rejected because of the intensity range close to saturation of the CCD. The value was selected conservatively in order to securely avoid non linearity effects in intensity measurement. A cut-off from the reference frame area of 50×50 pixels with stellar profiles is shown in the left Figure 8.9. Typical value of FWHM is $6 - 8$ pixels for a photometric night as discussed by Fruth (168; 171). Therefore, an inner aperture $r_{in} = 10$ pixels around the star was used for the determination of the stellar

flux and an outer aperture of $r_{out} = 30$ pixels around the stellar center was applied for the determination of the background level contribution. The structure of the aperture is shown in right Figure 8.9. The photometric accuracy of the reduced data reaches 1% level for several thousands of stars as will be discussed later. This level is sufficient for the detection of low amplitude variable stars and transits of Jupiter-sized extrasolar planets.

Astrometry and absolute magnitude calibration

The transformation from CCD coordinates into WCS coordinate system was done with help of 500 brightest detected stars which were successfully matched to USNO-A2.0 stellar catalog. After application of the transformation on all stars in the FOV a test of quality was performed to check that the transformation was successful. Therefore, all detected stars in the FOV were matched with the USNO-A2.0 catalog. The detailed statistics on the test can be found in Table 8.2. More than 66% of stars were identified in the LRa02 target field. The low number of uniquely identified stars in the LRa02b subfield of LRa02 was due to selected detection treshold. BEST II can detect also very faint stars in the crowded target fields (down to 19 mag) which do not have any catalog entry (see RMS plot in Figure 8.13 in Section 8.3). Nevertheless, these faint stars are not usable for further analysis and the complete statistic is shown for an overview on detected stars. The transformation is successfull if all bright catalog stars can be matched uniquely what was the case. For the field LRa02, all 500 stars used for the transformation determination were successfully cross-matched with USNO-A2.0 (see Table 8.2).

In figure 8.10 the 2000 stars from the USNO-A2.0 catalog contained in the LRa02 field are compared to stars which were detected with the astrometric routine. Bright catalog stars were removed from the BEST II images because they are saturated on the CCD chip. The figure shows that after coordinate transformation the BEST II coordinate system is in excellent agreement with the catalog coordinate system therefore implying a successful astrometry. Quantitatively, a subpixel precision (below 1.5 arcseconds) in the transformed coordinates was reached for the BEST II.

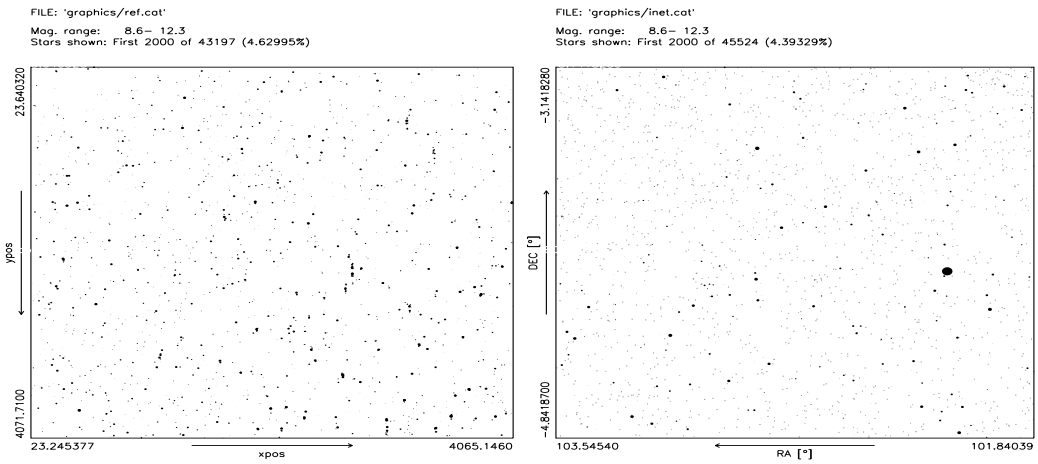

Figure 8.10: *Left panel presents the first* 2000 *stars detected with BEST II an identified with the* FIND *routine in BEST II LRa02 target field. The corresponding catalog stars in the same FOV are presented in right panel. The bright star from the catalog images is saturated in the BEST II data and, therefore removed.*

Table 8.2: *Statistics on the outcome of astrometric routine applied on the LRa02 data set.*

field	LRa02a	LRa02b
stars detected on reference frame	42582	84455
stars in the catalog	45524	84455
order of transformation	4	4
stars used for transformation	500	500
cross identified stars after transf.	34465 (81%)	47913 (66%)
uniquely identified (tolerance < 1 pix)	30849 (72%)	45342 (63%)

8.3 Photometric quality of the data

The final product of the BEST pipeline are light curves of stars from the observed target fields. Further analysis of the light curve requires high photometric quality, since the extrasolar planets cause the intensity decrease due to transit in the range of a few percents. Therefore, the potential of BEST II survey to discover such object will be discussed with the LRa02 observational data as an example.

8.3.1 Photometric conditions during observing nights

A simple but very robust way to estimate the photometric quality of observational data is to count the number of stars with a certain precision. This type of test is very sensitive for various effects that degrade the photometric quality. Furthermore, the photometric quality of the data obtained from different sites can be directly compared.

In order to do such test, the number of stars with *RMS* below 1%, 3% and 5% were plotted for every night from the BEST and BEST II campaigns. The interval from 1% to 3% is relevant for the ground based detection of hot Jupiters around Sun-like stars and in general transiting planets can show an intensity decrease up to 6% around M-dwarf stars (see Table 3.2 in Chapter 3).

In Figure 8.11 star counts for every night from the BEST LRc01 campaign are shown. In addition, the Moon phase corresponding to the date of observation is presented in the bottom panel. The figure presents numbers of light curves of stars with photometric quality below 1% and 3% for BEST LRc01 target field observations from OHP. Only data from a few observation nights (8) contain more than 5000 light curves with *RMS* below 1%.

In the upper panel of Figure 8.12 the same plot but for BEST II LRa02 data is presented. From there it is clear that at OCA many nights contain a stable number of light curves with a photometric quality below 1%. Only data from 5 nights contain less than 2000 light curves with $RMS < 1\%$. Number of 23 nights with more than 3000 stars with *RMS* below 1% were present, indicating outstanding photometric conditions.

For the BEST data the typical number of stars with $RMS < 1\%$ is about 2000. Only data for 14 nights out of total of 35 show more than 3000 stars with *RMS* $< 1\%$ with such a quality rating, only about 40% of all nights were excellent. For

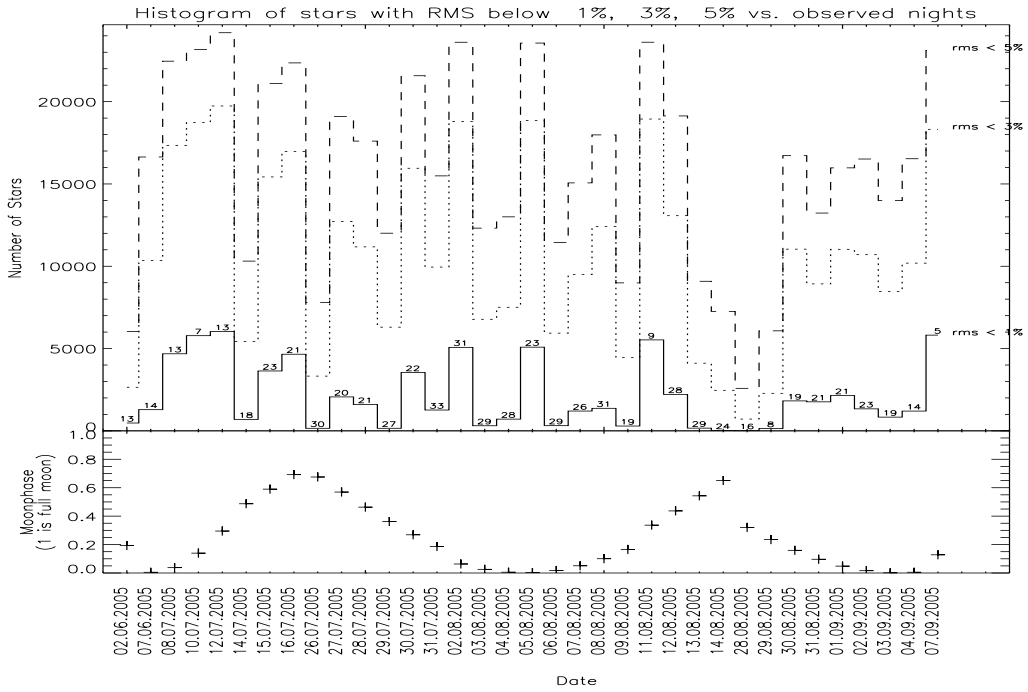

Figure 8.11: *Upper panel presents a histogram of stars with RMS below* 1% *(solid line),* 3% *(shor dashed line) and* 5% *(long dashed line) for every night in BEST LRc01 target field. In the lower box the corresponding Moon phase is shown. The number of scientific frames for each night is also given.*

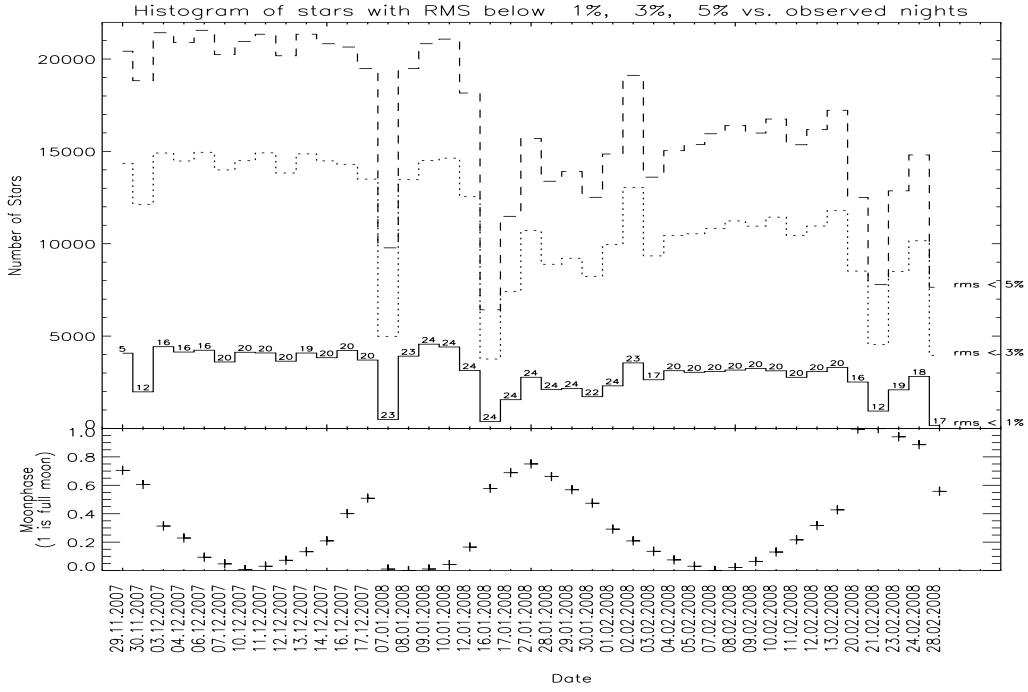

Figure 8.12: *Upper panel presents a histogram of stars with RMS below* 1% *(solid line),* 3% *(shor dashed line) and* 5% *(long dashed line) for every night in one of BEST II LRa02 target field. In the lower box the corresponding Moon phase is shown. The number of scientific frames for each night is also given.*

BEST II the same number is for $3000-4000$ stars for 23 out of 41 nights. Therefore, approximately 56% of the observing nights were acquired with excellent photometric conditions using the same criteria. It is remarkable that only in two nights less than 2000 stars with $RMS < 1\%$ were detected in the BEST II data. The stellar density and distribution was not taken into account for this test, however the BEST II fields are less populated than the BEST fields and still the photometric quality of the data is much better. The presented values clearly show that the OCA site of BEST II telescope allows a data acquisition with a much better photometric quality compared to the BEST site at OHP. Furthermore, the OCA site offers the same stable observing conditions over a long period of time.

8.3.2 Noise sources influencing the uncertainty of measurements

A theoretical background of the various noise contributions to the final photometric error budget were discussed in Chapter 5. Here, the noise statistics will be demonstrated on the BEST II LRa02 observational data. An exact determination of the uncertainty of the measurement is not performed with the BEST data pipeline because it would be too complex in terms of large volume of additional data. Also some noise contributions such as scintillation noise (σ_{sc} see chapter 5) are unknown. The limits of photometric quality of data can be estimated based on the total standard deviation (σ) which can be determined from the examination of the data set over the complete campaign. The σ can then be divided into different parts based on the function form. According to (191; 168) the standard deviation can be expressed as:

$$\sigma \approx \frac{1.0857}{\sqrt{S_{Star}}}\sqrt{\frac{n_B^{Star}\sigma_b}{S_{Star}}\left(1+\frac{1}{n_B^{sky}}\right)+\sigma_o S_{Star}+\frac{1}{g}} \tag{8.15}$$

where g is the CCD gain, S_{Star} is the signal incoming from the star in ADU and n_B is the number of pixels where the signal (either from the sky or star) is measured. The various noise contributors are described as follows:

Photon noise - white noise ($\sigma_p = \sqrt{S_S}/g$)
This noise depends on the incoming signal from the star. Therefore, it becomes relevant for the stars which populate the fainter part of the data set. This is because the photon noise depends on the square root of the detected signal which is low for faint objects.

Background noise (σ_b) - describes the contribution incoming from the sky background and it constraints the detection limit for faint objects. This is because the level of counts from objects is similar as the signal from the sky background.

Systematic noise sources (σ_o) - represents the contribution from all systematic effects affecting the data set, e.g. weather conditions (scintillation) and/or instrumental errors. This noise is known as correlated noise and its exact contribution will be described in the next section. In general, stars from brighter end of the data sets are more affected by this noise component. Therefore, the correlated noise constraints the achievable precision and potential transit detection rates.

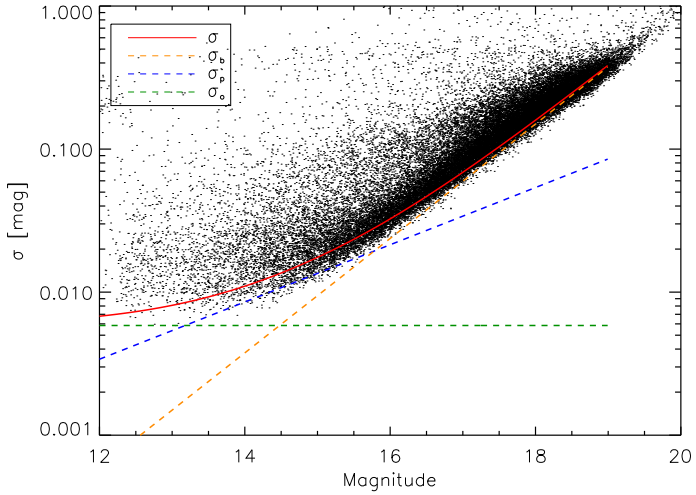

Figure 8.13: *The total error budget on the LRa02 data for the complete campaign observed with BEST II taken with* 240 *seconds exposure time. Dashed yellow line represents background noise (σ_b), blue dashed line represents photon noise (σ_p), dashed green line represents systematic noise sources (σ_o) and dashed red line shows the total noise (σ).*

Values of above described noise sources can be estimated directly from the *RMS* plot as shown in Figure 8.13. Here the *RMS* for all light curves over the whole campaign in the subfield of BEST II LRa02 data set are plotted against their mean magnitude. Different lines correspond to different noise sources. The dashed yellow line represents background noise (σ_b), the blue dashed line represents photon noise (σ_p), the dashed green line represents systematic noise sources (σ_o) and the dashed red line shows the total noise (σ) affecting the data set. In order to determine the value of the total noise (σ), the *RMS* plot was iteratively fitted with a polynomial function according to Equation (8.15) (168). The values of the fit are summarized in Table 8.3.

Table 8.3: *Systematic noise (σ_o) and background noise (σ_b) contributions to LRa02.*

Field	σ_o (mag)	σ_b (ADU)	χ^2
LRa02a	0.0058 ± 0.0052	3.11 ± 0.03	0.01
LRa02b	0.0088 ± 0.0002	25.1 ± 0.2	0.02

From the figure it is also clear shows that BEST II is capable of detecting objects in a magnitude range from 12 to 19 for the used 240 seconds exposure. Potential transit signals can be detected in magnitude range from 12 (given by the saturation limit) to 15 with the required precision of a few percent. In order to remove the systematic effects the SysRem based detrending algorithm (182) was applied on the data set. Only slight improvement was observed on the bright end of the magnitude scale. This is dominated by systematic effects.

The resulting magnitude interval can be adjusted with a change of the used exposure time in order to cover the bright stars if so desired. However, such an adjustment will lead to a smaller number of detected stars.

8.3.3 Test of correlated noise

The red noise component or correlated noise in the stellar light curves includes systematic effects like varying weather conditions and various instrumental effects. These effects are influencing the complete sample and therefore, the detection limit for transit events can be negatively influenced. The influence of such noise is present in all time-series but particularly on scales of hours which is the typical transit duration of a hot Jupiter planet. The resulting effect is that, stellar light curves can be affected by artificial transit like shapes leading to detections of false positives.

Pont et al. (2006) (192) suggested two tests to investigate the influence of the red noise in the observational data sets.

The first method is based on a noise level check in a boxcar averages determined over a typical transit duration. The obtained values are compared with values of the corresponding photon noise. Found differences correspond to the red noise component (compare Equation (8.16) and Equation (8.17)).

The second method investigates the consistency of the transit depth for detected planetary candidates with the detection limit in the presence of red noise.

The minimum for the transit depth is given by (192)

$$\delta = \mathrm{SNR} \times \frac{\sigma_p}{\sqrt{Nn}} \tag{8.16}$$

where SNR is the signal to noise ratio for a clear detection, σ_p the photon noise, N the number of points in a typical transit interval (normally 2.5 hrs.) and n the number of detected transit events. Equation (8.16) contains only the photon noise component. However, if correlated noise is present then Equation (8.16) is modified into (192)

$$\delta = \mathrm{SNR}\sqrt{\frac{\sigma_p^2}{Nn} + \frac{\sigma_r^2}{N}} \tag{8.17}$$

where σ_r represents the red noise contribution. Typical value of SNR was found to be between 7 and 10 for most ground based surveys (192).

Test of the BEST II correlated noise levels

In order to determine the influence of the red noise component on the BEST II data sets both tests described above were applied on the BEST II LRa02 data set.

The first test was applied under following conditions. The time scale of 2.5 hours which typically contains $7 - 8$ data points was used for the boxcar averages over complete light curves during the nights. The result is displayed in Figure 8.14 in the left panel. Black points represent boxcar averages for stars with constant light curves selected based on the low *RMS* values from one observing night. Blue points represent the photon noise in the light curve with a typical values of 0.002 mag. The red noise (σ_r) was estimated for every observing night as the difference between the fitted lines to the running boxes and photon noise (see Equation (8.17)). The right panel in Figure 8.14 shows a distribution of σ_r for all 41 nights in the observing campaign. The typical value was found to be $\sigma_r = 0.0023 \pm 0.0006$ mag.

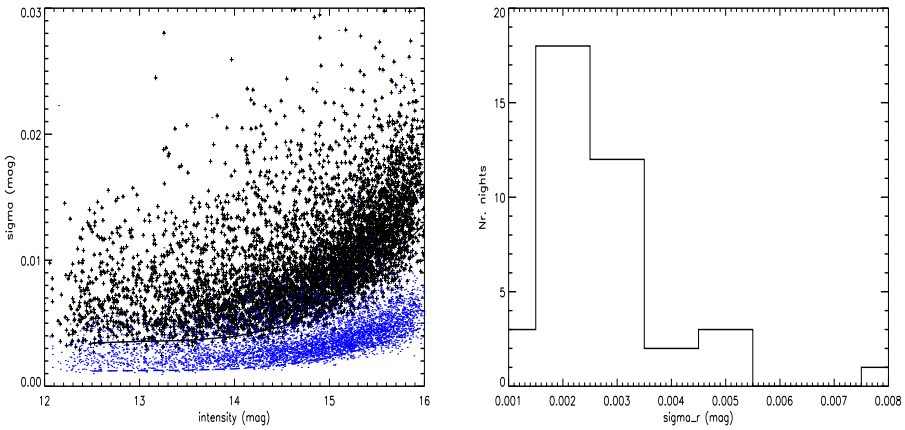

Figure 8.14: *The data on the left were obtained on the night of 04.12.2008. Blue line represents the σ limit given by the photon noise. The black line represents the σ of boxcar averages over typical transit duration of* 2.5 *hrs. for the same data set. Right panel presents a distribution of the red noise over the complete campaign of* 41 *nights. A typical value from the distribution was found to be* 0.0023 ± 0.0006 *mag.*

In the second test, predicted noise levels according to Equation (8.17) were compared to eclipse depths of binary systems and transit candidates. Typical values of SNR= 9, $N = 7$ and $n = 3$ were chosen for the BEST II data set. As test objects a sample of 2 planetary candidates and 20 low amplitude eclipsing binary stars was selected from the sample of detected variable light curves (see Chapter 9). The points in Figure 8.15 show the transit depths of the objects from the selected sample against their magnitudes. The red line represents red noise value of $\sigma_r = 0.0023$ which was determined in the previous test on the BEST II data set. The additional black lines in the figure represent the values of $\sigma_r = 0.002$ and $\sigma_r = 0.004$. Red noise values higher than ($\sigma_r = 0.004$ mag) begin to influence the detection significantly.

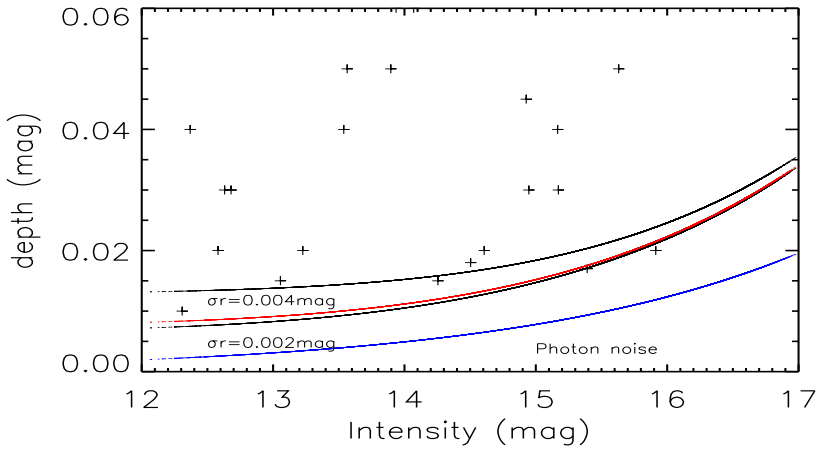

Figure 8.15: *Blue line represents the σ limit given by the photon noise. Black lines represent the red noise values $\sigma_r = 0.002$ mag, $\sigma_r = 0.004$ mag and the red line represents the typical red noise found in BEST II data set $\sigma_r = 0.0023$ mag.*

Conclusions

The first test indicated that the red noise level affecting the BEST II system has a value of approximately $0.002 - 0.004$ mag. This value is comparable with the red noise levels for similar surveys like OGLE and WASP. However, their results were reached after application of SysRem detrending algorithm on the tested data sets (192). The presented results of the test on BEST II data set was obtained without applying any detrending algorithm. For consistency a similar test on BEST II data set was performed also on our data set detrended with SysRem based algorithm implemented by Wiese (2007) (182). No significant variations in the red noise levels were found.

The second test with transit candidates and eclipsing binary stars showed that the determined value of red noise for BEST II system is consistent with detected eclipse depth of selected objects. However, the result is somewhat hampered by the limited number of objects included. Conclusively, the results of both tests showed consistency and that the red noise level in the BEST II data sets is low and comparable to other similar ground based surveys.

Influence of the air mass on the photometric quality

The final reduced BEST/BEST II data are corrected for first order extinction effects in the data pipeline. However, higher extinction terms might not be fully corrected and they might still influence the photometric quality of the collected data. In particular, at higher arimasses the effect can be noticeable. In order to determine the influence of the extinction on the photometric quality a test correlating the standard deviations of a sample of bright stars with the actual airmass was applied (168). In more detail, in the test an interval of the airmass ΔX around the value X_0 was chosen. In the selected interval the standard deviation of every data point $m_j(t_i)$ from the mean $\langle m_j \rangle$ in the bin was calculated. Then the value of ΔM_{X_0} is obtained as

$$\begin{aligned} \Delta M(X_0) &= \text{median}_{i \in \Omega(X_0),\ j} \, |m_j(t_i) - \langle m_j \rangle| \\ \text{with} \quad \Omega(X_0) &= \{\ i\ \ |\ X_0 - \Delta X/2 \leq X(t_i) < X_0 + \Delta X/2\} \end{aligned} \tag{8.18}$$

The brightest constant stars with low *RMS* (less than < 0.02 mag) were selected (2590 stars). The selection is necessary because the effect is small in comparison to other noise sources. For fainter stars white noise will dominate and potential extinction related effect will become negligible. In Figure 8.16 the $\Delta M(X_0)$ of the selected stars is plotted against the air mass for the complete campaign. It can be seen that $\Delta M(X_0)$ is influenced at higher airmass values for which it becomes to increase. The effect of the airmass is negligible for values of $X < 1.6$ where $\Delta M(X_0)$ is nearly constant.

The photometric quality does not change too much for the airmasses below 1.6. In these intervals no special corrections are needed and BEST II target fields are well within this interval. However, in case of observations at low altitudes above the horizon, e.g. CoRoT fields from OHP with BEST an effect reaching up to 4 mmag can occur. For this kind of data a second order extinction correction should be required.

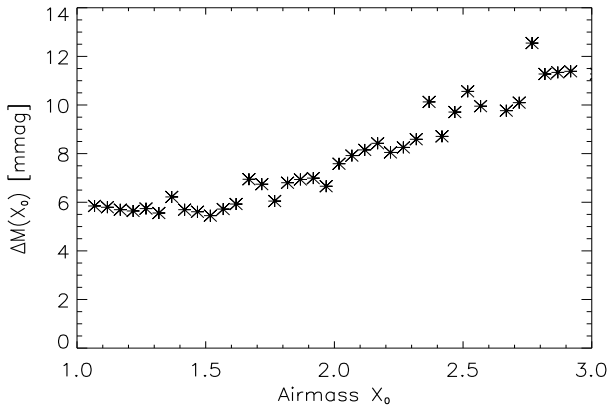

Figure 8.16: *The influence of the airmass on the photometric quality for BEST II data. The $\Delta M(X_0)$ for the selected sample of light curves of constant stars is plotted against the air mass for the complete campaign.*

8.4 Summary

The most important aspect of the data for the transit search is the photometric quality. This is influenced by observational conditions at the observatory. A comparison of similar (in terms of nights and seasons of the year) data sets collected with BEST from OHP and BEST II from OCA showed that observing conditions are more stable at OCA in terms of detected stars. At OCA approximately 56% of nights showed very high number of detected stars (> 3000). Furthermore, the number of detected stars with a certain *RMS* was stable over the whole campaign. On the other hand, BEST data from OHP showed an excellent quality, defined similar to the BEST II data, only for 40% of nights. These results demonstrate that OCA site is a suitable location for the transit search survey because much higher duty cycle and stable and high photometric quality, compared to OHP, can be achieved there.

Another limiting factor for the transit search is the noise level in the data sets. To address this influence, the noise level affecting the BEST II LRa02 data set was investigated. Different noise contributors such as background noise (σ_b), photon noise (σ_p) and correlated noise were determined. It was found that the detection rate is mainly constrained by the correlated noise component, since this affects the stars on the bright detection end. Therefore, two tests unveiling the level of correlated noise were performed. A value of σ_r between 0.002 and 0.004 mag was found to be characteristic for the BEST II data set. This result is comparable to other transit survey projects. Furthermore, it is an indication for an excellent quality of the observing site.

Chapter 9

Results of BEST surveys

The excellent photometric quality and the achieved duty cycle make it possible for the BEST project to conduct extensive surveys of the CoRoT target fields. The main science contribution of the project as a ground based support facility to the CoRoT space mission is illustrated in Figure 9.1. The three main directions are:

Periodic variable stars

The archived light curves from both BEST telescopes (yellow box) are searched for periodic variable stars and are provided to the CoRoT additional science programme on variable stars (blue box, also see Chapter 4). Especially, the information on several hundreds of newly detected periodic variable stars can extend the CoRoT light curves and improve the accuracy of ephemerids and other parameters. In addition, various types of variability, such as evolution of stellar spots or multiperiodicity in some particular type of stars, can be observed over longer time scales to see their long-term evolution.

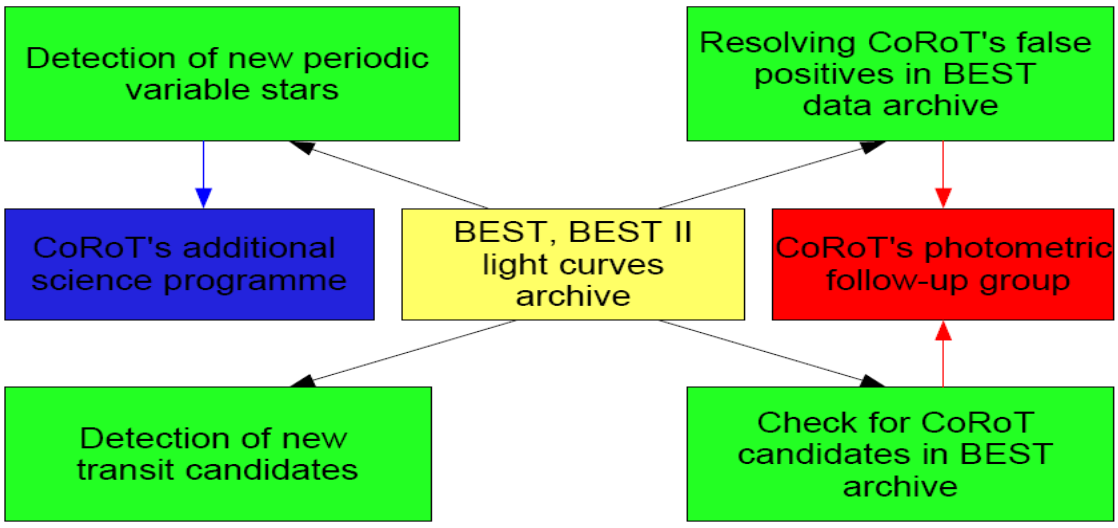

Figure 9.1: *The organization of BEST scientific programme. The main contributions are made to the CoRoT planetary candidate photometric follow-up observations and to the CoRoT additional science programme on variable stars. In addition, an independent transit search programme is performed with the project.*

The BEST/BEST II photometric follow-up observations of CoRoT planetary candidates

A significant contribution to the CoRoT's exoplanetary programme with the BEST telescopes is made in the context of the photometric follow-up programme on CoRoT planetary candidates (red box). The archived BEST data are searched for the transit-like events detected in the CoRoT data. If the event is detected also in the BEST data then the accuracy of the CoRoT ephemerids can be improved due to the fact that the BEST data are usually collected one year ahead of the CoRoT observations. In addition, a potential contamination of the CoRoT candidate from nearby variable stars is investigated and reported. In case of contamination with a spatially unresolved close variable star the follow-up priority is decreased or in obvious case the further follow-up observations are stopped (see Chapter 3).

Planetary transits survey

The BEST survey is able to discover its own planetary candidates. Especially, BEST II has a high duty cycle coverage and can observe multiple target fields at the same time.

The above described directions will be discussed in more detail in following three sections (9.1 - 9.3). This will also include some planetary candidates discovered with the BEST II survey. Finally, the completeness of the BEST data sets are discussed in more detail.

9.1 Variable stars survey

A complete catalog of new periodic variable stars detected with BEST and BEST II in the CoRoT initial and long run fields is included in Appendix A.2. Here, the process of detection of periodic variable stars will be exemplified by the results from the BEST II LRa02 data set.

9.1.1 Variability criterion

In the first step potentially variable stars in the calibrated and reduced data set must be selected. The data sets contain usually several thousands of light curves. Since the visual inspection of each single light curve would be too time consuming, a variability index j to automatically identify potential variable stars was used. The j index is determined for every star in the data set by examination of single points residuals with respect to the mean magnitude of the light curve. Data points located close to each other are considered with higher statistical weight than the data points separated with a large time difference. Large value of the j index indicates potential variability of the object while small values indicate constant stars (193). Quantitatively, the j index for every star is defined using the formula introduced by Stetson (193)

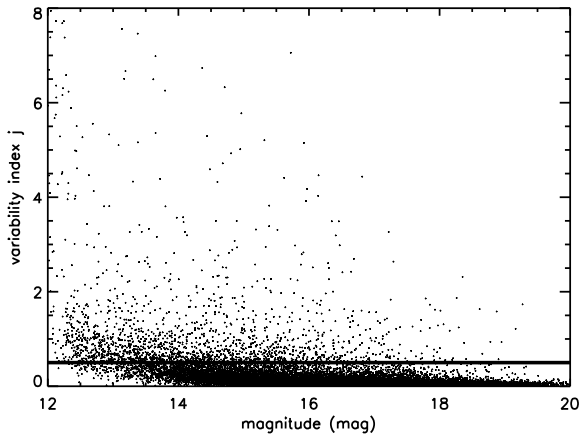

Figure 9.2: *Distribution of j index of stars in the BEST II LRa02 field against their magnitudes.*

$$j = \frac{\sum_{k=1}^{n} w_k sgn(P_k \sqrt{|P_k|})}{\sum_{k=1}^{n} w_k} \tag{9.1}$$

where k is number of pairs of observations, each with a weight w_k and

$$P_k = \begin{cases} \delta_{i(k)}\delta_{j(k)}, & \text{if } i(k) \neq j(k) \\ \delta_{i(k)}^2 - 1, & \text{if } i(k) = j(k) \end{cases} \tag{9.2}$$

where $\delta_{i(k)}$ and $\delta_{j(k)}$ are the residuals of normalized magnitudes from the mean magnitude of all data points for observations i and j within the pair k. An weighting factor was introduced according to Zhang et al. (2003) (194) as

$$w_{k,i} = \exp \frac{-\delta t_i}{\delta t} \tag{9.3}$$

In Figure 9.2 the distribution of the j index as a function of magnitude of the corresponding star is shown for the BEST II LRa02 target field. Similar plots for all other observed target fields can be found in (172; 173; 178; 179). From the obtained j index distribution we defined a limit of $j > 2$ for the BEST data and a limit of $j > 0.5$ for potentially variable stars in the BEST II data.

Table 9.1: *Statistics on different fields and relevant j index distributions.*

Field	Total # stars detected	# stars with var. flag	# periodic var.	j limit
IRa01	30426	3769	52	2
LRc01	30000	9112	86	2
LRa01	29830	6099	39	2
LRc02	98219	3443	426	0.5
LRa02	104335	3726	350	0.5

This value was determined from the examination of a subset of the data in which also light curves with low j indexes were examined manually to determine a conservative estimate what should be classified as stellar variability. Figure 9.2 shows that most

of the stars are distributed with a j index below 0.5. The distributions of the j index vary for different target fields therefore the limits need to be varied for BEST (OHP) data sets.

An overview on statistics in all long run fields is shown in Table 9.1. There, the total number of stars detected in the target field, the number of stars marked with a variability flag ($j >$ adopted limit) and the number of found periodic variable stars are given. It can be seen in Table 9.1 that only part of marked stars showed clear periodicity. The yield of BEST II survey in terms of numbers of periodic variable star is clearly higher compared to BEST. The main cause for this is the improved duty cycle in comparison to the BEST survey.

Visual inspection of some data sets showed that the rest of the stars with a high variable index showed usually variability but without a regular period or with an irregular structure. These structures were changing on long time scales so that the period can not be determined. In some cases the light curves were influenced by instrumental effects.

9.1.2 Detected periodic variables

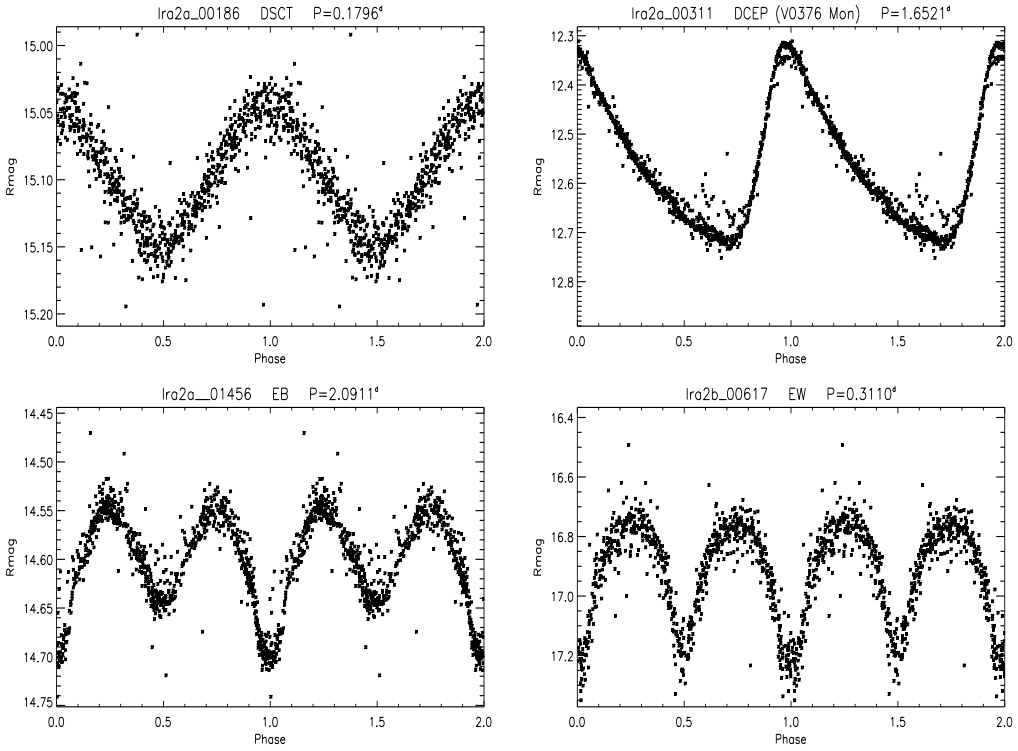

Figure 9.3: *An example of folded light curves of periodic variable stars detected in the LRa02 data set. The second phase is only an expanded image of the first phase and it is shown to increase the clarity. The BEST ID and the detected orbital period are presented above each figure.*

The light curves were searched for the period with an algorithm by (195) which fits a set of orthogonal periodic polynomials to the observational data. The variance statistics (ANOVA) is used for the evaluation of the quality of the fit. In principle,

the approach is very similar to an expansion into Fourier series. The period range searched was different for different target fields. In general, the period range between 0.05-60 days were searched because of the true length of the available data sets. As a last step, all suspected periodic variable stars were examined visually.

Table 9.2: *Example of a table with information on detected periodic variable stars with 2MASS catalog (196) identification for each star included.*

BEST ID	2MASS ID	α(J2000)	δ(J2000)	$\overline{m}$(mag)	P(days)	Amp.(mag)	Type
lra2a4*	06472576-0354198	6 47 25.8	-3 54 20.4	15.172	0.682	0.07	EW
lra2a74*	06475959-0335092	6 47 59.6	-3 35 09.4	12.937	0.989	0.04	SP
lra2a79*	06480297-0333011	6 48 03.0	-3 33 01.2	12.703	1.024	0.06	γDor
lra2a92	06473486-0357256	6 47 34.9	-3 57 26.1	15.166	1.402	0.08	EB
lra2a133*	06481854-0329035	6 48 18.6	-3 29 03.7	15.456	2.186	0.10	EA
lra2a134	06474958-0352496	6 47 49.6	-3 52 50.0	12.344	1.155	0.20	ASAS064750-0352.8
lra2a138*	06481445-0333074	6 48 14.5	-3 33 07.7	15.398	3.449	0.10	SP
lra2a143	06474412-0359120	6 47 44.1	-3 59 12.4	14.218	1.039	0.08	EA
lra2a159	06474131-0404558	6 47 41.3	-4 04 56.1	16.121	0.436	0.15	EW
lra2a186	06474594-0405436	6 47 46.0	-4 05 42.0	15.098	0.180	0.14	RRcLyr
lra2a194*	06484004-0324130	6 48 40.0	-3 24 13.2	15.631	1.950	0.10	EA
...	...	...	...	...	...	...	...
...	...	...	...	...	...	...	...

Some candidates were rejected in this process. Most of them showed periods around 1 day or multiples thereof what may be an influence of the diurnal cycle. The overall statistics on resulting number of detected periodic variable stars in CoRoT's target fields is presented in Table 9.1. Examples of the found parameters and the folded light curves are shown in Table 9.2 and Figure 9.3. In the table, the BEST ID, the corresponding 2Mass ID, astronomical coordinates, mean magnitude ($\overline{m}$), orbital period (P), amplitude of the variability (Amp.) and the type of the variability (see Section 9.1.4) is presented for each star. The complete catalog containing the some information for all observed CoRoT target fields with the BEST and BEST II telescopes is presented in Appendix A.2.

9.1.3 Variability classification

The classification of different types of stellar variability is based on the shape of the light curve, period and amplitude. More detailed description of variability classes used can be found in Chapter 2. We used a General Catalog of Variable Stars (GCVS)-based reduced classification (see Sterken & Jaschek, (1996) (197)) because the examined data sets possess only limited information about color or incomplete light curves due to the duty cycle.

The following classes were used: δCEP (δ Cep pulsating stars), DSCT (δ Sct type pulsating stars), RR Lyr - where possible also subtypes RRa, RRb, RRc - , SXPHE (prototype SX Phe), γ Dor (prototype γ Doradus). We also introduce a category PULS for the cases where we were not able to decide precisely about the type of pulsating star but the variability in the light curve is obvious. The groups used for eclipsing variables are EA (Algol type eclipsing stars), EB (β Lyr type eclipsing stars) and EW (W UMa type eclipsing stars). Stars showing variability characteristic for the spotted (stellar spots) or elliptical stars were classified as ELL and/or SP. Some stars were classified as α^2CVn whose light curve variation is due to their

rotation. Some stars in the BEST II data set possess longer periods of more than > 5 days. This group is marked as LP (long periodic) and the period may not be well determined. An extra class labeled as VAR includes the stars which did not match any criteria presented above but which shows variability in the light curve. The total number of these different types detected in BEST/BEST II target fields is summarized in Table 9.3.

9.1.4 Periodic variable stars found in BEST data sets

9.1.4.1 Pulsating variable stars

δ Scuti stars (DSCT) - Pulsating stars with periods below 0.3 days were classified as DSCT. However, a few stars with periods shorter than 0.1 days were classified as SXPHE due to the characteristic light curve and period for the prototype star SX Phoenicis. For the DSCT with periods below 0.3 days the classification should be fairly unique. In some cases the DSCT stars may show multi periodicity, for which a further frequency analysis of the light curves would be needed. Based on light curves some objects seemed to be DSCT stars too but their period was longer than 0.3 days. They might be W UMa objects but we are not able to distinguish them from DSCT in all cases.

γ Doradus stars (γDor) - A few stars were classified to this type based on the light curve shape, period range of 0.3 to 5 days and low amplitudes < 0.1 mag (198).

δ Cephei stars (DCEP) - Stars with periods longer than 1 day and amplitudes > 0.1 magnitudes were classified as δCEP stars.

RR Lyrae stars (RRLyr) - The RR Lyr stars were classified based on the char-

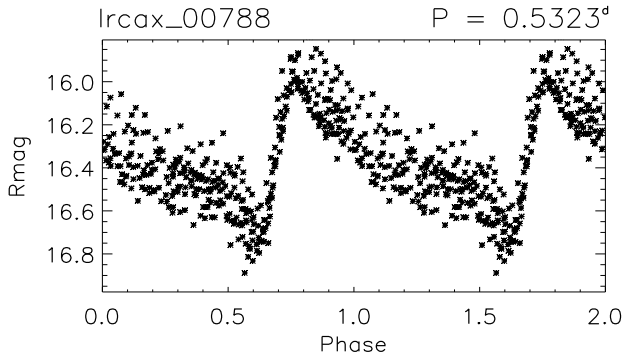

Figure 9.4: *Star from BEST II data set with the Blažko effect. The modulation of the main amplitude can be clearly seen in the folded light curve.*

acteristic shape of the light curve. They possess periods between 0.3 and 1 day. Some of the RR Lyr stars show a modulation of the main pulsation period in their light curves a feature known as the Blažko effect (199). Since the discovery of the alternative period modulation the physical process behind the effect still can not be satisfactory explained (200). Some examples of RR Lyr stars showing the Blažko

effect can be found in (201) or (202). A light curve of a star with Blažko effect from the BEST II survey is displayed in Figure 9.4

9.1.4.2 Eclipsing, elliptic/spotted and α^2CVn variable stars

Algol type eclipsing binaries (EA) - The eclipsing stars of EA class show nearly constant light curves between eclipses. In same cases, they can show the so-called reflection effect (203), (204) causing some small modulation of the light curve between eclipses. This effect is illustrated in Figure 9.5 for stars observed by BEST II.

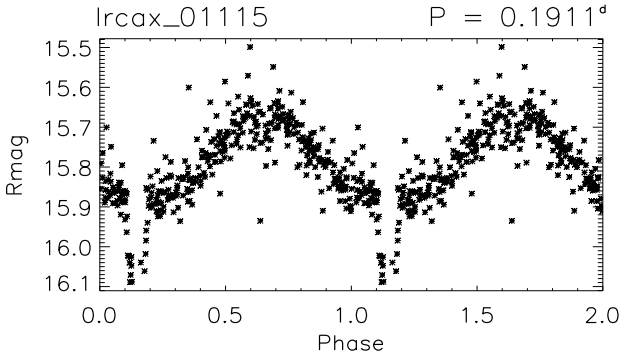

Figure 9.5: *A light curve of an EA type eclipsing binary with reflection effect slightly modulating the shape of the light curve between eclipses.*

β **Lyrae eclipsing binaries - (EB)** - Stars belonging to the EB class vary continuously between eclipses.

W Ursae Majoris eclipsing binaries - (EW) - Stars from the EW class have generally near equal depth and periods between 0.25 and 1 days. Several eclipsing binaries, primarily some EW, show the O'Connell-effect (see Figure 9.6) which is a deformation of the light curve due to the presence of stellar spots (205).

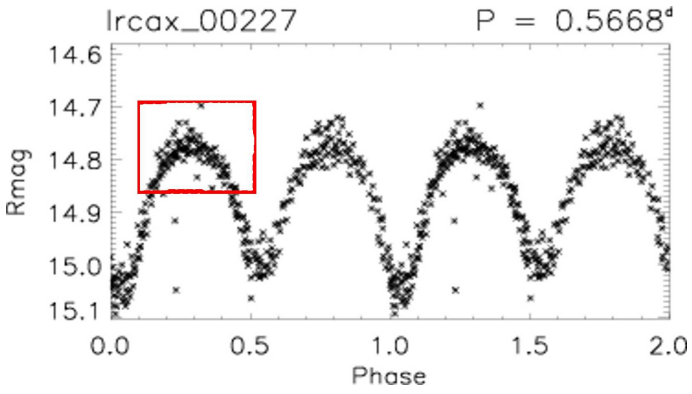

Figure 9.6: *An EW type eclipsing binary with the O'Connel effect indicated by deformed shape of the light curve marked with a red box.*

Ellipsoidal/Spotted variable stars - (ELL/SP) - The classification for the rotating and spotted stars ELL/SP is based on the changing minimums/maximums depth of the light curves. Some stars can show also an evidence for the stellar spots and thus perturbations in the periodicity. Some of the systems classified as spotted may be also cataclysmic variable stars in quiescent phase. Further color and spectroscopic information is needed to clarify this.

$\alpha^2 CVn$ **stars** - Stars showing a slight amplitude variability in the region of a few percent which do not fulfill the classification criteria for any of the above mentioned variability type were classified as $\alpha^2 CVn$. The prototype is Cor Caroli from the constellation Canum Venaticorum, and the characteristics are usually fast rotation and presence of emission lines in the CaII H, K and H_α bands indicating strong chromospheric activity (206).

Table 9.3: *Statistics on types of newly detected periodic variable stars in BEST/BEST II CoRoT's target fields.*

Field	RR Lyr	DCEP	DSCT	α^2CVn	EA	EB	EW	Others
IRa01	-	10	6	-	4	10	19	6
LRc01	-	49	-	-	43	-	-	-
LRa01	-	2	39	-	2	4	4	4
LRc02	41	18	35	7	45	67	172	40
LRa02	18	37	7	29	47	31	48	133

9.1.4.3 Limitation of the data sets

Color information

We possess only a limited data set with no color information which makes the proper identification of the stellar variability difficult for some particular cases. However, cross identification with 2MASS catalog (196) allowed to use the color information for matched stars. Color diagrams for newly detected periodic variable stars in observed long run fields are shown in Figure 9.7 with detected stars marked. A subgroup of pulsating stars is represented with asterisk and the subgroup of eclipsing stars with triangle. This figure can be useful for future studies of the evolutionary stages of the detected stars. In future publications interesting stars can be selected and implications for the spectral characteristic can be estimated from this figure case by case.

Stellar crowding

The second limiting factor is the pixel scale of 1.5" for BEST II and 5.5" for BEST which might still lead to multiple identifications of a single variable star due to overlapping PSFs. This is in particular true for crowded regions near the galactic center. The stars possibly influenced by their neighbors are marked with "c" in the summary of their parameters (see Table 9.2 and Appendix A.2).

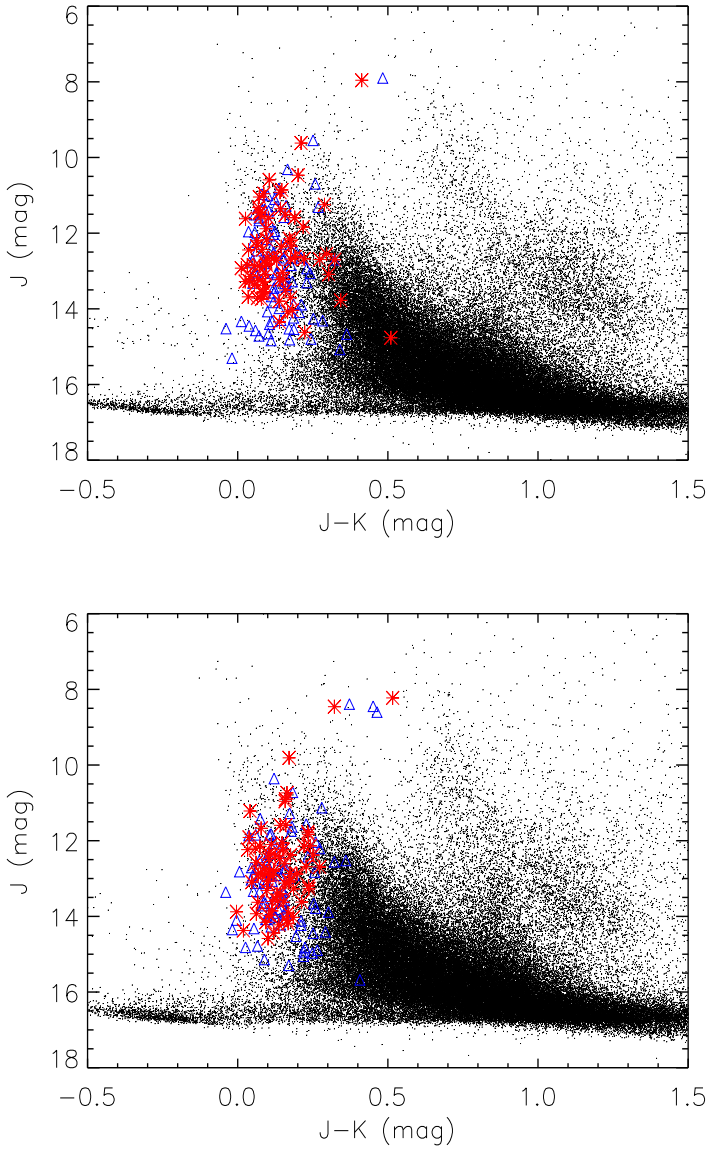

Figure 9.7: *Color J magnitude for all stars from the BEST II LRa02a field is plotted over color indices from the 2MASS catalog (196). The distribution of detected variable stars is marked with asterisk for pulsating and triangle for eclipsing variable stars (top). Similar plot is shown in the bottom Figure for LRa02b field (bottom).*

9.1.4.4 The BEST data sets and known variable stars

The BEST/BEST II data sets were checked if they contain variable stars which were detected previously by other surveys. For this purpose, the periodic variable stars found in BEST fields were compared with the General Catalogue of Variable Stars (GCVS) via a SIMBAD[1] and AAVSO catalog [2]. A summary on stars previously known is given in Table 9.4 with the references to the discovery publications. The corresponding BEST IDs are also included. In total, 30 previously known variable

[1]http://simbad.u-strasbg.fr/simbad/
[2]http://www.aavso.org/vsx/index.php

stars were identified in BEST data sets. More information about these stars can be found in (171; 172; 173; 178; 179)

Table 9.4: *Previously known variable stars in the BEST data sets.*

Star catalog ID	Reference	BEST ID	Field
V453 Mon	GCVS	2109	IRa01
V515 Mon	GCVS	2390	IRa01
ES Aql	GCVS	G1	LRc01
V0362 Aql	GCVS	G2	LRc01
V0381 Aql	GCVS	G3	LRc01
V0919 Aql	GCVS	G4	LRc01
V0920 Aql	GCVS	G5	LRc01
V0291 Aql	GCVS	G6	LRc01
V0922 Aql	GCVS	G7	LRc01
V0978 Aql	GCVS	G8	LRc01
V1127 Aql	GCVS	G9	LRc01
V1135 Aql	GCVS	G10	LRc01
V1215 Aql	GCVS	G11	LRc01
GU Mon	GCVS	2361	LRa01
DD Mon	GCVS	3550	LRa01
V404 Mon	GCVS	4559	LRa01
V501 Mon	GCVS	5239	LRa01
V501 Mon	GCVS	5239	LRa01
CD Mon	GCVS	25207	LRa01
NSVS 13906750	(207)		LRc02
NSVS 13910069	(207)	lrcby-1143	LRc02
V1116	(208)		LRc02
V0656 Oph	(209)		LRc02
V1117 Oph	GCVS	lrcax-132	LRc02
NSVS 13913191	(207)	lrcby-107	LRc02
ASAS 184150+0603.0	(210)	lrcbx-2519	LRc02
V0452 Mon	GCVS	lra2a788	LRa02
V0376 Mon (ASAS064848-0336.3)	(210), AAVSO	lra2a311	LRa02
XZ Mon (NSVS12585288)	AAVSO	lra2a1702	LRa02
ASAS064750-0352.8	(210)	lra2a134	LRa02
EIMon	(211)	lra2b469	LRa02

9.1.5 Summary on periodic variable stars

The BEST and BEST II telescopes observed the CoRoT's IRa01, LRc01, LRa01, LRc02, LRa02 target fields from the nominal mission period. All stars with suspected variability were identified and searched for periodicity. The corresponding folded light curves were visually inspected and stars showing regular periods were selected for publication (172; 171; 173; 178; 179) and provided to the CoRoT scientific community. In Appendix a full catalog based on these results is available.

The total number of stars observed by BEST and BEST II in all CoRoT target fields exceeds 250000. Typically, 3000 to 9000 stars per field are identified as variable stars, resulting in more than 25000 variable stars in total. Out of these 952 periodic variable stars could be identified in all target fields. Typical periods range from 0.05 to 100 days. We also found light curves of 31 periodic variable stars already known from other surveys (see Table 9.4).

The data on variable stars are further used by the CoRoT science team (212; 213). E.g. light curves from BEST surveys can be used to extend the light curves obtained with CoRoT space mission. In addition, the information about eclipsing binary stars can be helpful for the photometric follow-up of CoRoT candidates (108) presented in the following sections.

Table 9.5: *Statistics on BEST/BEST II detected variable stars in CoRoT target fields. A comparison is also made with the OGLE-I survey.*

	BEST	BEST II	OGLE-I (214)
Target fields	3	4	N/A
Observed stars	$\approx$ 90000	$\approx$ 200000	400000(215)
New periodic variables	177 (0.2%)	776 (0.4%)	1900 (0.5%) (215)

A quantitative overview in terms of detected periodic variable stars on results of the BEST surveys (see Table 9.5) shows that the BEST survey in comparison with the OGLE-I survey (214; 215) detected less periodic variable stars. In the case of BEST II the difference to OGLE-I is negligible and can be explained by the use of non-conservative criterion to detect variability. E.g. that light curves with periods near to multiples of one day were rejected. In case of BEST the important factor is the low duty cycle which is a factor two less compared to the OGLE-I survey (see Chapter 7).

The catalog of detected periodic variable stars presented here shows that small aperture automatized telescopes with large field-of-view and high duty cycle such as BEST and BEST II can contribute significantly to the detection and characterization of variable stars. The BEST surveys have been able to provide information in terms of high quality photometric light curves on more than 900 newly detected periodic stars. Since the duty cycle of BEST II survey will improve even better results are to be expected in a near future.

9.2 BEST/BEST II observations of CoRoT candidates & planets

9.2.1 BEST/BEST II contribution to the follow-up of CoRoT planetary candidates

The difficulties of the transit search method related to false positive detections were discussed in Chapter 3. In order to reject or confirm planetary candidates discovered within the CoRoT space mission a follow-up group is organized. The follow-up observations consist of spectroscopic (109) and photometric (108) campaigns. In this context, available light curves from the BEST/BEST II surveys and the information about the detected variable stars is used to check for contamination of CoRoT planetary candidates. Particularly, eclipsing variable stars can contaminate the flux incoming from the CoRoT candidate with mimicking the transit event. The mask of the CoRoT candidate (about 30 to 40 arcseconds - see Chapter 4) is checked if it contains previously detected variable star from BEST surveys which can disturb the flux from the candidate. If the close variable star is identified in the BEST data

sets, the corresponding light curves are visually inspected. In case the period of the CoRoT candidate is similar to the period detected by BEST for the variable star, the follow-up observation of such candidate is stopped.

Constraining factors are the angular resolution and the duty cycle coverage, therefore BEST survey from OHP contributed only slightly (angular resolution 5.5"/pixel in comparison to the CoRoT's 2.3"/pixel). Since BEST II posses better angular resolution (1.5 arcsecond/pixel) than CoRoT, two stars which are unresolved in the CoRoT mask will be separated in the BEST II data. Therefore, the BEST II data sets contribute more significantly to the identification of false positive detections. CoRoT candidates from the LRc01, LRa01 and IRa01 fields were verified in the data sets obtained with BEST at OHP. The CoRoT candidates from the LRc02 and LRa02 data sets were checked in the BEST II data sets (216). A typical example

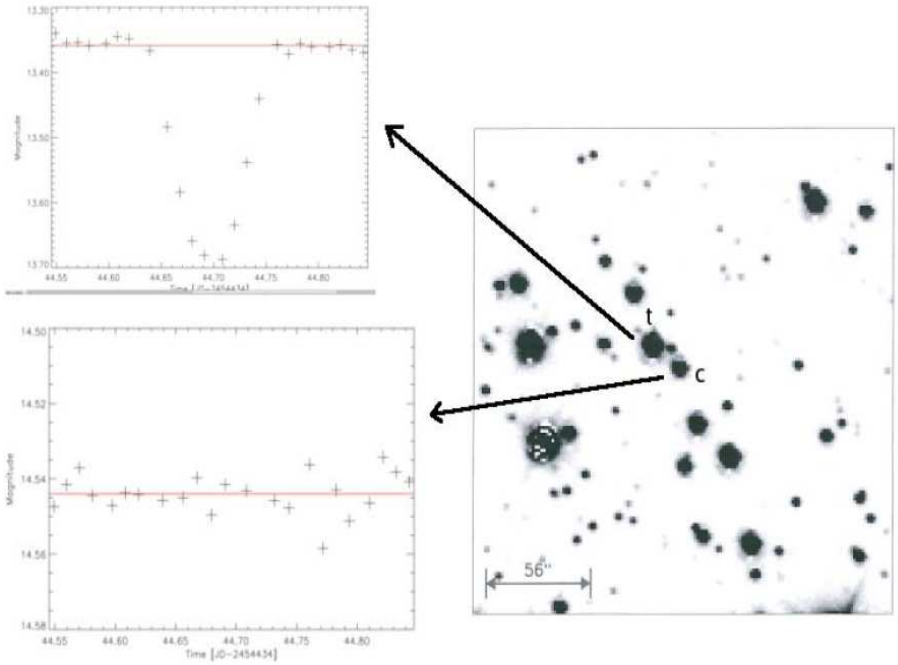

Figure 9.8: *BEST II image of star selected as planetary candidate from CoRoT light curves. BEST II data archive has been searched for the nearby variable stars (≈ 18") which can blend the candidate. Indeed, in BEST II data archive, a variable star in the right figure indicated with t and with period of P = 2.54521 days has been found. The period is the same as the one reported for the candidate c by the CoRoT team. The light curve of the contaminating variable stars with an eclipse is shown in upper left panel and a constant BEST II light curve of the CoRoT candidate is shown in bottom left panel.*

of the process is shown in Figure 9.8. One of the most recently detected CoRoT planetary candidate turned out to be blended by the close variable star. In this particular case, a planetary candidate with a period of $P = 2.55251$ days with a transit depth $\delta_c = 0.35\%$ was reported by CoRoT detection team (labeld c in Figure 9.8). Consequently, the BEST II data archive was searched for the closest objects to the reported CoRoT candidate. I.e., BEST II light curves of stars from the vicinity of the candidate were searched for potential variability. Indeed, a star t, previously selected as variable of Algol type with a period of $P = 2.54521$ days and transit depth of primary eclipse of $\delta_t = 0.35$ mag, was found. Since the period of the

variable star and the CoRoT candidate is exactly the same and the star t is located in the CoRoT photometry mask close to the candidate (18"), it is clear that this particular star contaminates the light curve of the CoRoT candidate. In addition, the depth of the CoRoT candidate can be explained by an Algol star, if 0.5% of the flux of this binary contaminates the flux of the CoRoT target. Consequently, the follow-up was terminated and the candidate was classified as a system blended with a nearby variable star.

The above described approach has been applied on 80 CoRoT candidates from LRc01, LRa01, IRa01 (BEST) and on 80 candidates from LRc02 and LRa02 BEST II data sets. The work is still ongoing and more similar cases are expected to be cleared in the near future.

9.2.2 BEST observations of planets CoRoT-1b & CoRoT-2b

An important contribution to the CoRoT space mission has been made with BEST telescope. Among pre-discovery observations of the first two planets discovered by CoRoT, transits of CoRoT 1b and CoRoT 2b were found in the archived BEST data sets of the IRa01 and LRc01 fields. The result is published in Rauer et al. (2009) (137) and summarized below.

9.2.2.1 CoRoT 1b

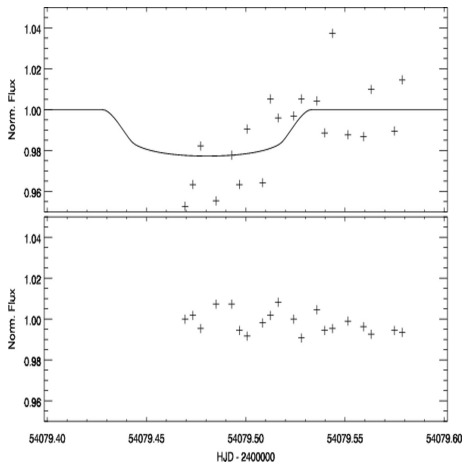

Figure 9.9: *Partial transit of confirmed planet CoRoT 1b as found in the BEST data set. Solid line in the upper panel represents the predicted event and the points are observational data whereas lower panel presents the measurements for a nearby comparison star. Image taken from (137)*

The BEST telescope observed the IRa01 field from November to December 2006, three months before CoRoT observations. Based on the analysis with the CoRoT alarm mode pipeline a planetary candidate was detected and later confirmed as CoRoT 1b (125). The candidate was selected by inspection of the CoRoT preliminary data containing the observations of only a few weeks. Consequently, the BEST data archive was searched for the potential transit events of the new planetary candidate. Indeed, BEST data taken on 10 December 2006 were predicted to contain

the egress of CoRoT 1b. However, the data reduced with BEST pipeline did not show an evidence of a transit event due to large radius (7 pixel) of an aperture selected for photometry. Thus the CoRoT 1b signal was influenced with the flux of close stars hiding the decrease in intensity due to the transit. Therefore, aperture photometry with an aperture of 5 pixels was applied manually on the BEST data and the egress was detected (137). The simple light curve is shown in Figure 9.9 where a high noise level is evident. This is because, the intensity of the object is on the fainter end of magnitude range . The host star of CoRoT 1b and a star of comparable magnitude are shown in Figure 9.9. Planetary parameters can be found in Table 9.6.

This observation provided useful information during the early stage of the organization of follow-up observations of the CoRoT planet detection (137).

9.2.2.2 CoRoT 2b

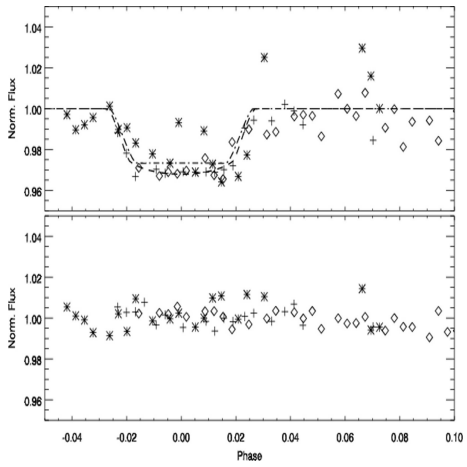

Figure 9.10: *The folded light curve of the transit events found for CoRoT 2b in the BEST data set. Long-short dashed line represents the model fit based on the BEST data (137) and the long dashed line represents the model fit based on the CoRoT data presented in (114). Figure taken from (137)*

The second CoRoT's planet CoRoT 2b (124) has been found in the LRc01 field. CoRoT observed the field from May to October 2007 as the first long run field. The BEST data were acquired between June and August 2005. Shortly after announcement of a planetary candidate by the CoRoT team (124) the BEST data archive was searched for the transit events. One almost complete transit event was found for the data from 14 July 2005 and on two other nights (July 28, August 4) partial transit events were were present in the BEST data.

Modeling of the transit event

The BEST light curve was folded with the period given in Alonso et al. (2008) (124) and the transit events in the folded light curves were modeled (217) using the quadratic limb-darkening model of (85). In this model the planet is dark without any observable radiation while the stellar disc is limb-darkened. Both objects are considered spherical. This model has seven free parameters: *orbital inclination*

Parameters	CoRoT-1b	CoRoT-2b	
	Barge et al. (2008)	Alonso et al. (2008)	Rauer et al. (2009) ((137))
$a/R_\star$	4.92 ± 0.08	6.70 ± 0.03	6.32 ± 0.15
$R_P/R_\star$	0.1388 ± 0.0021	0.1667 ± 0.0006	0.1633 ± 0.0012
$i[deg]$	85.1 ± 0.5	87.84 ± 0.10	85.23 ± 0.12
u_+	0.71 ± 0.16	0.471 ± 0.019	-0.014 ± 0.360
u_-	0.13 ± 0.30	0.34 ± 0.04	0.024 ± 0.200
$RA[J2000.0]$	$06^h48^m19.17^s$	$19^h27^m06.5^s$	
$Dec[J2000.0]$	$-03°06'07.78"$	$01°23'01.5"$	
V_{mag}	13.6	12.57	
$P[d]$	1.5089557 ± 0.0000064	1.7429964 ± 0.0000017	
$T_c[JD]$	2454159.4532 ± 0.0001	$2454237.53562 \pm 0.00014$	

Table 9.6: *The star and planet parameters for CoRoT 1b and CoRoT 2b. Table from Rauer et al. (2009) (137)*

(i), *radius* of the planet (R_{pl}) and the size of the *semi-major axis* (a), both of them are expressed in stellar radius unit (R_{st}), two *limb darkening coefficients* (u_+, u_-), the *period* (P) and the *epoch* (T_c). Since the *epoch* and *period* are well-known from the CoRoT measurements then instead of them we chose the phase-shift as a free parameter which was added to each phase. This is in order to allow for the adjustment of the phases since in the meantime small changes in the period might occur. To find the best agreement between the model and the data a Markov Chain Monte Carlo method complemented with the Metropolitan-Hastings algorithm (see e.g. (218)) was utilized. The final adopted values were estimated as the best fit in our chains while the errors were estimated from the distance of the parameter values at the both sides of the best value where the χ^2 reached the 68% confidence level. The resulting fit is shown in the figure. Furthermore the obtained parameters for CoRoT-2b are summarized in Table 9.6. There, also a comparison of the data published by Rauer et al. (2009) (137) and Alonso et al. 2008 (124) can be found. The found parameters from the BEST observations are in a good agreement with the values found for the CoRoT data (124).

Transit timing variations

A transit timing analysis based on BEST, CoRoT, AXA[3] and Vereš et al. (2009) (219) data for 15 transit events were presented by Rauer et al. (2009) (137). The resulting ephemerids found by (137) are:

$$T_{min}(HJD) = 2454237.53562(14) + 1.74297970(14) \times N \tag{9.4}$$

Only a slight improvement of one second was reported (137) for the orbital period in comparison with CoRoT ephemerids (124).

9.2.2.3 Conclusions

The detection of the transits in archival data was the first successful planet observation with BEST telescope. Unfortunately, the transit events were found only after the CoRoT 1b and CoRoT 2b were detected by the CoRoT space mission. This was

[3]AXA:Amateur eXoplanets Archive; see brucegary.net/AXA/x.htm

mainly due to the insufficient duty cycle of BEST from OHP, causing that only a part of the transit event was observed for CoRoT 1b and only one almost complete and two partial transit events were observed for CoRoT 2b. Nevertheless, the BEST data on CoRoT 1b and CoRoT 2b have proven that the BEST telescope is capable of detection of a Jupiter sized planet with an orbital period of a few days. In addition, both observations were used by the CoRoT follow-up group in the early stage of the alarm mode detection phase (see (124)).

9.3 Transit candidates from the BEST II LRa02 data set

One of the scientific objectives of the BEST/BEST II surveys was to detect planetary candidates.

The missing previous detections with the BEST telescope can be explained by the discussion in Section 7.3.1. There, it was shown that for the probability of the detecting three transit events only potential planets with orbital periods up to 1 day can be securely detected from the BEST data. None of the known Jupiter sized planets orbits its star in such a short period (6). The duty cycle was clearly limiting the yield from the BEST observations. This was demonstrated in Section 9.2.2 with the case of BEST observations of the transits of CoRoT 1b and CoRoT 2b where the transit data were available before CoRoT observations but insufficient to allow a clear detection. Additional attempts to find transiting planets in the BEST data sets were made by Wiese (2007) (182) who found some candidates for transit-like events. However, due to the lack of observational data for these objects no future action to investigate their nature was possible.

A major improvement in terms of duty cycle was demonstrated for the new BEST II survey (Chapter 7). Especially, the LRa02 data set was obtained with a high duty cycle in comparison with the other BEST/BEST II data sets, thereby significantly improving probability of the planet detection. In the following section new candidates detected in LRa02 data set will be presented.

9.3.1 Detected candidates

The cases found during the stellar variability characterization were inspected visually with the primary goal of searching for low amplitude periodic events on a scale of few days. Finally, four candidates were selected from the visual inspection of the corresponding light curves. The BEST ID, the corresponding 2MASS ID (196), coordinates mean magnitude, orbita period and the transit depth are presented in Table 9.7. The remaining cases were identified as variable stars or artificial effects.

Table 9.7: *Overview on the detected planetary candidates in the BEST II LRa02 field.*

BEST ID	mag	P(days)	$\Delta I(\%)$
lra2a00487	14.93	1.2183	2.5
lra2a00535	12.58	0.97191	1.8
lra2a00811	13.22	1.8160	6.0
lra2b00234	13.05	1.2895	1.8

9.3.1.1 Candidate *lra2a00487*

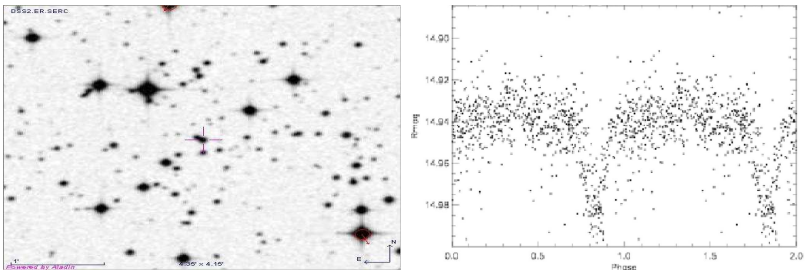

Figure 9.11: *Finding chart (left) and a folded light curve (right) for the planetary candidate lra2a00487.*

The host star was identified as 2MASS 06491875-0344029 with a mean magnitude of 14.93 mag (see Figure 9.11). In the light curve (see Figure 9.12), 6 complete and 4 partial transit-like events with a duration of about 2.64 hrs. were detected. The transit-like events (Figure 9.11) show a period of $P = 1.2183 \pm 0.0001$ days and an intensity decrease around 2.5%. The parameters of the system with ephemerids of the candidate *lra2a00487* are given in Table 9.8.

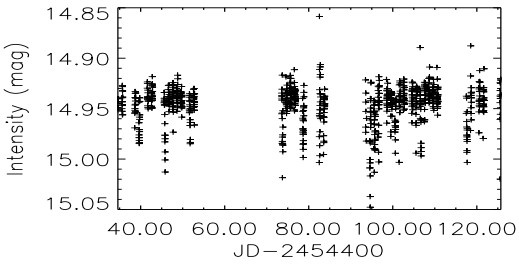

Figure 9.12: *Complete BEST II light curve for the planetary candidate Lra2a00487.*

Table 9.8: *Details for the candidate lra2a00487.*

Parameter	value
ID BEST II	lra2a00487
BEST II - R (mag)	14.93
ΔI (%)	2.5
P(days)	1.2183 ± 0.0001
ephemerids	$T = 2454473.782 \pm 0.002 + 1.2183 \pm 0.0001 \times N$

9.3.1.2 Candidate *Lra2a00535*

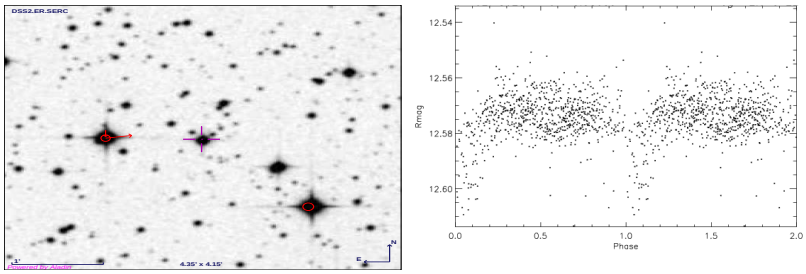

Figure 9.13: *Finding chart and a folded discovery light curve for the planetary candidate Lra02a00535.*

The host star was identified as 2MASS 06495670-0322498 with a BEST II magnitude of 12.58 mag (see Figure 9.13). The spectral class of the host star is not defined in any catalog. In the light curve (see Figure 9.14), 2 complete and 2 partial transit like events with a duration of 3.6 hrs. were detected. However the light curve is affected by a high level of noise. The events occurred with a period of 0.97191 days and an intensity decrease of 1.8%. The detected period indicates that the transit events might be due to an artificial effect since it repeats in a nearly diurnal cycle. Therefore, this candidate was ranked as a low priority candidate. The parameters of the system and the ephemerids of the candidate *Lra2a00535* are summarized in Table 9.9.

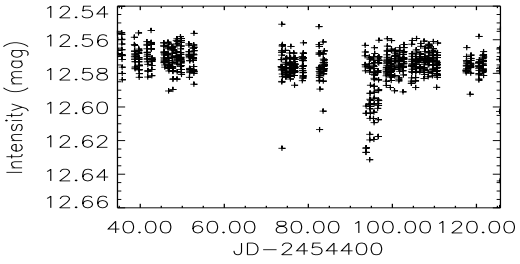

Figure 9.14: *Complete BEST II light curve for the planetary candidate Lra2a00535.*

Table 9.9: *Details for the candidate lra2a00535.*

Parameter	value
ID BEST II	lra2a00535
ID 2MASS	06495670-0322498
R (mag)	12.58
ΔI (%)	1.8
P(days)	0.971 ± 0.005
ephemerids	not clear

9.3.1.3 Candidate *lra2b00811*

The host star was identified as 2MASS 06503672-0341301 with a BEST II magnitude of 13.22 mag (see Figure 9.15). During the eclipse the intensity decrease is 6.0% and the eclipses have a periodicity of 1.816 ± 0.005 days. However, in the light curve (see Figure 9.16), a clear secondary eclipses can be seen and therefore discriminating the candidate from further follow-up observations. The system was classified to be most likely an EB type binary (see Section 9.1). The parameters for the system *lra2b00811* are summarized in Table 9.10.

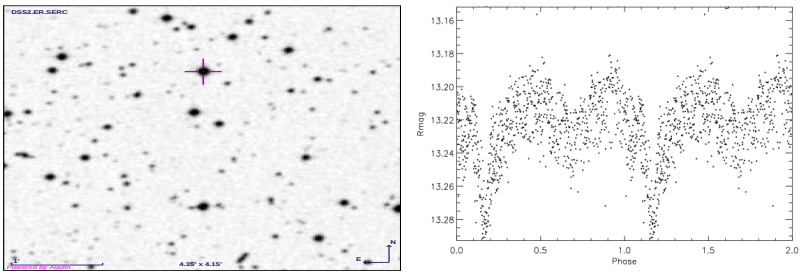

Figure 9.15: *Finding chart and a folded discovery light curve for the planetary candidate lra2b00811.*

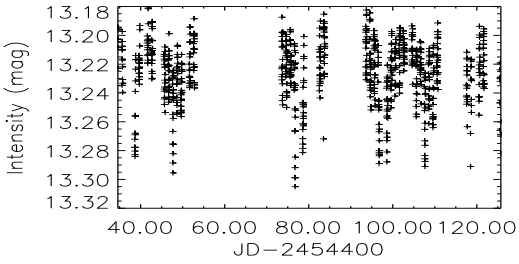

Figure 9.16: *Complete BEST II light curve for the planetary candidate Lra2a00811.*

Table 9.10: *Details for the candidate lra2b00811.*

Parameter	value
ID BEST II	lra2a00811
ID 2MASS	06503672-0341301
BESTII - R (mag)	13.22
depth (%)	6.0
P(days)	1.816 ± 0.005

9.3.1.4 Candidate *lra2b00234*

The host star was identified as 2MASS 06541159-0514025 with a BEST II magnitude of 13.05 mag (see Figure 9.17). The spectral class of the host star was determined as G5V by Gandolfi (2009) (220). In the light curve (see Figure 9.18), 3 complete

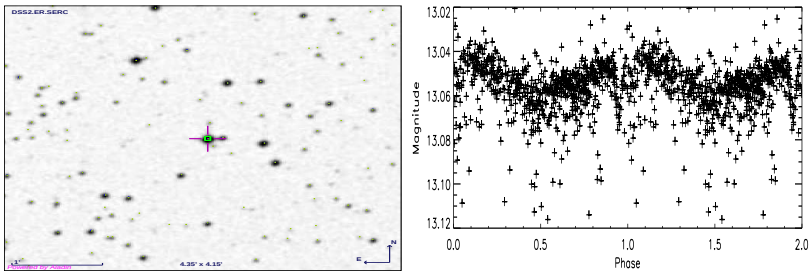

Figure 9.17: *Finding chart and a folded discovery light curve for the planetary candidate lra2b00234.*

and 3 partial transit like events of a duration of 1.92 hours were detected. The event occurred with a period $P = 1.2895$ days and with the intensity decrease of 1.8%. The parameters with ephemerids of the candidate *lra2b00234* are summarized in Table 9.11.

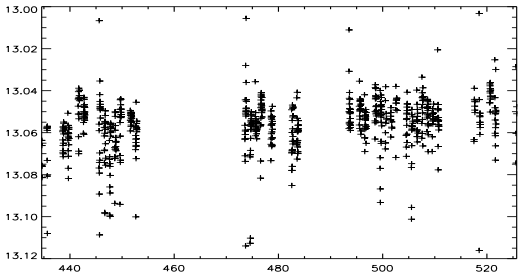

Figure 9.18: *Complete BEST II light curve for the planetary candidate lra2b00234.*

Table 9.11: *Details for the candidate lra2b00234.*

Parameter	value
ID BEST II	lra2b00234
R (mag)	13.05
depth (%)	1.8
P(days)	1.28955 ± 0.00006
ephemerids	$T = 2454499.700 \pm 0.001 + 1.28955 \pm 0.00006 \times N$

9.3.2 Follow-up and models of the candidate systems

In order to confirm the nature of these planetary candidates follow-up observations, as discussed in Chapter 3, are needed. In an ideal general case, the photometric follow-up with high angular resolution are performed to confirm the transit event and to reject possible contamination from the potential unresolved background binaries. Simultaneously, one spectrum of the system is obtained in order to determine the spectral type of the host star. Additional information can be provided with the numerical modeling of the transit event performed with the routine by Csizmadia (217) (see Section 9.2.2).

If the parameters obtained from all these steps indicate that the candidate could be a planet, high resolution radial velocity measurement should be started (see Chapter 3). After successful RV measurement the candidate can be confirmed. The whole follow-up process can take a number of years due to limited visibility of the candidates on the sky during the year.

Rejected candidates

The selection of the four candidates were carefully examined visually and the original science frames containing the transit event checked for artificial effects. In that process the following candidates were removed from the further follow-up process:

Lra2a00535 - high noise level, period close to 1 day

lra2a00811 - binary system

This left two candidates which were considered for further modeling and follow-up observations. These two remaining candidates *lra2b00234* and *lra2a00487* will be discussed in more detail below.

9.3.2.1 Analysis of the priority candidate *lra2b00234*

The transit depth, duration and orbital period of the candidate were matching typical parameters of the Jupiter-sized planet if the spectral type of the star would be similar to Sun. Therefore, firstly the candidate was selected for the further spectroscopic follow-up observations in order to determine the spectral type of the host star. A few spectra were taken by Günther et al. (2009) (221) with the AAOmega instrument installed at Anglo-Australian Telescope, Australia. The AAOmega is a general purpose facility providing multi-object (resolution $R = 1200 - 10000$) and integral field spectroscopy ($R = 2000 - 16000$) (222). The BEST II candidate was selected for a multi-object mode as one of 392 targets. The resulting spectrum is shown in Figure 9.19 and a fitted template (red line in figure) confirms a spectral type G5V for the host star (220) with a typical radius of $R_{G5V} = 1.05 R_{Sun}$ (223). The obtained information on spectral type was used for further models and calculations of planetary parameters. Using the known stellar radius $R_{star} = 1.05 R_{Sun}$ and the determined transit depth (δ) of 0.018 ± 0.001 the radius of the object can be estimated directly from the equation (3.3):

$$R_{pl} = \sqrt{\delta R_{star}^2} \tag{9.5}$$

which gives $R_{pl} = 0.14 \pm 0.007 R_{Sun}$ or $1.370 \pm 0.007 R_{Jupiter}$. This radius would fit into the range of planetary sizes.

During the second step, the photometric light curve of the candidate *lra2b00234* was folded and then the transit event was fitted with a routine by Csizmadia (2009) (217). The result presenting the fitted folded light curve of a transit event and the residuals

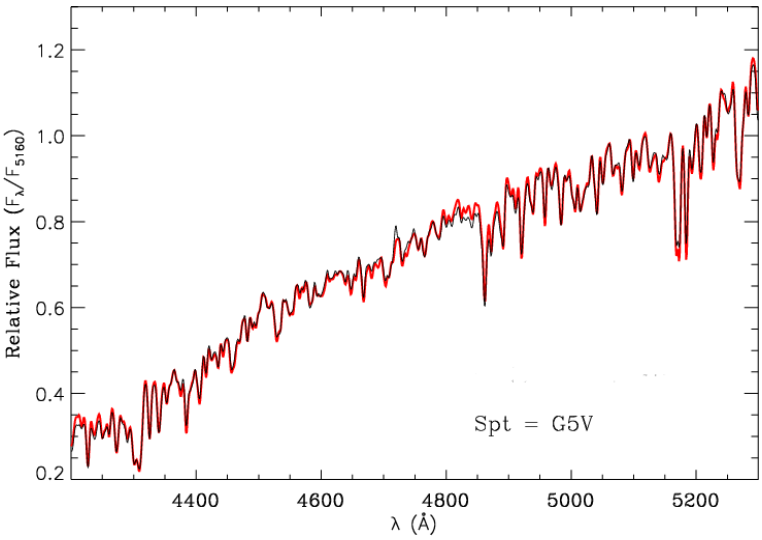

Figure 9.19: *Spectrum of the host star of candidate lra2a00487 confirming the G5V spectral type. Spectrum was taken with AAOmega instrument installed at Anglo Australian Telescope, Australia. Image was taken from (220).*

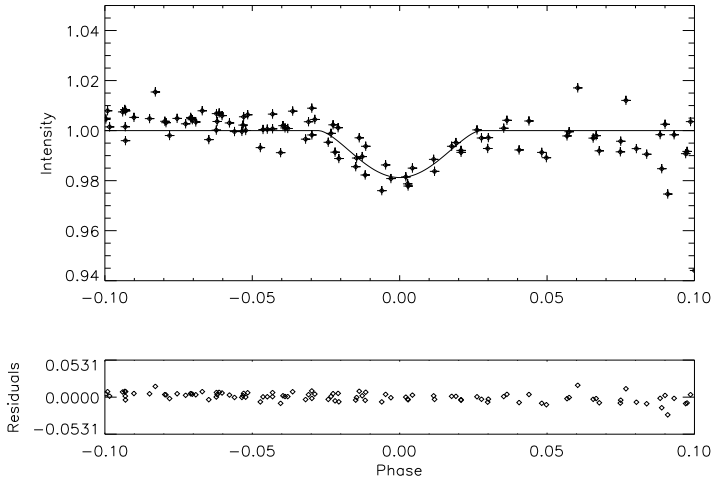

Figure 9.20: *Transit of a planetary candidate fitted with routine by Csizmadia (2009) (217).*

representing the goodness of the fit is shown in Figure 9.20. The determined values will be compared with values obtained from Equation (9.5).

The parameters obtained from the preliminary fit are given in Table 9.12. They include the semi-major axis (a), the radius of the planet (R_{pl}), the radius of the star (R_{Star}) and the planetary inclination (i). From the parameters in the table the radius of the candidate was determined to be $R_{planet} = 0.14 \pm 0.03 R_{Sun} = 1.36 \pm 0.03 R_{Jupiter}$.

The results from the fit and from Equation (9.5) are compatible, indicating a Jupiter-sized planet. In order to securely confirm the planetary nature of the candidate further photometric follow-up observations are planned for the season beginning with September 2009 to finally confirm the transit event and to refine the ephemerids.

Table 9.12: *Preliminary parameters obtained from the fit of the folded light curve for candidate lra2b00234. All in units of stellar radii.*

parameter	
a $(in R_{star})$	2.4 ± 0.2
R_{planet}/R_{star}	0.14 ± 0.03
i (deg)	56 ± 6

In parallel high precision RV follow-up observations are also scheduled for October-March 2009/2010 season.

In the case that a planetary nature would be rejected with follow-up observations, a scenario for a low mass stellar companion would be an alternative. Since it would be a system containing the G5V and M dwarf stars, it would be still very interesting. Only a few similar systems are known until now. Halbwachs et al. (2003) (224) found a peak in the distribution of the close binary system near a mass ratio 1. In addition, Mazeh et al. (2003) (225) reported a lack of low mass ratio (mass ratios between 0.3-1.0) close binary systems. Therefore, also if the candidate *lra2b00234* would be identified as a stellar object the system would remain very interesting.

9.3.2.2 Analysis of the priority candidate *lra2a00487*

As in case of candidate lra2b00234 the parameters were matching a Jupiter-sized planet if the spectral type of the star would be similar to the Sun. This candidate was also selected for follow-up observation using the multi-object mode of the AAOmega cam (221). The resulting spectrum is shown in Figure 9.21 and a fitted template (red line in the figure) confirms a spectral type of G0V for the host star (220). The typical radius of a G0V star is about $R_{star} = 1.15\ R_{Sun}$ (223). The obtained information on spectral type was used as an input for further models and calculations of planetary parameters. Using Equation (3.3), the determined radius $R_{star} = 1.15\ R_{Sun}$ and the detected transit depth (δ) of 3% the candidate would posses a radius of approximately $R_{planet} 0.182 \pm 0.007 R_{Sun}$ which is an equivalent of $1.81 \pm 0.07 R_{Jupiter}$.

In addition, the light curve was folded with a period 1.218520 days and binned into 200 bins. Then points which deviated from median value more than 3σ were removed and the median and the standard error was recalculated. The resulting folded light curve was then fitted with a transit fitting routine written by (217) and the fitted transit event can be seen in Figure 9.22 with obtained parameters summarized in Table 9.13. The results obtained from the model imply that the candidate orbits its host star in the distance of $a = 1.87$ stellar radii. The candidate would posses a radius of $R_{pl} = 0.157 \pm 0.002 R_{sun}$ which is equivalent to $1.7553 \pm 0.02 R_{Jupiter}$.

The radius resulting from the fit and the estimated radius are compatible within the error bars. None of the known planets have such a large size ($1.8 R_{Jupiter}$). This fact implies that the true nature of the system could be a brown dwarf. The brown dwarf scenario would be also interesting case because until now only one brown dwarf (CoRoT 3b) (27) has been confirmed with the transit method. Also in this case the photometric and spectroscopic follow-up observations are scheduled for the October-March 2009/2010 season.

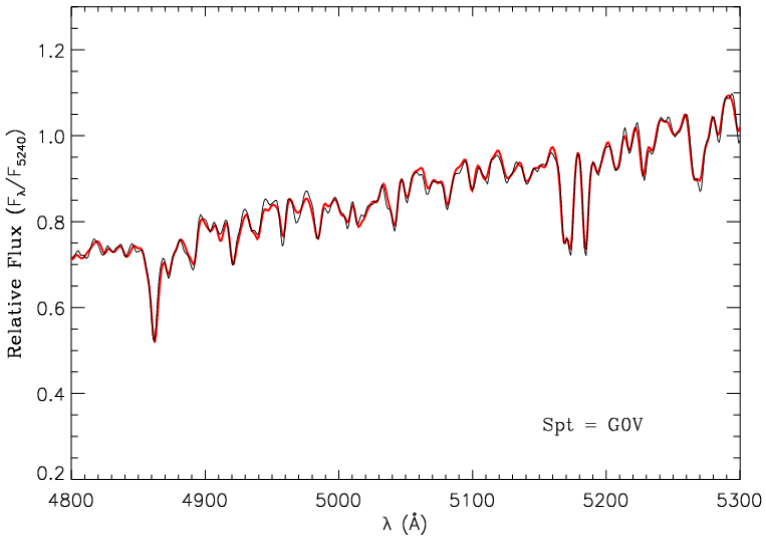

Figure 9.21: *Spectrum of the host star of candidate lra2a00487 confirming the G0V spectral type. Spectrum was taken with the AAOmega instrument installed at Anglo Australian Telescope, Australia. Image was taken from (220).*

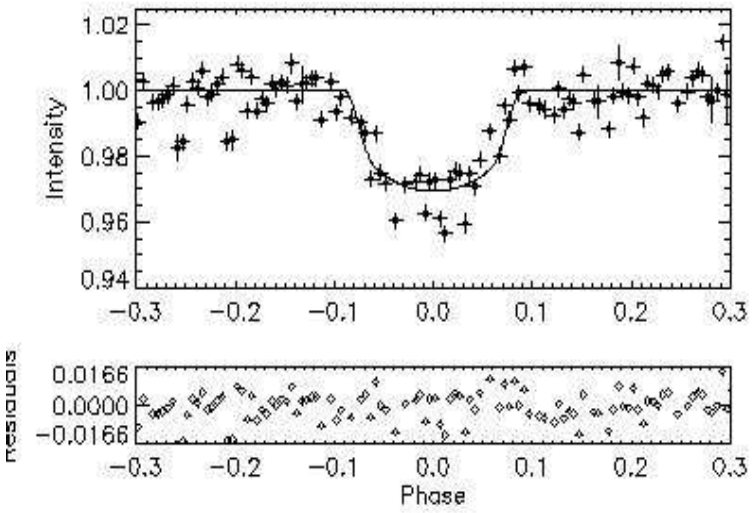

Figure 9.22: *Transit of a planetary candidate fitted with routine by Csizmadia (2009) (217).*

Table 9.13: *Parameters obtained from the fit of the folded light curve for candidate lra2a00487.*

parameter	
a $(in R_{star})$	2.159 ± 0.008
R_{planet}/R_{star}	0.157 ± 0.002
i (deg)	88.0 ± 0.2

9.4 Completeness of the BEST survey

In general, the problem for planet as well as variable stars detections is the intended duty cycle (see Chapter 7). Furthermore, observations without any filters can be one

of limitations in the photometric precision (see Chapter 5). However, the obtained data allow some simple statistical analysis of completeness. The BEST II LRa02 target field was selected as an example because of the high duty cycle coverage and high number of detected stars and the two high priority planetary candidates. Therefore, it is also interesting to use the same field in order to estimate the completeness of the BEST survey.

9.4.1 Comparison of BEST variables with the Hipparchos catalog

The detection rate on eclipsing binaries identified with BEST II was compared to a Hiparchos catalog of eclipsing binaries. A completeness estimate of the BEST II survey indicates how many periodic variable stars were really detected with BEST II and how many were missed relatively to Hipparchos catalog. Such a comparison also indicates the potential use of the BEST survey in more general terms. The detection process for the Hipparchos eclipsing binaries is described in detail in

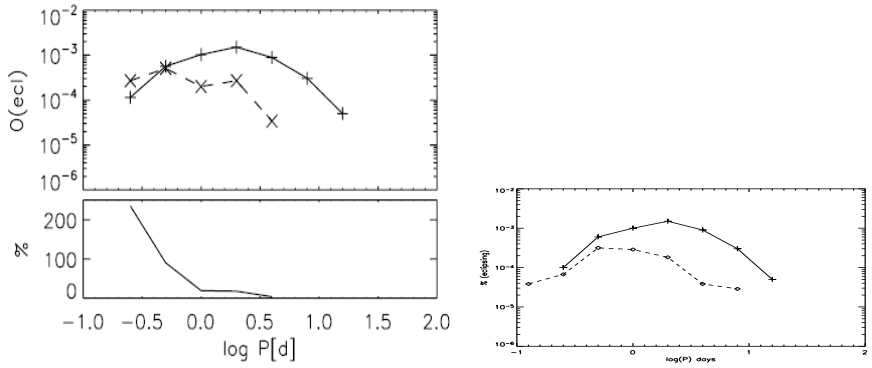

Figure 9.23: *A comparison of detected eclipsing binaries with BEST II (dashed line) with Hipparchos (solid line) data (right). The y abscissa represents the detection rate and the logarithmic x abscissa represents the orbital period of the eclipsing binary system. The same Figure is shown for BEST LRc01 data set in left plot.*

Söderhjelm & Dischler (2005) (226). A similar comparison was performed in Karoff et al. 2007 (171) on eclipsing binaries from BEST LRc01 data set. The Hipparchos sample consists of two subgroups with different absolute magnitude bins. These two subgroups correspond to different parallax bins (171). However, the parallax is in general unknown for stars observed with BEST II and also the absolute magnitude is not known. The values for Hipparchos eclipsing binaries were taken from Karoff et al. (2007) (171) and shown in left panel of Figure 9.23. In the figure y axis represents the number of detected eclipsing systems and the logarithmic x axis represents the orbital period of these systems. The solid line expresses the number of eclipsing systems against their period detected by Hipparchos according to (226). The dashed lines in left and right panels are presenting the same detection rates for BEST and BEST II surveys. The comparison was made for the stars with amplitudes < 0.4 mag from the Hipparchos data which can be easily found with ground based surveys.

The result shows how good the BEST II survey is compared to Hipparchos survey. BEST II detects most of eclipsing binaries with periods between $0.3 - 0.8$ days and

therefore it is comparable with Hipparchos in terms of detection rate.

The detection rate for BEST II with Hipparchos for period values $P > 0.9$ is worse due to duty cycle coverage also a slight decrease around periods of 1 day is due to conservative selection criteria for the periodic variable stars. Nevertheless, BEST II has a comparable detection rate as Hipparchos for this period interval. On the other hand, BEST II is worse compared to Hipparchos for orbital periods longer than 1 day. This constrain is given due to a duty cycle limitations for ground based surveys. However, the improvement can be seen for the same interval of periods when the detection rates for BEST and BEST II are compared. The BEST II survey operates with better duty cycle than BEST and therefore, it is possible to detect eclipsing systems with lower periods compared to BEST.

9.4.2 How many planets can be detected with BEST?

9.4.2.1 Probability of detection of transiting Jupiter sized planet with BEST II

The detection rate of the transiting planets with the photometric method can be expressed with (86):

$$N_{transit} = N_{lcs} \times f_{tar} \times f_d \times f_{geom} \times f_{HJ} \times f_{fc} \tag{9.6}$$

where, N_{lcs} represents the number of high precision photometric light curves, f_{tar} is the fraction of suitable target stars, f_d is the fraction of transit signals detectable from the ground, f_{geom} is the geometric probability (see Chapter 3) of a transit, f_{HJ} is the number of stars harboring hot Jupiter planets (see Chapter 3) and f_{fc} is the probability of detection of three transit events (see Chapter 7).

In this case the LRa02 target field will be investigated because of high achieved duty cycle. In addition, two high priority transit candidates were detected in this target field and thus direct comparison of the theoretical detection rate with the real detections can be made. In the following text a hot Jupiter planet with a typical radius $R = 1.1R_{Jupiter}$ will be assumed (6; 227) since the corresponding transit events would be easily detectable with a small ground based survey. The following values were estimated for the LRa02 target field:

N_{lcs} - This represents the number of high quality photometric light curves. The intensity decrease due to hot Jupiter is about 1.20% for a planet $R = 1.1R_{Jupiter}$ orbiting F5V type star and ranges up to 4.50% for K5V star (see Chapter 3). LRa02 contains mean number $N_{lcs} = 8000$ (both subfields - 1% rms), $N_{lcs} = 20000$ (3% rms) of light curves with *rms* below 4.5% (see histogram plots in Section 8.4.1).

f_{geom} - Typical geometric probability of a transit of hot Jupiter planet is $f_{geom} = 10\%$ (see Chapter 3)

f_{HJ} - The fraction of stars hosting hot Jupiter planets was estimated to be $f_{HJ} = 1\%$ (79)

f_{fc} - The probability to detect three transit events in LRa02 data set with an orbital period below 4 days is approximately 50% in LRa02 target field based on the obtained duty cycle (see Chapter 7).

The two remaining parameters f_{tar} and f_d need to be discussed in more detail as follows:

f_{tar} - the fraction of stars suitable for harboring a planet in terms of spectral type depends on the selection of the target field. The Galactic bulge and the Galactic plane contain many very bright objects which contaminate the FOV. More favorable directions for the target fields are near the Galactic plane. The CoRoT target fields were selected from these regions around the Galactic plane. The distribution of main sequence stars in the CoRoT's LRa02 found with Besançon model[4] is shown in Table 9.14. The total number of suitable stars from Besançon model is 1217 stars

Table 9.14: *Suitable stars for transit search in the LRa01 CoRoT's FOV with brighter than* 16 *mag found with Besançon model.*

field	total #	# 12 < R (mag) < 13	# 13 < R (mag) < 14	# 14 < R (mag) < 15	# 15 < R (mag) < 16
LRa01	1217	112	246	350	509

in range between 12 and 16 magnitude which is relevant for BEST II survey.

In the BEST II LRa02 (lra2a+lra2b) data 20744 stars in range of $12 < \mathrm{R} < 16$ mag[5] were detected. Therefore the fraction of suitable stars for harboring a planet can be estimated as $f_{tar} = \frac{\text{suitable}}{\text{total detected}} = \frac{1217}{20744} \approx 0.06$. However, an alternative source claims that the typical CoRoT anticenter field such as LRa02 possesses about 7000 suitable stars (Sun-like) (119). Here, the results for the detection rate for both numbers will be presented. This number would correspond to $f_{tar} = \frac{7000}{20744} = 0.34$.

f_d - unfortunately not every hot Jupiter like planet around a suitable star can be detected with a ground based survey. In fact only systems with intensity decrease during the transit higher than 1% can be observed from the ground. The complete range of transit depths includes the interval from 0.3% to 3% for Sun like host stars[6] (183). If we assume a planetary radius of $R_{planet} = 1.1 R_{Jupiter}$ to be representative for the transiting hot Jupiters (see (6)) then approximately 64% of the suitable stars will show an intensity decrease detectable with a ground based survey (transit depth > 1%). Figure 9.24 illustrates the distribution of proability of detection vs. fractional depth of a transit for described conditions.

Now the probability of a detection of a hot Jupiter type extrasolar planet in LRa02 BEST II target field can be determined from Equation (9.6) as:

$$N_{transit} = 8000(20000) \times 0.06 \times 0.64 \times 0.10 \times 0.01 \times 0.5 \approx 0.15(0.38) \qquad (9.7)$$

[4]http://model.obs-besancon.fr

[5]lra2a: 9351; lra2b: 11393

[6]stellar radii for magnitude limited surveys from 0.8 to 1.3 R_{Sun} - spectral types F2 to K8

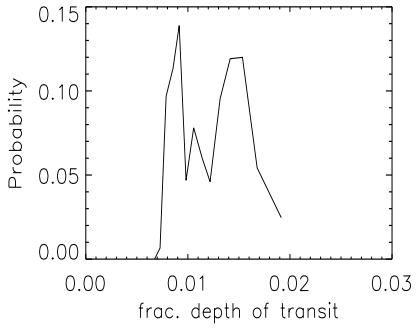

Figure 9.24: *A probability of detection of a hot Jupiter planet around suitable stars. The radius of the planet is fixed at* $1.1R_{Jupiter}$ *and the number of suitable stars was obtained from the Besançon model for the LRa02 target field (see Table 9.14). The stellar radii for F2 to K8 stars were taken from Table VIII in (223). For ground-based transit surveys the transit events with intensity decrease* $> 1\%$ *are relevant. In this case,* 64% *of suitable systems would show transit depth* $> 1\%$*.*

Values in brackets are the numbers corresponding to the number of light curves (N_{lc}) having the precision below 3%. Estimated values predict the probability of a planet detection to be nearly zero. It can be seen that main parameters influencing the number of detectable planets are the N_{lc} and the number of suitable stars. The number of high precision light curves is survey and target field specific. This number can vary due to observing conditions or due to target selection.

Even more important is the number of suitable Sun-like target stars. The M dwarf stars are not taken into account since they are less represented in the magnitude range of BEST II and begin to be significant only for the magnitudes > 16 mag. If the number of $f_{tar} = 0.34$ estimated from values of suitable stars presented by (119) than the Equation (9.8) woul have a form:

$$N_{transit} = 8000(20000) \times 0.34 \times 0.64 \times 0.10 \times 0.01 \times 0.5 \approx 0.88(2.20) \qquad (9.8)$$

Therefore, in a very optimistic case of acquisition of 20000 high precision photometric light curves and with the field containing 7000 suitable stars out of 20744 the maximum detection rate could be about 2 planets.

The estimated numbers of $0 - 2$ potential planet detections for LRa02 are clearly in a good agreement with the result from the real data. In total two planetary candidates were detected in the BEST II LRa02 data set. However, in order to confirm or reject the estimates presented here more observations with BEST II are needed.

9.4.2.2 General probability of detection of a transiting planet

Brown (2003) (228) estimated the detection rates for different types of detections (false positives, real planets, etc. see Chapter 3). Brown estimates probabilities of the occurrence of various cases from the statistical properties of stellar distribution (229) and from the content of a typical stellar field observed with a small

ground based survey. An original graph by (228) is presented in Figure 9.25 (left) and contains the probabilities for detection of Jupiter sized planets, diluted binary systems (MSD), undiluted binaries (MSU). In the same figure on right the distribution of eclipsing binaries in LRa02 BEST II data is shown. In addition, the dashed line represents the planet distribution from the original graph by (228).

Two BEST II planetary candidates are marked with crosses in the graph. It can be also seen that current two high level BEST II planetary candidates satisfy the detection rate distribution by Brown (2003) (228) because they are located in the planetary detection region.

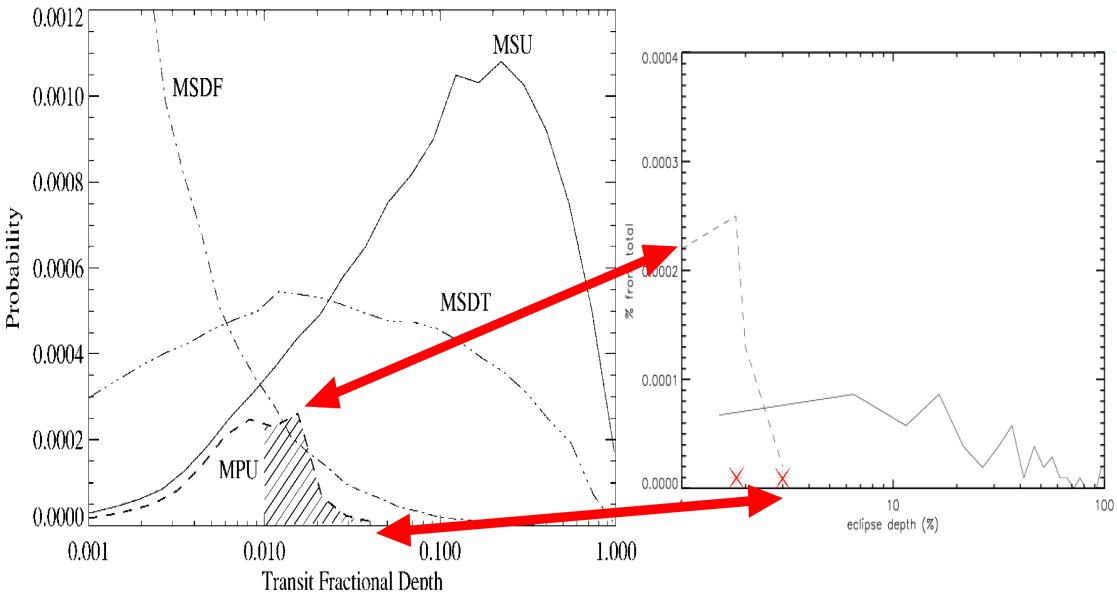

Figure 9.25: *The distribution of detection probabilities can be seen in the left figure. The right figure shows the same plot for the BEST II .Right image taken from (228).*

9.4.2.3 Summary on survey completeness and planetary detection rates

The comparison of the BEST II and Hipparchos data on eclipsing variable stars showed that BEST II is well comparable for the stars with period below 1 to Hipparchos. An additional comparison with BEST detection rate showed that BEST II has an improved sensibility for the periods longer than 1 day than BEST. This is due to improved duty cycle of the BEST II survey.

The probability of a transit detection of extrasolar planet with BEST II was determined with the help of Equation (9.6). The detection probability depends mainly on two factors, one is the number of high precision photometric light curves which is in case of BEST II above 8000. The second factor is the number of suitable stars which can host a Jupiter sized planet. From the adopted values for the BEST II LRa02 data set the minimum probability of the detection was found to be 0.15 planets. Another estimate using the values for the number of suitable stars in the CoRoT target field published by (180) gives the probability value for the same field of detecting two planets. Therefore, the expected rate should be in range from 0 to 2 detected extrasolar planets in LRa02 target field with BEST II.

In reality, two high priority planetary candidates were detected in the LRa02 data set with BEST II during the campaign 2007/2008. The status of the candidates is still unresolved because further follow-up observations are needed. If the planetary nature of these candidates is confirmed then the obtained result is in agreement with the probability value obtained from Equation (9.6) with values based on (180).

In more general terms, considering all the uncertainties the statistical approach can still be useful for the selection of the target field and observing strategy. Especially, target fields rich on star and with high dwarf star content should be selected in order to obtain a higher yield in terms of planetary detections. Also observing of multiple targets should increase the detection rate.

Chapter 10

Summary

10.1 Conclusions

The aim of this thesis is to present and summarize the results from photometric observations with the Berlin Exoplanet Search Telescope (BEST) and Berlin Exoplanet Search Telescope II (BEST II). Both small aperture telescopes with wide field-of-view dedicated to stellar variability characterization in CoRoT target fields. The thesis work can be divided into two parts. In the first part the design installation, commissioning, operation and observations with BEST II telescope are described based on the experience obtained from the first BEST telescope. The work includes a design and test phase at DLR and an installation phase of the telescope BEST II in Chile where the telescope is located. In the second part of the thesis the analysis of photometric data with regard to extrasolar planets and variable stars was presented. The final results are presented in form of a catalog of periodic variable stars and planetary candidates detected with BEST and BEST II.

The experience gained from the remote mode operation of the BEST telescope located at OHP, France was used for the setup of the new BEST II survey which should work as a ground based support for the CoRoT space mission and as a transit survey. In addition, valuable data on CoRoT initial run and long run fields were acquired with BEST one year ahead of CoRoT observations.

The BEST II system

The new BEST II survey telescope is currently operated in an automatic mode. This means that a script is submitted from DLR Berlin and then the observations are performed automatically. The system also monitors the weather conditions and in case of a strong wind it can close autonomously. A high observational yield can be reached since no operators are needed. Currently, the system is fully operational and performs observations every night if the weather conditions permit.

The duty cycle of BEST II

Only about 50 nights per year are lost due to bad weather conditions. Therefore, also a duty cycle is approximately doubled in comparison to the BEST. In addition, the BEST II duty cycle compared to OGLE was found to be very similar for the first test campaign 2007/2008. The preliminary results of the ongoing campaigns indicate that it might be even slightly better compared to OGLE. A comparison of

the probabilities for detecting three transit events with BEST and BEST II, based on real duty cycles, showed that BEST II can detect transiting planets with orbital periods up to 4 days with a probability of 50%. BEST telescope can achieve same 50% detection probability only for planets with maximal orbital period of 1.5 days. The high duty cycle makes BEST II an excellent instrument for detecting transit events of extrasolar planets.

The BEST and BEST II data sets

An advantage of the BEST II site in comparison with the BEST site is the photometric quality of nights. The observational data sets acquired with BEST II showed that the number of detected stars with *RMS* below certain level is very stable over the whole campaign. This is not the case for the BEST site, where the counts of detected low *RMS* stars are very different for each night and usually less than 2000 stars with low *RMS* are detected. Furthermore, 56% of nights at BEST II site are with excellent observing conditions, when more than 3000 stars with *RMS* below 1% are detected from total number of 41 nights. In case of OHP only 40% out of 35 nights were with similar excellent conditions.

Precision of the measurement

The tests performed on the BEST II data set showed that the level of the correlated noise affecting the data is as low as $\sigma_r = 0.002-0.004$ mag. This result is comparable to any other small ground based planet survey.

The most important scientific topics discussed in this thesis include the detection of new periodic variable stars, contribution to the follow-up observations of the CoRoT planetary candidates and the results from the transit survey. These main scientific topics in the thesis are described in more detail as follows:

Stellar variability in CoRoT fields

This thesis presents a catalog of more than 900 new periodic variable stars detected with both BEST telescopes in the CoRoT target fields IRa01 (172), LRc01 (171), LRa01 (173), LRc02 (178) and LRa02 (179). In addition, 31 already known periodic variable stars are found in BEST data sets and the collected data can extend the available time baseline of observation of these stars.

Contribution to follow-up observations of the CoRoT candidates and planets

An important justification of the BEST project has been proven by the contribution to the follow-up observations of the CoRoT's planetary candidates.

The detection of the CoRoT's planets CoRoT 1b and CoRoT 2b in BEST data archive (137) has showed the ability of small ground based telescopes to refine the ephemerids in the early phase of CoRoT's detection and confirm the observation of transit events of Jupiter-sized planets. In addition, an extended time baseline of the data collected for CoRoT 2b allowed more detailed investigation of the potential transit timing variation. The described results make use of BEST observations which were taken about two years before CoRoT data.

BEST II transit candidates

In the last part of the thesis, four transiting planetary candidates obtained from the analysis of LRa02 data collected with BEST between November and March 2007/2008 are introduced. The selection process of candidates for follow-up observations and modeling is described and two candidates remain as high priority cases. The results from the spectroscopic follow-up observations and the numerical modeling for these two high priority candidates are included. The estimated sizes of the two planetary candidates are $R_{planet1} = 1.38 R_{Jupiter}$ and $R_{planet2} = 1.80 R_{Jupiter}$. The first smaller candidate fits well into the class of hot Jupiter-like planets whereas the second candidate could be a very interesting brown dwarf. This work is a motivation for more extensive follow-up observations of these two candidates scheduled for the upcoming season 2009/2010.

Detection rates of BEST II survey

The ideal and the real detection rates, limited by a real duty cycle, of BEST II survey are compared with Hipparchos catalog for variable stars and with the similar test on BEST data made by Karoff et al. (2007) (171). The results show that BEST and BEST II have comparable detection rates with Hipparchos for the orbital periods < 1 day. In addition, BEST II has an improved detection rate also for longer periods in comparison to BEST. This is due to an improved duty cycle.

Theoretical probability of the planetary detection of BEST II survey is compared with detected planetary candidates in the last section of the thesis confirming the assumed numbers of $0 - 2$ planetary detections. Also a consistency of the assumed detection rates by Brown (2003) (228) and BEST II detected planetary candidates was found.

This thesis is based on the 3 years and 4 months of work on a ground based survey dedicated to stellar variability characterization. The aim is to present the justification of these kind of projects based on the presented results and also on contributions to the CoRoT space mission.

10.2 Suggestions for the future work based on experience from BEST/BEST II

All the presented results show the capability of the systems like BEST/BEST II to be a ground based support of space mission like CoRoT. Since the precision of the photometry of CoRoT is much better then the millimagnitude precision obtained with BEST/BEST II ground based systems can not compete with space missions. Therefore, such projects have to be focused on scientific goals which complement the aims of space missions or extend the potential yield. Therefore, the following suggestions for the future programs based on an experience with BEST/BEST II will be presented:

- **Networks**
  Telescope network will provide a continuous duty cycle coverage in the ideal

case. The duty cycle of a space mission is about 90% (133), therefore at least three telescopes around the globe can already significantly improve the ground based duty cycle and make it more comparable with space missions. More detailed information on this topic was presented in (176) and in (168). In particular the BEST II telescope based on the result presented in this thesis could be used as a first step for such a project.

- **Long duty cycle**
  Since the space missions like CoRoT observe one selected field only for a limited period of time, ground based systems can significantly improve the time base of the observation. Theoretically, a ground based telescope can observe the same stellar field over years. If the field is selected carefully, an interval of $7-8$ months of observations per year may be reached (168). The alternation between more targets may improve also the detection rate. Obviously long term monitoring of one stellar field may provide the information about the planets with longer orbital periods. Furthermore, observations obtained over long time scales may also contribute to the characterization of the planetary systems searching for transit timing variations (137).

- **Follow up of planetary candidates**
  Ground based small telescopes are very useful tools for the follow up of planetary candidates detected by other methods. However, the range of planets which may be confirmed is limited to Jupiter-sized planets.

The science on this field is dynamically expanding and offers unique possibilities for the future projects in terms of detection and physical characterization of extrasolar planets. Ground based survey telescopes have their secure place in this intriguing scientific topic.

Appendix A

Appendix

A.1 BEST II ISIS configuration file

Table A.1: *Parameters used for the ISIS config file.*

Parameter	value
nstamps_x	10
nstamps_y	10
sub_x	2
sub_y	2
half_mesh_size	9
half_stamp_size	15
deg_bg	2
saturation	55000
pix_min	30
min_stamp_center	6000
ngauss	3
deg_gauss1	6
deg_gauss2	4
deg_gauss3	2
sigma_gauss1	0.7
sigma_gauss2	1.0
sigma_gauss3	1.2
deg_spatial	2

A.2 Catalog of CoRoT fields observed with BEST telescopes

The following catalog summarizes a general information on the observed CoRoT fields by BEST or BEST II. The fields presented are: IRa01, LRa01, LRc01, LRa02, LRc02. A section divided into two parts is dedicated to each field. The first part of each section contains information about the orientation of the field with respect to the CoRoT field, a plot with the statistic on the photometric quality of observing nights in terms of detected stars (see Chapter 8), an *RMS* plot.

The second part of each chapter contains of table with following header entries:

BEST IDs, corresponding 2MASS IDs, coordinates (J200.0), Period (days), Amplitude, Type (of variability), Note (if the star was previously known then its catalog name appears here).

In addition, figures with folded light curves for every found star from the observed fields are included. The catalog is based on BEST/BEST II observations performed between years 2005 - 2008 and newly found periodic variable stars were published separately in (171; 172; 173; 178; 179).

Target field IRa01

Target field parameters

IRa01: $\alpha = 06^h\ 46^m\ 24^s$ and $\delta = -01^\circ\ 54'\ 00"$

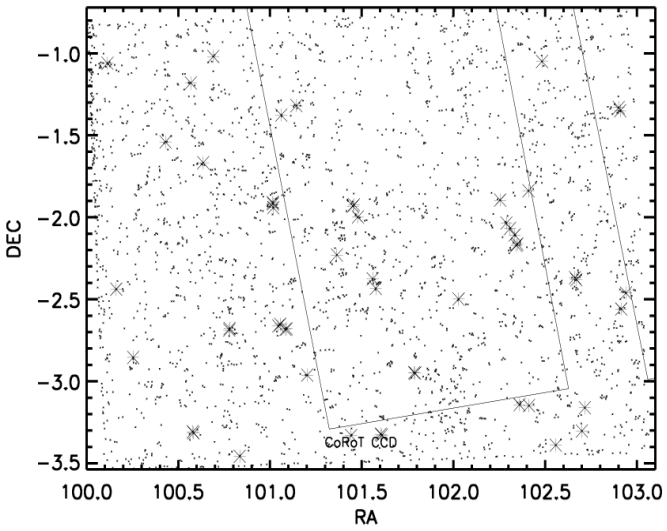

Figure A.1: *The orientation of BEST IRa01 FOV with respect to CoRoT FOV with dots representing detected stars. Image taken from (172).*

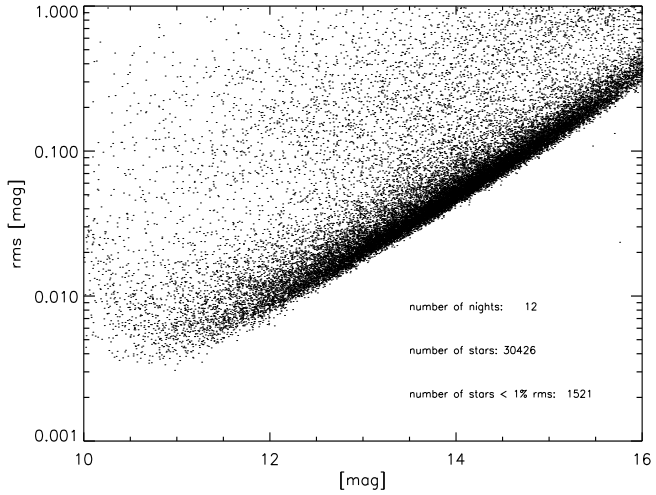

Figure A.2: *An RMS plot for the complete campaign of the BEST field IRa01.*

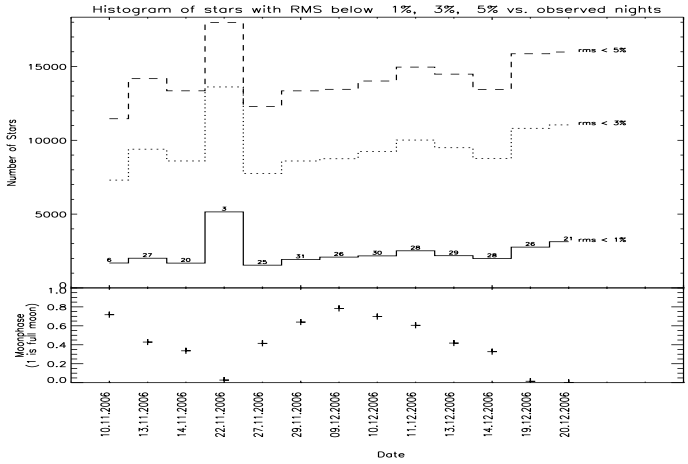

Figure A.3: *Photometric quality of nights for the BEST IRa01 field. Numbers above the histogram plot represent the total number of frames for the given night. The number of stars with precision of* 1%, 3% *and* 5% *is presented in plots.*

Periodic variable stars

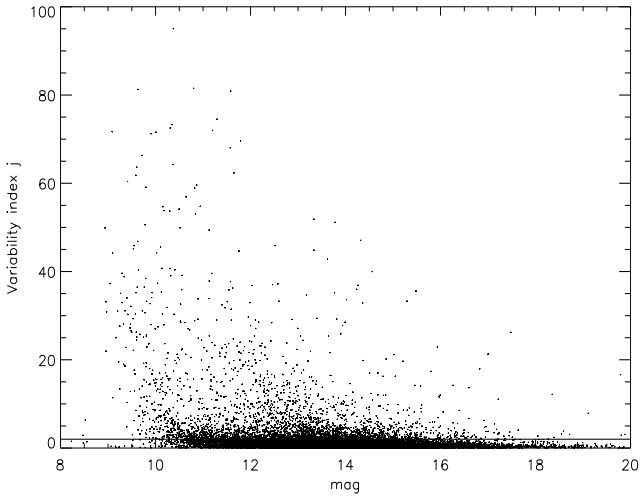

Figure A.4: *Variability index j against magnitude for stars in IRa01 target field.*

Table A.2: *Periodic variable stars detected. Magnitudes are based on calibration against USNO catalogue only. IDs marked with asterisk are within CoRoT field of view.*

BEST ID	α(J2000)	δ(J2000)	P(days)	Amp.(mag)	$\overline{m}$(mag)	Type
1101	$06^h43^m20^s$	-3° 27' 25.5"	1.265	13.10	0.20	ELL
1104	$06^h50^m14^s$	-3° 23' 21.0"	0.576	13.72	0.19	CEP
1180	$06^h50^m48^s$	-3° 18' 11.3"	1.183	12.08	0.07	ELL
1187	$06^h46^m26^s$	-3° 19' 42.7"	0.442	13.82	0.40	EB
1194	$06^h45^m46^s$	-3° 19' 51.7"	1.825	10.47	0.10	?
1197	$06^h46^m25^s$	-3° 19' 22.2"	0.569	13.34	0.21	CEP
1234	$06^h42^m20^s$	-3° 18' 54.3"	0.579	12.88	0.25	CEP
1239	$06^h42^m19^s$	-3° 18' 25.9"	1.377	12.81	0.27	CEP
1318	$06^h50^m52^s$	-3° 09' 39.9"	0.357	13.53	0.29	EW
1334	$06^h49^m39^s$	-3° 08' 54.6"	0.777	12.94	0.60	EB
1340	$06^h49^m26^s$	-3° 08' 34.8"	0.205	12.98	0.28	EW
1549*	$06^h47^m10^s$	-2° 57' 0.7"	1.105	12.85	0.30	EB
1554*	$06^h47^m09^s$	-2° 56' 52.0"	0.382	12.90	0.23	EW
1566	$06^h44^m49^s$	-2° 57' 43.4"	0.131	13.75	0.26	EW
1711	$06^h41^m01^s$	-2° 51' 17.2"	0.247	13.02	0.17	EW
1848	$06^h44^m20^s$	-2° 41' 0.2"	0.175	14.02	0.30	EW
1853	$06^h44^m22^s$	-2° 40' 47.7"	0.175	13.72	0.20	EW
1858	$06^h43^m07^s$	-2° 41' 13.2"	0.638	12.10	0.30	EA
1865	$06^h43^m07^s$	-2° 40' 40.0"	3.534	12.08	0.21	EB
1869	$06^h44^m10^s$	-2° 39' 45.6"	0.415	12.69	0.18	EW
1881	$06^h44^m13^s$	-2° 39' 11.4"	0.208	13.38	0.32	EW
1898	$06^h51^m39^s$	-2° 33' 33.6"	0.958	11.07	0.07	?
1990*	$06^h48^m07^s$	-2° 29' 55.0"	0.233	11.94	0.06	EA
1993*	$06^h51^m46^s$	-2° 27' 43.9"	2.709	11.35	0.15	ELL
2083*	$06^h46^m18^s$	-2° 26' 2.4"	0.284	11.68	0.04	DSCT
2091*	$06^h50^m41^s$	-2° 22' 51.8"	0.169	12.40	0.07	DSCT
2109	$06^h50^m39^s$	-2° 22' 6.7"	0.256	10.66	0.60	EW
2141	$06^h40^m39^s$	-2° 26' 18.9"	0.239	12.68	0.60	DSCT
2158	$06^h46^m14^s$	-2° 22' 30.8"	0.120	12.91	0.50	EW
2325*	$06^h45^m27^s$	-2° 13' 47.6"	0.255	13.59	0.26	EW
2349*	$06^h49^m22^s$	-2° 10' 15.6"	0.452	11.16	0.40	EB
2354*	$06^h49^m24^s$	-2° 09' 45.8"	0.827	10.31	0.40	EB
2390*	$06^h49^m21^s$	-2° 06' 48.5"	0.874	11.60	0.50	EB
2440	$06^h49^m14^s$	-2° 04' 04.4"	4.006	12.02	0.08	CEP
2484*	$06^h49^m09^s$	-2° 02' 06.4"	0.213	14.10	0.22	DSCT
2556*	$06^h45^m55^s$	-1° 59' 54.4"	0.193	14.26	0.30	DSCT
2628*	$06^h45^m49^s$	-1° 55' 57.0"	0.518	11.39	0.26	EB
2630*	$06^h49^m01^s$	-1° 53' 42.8"	0.374	11.93	0.28	EW
2632	$06^h44^m04^s$	-1° 56' 27.6"	2.251	12.43	0.05	CEP
2633	$06^h45^m50^s$	-1° 55' 24.2"	1.038	12.49	0.30?	?
2651	$06^h44^m04^s$	-1° 55' 05.0"	1.790	11.88	0.07	CEP
2661	$06^h44^m04^s$	-1° 54' 33.5"	2.246	12.05	0.09	CEP
2681*	$06^h49^m38^s$	-1° 50' 18.9"	0.572	14.98	0.80	EW
2927	$06^h42^m33^s$	-1° 40' 02.1"	0.238	10.91	0.05	EW
3041	$06^h41^m43^s$	-1° 32' 25.8"	0.376	14.47	0.60	EW
3159	$06^h51^m38^s$	-1° 21' 01.4"	0.648	12.69	0.14	CEP
3175*	$06^h51^m36^s$	-1° 19' 51.1"	6.489	13.89	0.65	CEP
3203*	$06^h44^m15^s$	-1° 22' 34.7"	1.268	12.15	0.15	EA
3252*	$06^h44^m35^s$	-1° 19' 08.7"	0.415	13.00	0.24	EA
3380	$06^h42^m16^s$	-1° 10' 50.9"	0.425	13.18	0.25	EW
3418	$06^h49^m56^s$	-1° 02' 59.3"	0.208	13.74	0.25	EW
3512	$06^h40^m27^s$	-1° 03' 38.3"	0.297	13.35	0.50	DSCT
3531	$06^h42^m46^s$	-1° 01' 09.7"	0.532	11.31	0.04	EB
3724*	$06^h45^m39^s$	-0° 47' 33.8"	0.122	13.03	0.03	EW

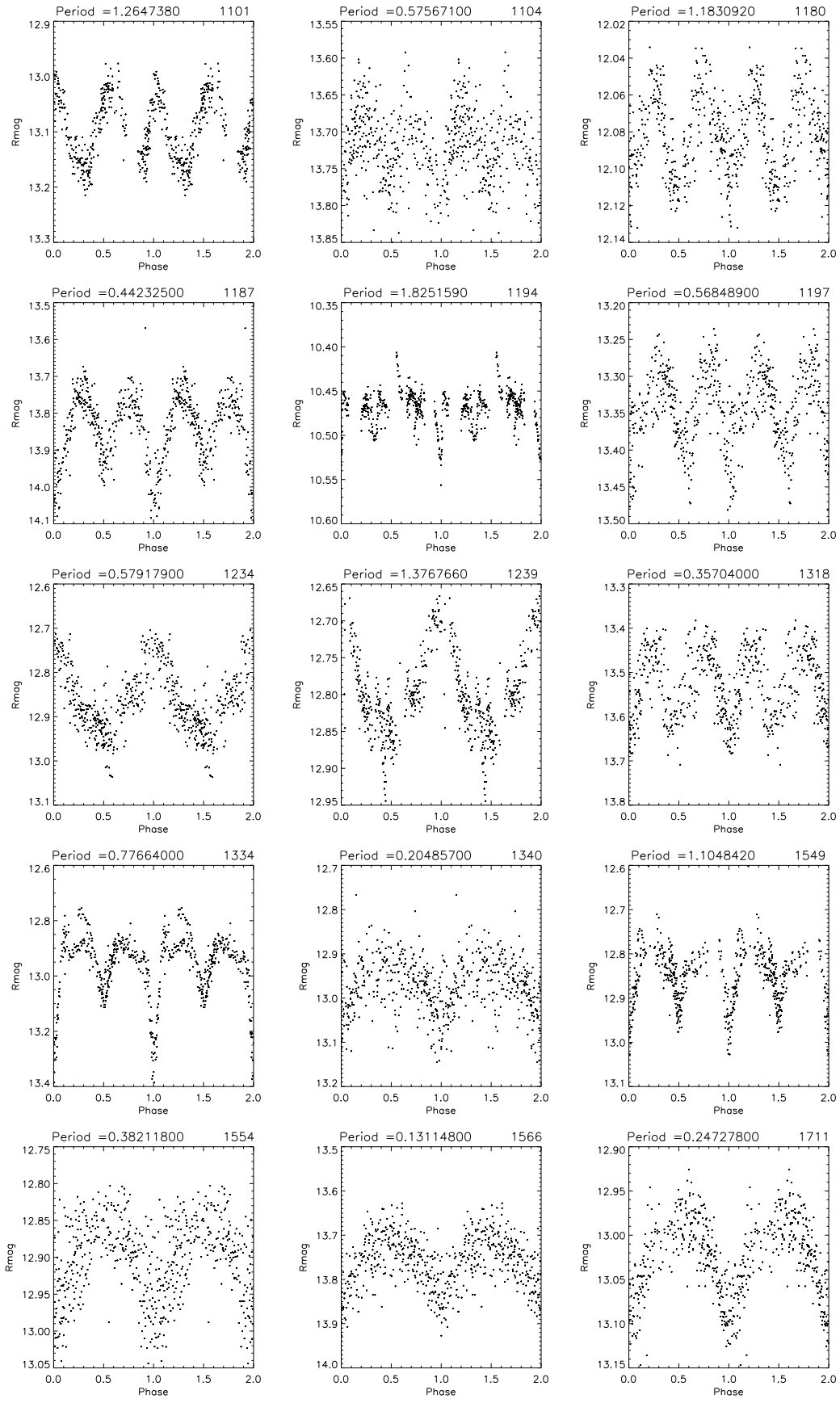
Period =1.2647380 1101
Period =0.57567100 1104
Period =1.1830920 1180
Period =0.44232500 1187
Period =1.8251590 1194
Period =0.56848900 1197
Period =0.57917900 1234
Period =1.3767660 1239
Period =0.35704000 1318
Period =0.77664000 1334
Period =0.20485700 1340
Period =1.1048420 1549
Period =0.38211800 1554
Period =0.13114800 1566
Period =0.24727800 1711
Rmag
Phase

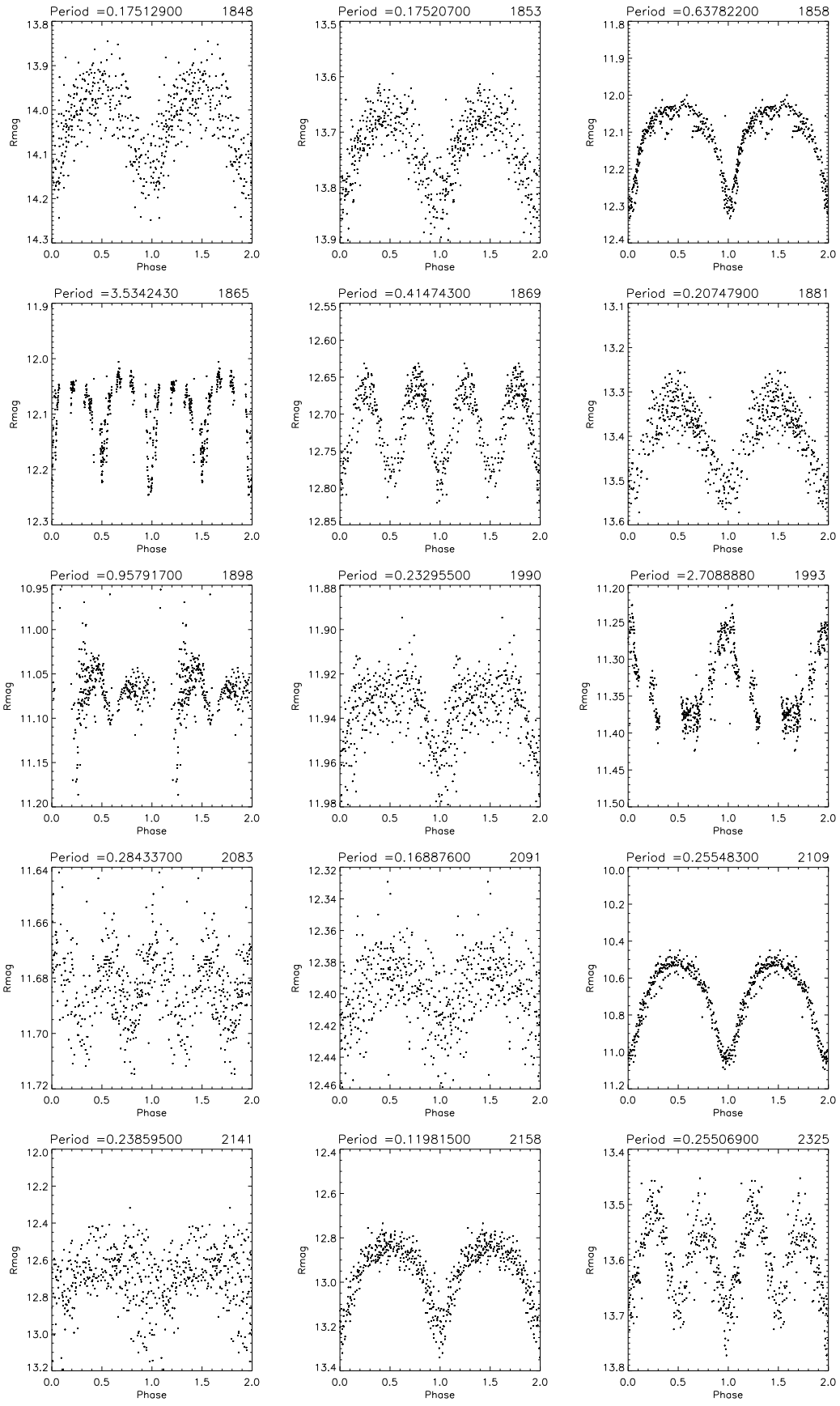
Period =0.17512900 1848
Period =0.17520700 1853
Period =0.63782200 1858
Period =3.5342430 1865
Period =0.41474300 1869
Period =0.20747900 1881
Period =0.95791700 1898
Period =0.23295500 1990
Period =2.7088880 1993
Period =0.28433700 2083
Period =0.16887600 2091
Period =0.25548300 2109
Period =0.23859500 2141
Period =0.11981500 2158
Period =0.25506900 2325
Rmag
Phase

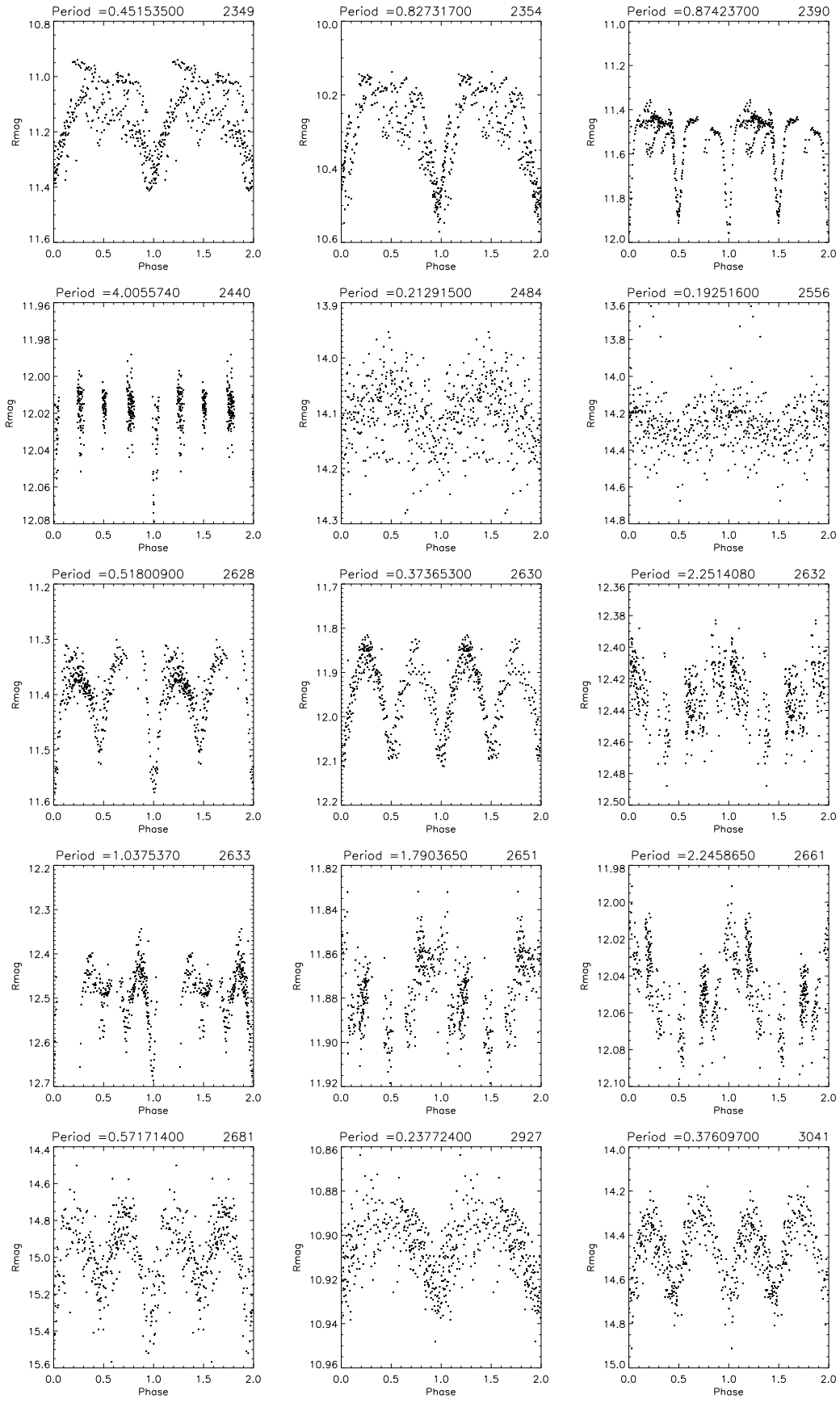
Period =0.45153500 2349
Period =0.82731700 2354
Period =0.87423700 2390
Period =4.0055740 2440
Period =0.21291500 2484
Period =0.19251600 2556
Period =0.51800900 2628
Period =0.37365300 2630
Period =2.2514080 2632
Period =1.0375370 2633
Period =1.7903650 2651
Period =2.2458650 2661
Period =0.57171400 2681
Period =0.23772400 2927
Period =0.37609700 3041
Rmag
Phase

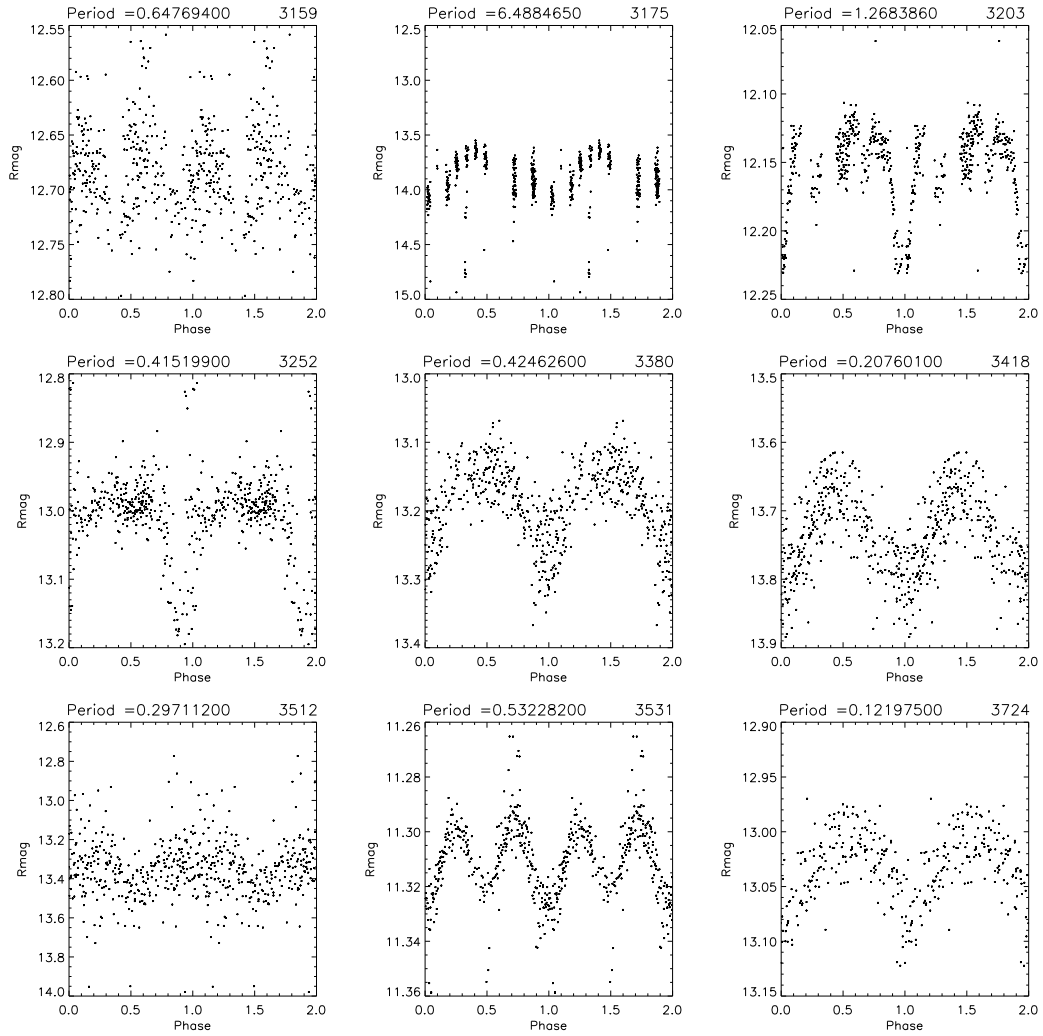

Figure A.5: *Phased lightcurves of periodic variables. The BEST-ID is shown in the upper right corner of each graph.*

Target field LRc01

Target field parameters

LRc01: $\alpha = 19^h\ 00^m\ 00^s$ and $\delta = +00°\ 01'\ 55"$

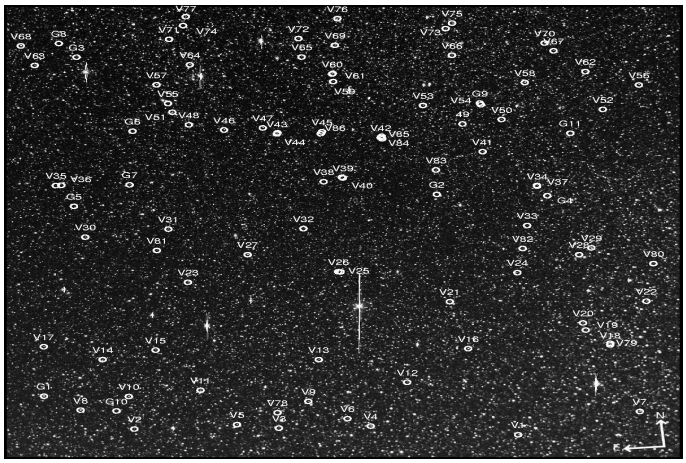

Figure A.6: *BEST LRc01 target field with detected periodic variable stars marked with circles. Image taken from (171).*

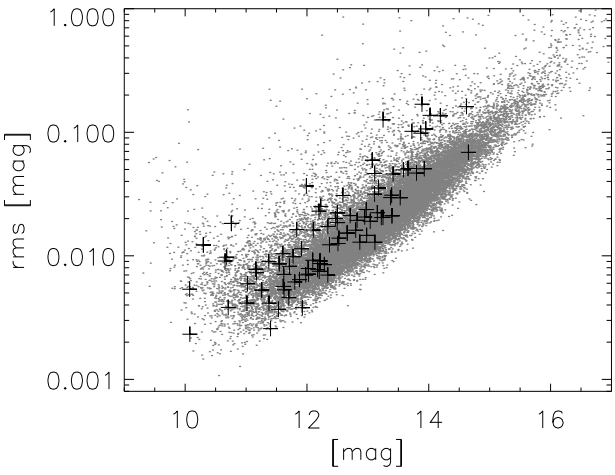

Figure A.7: *RMS plot for stars in LRc01 target field. Periodic variable stars are marked with diamonds. Image taken from (171).*

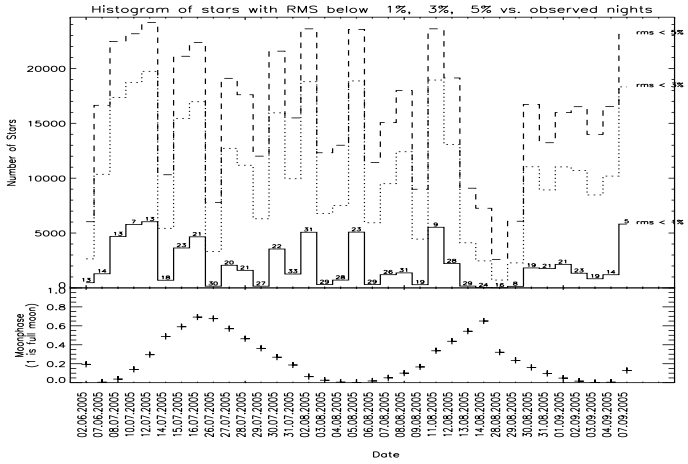

Figure A.8: *Photometric quality of nights for the BEST LRc01 field. Numbers above the histogram plot represent the total number of frames for the given night. The number of stars with precision of* 1%, 3% *and* 5% *is presented in plots.*

Periodic variable stars

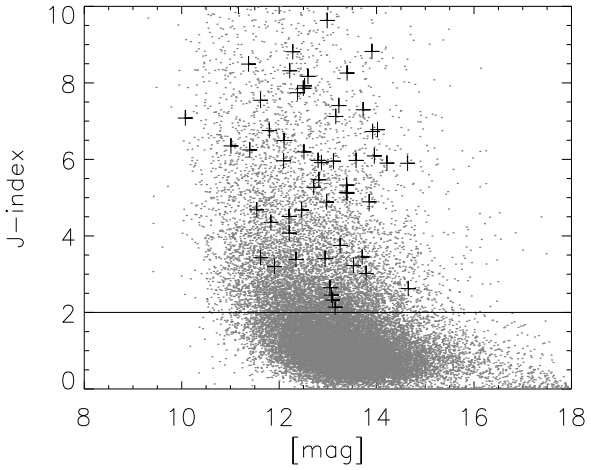

Figure A.9: *Variability index j against magnitude for stars in LRc01 target field. Periodic variable stars are marked with diamonds. Image taken from (171).*

Table A.3: *Periodic variable stars detected in LRa2b. Magnitudes are based on calibration against USNO catalogue only. Stars with asterisk are located in the CoRoT's exoplanetary field-of-view. Potential stellar crowding affecting the light curve of stars is marked with c.*

BEST ID	USNO ID	α(J2000)	δ(J2000)	Period (days)	Mean mag(mag)	Amplitude (mag)	Type
V1	U0825_15631497	19 23 50.63	-00 34 53.9	1.908	12.21	0.05	PPV
V2	U0825_16062830	19 30 46.56	-00 26 26.0	11.932	13.40	0.16	PPV
V3	U0825_15906821	19 28 09.70	-00 28 21.7	0.487	13.70	0.15	EB
V4	U0825_15803107	19 26 29.85	-00 28 59.0	2.113	11.54	0.04	EB
V5	U0825_15951762	19 28 54.77	-00 26 13.9	79.478	12.66	0.09	PPV
V6	U0825_15828621	19 26 54.41	-00 25 32.8	0.331	13.07	0.09	EB
V7	U0825_15479782	19 21 36.79	-00 27 18.2	1.967	11.17	0.06	PPV
V8	U0825_16122557	19 31 43.22	-00 17 50.6	67.898	10.30	0.12	PPV
V9	U0825_15871361	19 27 35.18	-00 17 49.5	48.124	12.50	0.07	PPV
V10	U0825_16065804	19 30 49.50	-00 12 59.4	6.555	11.26	0.02	PPV
V11	U0825_15987353	19 29 31.05	-00 11 33.6	96.016	10.76	0.06	PPV
V12	U0825_15757192	19 25 46.21	-00 11 33.5	90.120	12.80	0.15	PPV
V13	...	19 27 19.88	-00 00 52.6	59.590	11.87	0.15	PPV
V14	U0900_15449170	19 31 14.35	00 02 33.5	102.780	11.37	0.10	PPV
V15	U0900_15370565	19 30 15.97	00 05 37.6	2.273	12.51	0.03	EB
V16	U0900_14944293	19 24 36.78	00 01 16.5	32.344	11.01	0.29	PPV
V17	U0900_15533956	19 32 17.06	00 08 47.7	1.902	12.22	0.05	EB
V18	U0900_14773005	19 22 02.23	00 00 30.4	1.135	12.22	0.13	EB
V19	U0900_14801088	19 22 27.37	00 06 59.9	1.870	13.15	0.05	EB
V20	U0900_14803632	19 22 29.64	00 09 57.4	0.975	13.16	0.18	EB
V21	U0900_14963651	19 24 52.18	00 20 50.3	85.208	12.94	0.09	PPV
V22	...	19 21 18.72	00 17 50.8	93.828	12.51	0.12	PPV
V23	U0900_15317860	19 29 34.44	00 32 54.9	15.250	11.77	0.08	PPV
V24	U0900_14875071	19 23 36.07	00 31 39.4	0.678	11.91	0.04	EB
V25	U0900_15102073	19 26 47.78	00 34 47.2	78.260	12.52	0.07	PPV
V26	U0900_15105221	19 26 50.33	00 34 53.4	77.540	12.09	0.11	PPV
V27	U0900_15227975	19 28 26.95	00 43 19.9	116.850	10.64	0.12	PPV
V28	U0900_14801012	19 22 27.34	00 38 02.4	0.670	12.46	0.02	EB
V29	U0900_14785145	19 22 13.39	00 40 37.7	43.135	10.71	0.04	PPV
V30	U0900_15459522	19 31 21.44	00 53 04.3	55.864	11.70	0.07	PPV
V31	U0900_15338939	19 29 50.48	00 55 01.6	4.420	12.28	0.04	EB
V32	U0900_15147997	19 27 23.94	00 53 07.7	0.454	13.38	0.08	EB
V33	U0900_14857685	19 23 20.96	01 50 48.6	0.324	14.64	0.19	EB
V34	U0900_14842306	19 23 06.29	01 06 49.3	0.549	12.71	0.06	EB
V35	...	19 31 48.52	01 14 41.7	0.306	13.72	0.13	EB
V36	U0900_15489834	19 31 42.44	01 14 44.2	67.996	12.38	0.07	PPV
V37	U0900_14842441	19 23 06.42	01 07 06.8	1.174	12.82	0.09	EB
V38	U0900_15096269	19 26 42.91	01 11 48.7	0.452	12.20	0.07	EB
V39	U0900_15088039	19 26 36.27	01 13 15.5	0.942	13.53	0.10	PPV
V40	U0900_15245627	19 26 37.33	01 13 33.9	1.783	14.65	0.10	EB
V41	U0900_14903885	19 24 02.05	01 21 50.2	39.304	12.18	0.20	PPV
V42	U0900_15033451	19 25 51.33	01 29 12.5	0.431	14.02	0.18	EB
V43	U0900_15172322	19 27 43.57	01 32 23.8	63.682	11.62	0.03	PPV
V44	U0900_15110355	19 27 42.76	01 32 50.7	1.942	11.37	0.03	EB
V45	U0900_15171348	19 26 54.39	01 32 32.1	1.110	13.23	0.10	PPV
V46	U0900_15245627	19 28 40.54	01 34 50.4	1.966	11.53	0.06	EB
V47	U0900_15190277	19 27 58.26	01 35 04.1	1.439	11.61	0.07	EB
V48	U0900_15295393	19 29 18.23	01 37 29.9	55.496	12.99	0.10	PPV
V49	U0900_14925806	19 24 21.19	01 33 31.7	0.334	12.98	0.04	EB
V50	U0900_14877836	19 23 38.36	01 34 44.0	1.383	12.35	0.06	EB
V51	U0900_15318544	19 29 34.91	01 42 55.4	52.763	11.17	0.05	PPV
V52	U0900_14757657	19 21 47.43	01 37 15.3	0.414	13.91	0.18	EB
V53	U0900_14975844	19 25 02.35	01 41 43.0	0.355	11.83	0.04	EB
V54	...	19 23 59.33	01 41 30.1	1.110	13.85	0.18	PPV
V55	U0900_15323691	19 29 38.78	01 46 35.4	94.240	11.99	0.19	PPV
V56	U0900_14715405	19 21 05.86	01 46 41.9	89.746	11.80	0.06	PPV
V57	U0900_15337670	19 29 49.43	01 54 27.4	38.362	12.10	0.02	PPV
V58	U0900_14845601	19 23 09.52	01 49 30.9	47.360	10.07	0.10	PPV
V59	...	19 26 37.45	01 52 57.2	0.286	13.11	0.08	EB
V60	U0900_15090051	19 26 37.87	01 56 02.9	90.288	12.02	0.10	PPV
V61	U0900_15089049	19 26 37.11	01 56 17.0	2.045	12.02	0.06	EB
V62	U0900_14770477	19 22 02.70	01 53 01.5	74.072	12.34	0.11	PPV
V63	U0900_15513261	19 32 00.07	02 04 19.9	51.242	11.60	0.06	PPV
V64	U0900_15286457	19 29 11.40	02 02 07.5	75.340	11.92	0.06	PPV
V65	U0900_15129182	19 27 08.90	02 04 04.2	0.349	12.59	0.05	EB
V66	U0900_14931322	19 24 25.96	02 01 51.4	94.194	11.70	0.08	PPV
V67	U0900_14809956	19 22 35.19	02 02 04.5	1.362	12.87	0.09	EB
V68	U0900_15529595	19 32 13.30	02 12 33.4	73.852	10.69	0.08	PPV
V69	U0900_15083048	19 26 32.09	02 07 48.6	76.042	11.40	0.03	PPV
V70	U0900_14819436	19 22 44.20	02 05 24.1	93.784	11.02	0.10	PPV
V71	U0900_15313364	19 29 31.49	02 12 54.6	0.655	13.92	0.05	EB
V72	U0900_15131911	19 27 11.01	02 11 09.9	0.357	13.10	0.14	EB
V73	U0900_14936196	19 24 30.18	02 12 53.3	0.456	13.26	0.18	EB
V74	U0900_15290990	19 29 14.99	02 18 20.5	0.588	13.77	0.10	EB
V75	U0900_14927833	19 24 22.78	02 15 02.3	1.028	11.62	0.01	EB
V76	U0900_15076715	19 26 26.80	02 18 43.4	1.793	10.07	0.02	EB
V77	U0900_15286206	19 29 11.29	02 21 55.2	0.392	11.99	0.06	EB
V78	U0825_15906838	19 28 09.62	-00 21 58.2	0.495	14.21	0.4	EB
V79	U0900_14772878	19 22 02.07	00 01 07.5	0.723	13.39	0.2	EB
V80	U0900_14716806	19 21 07.48	00 33 09.9	1.188	13.25	0.07	PPV
V81	U0900_15357089	19 30 05.04	00 46 28.7	0.307	13.40	0.1	EB
V82	...	19 23 28.00	00 41 29.1	0.395	13.04	0.05	EB
V83	U0900_14966595	19 24 54.54	01 15 03.3	5.872	12.20	0.04	PPV
V84	U0900_15033451	19 25 49.73	01 28 43.2	0.549	13.95	0.12	EB
V85	...	19 25 50.12	01 29 43.5	0.354	13.95	0.2	EB
V86	U0900_15116292	19 26 55.97	01 31 47.0	2.504	13.11	0.6	PPV

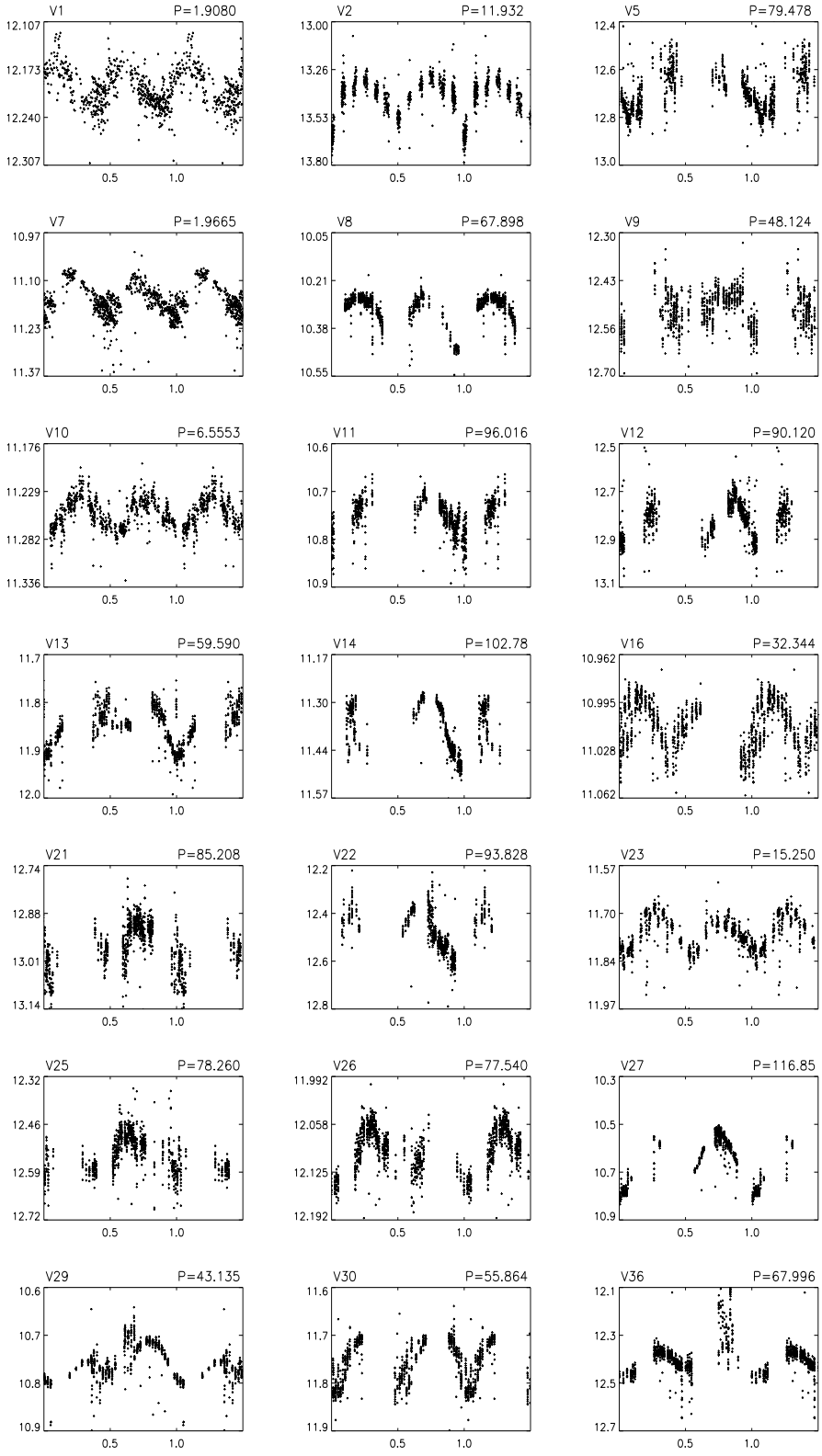
V1 P=1.9080
12.107
12.173
12.240
12.307
V2 P=11.932
13.00
13.26
13.53
13.80
V5 P=79.478
12.4
12.6
12.8
13.0
V7 P=1.9665
10.97
11.10
11.23
11.37
V8 P=67.898
10.05
10.21
10.38
10.55
V9 P=48.124
12.30
12.43
12.56
12.70
V10 P=6.5553
11.176
11.229
11.282
11.336
V11 P=96.016
10.6
10.7
10.8
10.9
V12 P=90.120
12.5
12.7
12.9
13.1
V13 P=59.590
11.7
11.8
11.9
12.0
V14 P=102.78
11.17
11.30
11.44
11.57
V16 P=32.344
10.962
10.995
11.028
11.062
V21 P=85.208
12.74
12.88
13.01
13.14
V22 P=93.828
12.2
12.4
12.6
12.8
V23 P=15.250
11.57
11.70
11.84
11.97
V25 P=78.260
12.32
12.46
12.59
12.72
V26 P=77.540
11.992
12.058
12.125
12.192
V27 P=116.85
10.3
10.5
10.7
10.9
V29 P=43.135
10.6
10.7
10.8
10.9
V30 P=55.864
11.6
11.7
11.8
11.9
V36 P=67.996
12.1
12.3
12.5
12.7
0.5
1.0

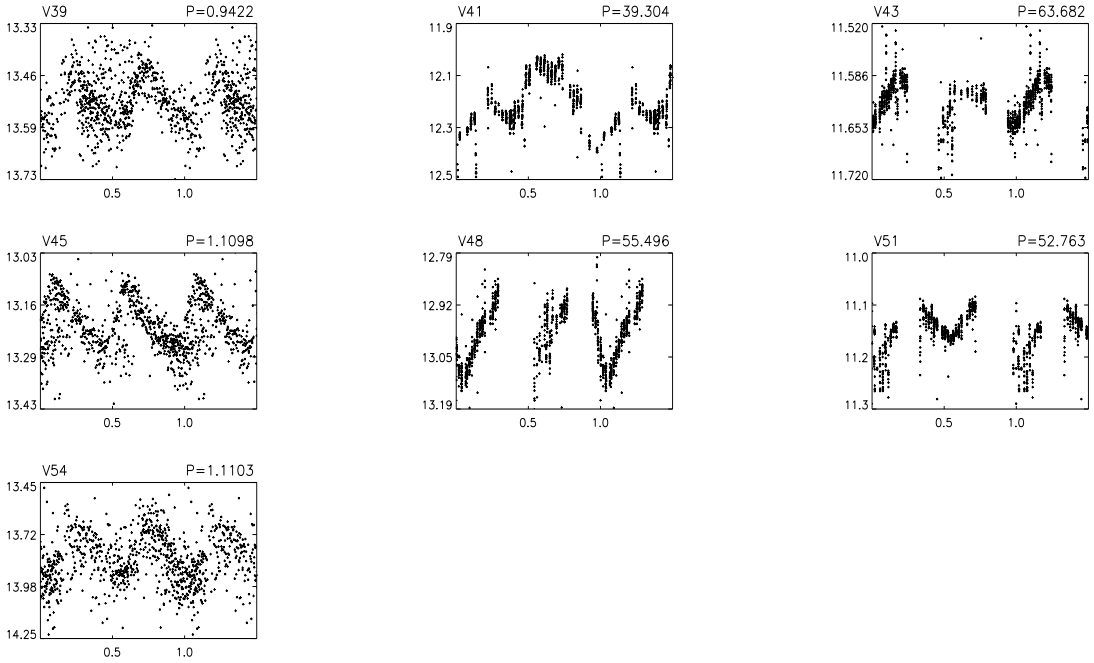

Figure A.9: *Light curves of 43 periodic pulsating stars in R. Magnitude is shown versus phase. The period is given in the upper right of each diagram is days.*

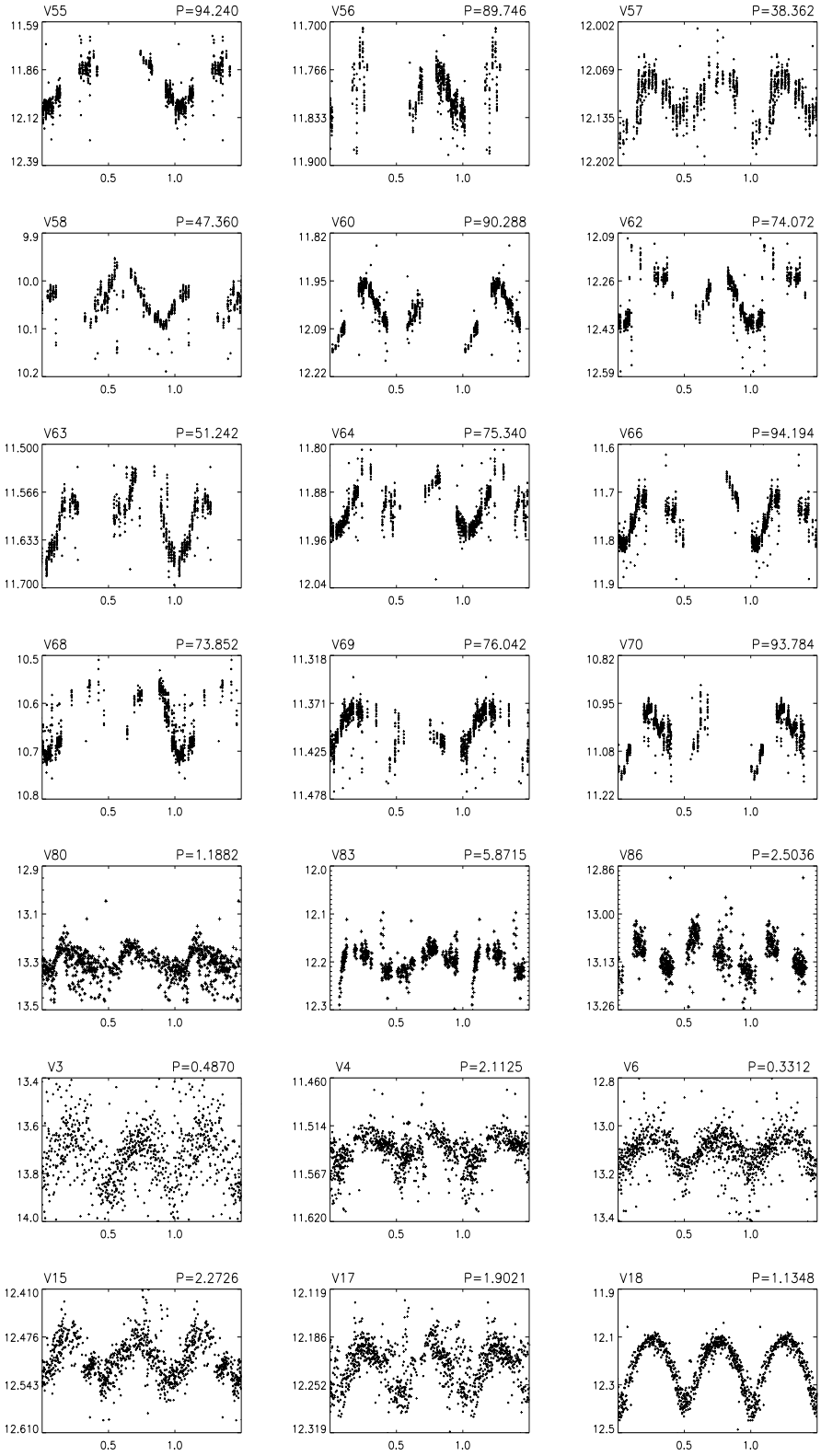

Figure A.9: *Continued*

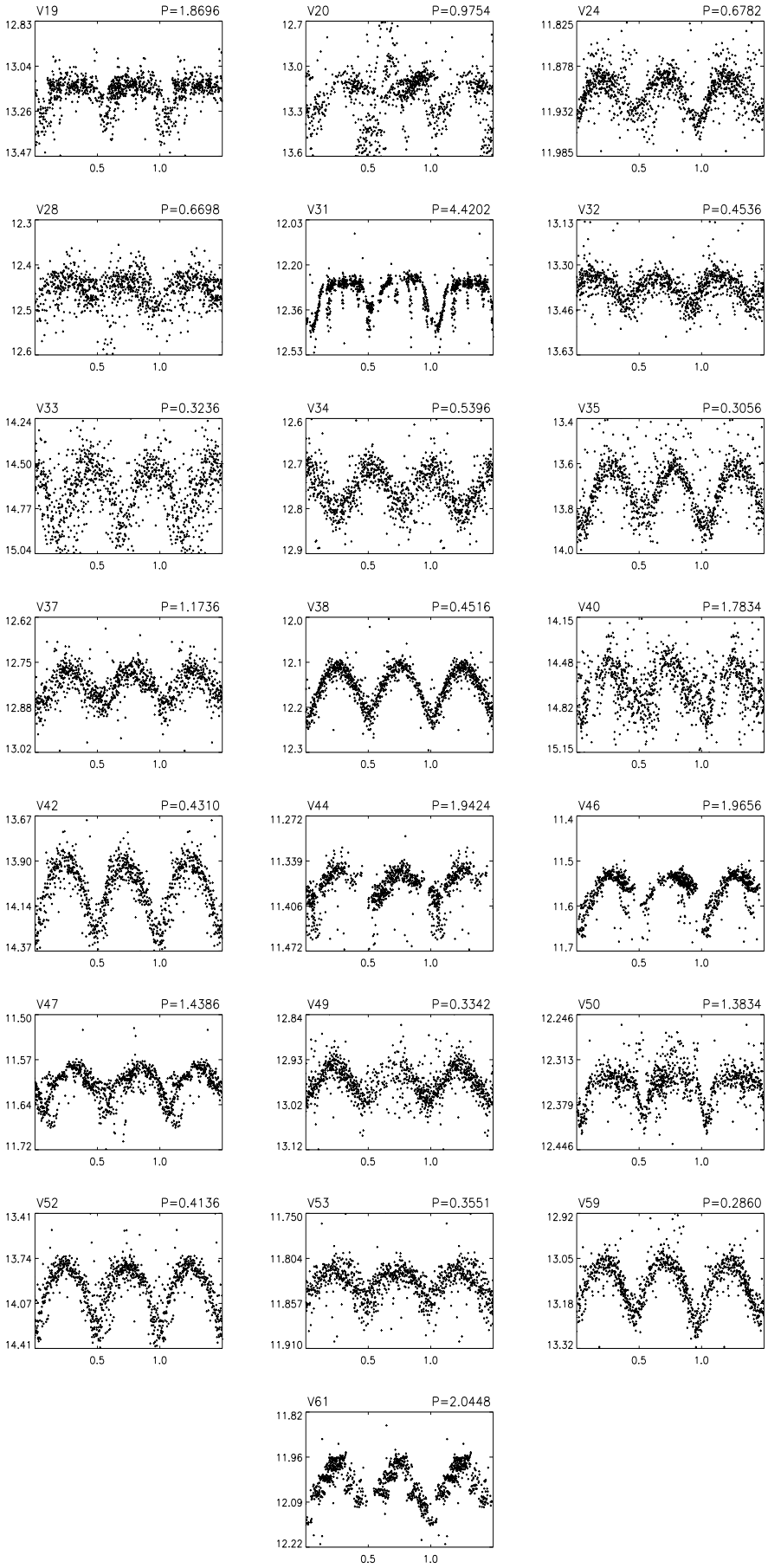

Figure A.10: *Light curves of 43 eclipsing binaries in R. See caption in Fig. A.9. Figures taken from (171)*

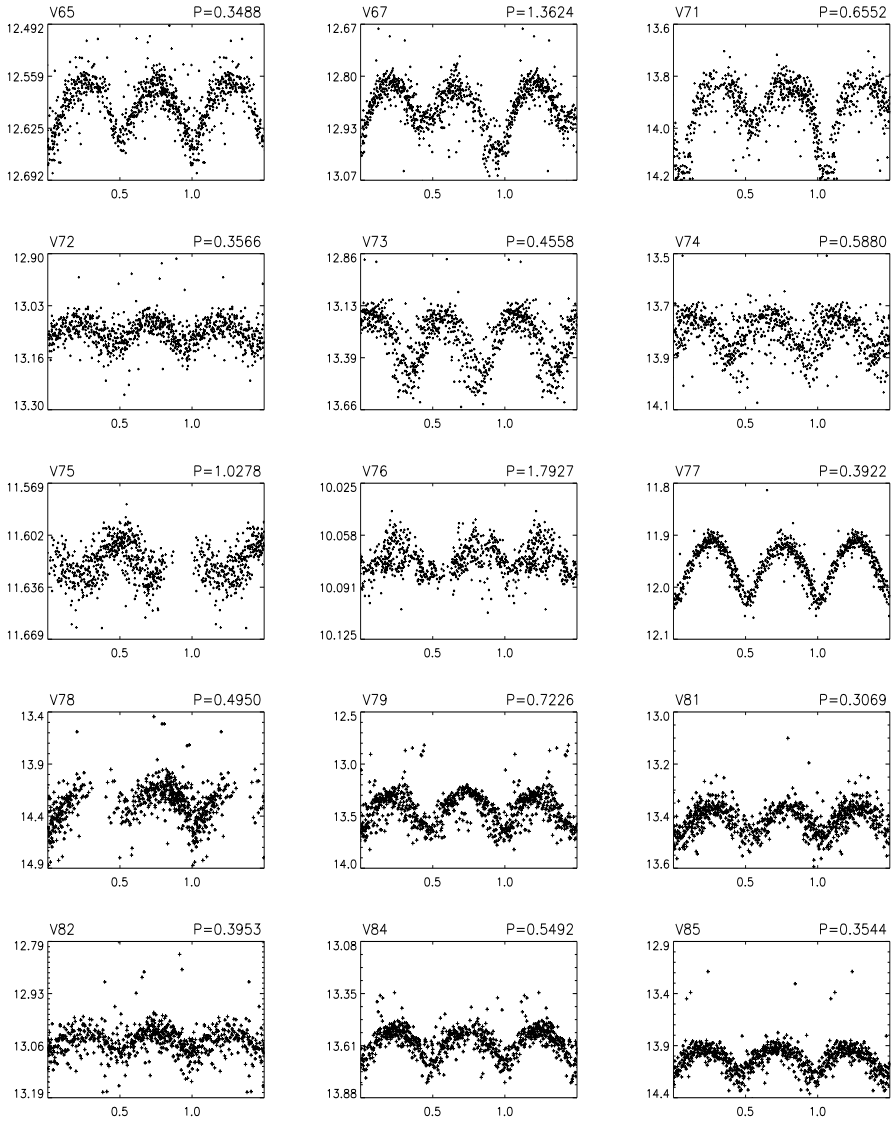

Figure A.10: *Continued*

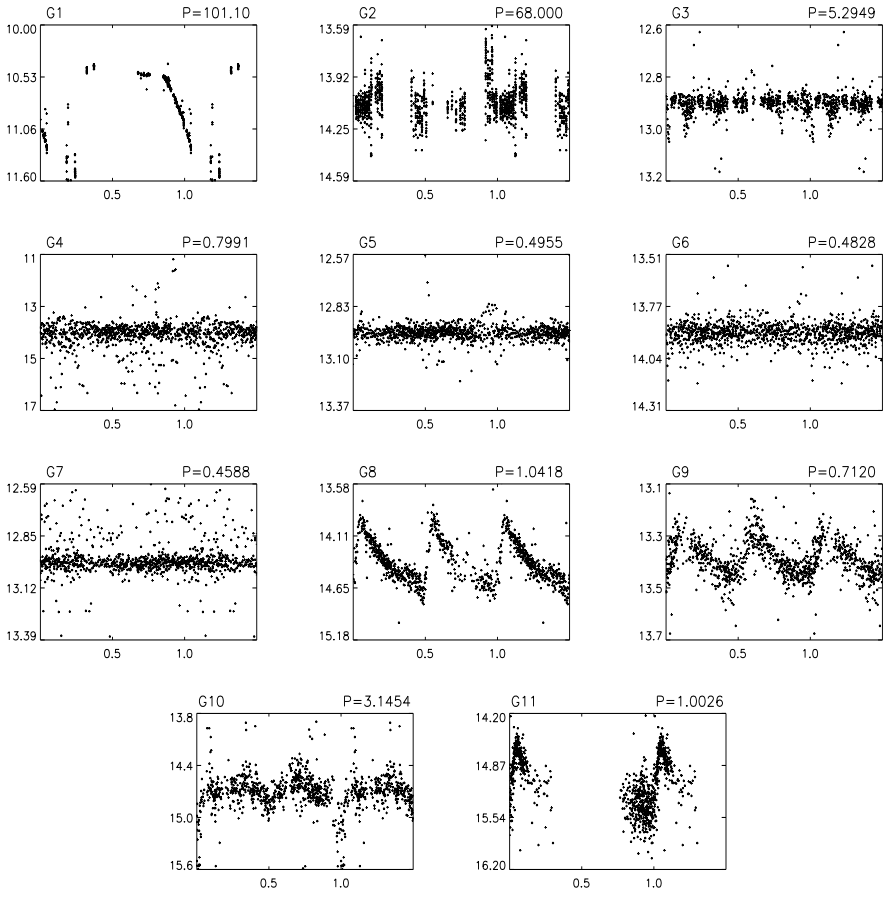

Figure A.11: *BEST light curves of variable stars known from the General Catalog of Variable Stars. See caption in Fig. A.9. Figures taken from (171).*

Target field LRa01

Target field parameters

LRa01: $\alpha = 06^h\ 46^m\ 24^s$ and $\delta = -01^\circ\ 54'\ 00"$

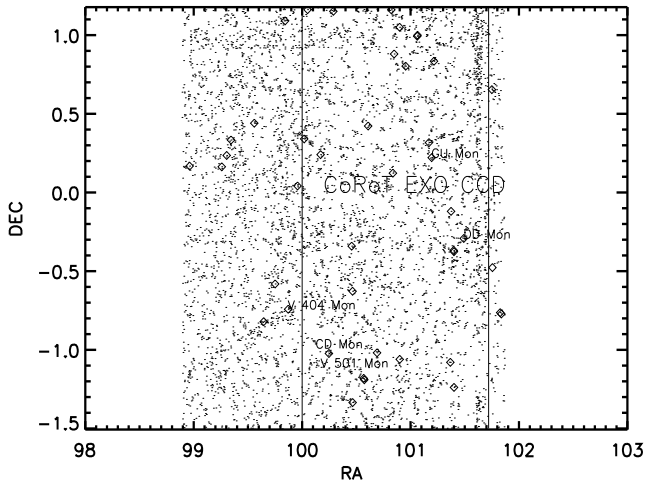

Figure A.12: *The orientation of BEST LRa01 FOV with respect to CoRoT FOV with dots representing detected stars.*

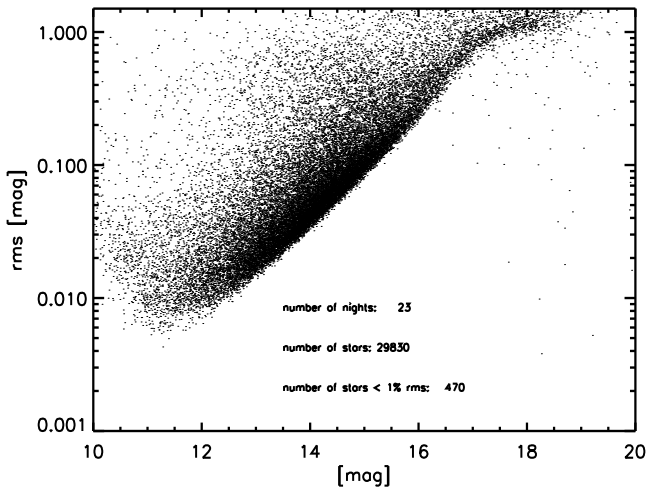

Figure A.13: *An RMS plot for stars detected in the BEST LRa01 field.*

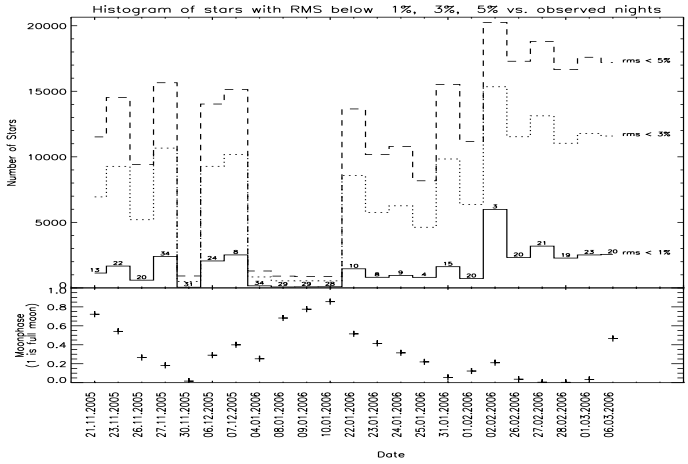

Figure A.14: *Photometric quality of nights for the BEST LRa01 field. Numbers above the histogram plot represent the total number of frames for the given night. The number of stars with precision of* 1%, 3% *and* 5% *is presented in plots.*

Periodic variable stars

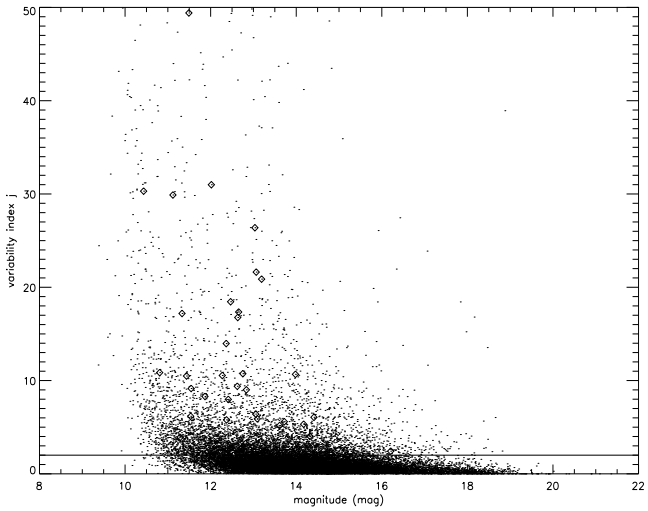

Figure A.15: *Variability index j against magnitude for stars in LRa01 target field. Detected periodic variable stars are marked with diamonds.*

Table A.4: *Periodic variable stars detected. Magnitudes are based on calibration against USNO catalogue only. IDs marked with asterisk are within CoRoT field of view.*

BEST ID	α (J2000)	δ (J2000)	Period (days)	Amplitude (mag)	Mean mag (mag)	Type
34*	6 40 12	1 9 43	0.865	12.815	0.170	CEP
47*	6 43 17	1 9 39	1.921	13.035	0.420	CEP
70*	6 41 9	1 9 5	0.837	13.250	0.200	CEP
211	6 39 22	1 5 28	0.429	10.434	0.080	CEP
326*	6 43 36	1 3 1	0.497	14.004	0.400	CEP
489*	6 44 15	0 59 58	0.543	13.090	0.090	EB
515*	6 44 15	0 59 35	0.213	13.053	0.160	DSCT
856*	6 43 24	0 52 48	0.183	14.151	0.240	DSCT
935*	6 44 52	0 50 4	1.923	11.543	0.080	ELL
995*	6 43 49	0 48 10	0.367	12.655	0.170	ELL
1358	6 47 0	0 39 14	1.095	12.413	0.100	ELL
1835	6 38 14	0 26 25	0.550	12.467	0.250	EW
1873*	6 42 26	0 25 21	0.275	11.491	0.200	EW
2044*	6 40 5	0 20 25	7.976	12.363	0.200	CEP
2057	6 37 23	0 20 0	0.485	14.418	0.500	CEP
2119*	6 44 41	0 19 2	0.289	13.065	0.700	CEP
2300*	6 40 41	0 14 26	0.423	11.290	0.120	CEP
2311	6 37 13	0 14 8	1.295	13.982	0.950	EB
2361*	6 44 47	0 13 18	0.897	11.821	0.550	GU Mon
2453	6 35 51	0 10 4	0.469	14.268	0.500	CEP
2462	6 37 2	0 9 48	0.193	12.272	0.170	DSCT
2570*	6 43 21	0 7 23	0.404	12.701	0.080	CEP
2751	6 39 50	0 2 30	2.624	11.118	0.200	CEP
3121*	6 45 30	-0 7 11	0.303	14.338	0.250	EW
3550*	6 45 58	-0 17 31	0.568	10.610	0.480	DD Mon
3693*	6 41 50	-0 20 27	0.960	11.331	0.180	CEP
3776*	6 45 36	-0 22 5	0.347	14.414	0.800	CEP
3796*	6 45 36	-0 22 33	1.142	14.173	0.550	EB
4008	6 47 1	-0 28 38	0.384	16.208	0.250	EW
4244	6 39 0	-0 34 53	0.359	13.612	0.270	CEP
4342*	6 41 52	-0 37 40	1.213	13.191	0.500	EA
4559	6 39 29	-0 44 31	2.447	12.378	0.400	V404 Mon
4622*	6 47 18	-0 45 48	0.296	12.622	0.170	EA
4640	6 47 21	-0 46 19	1.597	14.320	0.450	EB
4729	6 38 35	-0 49 14	0.529	11.534	0.400	EA
5118*	6 42 46	-1 1 8	0.533	11.436	0.150	ELL
5125*	6 40 59	-1 1 23	0.761	10.809	0.060	CEP
5197*	6 43 36	-1 3 37	0.555	11.868	0.080	CEP
5239*	6 45 28	-1 4 46	7.052	12.450	0.070	V501 Mon
5453*	6 42 16	-1 10 52	0.425	12.835	0.140	CEP
5472*	6 42 18	-1 11 24	0.425	13.722	0.250	CEP
5581*	6 45 36	-1 14 19	21.631	12.752	0.140	CEP
5765*	6 41 52	-1 20 05	2.798	11.800	0.200	CEP
25207*	6 40 30	-1 4 45	—	14.6369	—	CD Mon

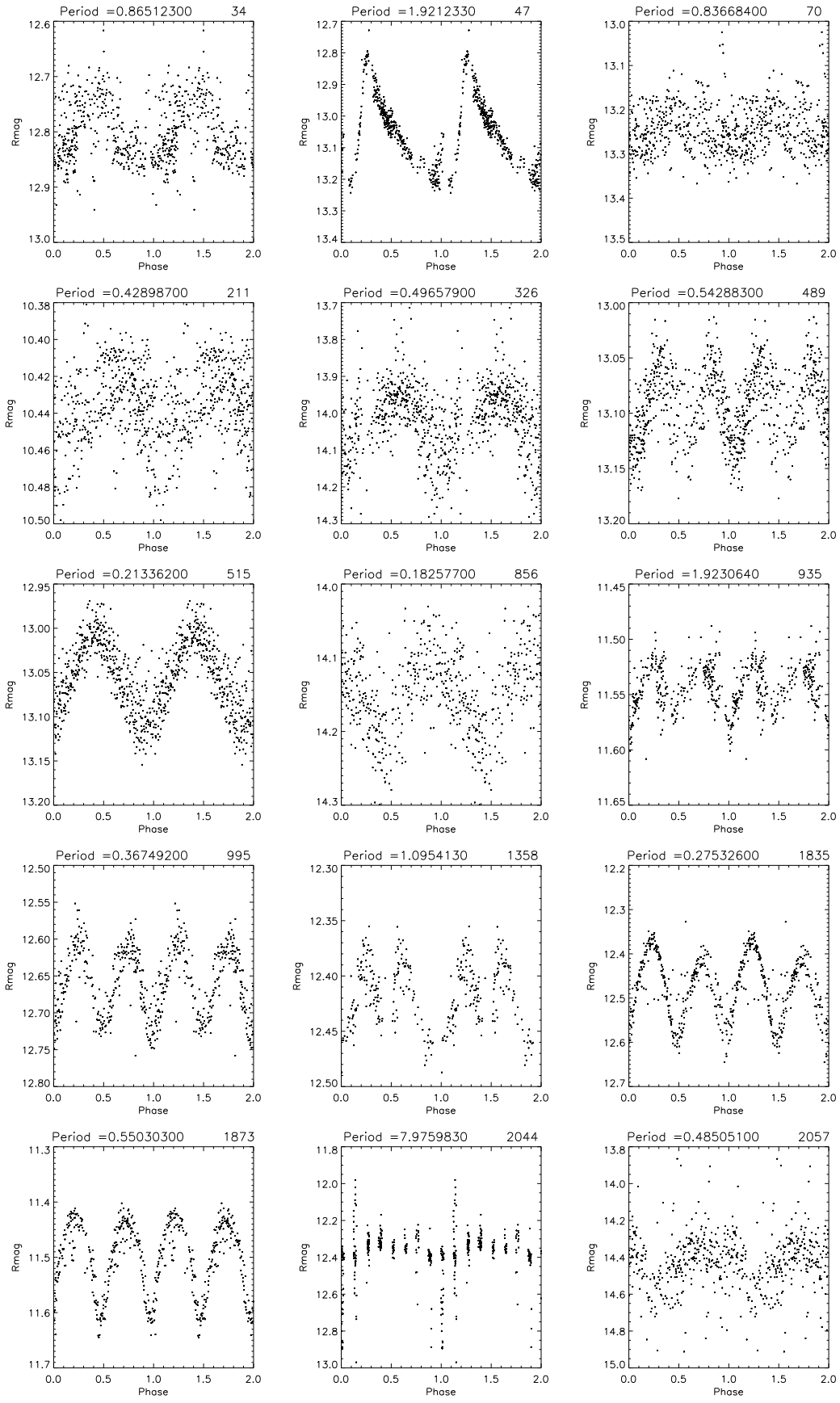
Period =0.86512300 34
Period =1.9212330 47
Period =0.83668400 70
Period =0.42898700 211
Period =0.49657900 326
Period =0.54288300 489
Period =0.21336200 515
Period =0.18257700 856
Period =1.9230640 935
Period =0.36749200 995
Period =1.0954130 1358
Period =0.27532600 1835
Period =0.55030300 1873
Period =7.9759830 2044
Period =0.48505100 2057
Rmag
Phase

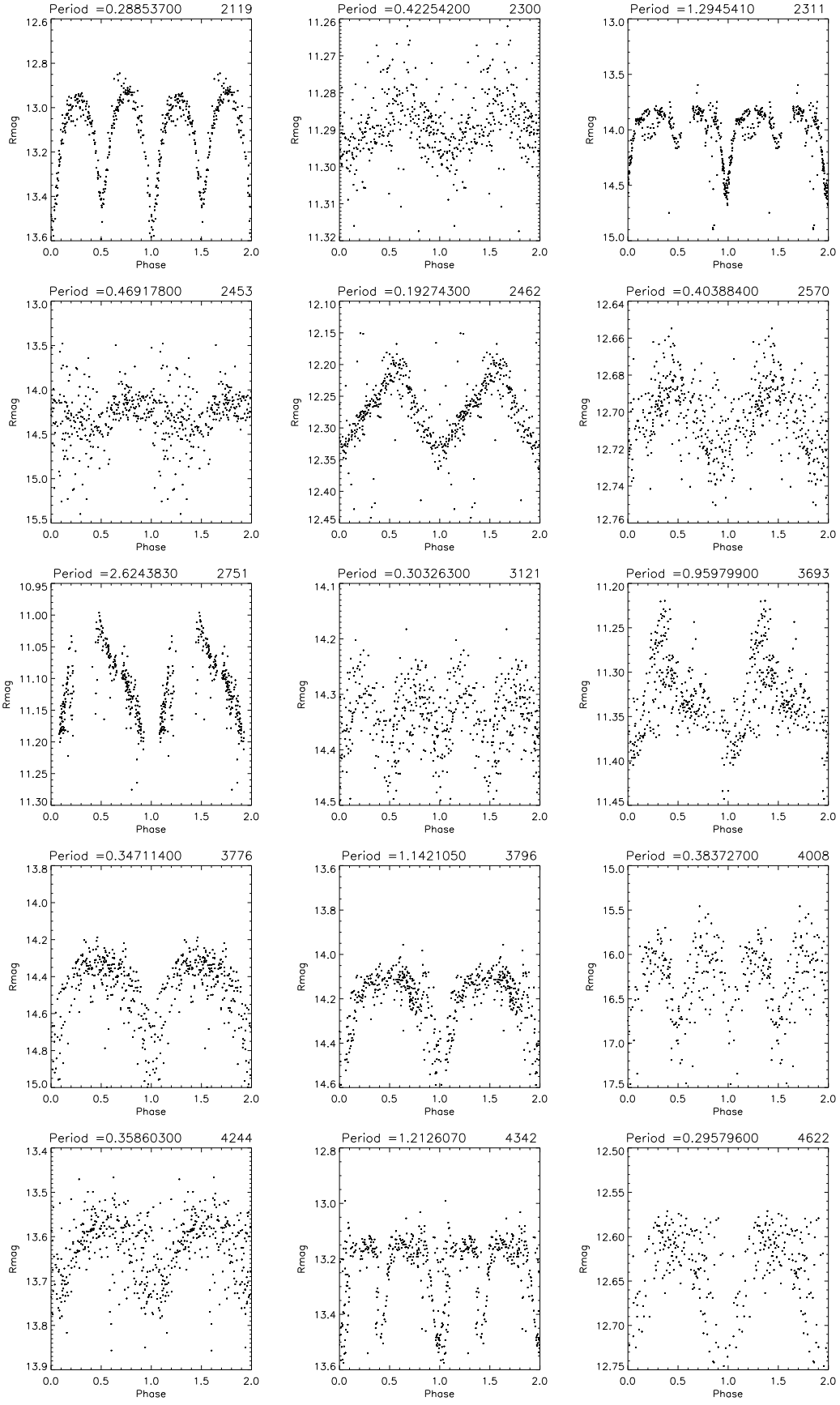
Period =0.28853700 2119
Period =0.42254200 2300
Period =1.2945410 2311
Period =0.46917800 2453
Period =0.19274300 2462
Period =0.40388400 2570
Period =2.6243830 2751
Period =0.30326300 3121
Period =0.95979900 3693
Period =0.34711400 3776
Period =1.1421050 3796
Period =0.38372700 4008
Period =0.35860300 4244
Period =1.2126070 4342
Period =0.29579600 4622
Rmag
Phase

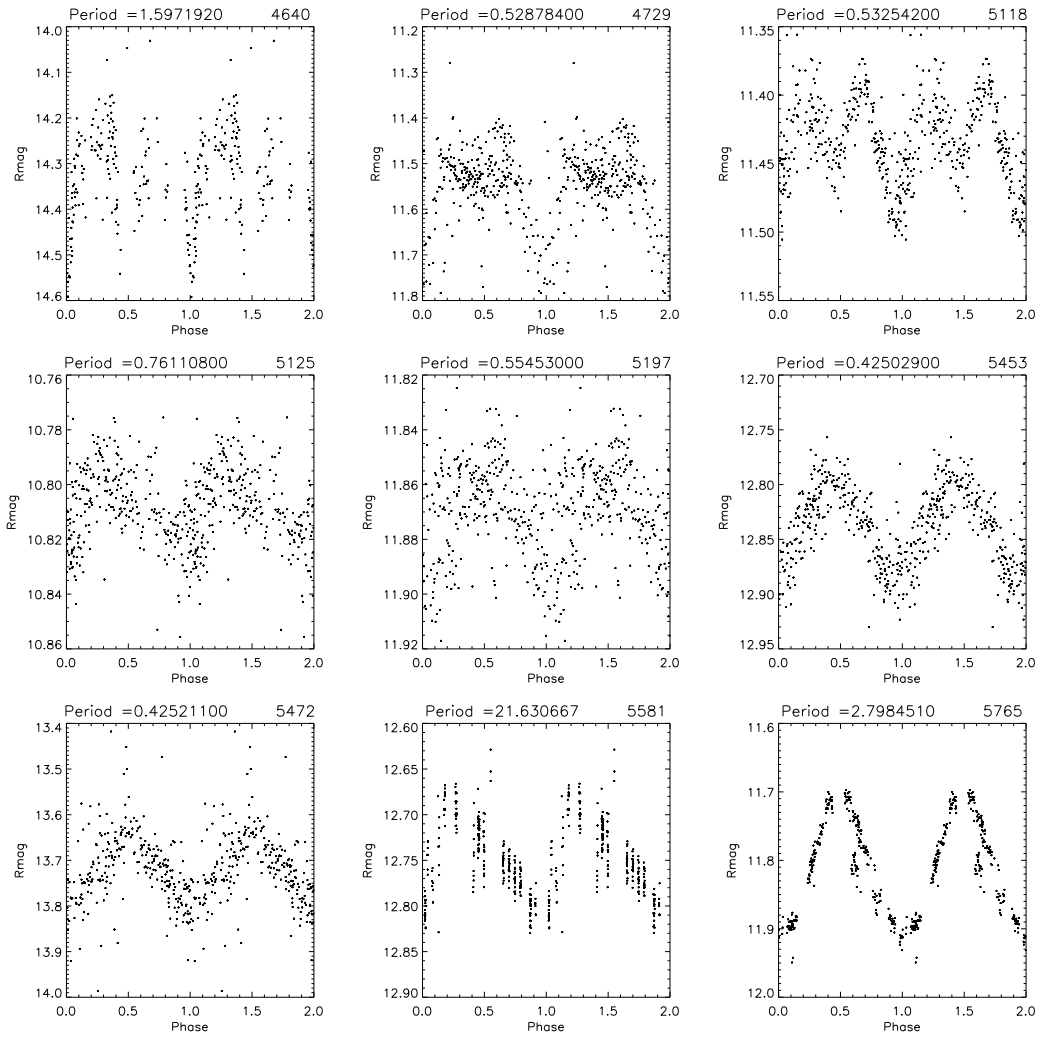

Figure A.16: *Variable stars newly identified in the* 2006 *campaign in the LRa1 field.*

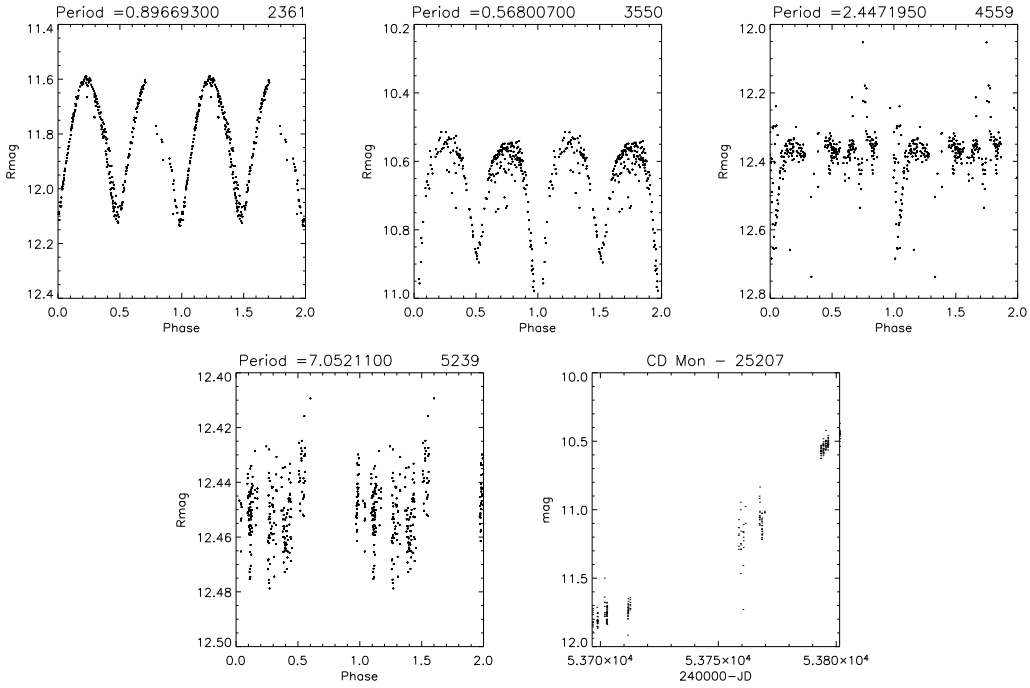

Figure A.17: *The folded lightcurves of stars GU Mon (2361), DD Mon (3550), V 404 Mon (4559), V 501 Mon (5239) and a lightcurve of Mira-type star CD Mon (25207) are shown.*

Target field LRc02

Target field parameters

LRc02a: $\alpha_a = 18^h\ 41^m\ 02^s$, $\delta_a = +07^\circ\ 12'\ 54''$
LRc02b: $\alpha_b = 18^h\ 43^m\ 33^s$, $\delta_b = +05^\circ\ 59'\ 53''$

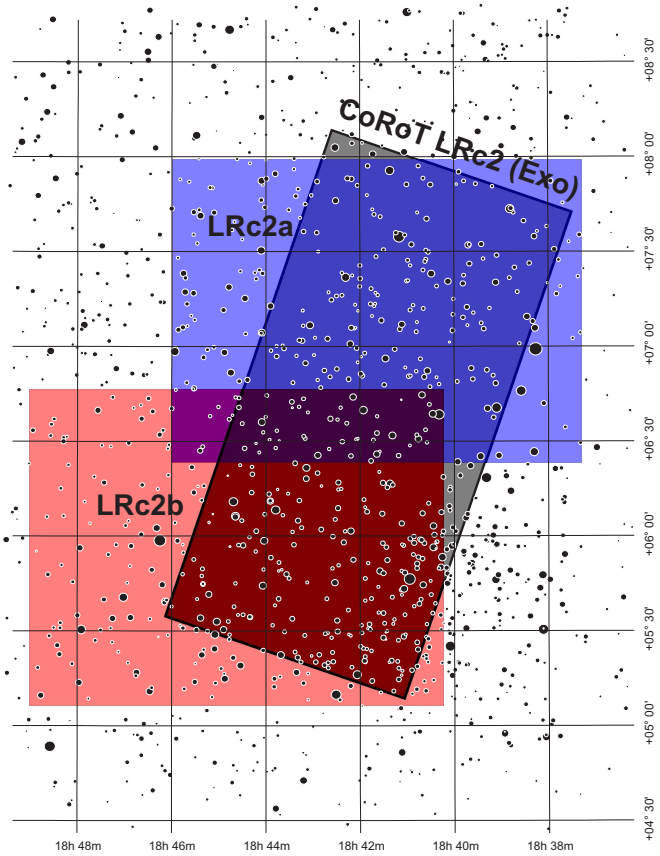

Figure A.18: *Orientation of LRc02 subfields with respect to CoRoT exoplanetary field.*

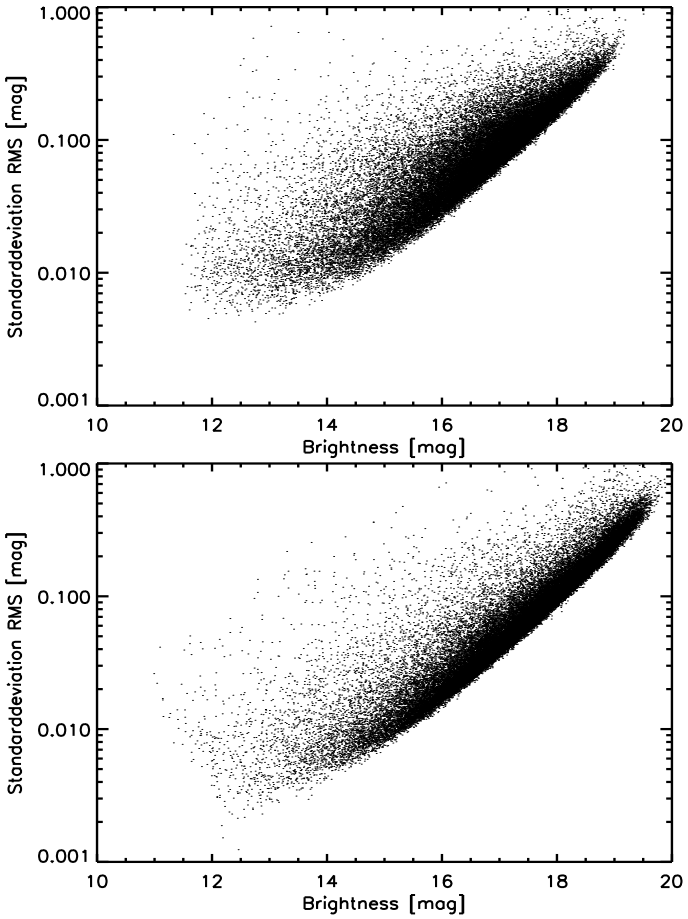

Figure A.19: *RMS plot for BEST II fields LRc02a (upper panel) and LRc02b (lower panel). Red line presents the limiting total noise and red crosses represent the detected variable stars.*

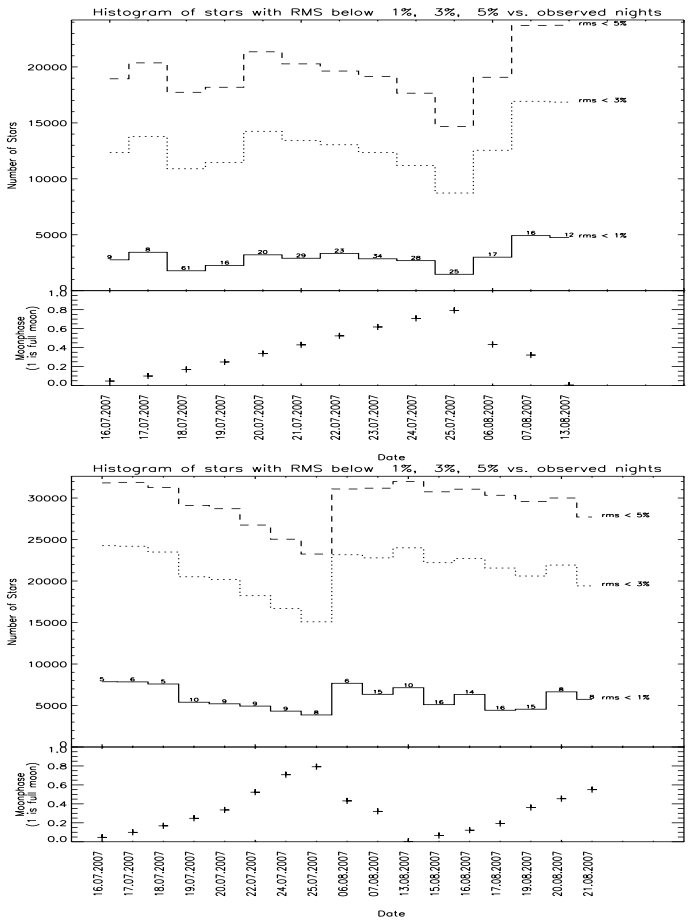

Figure A.20: *Photometric quality of nights for the BEST II LRc02a (upper panel) and LRc02b (lower panel) fields. Numbers above the histogram plot represent the total number of frames for the given night. The number of stars with precision of* 1%, 3% *and* 5% *is presented in plots.*

Periodic variable stars

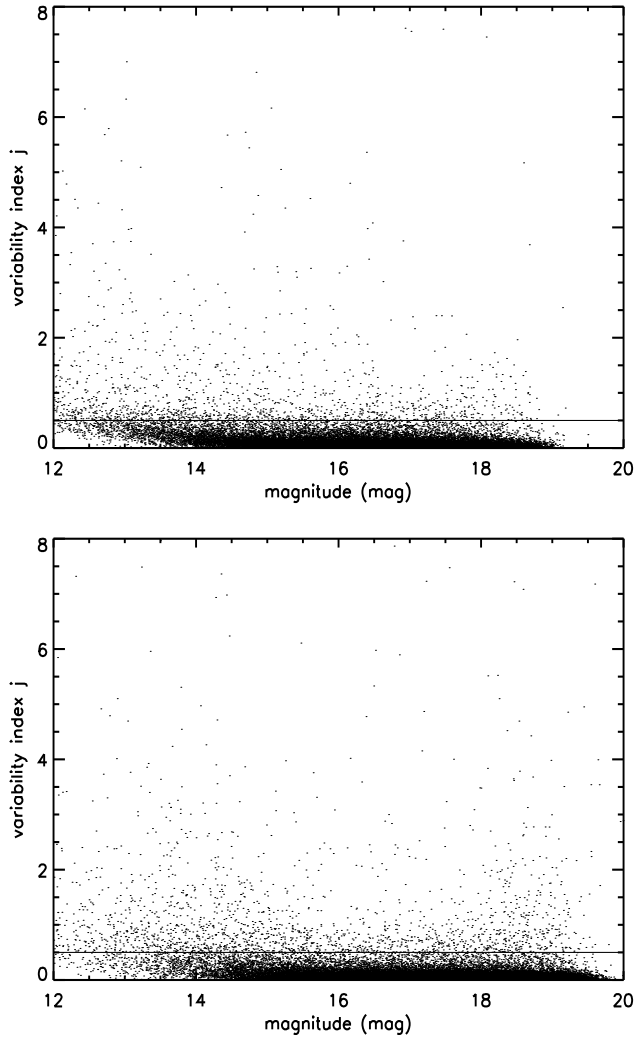

Figure A.21: *Variability index j against magnitude for stars in LRc02a (left) and LRc02b (right) target fields.*

Table A.5: *Periodic variable stars detected in BEST II lrcb stellar field. Magnitudes are based on calibration against USNO catalogue only. Stars marked with c may be affected by crowding and thus the variability information can be influenced by the nearby neighbour.*

BEST ID	2MASS ID	α(J2000)	δ(J2000)	$\overline{m}$(mag)	P(days)	Amp.(mag)	Type
lrca1a-91	18432875+0750508	18 43 28.75	7 50 50.8	15.246	0.472	0.45	EW
lrca1a-817	18404845+0747198	18 40 48.45	7 47 19.8	16.571	0.360	0.40	EW
lrca1a-828c	18404510+0742510	18 40 45.10	7 42 51.0	15.657	0.549	0.60	RR Lyr
lrca1a-831c	18404472+0742554	18 40 44.73	7 42 55.4	15.743	0.551	0.50	RR Lyr
lrca1a-838c	18404364+0746559	18 40 43.65	7 46 55.9	14.823	0.086	0.26	SXPHE
lrca1a-840c	18404325+0746596	18 40 43.26	7 46 59.7	14.642	0.086	0.30	SXPHE
lrca1a-926	18402674+0640416	18 40 26.74	6 40 41.7	15.691	0.384	0.20	EW
lrca1a-974	18401815+0754065	18 40 18.15	7 54 06.5	16.663	0.419	0.20	EW
lrca1a-984		18 40 17.07	7 51 49.4	17.011	0.157	0.30	EW/DSCT
lrca1a-989	18401605+0756184	18 40 16.05	7 56 18.4	16.187	0.429	0.40	EW
lrca1a-994	18401364+0649361	18 40 13.65	6 49 36.2	15.589	0.732	0.20	RR Lyr
lrca1a-1010c	18401154+0749588	18 40 11.54	7 49 58.8	15.857	0.320	0.18	EW
lrca1a-1011c	18401146+0749538	18 40 11.47	7 49 53.9	15.817	0.320	0.18	EW
lrca1a-1012c	18401155+0755409	18 40 11.56	7 55 40.9	15.448	0.374	0.17	EW
lrca1a-1014c	18401123+0755432	18 40 11.24	7 55 43.3	15.649	0.374	0.20	EW
lrca1a-1037	18400611+0738383	18 40 06.11	7 38 38.4	16.235	0.181	0.14	DSCT
lrca1a-1112	18395058+0707130	18 39 50.58	7 7 13.1	13.785	0.353	0.80	EW
lrca1a-1136	18394597+0730542	18 39 45.97	7 30 54.3	14.961	0.416	0.20	ELL/SP
lrca1a-1148	18394322+0731173	18 39 43.22	7 31 17.4	18.261	0.287	1.20	EW
lrca1a-1168c	18393769+0659487	18 39 37.69	6 59 48.7	15.264	0.468	0.16	EW
lrca1a-1169c	18393749+0659522	18 39 37.50	6 59 52.2	15.161	0.379	0.16	EW
lrca1a-1170c	18393718+0659481	18 39 37.18	6 59 48.1	15.289	0.379	0.16	EW

Table A.5: *continued.*

BEST ID	2MASS ID	α(J2000)	δ(J2000)	$\overline{m}$(mag)	P(days)	Amp.(mag)	Type
lrca1a-1182	18393331+0635367	18 39 33.31	6 35 36.7	15.951	0.352	0.17	EW
lrca1a-1198	18393086+0726535	18 39 30.86	7 26 53.5	14.963	0.572	0.70	RR Lyr
lrca1a-1215	18392631+0659357	18 39 26.31	6 59 35.8	14.602	0.384	0.17	EW
lrca1a-1216	18392626+0659410	18 39 26.26	6 59 41.1	14.611	0.384	0.15	EW
lrca1a-1223	18392410+0654157	18 39 24.10	6 54 15.8	16.798	0.299	0.30	DSCT
lrca1a-1245	18391971+0716326	18 39 19.71	7 16 32.7	16.820	0.412	0.40	EW
lrca1a-1249	18391902+0717255	18 39 19.02	7 17 25.5	14.512	0.458	0.19	EW
lrca1a-1257	18391753+0633298	18 39 17.54	6 33 29.9	15.877	0.568	0.30	EW
lrca1a-1260	18391758+0740346	18 39 17.58	7 40 34.7	16.900	0.369	0.70	EW
lrca1a-1274	18391124+0628102	18 39 11.25	6 28 10.3	16.328	0.290	0.60	EW
lrca1a-1295	18390877+0742139	18 39 8.77	7 42 13.9	17.997	0.307	1.57	EB
lrca1a-1298	18390778+0721202	18 39 7.79	7 21 20.3	16.685	0.377	0.30	EW
lrca1a-1327	18390215+0701596	18 39 2.15	7 1 59.7	14.441	0.840	0.15	EB
lrca1a-1331	18390115+0647212	18 39 1.16	6 47 21.2	13.558	1.615	0.30	EA
lrca1a-1334	18390069+0647226	18 38 0.70	6 47 22.7	13.922	0.884	0.15	EB
lrca1a-1339	18390091+0748007	18 38 0.92	7 48 0.7	14.405	0.151	0.05	DSCT
lrca1a-1354	18385704+0640347	18 38 57.05	6 40 34.8	16.856	0.690	0.40	EW
lrca1a-1372	18385500+0755452	18 38 55.01	7 55 45.3	14.846	0.467	0.22	EB
lrca1a-1387c	18385089+0722208	18 38 50.89	7 22 20.8	15.632	0.344	0.22	EW
lrca1a-1390c	18385061+0722229	18 38 50.61	7 22 22.9	15.696	0.344	0.30	EW
lrca1a-1392c		18 38 50.23	7 22 28.9	17.518	0.344	0.45	EB
lrca1a-1452	18383764+0729010	18 38 37.64	7 29 1.1	13.956	0.291	0.16	EW
lrca1a-1470	18383152+0639470	18 38 31.52	6 39 47.1	15.128	0.339	0.20	EW
lrca1a-1474c	18383257+0752144	18 38 32.57	7 52 14.4	14.840	0.278	0.27	EW
lrca1a-1478c	18383205+0752147	18 38 32.05	7 52 14.7	14.320	0.278	0.08	EW
lrca1a-1480	18383068+0712590	18 38 30.69	7 12 59.1	15.172	0.574	0.20	EB
lrca1a-1482	18383027+0646573	18 38 30.28	6 46 57.4	15.193	0.422	0.50	EW
lrca1a-1506c	18382544+0720456	18 38 25.44	7 20 45.7	15.240	0.915	0.28	EB
lrca1a-1509c	18382523+0720503	18 38 25.23	7 20 50.3	15.122	0.915	0.28	EB
lrca1a-1525	18382382+0754087	18 38 23.83	7 54 8.8	14.288	0.280	0.30	EW
lrca1a-1526	18382244+0633587	18 38 22.44	6 33 58.8	16.278	0.210	0.20	DSCT
lrca1a-1544	18381735+0634091	18 38 17.35	6 34 9.1	17.765	0.351	0.70	EB
lrca1a-1551	18381456+0731389	18 38 14.56	7 31 38.9	16.237	0.440	0.30	EW
lrca1a-1565	18380968+0702398	18 38 9.69	7 2 39.2	13.879	0.478	0.13	EB
lrca1a-1567	18380959+0743562	18 38 9.59	7 43 56.3	14.956	0.373	0.50	SP
lrca1a-1574	18380757+0755096	18 38 7.58	7 55 9.6	15.202	0.475	0.40	RR Lyr
lrca1a-1575	18380693+0740374	18 38 6.93	7 40 37.4	15.938	0.336	0.80	EB
lrca1a-1583	18380477+0710206	18 38 4.77	7 10 20.7	15.624	0.282	0.17	EW
lrca1a-1641	18375123+0712220	18 37 51.24	7 12 22.0	16.520	0.314	0.30	EW
lrca1a-1665	18374614+0730272	18 37 46.15	7 30 27.2	15.910	0.593	0.30	EW
lrca1a-1671c	18374503+0733092	18 37 45.03	7 33 9.2	15.397	1.288	0.15	DCEP
lrca1a-1673c	18374472+0733054	18 37 44.72	7 33 5.4	15.798	1.288	0.30	DCEP
lrca1a-1679	18374246+0714348	18 37 42.46	7 14 34.9	15.051	0.130	0.08	DSCT
lrca1a-1692	18373901+0638385	18 37 39.01	6 38 38.5	15.853	0.737	0.20	EB
lrca1a-1698	18373865+0720368	18 37 38.66	7 20 36.9	17.324	0.354	0.33	EB
lrca1a-1708	18373663+0634144	18 37 36.63	6 34 14.5	14.649	0.617	0.20	EW
lrca1a-1711	18373622+0636025	18 37 36.23	6 36 2.6	13.255	1.351	0.25	PULS
lrca1a-1736	18372915+0646246	18 37 29.15	6 46 24.6	15.185	0.171	0.08	DSCT
lrca1a-1752	18372406+0653588	18 37 24.07	6 53 58.8	14.925	0.368	0.15	EB
lrca2-35	18455019+0643232	18 45 50.20	6 43 23.3	16.528	0.315	0.23	EW
lrca2-166	18445784+0654263	18 44 57.85	6 54 26.3	15.497	0.572	0.60	RR Lyr
lrca2-193	18444383+0722118	18 44 43.84	7 22 11.9	15.084	0.274	0.40	EW
lrca2-213	18443855+0722245	18 44 38.55	7 22 24.6	16.518	0.082	0.40	SXPHE
lrca2-234c	18443063+0642575	18 44 30.64	6 42 57.5	16.134	0.747	0.30	EA
lrca2-235c	18443056+0642531	18 44 30.57	6 42 53.1	16.154	0.747	0.30	EA
lrca2-263	18442311+0732593	18 44 23.11	7 32 59.4	13.143	0.613	0.40	EW
lrca2-267	18442231+0743120	18 44 22.31	7 43 12.0	16.578	0.410	0.40	EW
lrca2-276	18441879+0651542	18 44 18.80	6 51 54.2	13.325	0.133	0.03	DSCT
lrca2-342	18435940+0744221	18 43 59.41	7 44 22.1	12.995	0.444	0.15	RR Lyr(c)
lrca2-445	18433242+0738586	18 43 32.42	7 38 58.7	12.593	0.315	0.18	EW
lrca2-492	18431889+0743352	18 43 18.90	7 43 35.3	16.485	1.114	0.35	EA
lrca2-634	18424426+0710194	18 42 44.26	7 10 19.4	14.697	0.210	0.08	EW
lrca2-660	18423848+0737087	18 42 38.49	7 37 8.8	16.838	0.136	0.30	DSCT
lrca2-672	18423563+0740453	18 42 35.63	7 40 45.3	14.839	0.718	0.10	EW
lrca2-725	18422230+0731241	18 42 22.31	7 31 24.1	17.156	0.368	0.80	EW
lrca2-836	18415948+0649516	18 41 59.49	6 49 51.6	14.646	3.618	0.10	EA
lrca2-852	18415601+0742186	18 41 56.02	7 42 18.6	16.445	0.322	0.25	EW
lrca2-867c	18415223+0659462	18 41 52.24	6 59 46.2	15.543	0.317	0.35	EW
lrca2-1045	18412084+0747134	18 41 20.84	7 47 13.5	16.746	0.361	0.30	EW
lrca2-1083c	18411542+0743095	18 41 15.43	7 43 9.6	15.520	0.329	0.30	EW
lrca2-1084c	18411544+0743154	18 41 15.44	7 43 15.4	15.649	0.329	0.27	EW
lrca2-1243	18405364+0644394	18 40 53.64	6 44 39.5	16.740	0.456	1.00	RR Lyr
lrca2-1352	18404028+0643427	18 40 40.28	6 43 42.8	16.877	0.350	0.30	EW
lrcax-5	18434167+0643519	18 43 41.67	6 43 52.0	11.477	0.254	0.035	ELL/SP
lrcax-10	18434162+0733296	18 43 41.63	7 33 29.6	16.568	0.823	0.30	EA
lrcax-30	18433773+0714105	18 43 37.74	7 14 10.5	15.503	2.902	0.50	EA
lrcax-32	18433791+0737127	18 43 37.91	7 37 12.8	15.958	1.889	1.20	EA
lrcax-59	18433066+0647232	18 43 30.66	6 47 23.3	15.143	0.891	0.10	EB
lrcax-70	18432912+0732547	18 43 29.12	7 32 54.8	14.371	7.901	0.08	EB
lrcax-92	18432368+0704421	18 43 23.69	7 4 42.1	15.883	0.328	0.17	EW
lrcax-105c		18 43 20.79	7 10 7.6	17.368	0.483	0.80	RR Lyr
lrcax-109c		18 43 20.42	7 10 10.7	17.573	0.483	1.20	RR Lyr
lrcax-111	18431942+0700188	18 43 19.42	7 0 18.8	16.428	9.131	0.32	DCEP
lrcax-114	18431869+0634267	18 43 18.70	6 34 26.7	16.393	0.342	0.34	EW
lrcax-122	18431795+0657021	18 43 17.96	6 57 2.2	15.526	0.180	0.13	DSCT
lrcax-131	18431527+0650487	18 43 15.27	6 50 48.7	14.711	8.413	0.10	DCEP
lrcax-132	18431534+0706572	18 43 15.34	7 6 57.3	13.995	1.467	1.50	V1117Oph
lrcax-153	18431132+0738226	18 43 11.32	7 38 22.6	15.498	0.739	0.20	RR Lyr
lrcax-157	18430977+0657253	18 43 9.78	6 57 25.3	15.532	0.362	0.25	EW
lrcax-187	18430463+0727566	18 43 4.63	7 27 56.6	16.427	0.399	0.32	EW
lrcax-189	18430368+0639281	18 43 3.69	6 39 28.1	15.553	4.735	0.30	EA
lrcax-200	18430146+0729413	18 43 1.46	7 29 41.4	17.789	0.255	1.00	EW
lrcax-203	18430099+0730219	18 43 0.99	7 30 22.0	13.552	0.149	0.03	DSCT
lrcax-218	18425768+0642438	18 42 57.68	6 42 43.9	17.952	0.539	1.20	EW
lrcax-224	18425764+0723323	18 42 57.64	7 23 32.3	16.178	0.784	0.80	RR Lyr
lrcax-227c	18425699+0659218	18 42 56.99	6 59 21.9	14.875	0.567	0.40	EW
lrcax-229c		18 42 56.48	6 59 21.0	15.900	0.567	0.40	EW

Table A.5: *continued.*

BEST ID	2MASS ID	α(J2000)	δ(J2000)	$\overline{m}$(mag)	P(days)	Amp.(mag)	Type
lrcax-230	18425653+0704546	18 42 56.54	7 4 54.6	16.124	0.272	0.25	DSCT
lrcax-237	18425480+0638557	18 42 54.81	6 38 55.7	17.020	4.425	0.50	DCEP
lrcax-238	18425502+0654385	18 42 55.03	6 54 38.6	13.922	4.639	0.08	α^2CVn
lrcax-240	18425483+0704003	18 42 54.84	7 4 0.4	14.814	1.200	0.18	EW
lrcax-274	18424976+0713167	18 42 49.77	7 13 16.8	16.555	0.822	0.30	EW
lrcax-276c	18424873+0640088	18 42 48.73	6 40 8.8	15.480	0.301	0.15	EW
lrcax-277c	18424849+0640029	18 42 48.50	6 40 3.0	15.812	0.301	0.15	EW
lrcax-280	18424868+0703401	18 42 48.69	7 3 40.1	14.431	0.554	0.08	SP
lrcax-315	18424423+0648104	18 42 44.24	6 48 10.4	14.693	5.577	0.17	DCEP
lrcax-316	18424426+0710194	18 42 44.26	7 10 19.4	14.336	0.105	0.05	DSCT
lrcax-320c	18424316+0655350	18 42 43.17	6 55 35.0	14.986	0.724	0.20	EB
lrcax-321c	18424315+0655414	18 42 43.16	6 55 41.4	14.820	0.724	0.20	EB
lrcax-323c	18424274+0655394	18 42 42.74	6 55 39.5	14.887	0.723	0.22	EB
lrcax-331	18424028+0653264	18 42 40.28	6 53 26.4	16.294	0.359	0.25	EW
lrcax-338	18423892+0742228	18 42 38.93	7 42 22.8	15.008	1.467	—	EA
lrcax-342	18423848+0737087	18 42 38.49	7 37 8.8	16.502	0.271	0.40	EW
lrcax-344	18423754+0654399	18 42 37.54	6 54 40.0	18.205	0.208	1.30	EW
lrcax-349	18423680+0730351	18 42 36.80	7 30 35.2	12.443	0.593	0.19	EW
lrcax-360	18423563+0740453	18 42 35.63	7 40 45.3	14.468	0.719	0.14	EW
lrcax-361c	18423488+0650166	18 42 34.89	6 50 16.6	14.997	0.425	0.16	EW
lrcax-362c	18423447+0650151	18 42 34.48	6 50 15.1	14.885	0.425	0.16	EW
lrcax-364	18423427+0649328	18 42 34.28	6 49 32.9	16.919	0.363	0.32	EW
lrcax-368	18423385+0700075	18 42 33.86	7 00 7.5	16.872	0.455	0.31	EB
lrcax-392c		18 42 29.20	6 56 4.8	16.300	0.380	0.20	EB
lrcax-394	18422944+0732132	18 42 29.44	7 32 13.3	16.405	3.762	0.50	PULS
lrcax-396c	18422862+0656031	18 42 28.63	6 56 3.1	15.154	0.380	0.22	EB
lrcax-424	18422230+0731241	18 42 22.31	7 31 24.1	16.725	0.367	0.80	EW
lrcax-435c	18422070+0732180	18 42 20.71	7 32 18.0	17.419	0.404	0.43	EW
lrcax-436c	18422069+0732258	18 42 20.70	7 32 25.8	16.272	0.404	0.40	EW
lrcax-437c	18422070+0732333	18 42 20.71	7 32 33.3	16.553	0.404	0.32	EW
lrcax-497	18421012+0633049	18 42 10.13	6 33 5.0	14.016	0.279	0.50	RR Lyr (c)
lrcax-501	18421058+0738516	18 42 10.58	7 38 51.7	15.828	0.169	0.14	DSCT
lrcax-503	18420918+0734534	18 42 9.18	7 34 53.4	12.117	0.079	0.10	SXPHE
lrcax-512	18420805+0714198	18 42 8.05	7 14 19.8	16.490	0.315	0.42	EW
lrcax-521	18420590+0640220	18 42 5.91	6 40 22.1	15.105	0.619	0.13	EB
lrcax-565c	18420041+0738050	18 42 0.42	7 38 5.0	14.159	0.854	0.03	RR Lyr
lrcax-567c	18415964+0738102	18 41 59.64	7 38 10.2	16.096	0.855	0.17	RR Lyr
lrcax-579	18415601+0742186	18 41 56.02	7 42 18.6	16.085	0.322	0.22	EW
lrcax-610c	18415223+0659462	18 41 52.24	6 59 46.2	15.214	0.317	0.40	EW
lrcax-615c	18415197+0659398	18 41 51.97	6 59 39.9	15.558	0.317	0.26	EW
lrcax-632c	18414841+0636101	18 41 48.41	6 36 10.1	17.296	0.295	0.60	EW
lrcax-635c		18 41 48.05	6 36 12.4	17.887	0.295	0.70	EW
lrcax-637	18414822+0717337	18 41 48.22	7 17 33.7	12.764	2.929	0.10	EB
lrcax-638	18414789+0657295	18 41 47.90	6 57 29.5	15.016	0.212	0.05	DSCT
lrcax-648	18414648+0655495	18 41 46.48	6 55 49.5	13.581	0.207	0.04	DSCT
lrcax-649	18414572+0658281	18 41 45.72	6 58 28.2	16.624	0.359	0.30	EW
lrcax-651	18414533+0706237	18 41 45.33	7 6 23.8	16.257	0.408	0.40	EW
lrcax-671	18414254+0703240	18 41 42.55	7 3 24.1	15.515	0.374	0.19	EW
lrcax-675	18414228+0719559	18 41 42.28	7 19 55.9	14.542	3.256	0.12	EW
lrcax-700	18413849+0638579	18 41 38.50	6 38 57.9	16.231	0.591	0.20	EA
lrcax-707	18413768+0718207	18 41 37.69	7 18 20.8	15.118	0.332	0.50	EW
lrcax-729	18413431+0635186	18 41 34.31	6 35 18.6	15.568	1.651	0.10	EA
lrcax-731	18413408+0726009	18 41 34.08	7 26 0.9	15.339	0.484	0.10	EA
lrcax-747	18413168+0631013	18 41 31.69	6 31 1.3	13.056	1.109	0.04	γDOR
lrcax-753	18413017+0643091	18 41 30.18	6 43 9.2	13.240	0.168	0.02	DSCT
lrcax-766	18412851+0633387	18 41 28.51	6 33 38.7	15.669	3.539	0.20	PULS
lrcax-788	18412581+0643359	18 41 25.82	6 43 35.9	16.356	0.532	0.86	RR Lyr
lrcax-801	18412388+0647029	18 41 23.88	6 47 3.0	15.832	0.518	0.20	EA
lrcax-814	18412295+0741504	18 41 22.96	7 41 22.96	14.719	0.364	0.46	EW
lrcax-825c		18 41 21.22	7 47 18.7	16.916	0.361	0.30	EW
lrcax-826	18412071+0651213	18 41 20.71	6 51 21.4	17.136	0.472	0.45	EB
lrcax-828c	18412084+0747134	18 41 20.84	7 47 13.5	16.290	0.361	0.40	EW
lrcax-836	18411967+0734546	18 41 19.68	7 34 54.7	15.560	0.471	1.00	RR Lyr
lrcax-863c	18411582+0743091	18 41 15.82	7 43 9.1	15.348	0.329	0.20	EW
lrcax-864c	18411542+0743095	18 41 15.43	7 43 9.6	15.158	0.329	0.24	EW
lrcax-865c	18411544+0743154	18 41 15.44	7 43 15.4	15.196	0.329	0.24	EW
lrcax-866	18411523+0733420	18 41 15.24	7 33 42.1	14.470	6.822	0.13	α^2CVn
lrcax-867	18411503+0740129	18 41 15.03	7 40 13.0	16.397	0.182	0.23	DSCT
lrcax-874	18411341+0652276	18 41 13.41	6 52 27.7	15.869	0.698	0.15	EW/DSCT
lrcax-890	18411167+0707181	18 41 11.68	7 7 18.2	14.947	3.280	0.10	EB/EW
lrcax-896	18411083+0736349	18 41 10.84	7 36 34.9	15.236	0.180	0.14	DSCT
lrcax-911	18410771+0655074	18 41 7.72	6 55 7.4	14.744	0.618	0.44	EB
lrcax-919	18410626+0634269	18 41 6.27	6 34 26.9	13.788	0.165	0.05	DSCT
lrcax-921	18410607+0702389	18 41 6.07	7 2 39.0	17.151	0.343	0.50	EW
lrcax-928	18410579+0740461	18 41 5.79	7 40 46.2	15.204	4.405	0.28	DCEP
lrcax-930	18410540+0716573	18 41 5.41	7 17 7.8	13.744	1.595	0.16	EA
lrcax-947	18410309+0657228	18 41 3.09	6 57 22.9	14.675	6.151	0.17	DCEP
lrcax-948	18410321+0717325	18 41 3.21	7 17 32.6	15.408	0.359	0.36	RR Lyr
lrcax-959	18410140+0651262	18 41 1.41	6 51 26.2	15.494	0.743	0.10	RR Lyr
lrcax-966	18410030+0717467	18 41 0.30	7 17 46.8	16.401	0.378	0.65	EW
lrcax-967c	18405989+0631259	18 40 59.90	6 31 26.0	14.306	0.551	0.10	SP/EB
lrcax-970c	18405943+0631233	18 40 59.44	6 31 23.3	14.411	0.551	0.10	SP/EB
lrcax-983c	18405787+0650343	18 40 57.88	6 50 34.3	17.297	0.585	0.60	RR Lyr
lrcax-984c	18405772+0650274	18 40 57.73	6 50 27.4	16.701	0.585	0.42	RR Lyr
lrcax-988	18405751+0656445	18 40 57.52	6 56 44.6	13.721	0.296	0.08	SP/EW
lrcax-989	18405790+0747067	18 40 57.90	7 47 6.8	14.882	0.173	0.12	DSCT
lrcax-994	18405698+0636479	18 40 56.99	6 36 48.0	15.430	0.297	0.30	EW
lrcax-998	18405704+0740220	18 40 57.04	7 40 22.0	17.019	0.609	0.80	RR Lyr
lrcax-1011	18405540+0654554	18 40 55.41	6 54 55.4	15.449	0.472	0.15	EB
lrcax-1023	18405364+0644394	18 40 53.64	6 44 39.5	16.448	0.455	0.98	RR Lyr
lrcax-1024c	18405397+0737300	18 40 53.98	7 37 30.0	14.745	0.614	0.14	EB
lrcax-1027c	18405361+0737355	18 40 53.61	7 37 35.5	14.969	0.614	0.08	EB
lrcax-1082	18404583+0644444	18 40 45.83	6 44 44.4	16.548	0.403	0.30	EW
lrcax-1092c	18404510+0742510	18 40 45.10	7 42 51.0	15.349	0.549	0.20	RR Lyr
lrcax-1094c	18404472+0742554	18 40 44.73	7 42 55.4	15.512	0.549	0.50	RR Lyr
lrcax-1097	18404390+0656461	18 40 43.91	6 56 46.2	15.950	3.241	0.30	EB
lrcax-1101	18404398+0744338	18 40 43.98	7 44 33.9	15.535	0.879	0.15	EB

Table A.5: *continued.*

BEST ID	2MASS ID	α(J2000)	δ(J2000)	$\overline{m}$(mag)	P(days)	Amp.(mag)	Type
lrcax-1107	18404325+0746596	18 40 43.26	7 46 59.7	14.388	0.086	0.33	SXPHE
lrcax-1110c		18 40 42.49	6 37 46.1	16.861	2.823	0.58	EA
lrcax-1111c	18404252+0637530	18 40 42.53	6 37 53.1	16.046	2.823	0.60	EA
lrcax-1115	18404240+0703219	18 40 42.41	7 3 22.0	15.806	0.191	0.50	EA
lrcax-1116	18404225+0639244	18 40 42.25	6 39 24.4	17.054	0.401	0.60	EW
lrcax-1129	18404028+0643427	18 40 40.28	6 43 42.8	16.469	0.350	0.40	EW
lrcax-1133	18404004+0651057	18 40 40.04	6 51 5.7	15.163	0.219	0.06	DSCT
lrcax-1141	18403941+0741007	18 40 39.41	7 41 0.7	14.056	6.613	0.08	α^2CVn
lrcax-1151	18403829+0711299	18 40 38.30	7 11 30.0	16.413	0.668	0.80	RR Lyr
lrcax-1168	18403640+0742164	18 40 36.41	7 42 16.4	14.517	6.397	3.00	EA
lrcax-1183c	18403411+0726056	18 40 34.11	7 26 5.7	16.551	0.790	0.30	EW
lrcax-1186c	18403361+0726014	18 40 33.62	7 26 1.4	16.043	0.790	0.60	EW
lrcax-1188c	18403334+0652312	18 40 33.34	6 52 31.2	15.253	0.406	0.30	EW
lrcax-1192c		18 40 32.83	6 52 30.9	16.154	0.406	0.30	EW
lrcax-1196	18403256+0723188	18 40 32.57	7 23 18.8	15.299	0.397	0.10	EW
lrcax-1211c	18402969+0647581	18 40 29.69	6 47 58.2	15.953	0.449	0.40	EW
lrcax-1212c	18402963+0648040	18 40 29.64	6 48 4.1	15.929	0.449	0.30	EW
lrcax-1215	18402981+0743360	18 40 29.81	7 43 36.1	14.661	2.312	0.12	α^2CVn
lrcax-1239c	18402712+0640391	18 40 27.12	6 40 39.2	15.421	0.383	0.40	EW
lrcax-1246c	18402688+0640470	18 40 26.88	6 40 47.1	15.660	0.383	0.20	EW
lrcax-1256	18402579+0649188	18 40 25.79	6 49 18.8	15.502	0.276	0.17	DSCT
lrcax-1262	18402543+0718575	18 40 25.43	7 18 57.5	15.172	1.340	0.20	EW
lrcax-1270	18402388+0653577	18 40 23.89	6 53 57.7	15.169	1.029	0.30	EW
lrcax-1284	18402136+0630560	18 40 21.37	6 30 56.0	14.800	0.283	0.15	EW
lrcax-1311	18401845+0733081	18 40 18.46	7 33 8.1	16.602	0.368	0.43	EW
lrcax-1317	18401758+0735161	18 40 17.58	7 35 16.1	16.556	0.372	0.40	EW
lrcax-1319	18401729+0739481	18 40 17.29	7 39 48.2	16.163	0.467	0.80	EW
lrcax-1331c	18401507+0703189	18 40 15.08	7 3 19.0	15.943	0.657	0.30	RR Lyr
lrcax-1333c	18401495+0703255	18 40 14.95	7 3 25.6	16.330	0.657	0.40	RR Lyr
lrcax-1358	18401275+0645166	18 40 12.75	6 45 16.7	16.231	0.382	0.25	EW
lrcax-1387	18400956+0654042	18 40 9.57	6 54 4.3	12.876	> 10	0.07	α^2CVn
lrcax-1392	18400904+0741532	18 40 9.04	7 41 53.2	15.307	0.757	0.25	EA
lrcax-1395	18400837+0653005	18 40 8.37	6 53 0.5	16.410	0.336	0.30	EW
lrcax-1452c	18400159+0739425	18 40 1.59	7 39 42.5	16.136	0.346	0.44	EW
lrcax-1457c	18400113+0739411	18 40 1.13	7 39 41.2	15.677	0.346	0.64	EW
lrcax-1459	18400026+0641127	18 40 0.27	6 41 12.7	14.586	0.769	0.44	EW

Table A.6: *Periodic variable stars detected in BEST II lrcb stellar field. Magnitudes are based on calibration against USNO catalogue only. Stars marked with c may be affected by crowding and thus the variability information can be influenced by the nearby neighbour.*

BEST ID	2MASS ID	α(J2000)	δ(J2000)	$\overline{m}$(mag)	P(days)	Amp.(mag)	Type
lrcbx-201	18454511+0518256	18 45 45.11	5 18 25.7	18.384	0.340	0.66	EW
lrcbx-459	18450212+0517534	18 45 2.13	5 17 53.5	17.774	0.345	0.42	EW
lrcbx-472	18450116+0538116	18 45 1.17	5 38 11.7	12.295	0.332	0.01	DSCT
lrcbx-535	18445250+0516319	18 44 52.51	5 16 31.9	16.152	0.354	0.10	EB
lrcbx-631	18444160+0601340	18 44 41.61	6 1 34.1	13.375	2.680	0.05	α^2CVn
lrcbx-645	18444095+0618481	18 44 40.95	6 18 48.2	14.391	0.529	0.23	RR Lyr
lrcbx-673	18443905+0618245	18 44 39.06	6 18 24.6	14.132	0.694	0.06	SP
lrcbx-958	18441365+0608576	18 44 13.66	6 8 57.7	13.509	2.541	0.08	SP
lrcbx-1039	18440691+0610058	18 44 6.92	6 10 5.8	13.772	2.115	0.06	SP
lrcbx-1069	18440322+0516467	18 44 3.22	5 16 46.8	17.105	0.412	0.30	EW
lrcbx-1087	18440152+0540550	18 44 1.52	5 40 55.1	14.161	2.851	–	α^2CVn
lrcbx-1130	18435780+0532169	18 43 57.80	5 32 17.0	14.002	2.177	0.04	EW
lrcbx-1152	18435502+0515506	18 43 55.02	5 15 50.6	15.482	1.145	0.07	EB
lrcbx-1916	18424632+0536417	18 42 46.33	5 36 41.8	18.430	0.426	0.45	EW/RR Lyr
lrcbx-2021	18423680+0621529	18 42 36.81	6 21 53.0	15.725	0.190	0.06	DSCT
lrcbx-2079	18422991+0531467	18 42 29.91	5 31 46.7	13.646	2.175	0.03	PULS
lrcbx-2139	18422389+0531169	18 42 23.90	5 31 16.9	17.066	0.346	0.17	EB
lrcbx-2158	18422192+0525190	18 42 21.93	5 25 19.1	14.826	1.610	0.06	EW
lrcbx-2181	18421972+0557084	18 42 19.72	5 57 8.4	16.672	0.262	0.17	EA
lrcbx-2273	18421219+0542452	18 42 12.20	5 42 45.2	17.619	0.629	0.30	EB
lrcbx-2364	18420547+0519519	18 42 5.48	5 19 52.0	17.777	0.281	0.70	EW
lrcbx-2387	18420378+0616072	18 42 3.79	6 16 7.3	17.298	0.425	0.50	EW
lrcbx-2389	18420315+0524493	18 42 3.15	5 24 49.4	17.511	0.439	1.20	RR Lyr
lrcbx-2429	18415866+0524459	18 41 58.67	5 24 45.9	16.120	0.253	0.15	DSCT
lrcbx-2431	18415859+0539489	18 41 58.60	5 39 48.9	16.781	0.352	0.60	EW
lrcbx-2453	18415681+0607180	18 41 56.82	6 7 18.1	16.192	0.167	0.10	DSCT
lrcbx-2491c	18415228+0541275	18 41 52.28	5 41 27.5	14.925	0.107	0.44	RR Lyr
lrcbx-2498c	18415176+0541201	18 41 51.76	5 41 20.1	16.739	0.107	0.30	RR Lyr
lrcbx-2519	18415015+0603041	18 41 50.15	6 3 4.1	13.625	0.382	0.60	ASAS184150+0603.0
lrcbx-2559		18 41 45.83	6 16 15.7	18.517	0.442	0.63	EB
lrcbx-2574	18414348+0600284	18 41 43.48	6 0 28.5	16.915	0.394	0.20	EW
lrcbx-2575	18414357+0609504	18 41 43.57	6 9 50.4	17.230	0.441	0.20	EW
lrcbx-2581	18414298+0534361	18 41 42.99	5 34 36.1	13.322	0.581	0.07	SP
lrcbx-2661	18413540+0520318	18 41 35.41	5 20 31.9	17.904	0.320	0.70	EB
lrcbx-2664	18413526+0542550	18 41 35.26	5 42 55.0	16.096	0.698	0.15	EA
lrcbx-2685	18413314+0533506	18 41 33.14	5 33 50.7	15.793	4.100	0.18	DCEP
lrcbx-2723	18413016+0554578	18 41 30.17	5 54 57.9	14.580	0.409	0.14	EA
lrcbx-2758	18412678+0536286	18 41 26.79	5 36 28.7	18.317	0.363	0.80	EW
lrcbx-2859	18411911+0621528	18 41 19.12	6 21 52.8	12.895	0.604	0.08	ELL/SP
lrcbx-2903	18411548+0527022	18 41 15.49	5 27 2.2	17.177	0.251	0.38	EW
lrcbx-2933	18411322+0555040	18 41 13.23	5 55 4.0	15.784	0.385	0.18	EW
lrcbx-2987c	18410811+0530123	18 41 8.11	5 30 12.4	17.037	0.387	0.30	EB
lrcbx-2992c	18410794+0530051	18 41 7.95	5 30 5.2	16.968	0.387	0.17	EB
lrcbx-3033	18410260+0555313	18 41 2.60	5 55 31.3	16.925	0.852	0.20	EB
lrcbx-3083	18405693+0548507	18 40 56.93	5 48 50.8	17.587	0.299	0.40	EW/DSCT
lrcby-2	18461655+0551583	18 46 16.55	5 51 58.4	17.931	0.249	0.60	DSCT/EW
lrcby-13	18461532+0606203	18 46 15.33	6 6 20.4	16.075	0.471	0.17	EB
lrcby-18	18461311+0534196	18 46 13.11	5 34 19.6	13.293	0.102	0.03	DSCT/EW
lrcby-21	18461280+0602134	18 46 12.80	6 2 13.5	14.582	0.377	0.10	EB
lrcby-23	18461120+0518501	18 46 11.20	5 18 50.1	17.274	0.310	0.38	EW
lrcby-27	18461215+0602118	18 46 12.15	6 2 11.8	16.008	0.377	0.15	EW
lrcby-28	18461149+0541330	18 46 11.50	5 41 33.0	15.289	5.305	0.05	DCEP
lrcby-65	18460564+0613088	18 46 5.64	6 13 8.8	17.880	0.473	0.60	EW
lrcby-107	18455801+0553261	18 45 58.02	5 53 26.2	12.521	0.824	0.20	NSVS13913191
lrcby-111	18455640+0522343	18 45 56.41	5 22 34.4	18.530	0.425	0.80	EW
lrcby-128	18455405+0619231	18 45 54.06	6 19 23.1	17.458	0.593	0.60	EW
lrcby-143	18455175+0618410	18 45 51.76	6 18 41.1	16.688	0.141	0.20	DSCT
lrcby-168	18454776+0559337	18 45 47.77	5 59 33.8	16.453	0.610	0.40	EW
lrcby-174	18454647+0543413	18 45 46.47	5 43 41.3	18.723	0.461	1.00	EW
lrcby-184	18454523+0548474	18 45 45.24	5 48 47.5	15.823	2.184	1.00	EA
lrcby-188	18454500+0556050	18 45 45.00	5 56 5.1	16.688	0.390	0.20	EW
lrcby-195	18454378+0548552	18 45 43.78	5 48 55.2	14.294	5.531	0.11	SP
lrcby-198c	18454328+0545590	18 45 43.29	5 45 59.0	15.100	0.755	0.07	EA
lrcby-200c	18454292+0545568	18 45 42.92	5 45 56.8	15.651	0.755	0.15	EA
lrcby-217	18454004+0616594	18 45 40.05	6 16 59.5	16.170	0.719	0.45	EA
lrcby-219	18453860+0545322	18 45 38.60	5 45 32.3	16.798	0.485	0.25	EW
lrcby-223	18453642+0521364	18 45 36.43	5 21 36.4	16.900	0.181	0.28	EW
lrcby-240	18453356+0520050	18 45 33.56	5 20 5.1	14.613	7.445	0.15	LP
lrcby-370	18451394+0539221	18 45 13.95	5 39 22.2	13.704	0.118	0.02	DSCT
lrcby-403	18451088+0605284	18 45 10.88	6 5 28.5	13.643	0.656	0.04	ELL
lrcby-429	18450814+0611544	18 45 8.14	6 11 54.4	16.648	2.222	0.80	EA
lrcby-444	18450390+0518149	18 45 3.90	5 18 15.0	14.660	1.059	0.05	γDor
lrcby-454	18450308+0616596	18 45 3.09	6 16 59.7	16.757	0.848	0.40	EW
lrcby-476	18445937+0532269	18 44 59.38	5 32 27.0	13.654	0.367	0.10	DSCT
lrcby-502	18445559+0605403	18 44 55.59	6 5 40.3	16.745	0.324	0.50	EW
lrcby-510	18445481+0620502	18 44 54.81	6 20 50.2	14.648	0.371	0.06	EB
lrcby-513	18445387+0559324	18 44 53.87	5 59 32.4	16.151	2.650	0.20	EA
lrcby-515	18445309+0536168	18 44 53.09	5 36 16.8	15.970	0.644	0.12	EA
lrcby-525	18445249+0625141	18 44 52.50	6 25 14.1	14.281	2.596	0.20	DCEP
lrcby-606	18444326+0631107	18 44 43.27	6 31 10.8	15.443	2.113	0.09	EB
lrcby-611	18444180+0601596	18 44 41.80	6 1 59.6	15.354	0.600	0.08	EB
lrcby-659	18443833+0555254	18 44 38.33	5 55 25.5	13.738	0.417	0.08	EB
lrcby-668	18443664+0527552	18 44 36.64	5 27 55.2	15.549	2.267	1.00	DCEP
lrcby-670	18443611+0518521	18 44 36.12	5 18 52.2	15.408	1.051	0.40	EA
lrcby-674	18443610+0538239	18 44 36.11	5 38 24.0	16.748	0.249	0.27	DSCT
lrcby-698	18443448+0633024	18 44 34.48	6 33 2.4	14.224	0.332	0.06	DSCT
lrcby-711	18443238+0552275	18 44 32.39	5 52 27.5	15.587	0.436	0.08	EB/EW
lrcby-723	18443082+0604548	18 44 30.83	6 4 54.9	16.458	0.701	0.13	EW
lrcby-749	18442872+0608251	18 44 28.72	6 8 25.1	17.017	0.459	0.50	EW
lrcby-757c	18442638+0520218	18 44 26.38	5 20 21.9	16.862	0.460	0.40	EW
lrcby-761c	18442614+0520157	18 44 26.14	5 20 15.7	16.682	0.460	0.45	EW
lrcby-787	18442354+0622022	18 44 23.54	6 22 2.3	17.035	0.710	0.30	EB
lrcby-809	18442011+0540223	18 44 20.12	5 40 22.3	17.555	0.538	0.40	EW

Table A.6: *continued.*

BEST ID	2MASS ID	α(J2000)	δ(J2000)	$\overline{m}$(mag)	P(days)	Amp.(mag)	Type
lrcby-820	18441824+0530222	18 44 18.25	5 30 22.2	16.321	0.726	0.25	EW
lrcby-830	18441722+0519567	18 44 17.22	5 19 56.7	15.782	0.604	0.15	EB
lrcby-854	18441600+0523489	18 44 16.01	5 23 48.9	16.857	0.448	0.50	EW
lrcby-879	18441468+0613567	18 44 14.68	6 13 56.8	14.269	0.393	0.30	EW
lrcby-901		18 44 12.74	6 12 2.9	19.078	0.410	1.30	RR Lyr
lrcby-908	18441225+0613529	18 44 12.25	6 13 53.0	15.247	1.236	0.09	EB
lrcby-919	18441006+0533292	18 44 10.06	5 33 29.3	16.217	0.363	0.08	DSCT
lrcby-946c	18440816+0610168	18 44 8.17	6 10 16.9	17.193	0.244	0.70	EW
lrcby-968	18440522+0552260	18 44 5.23	5 52 26.0	18.588	0.423	1.70	RR Lyr
lrcby-973	18440359+0522051	18 44 3.59	5 22 5.2	16.403	1.481	0.15	EB
lrcby-984	18440252+0548242	18 44 2.52	5 48 24.3	14.701	0.463	0.15	EA
lrcby-995c		18 44 0.8	5 19 2.2	15.553	0.725	0.15	EB
lrcby-996c	18440110+0535444	18 44 1.10	5 35 44.5	12.878	0.321	0.16	EW
lrcby-999c	18440041+0519072	18 44 0.42	5 19 7.3	15.059	0.725	0.13	EB
lrcby-1000	18440086+0535361	18 44 0.87	5 35 36.1	14.000	0.321	0.08	EW/DSCT
lrcby-1008	18435927+0521464	18 43 59.28	5 21 46.4	16.409	3.061	0.20	DCEP
lrcby-1029c	18435859+0628020	18 43 58.59	6 28 2.1	13.794	0.633	0.07	EB
lrcby-1030c	18435839+0628123	18 43 58.39	6 28 12.3	15.470	0.633	0.06	EB
lrcby-1034c	18435802+0628075	18 43 58.03	6 28 7.6	15.516	0.633	0.08	EB
lrcby-1044	18435520+0522548	18 43 55.20	5 22 54.8	16.651	0.314	0.20	EW
lrcby-1071	18435337+0548475	18 43 53.38	5 48 47.5	16.501	0.575	0.37	EB
lrcby-1072	18435362+0600168	18 43 53.62	6 0 16.9	15.725	0.772	0.30	EA
lrcby-1104	18434910+0609245	18 43 49.10	6 9 24.6	15.893	1.190	0.20	EW
lrcby-1120	18434697+0556585	18 43 46.98	5 56 58.6	17.576	0.395	0.40	EW
lrcby-1143	18434372+0602256	18 43 43.73	6 2 25.6	11.511	0.759	0.17	NSVS13910069
lrcby-1144	18434375+0603272	18 43 43.75	6 3 27.2	17.779	0.347	0.60	EW
lrcby-1190		18 43 36.53	5 26 28.2	18.299	0.321	1.20	EW
lrcby-1205	18433530+0621419	18 43 35.30	6 21 41.9	17.126	0.469	0.50	EB
lrcby-1215	18433327+0551450	18 43 33.27	5 51 45.1	17.023	0.288	0.72	EW
lrcby-1235	18433091+0539138	18 43 30.91	5 39 13.8	15.470	0.610	0.50	RR Lyr
lrcby-1242	18433143+0620232	18 43 31.44	6 20 23.3	17.254	0.130	0.55	RR Lyr
lrcby-1243	18433110+0611439	18 43 31.11	6 11 44.0	15.419	1.056	0.08	γDor
lrcby-1295	18432683+0620413	18 43 26.83	6 20 41.3	16.552	0.416	0.33	EW
lrcby-1309	18432485+0552266	18 43 24.86	5 52 26.7	15.371	0.540	0.15	EW
lrcby-1317	18432354+0520344	18 43 23.55	5 20 34.5	16.155	0.665	0.15	PULS
lrcby-1324	18432378+0609309	18 43 23.78	6 9 30.9	15.546	1.660	0.13	DCEP
lrcby-1337	18432149+0537507	18 43 21.49	5 37 50.7	13.090	2.119	0.03	EB
lrcby-1368		18 43 19.47	5 28 54.9	18.242	0.249	0.80	RR Lyr
lrcby-1389	18431869+0634267	18 43 18.70	6 34 26.7	16.863	0.342	0.30	EW
lrcby-1397	18431763+0623557	18 43 17.64	6 23 55.7	17.022	1.719	0.60	EB
lrcby-1401	18431695+0558002	18 43 16.95	5 58 0.3	11.632	1.847	0.20	EA
lrcby-1404	18431628+0533089	18 43 16.28	5 33 9.0	15.993	0.249	0.14	DSCT
lrcby-1448	18431282+0614350	18 43 12.82	6 14 35.7	17.179	0.820	0.40	EA
lrcby-1453c		18 43 11.29	5 17 49.2	16.466	12.433	0.37	DCEP
lrcby-1454c		18 43 11.19	5 17 56.2	16.347	12.382	0.50	DCEP
lrcby-1461c	18431091+0517531	18 43 10.92	5 17 53.2	15.659	12.390	0.30	DCEP
lrcby-1465	18431101+0539539	18 43 11.02	5 39 54.0	16.684	0.785	0.40	EW
lrcby-1476	18431107+0611448	18 43 11.08	6 11 44.8	12.332	1.085	0.17	EA
lrcby-1489		18 43 9.34	5 43 12.2	17.094	0.913	0.40	EW
lrcby-1506	18430703+0522468	18 43 7.03	5 22 46.9	15.793	2.461	0.13	DCEP
lrcby-1529	18430490+0538423	18 43 4.91	5 38 42.3	16.764	0.546	0.50	RR Lyr
lrcby-1531	18430533+0608291	18 43 5.33	6 8 29.2	14.512	0.413	0.33	EA
lrcby-1544	18430405+0617154	18 43 4.05	6 17 15.5	17.875	0.189	0.47	EW/DSCT
lrcby-1549	18430274+0525313	18 43 2.75	5 25 31.3	16.929	0.477	0.25	EW/EB
lrcby-1551	18430242+0518533	18 43 2.42	5 18 53.3	13.956	0.302	0.03	EW
lrcby-1583c	18425952+0552076	18 42 59.52	5 52 7.7	17.842	0.390	0.50	EW
lrcby-1589c	18425926+0552101	18 42 59.27	5 52 10.2	17.551	0.390	0.30	EW
lrcby-1603	18425868+0629391	18 42 58.69	6 29 39.1	12.055	2.118	0.07	EB
lrcby-1608	18425746+0551389	18 42 57.46	5 51 39.0	17.389	0.450	0.31	EB
lrcby-1614c	18425702+0549171	18 42 57.03	5 49 17.2	12.606	1.238	0.03	EA
lrcby-1619c	18425659+0549147	18 42 56.59	5 49 14.7	12.902	1.239	0.07	EA
lrcby-1638	18425372+0543184	18 42 53.73	5 43 18.4	16.585	0.634	0.30	EB
lrcby-1642	18425346+0614546	18 42 53.46	6 14 54.7	13.531	0.332	0.02	DSCT
lrcby-1667	18425061+0553088	18 42 50.62	5 53 8.8	13.363	0.449	0.60	EW
lrcby-1668	18425120+0625117	18 42 51.21	6 25 11.8	16.478	0.249	0.20	EA
lrcby-1732c	18424516+0554192	18 42 45.17	5 54 19.2	15.760	0.418	0.15	EW
lrcby-1735c	18424493+0554233	18 42 44.94	5 54 23.3	15.722	0.418	0.15	EW
lrcby-1739		18 42 43.95	5 19 60.0	18.000	0.885	1.30	EA
lrcby-1748	18424444+0627201	18 42 44.45	6 27 20.2	16.287	0.374	0.20	EB
lrcby-1754	18424315+0540436	18 42 43.15	5 40 43.6	13.537	0.878	0.40	EA
lrcby-1770	18424218+0533202	18 42 42.18	5 33 20.3	16.390	0.285	0.44	RR Lyr(c)
lrcby-1777	18424182+0549068	18 42 41.83	5 49 6.9	13.644	1.062	0.09	γDor
lrcby-1811	18423814+0615397	18 42 38.14	6 15 39.7	15.755	1.551	0.20	EA
lrcby-1814	18423764+0609351	18 42 37.65	6 9 35.1	14.459	1.138	0.30	EA
lrcby-1816	18423659+0524147	18 42 36.59	5 24 14.8	16.671	0.501	0.30	EB
lrcby-1867	18423147+0603367	18 42 31.47	6 3 36.8	13.137	0.488	0.02	DSCT
lrcby-1872	18423061+0536274	18 42 30.61	5 36 27.4	14.707	0.522	0.10	RR Lyr
lrcby-1878		18 42 29.54	5 29 17.5	19.009	0.445	1.70	RR Lyr
lrcby-1897	18422847+0613235	18 42 28.48	6 13 23.6	16.258	0.360	0.24	EW
lrcby-1918	18422528+0532596	18 42 25.29	5 32 59.7	13.664	2.136	0.05	EB
lrcby-1929	18422581+0632581	18 42 25.81	6 32 58.1	17.356	0.725	0.30	EW
lrcby-1935	18422389+0531169	18 42 23.90	5 31 16.9	16.971	0.346	0.17	EB
lrcby-1945	18422280+0520313	18 42 22.81	5 20 31.3	17.335	0.423	0.34	EW
lrcby-1971	18422109+0605350	18 42 21.09	6 5 35.1	17.238	0.408	0.30	EB
lrcby-1976	18422012+0557102	18 42 20.13	5 57 10.2	16.654	0.262	0.25	EA

Table A.7: *Statistical overwiev on the detected variable stars with BEST II in LRc02 target fields. Percentages given are related to number of stars detected for each field.*

	LRc2a	LRc2b
Nr. of stars detected	43616	54603
Stars with $j > 0.5$	1467 (3.4%)	1976 (3.6%)
Periodic variable stars	251 (0.6%)	175 (0.3%)
DSCT	22	13
DCEP	8	10
RR Lyr	28	13
α^2CVn	5	2
EA(Algol)	20	25
EB(β Lyr)	31	36
EW (W Uma)	117	55
other	19	21

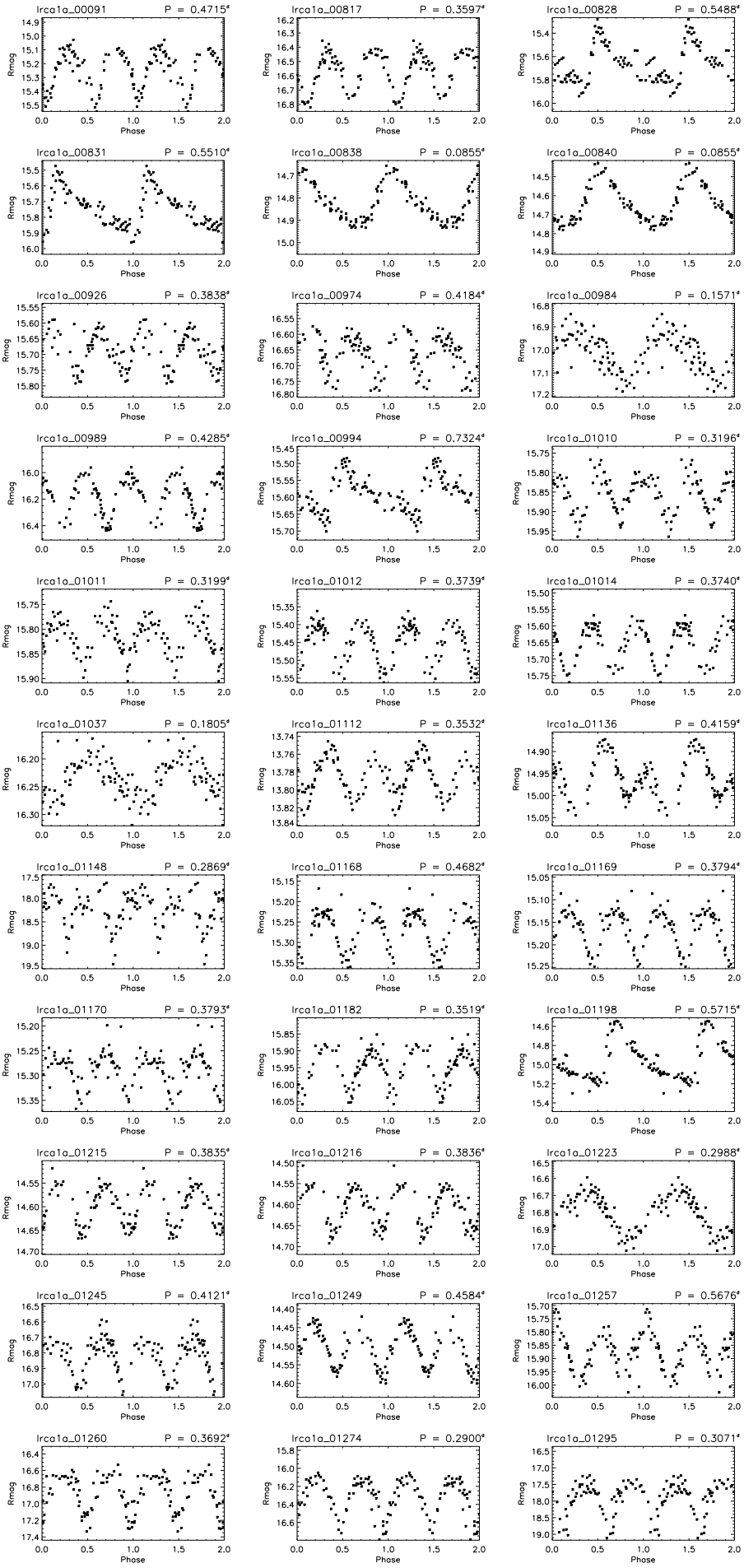
lrca1a_00091 P = 0.4715d
lrca1a_00817 P = 0.3597d
lrca1a_00828 P = 0.5488d
lrca1a_00831 P = 0.5510d
lrca1a_00838 P = 0.0855d
lrca1a_00840 P = 0.0855d
lrca1a_00926 P = 0.3838d
lrca1a_00974 P = 0.4184d
lrca1a_00984 P = 0.1571d
lrca1a_00989 P = 0.4285d
lrca1a_00994 P = 0.7324d
lrca1a_01010 P = 0.3196d
lrca1a_01011 P = 0.3199d
lrca1a_01012 P = 0.3739d
lrca1a_01014 P = 0.3740d
lrca1a_01037 P = 0.1805d
lrca1a_01112 P = 0.3532d
lrca1a_01136 P = 0.4159d
lrca1a_01148 P = 0.2869d
lrca1a_01168 P = 0.4682d
lrca1a_01169 P = 0.3794d
lrca1a_01170 P = 0.3793d
lrca1a_01182 P = 0.3519d
lrca1a_01198 P = 0.5715d
lrca1a_01215 P = 0.3835d
lrca1a_01216 P = 0.3836d
lrca1a_01223 P = 0.2988d
lrca1a_01245 P = 0.4121d
lrca1a_01249 P = 0.4584d
lrca1a_01257 P = 0.5676d
lrca1a_01260 P = 0.3692d
lrca1a_01274 P = 0.2900d
lrca1a_01295 P = 0.3071d
Rmag
Phase

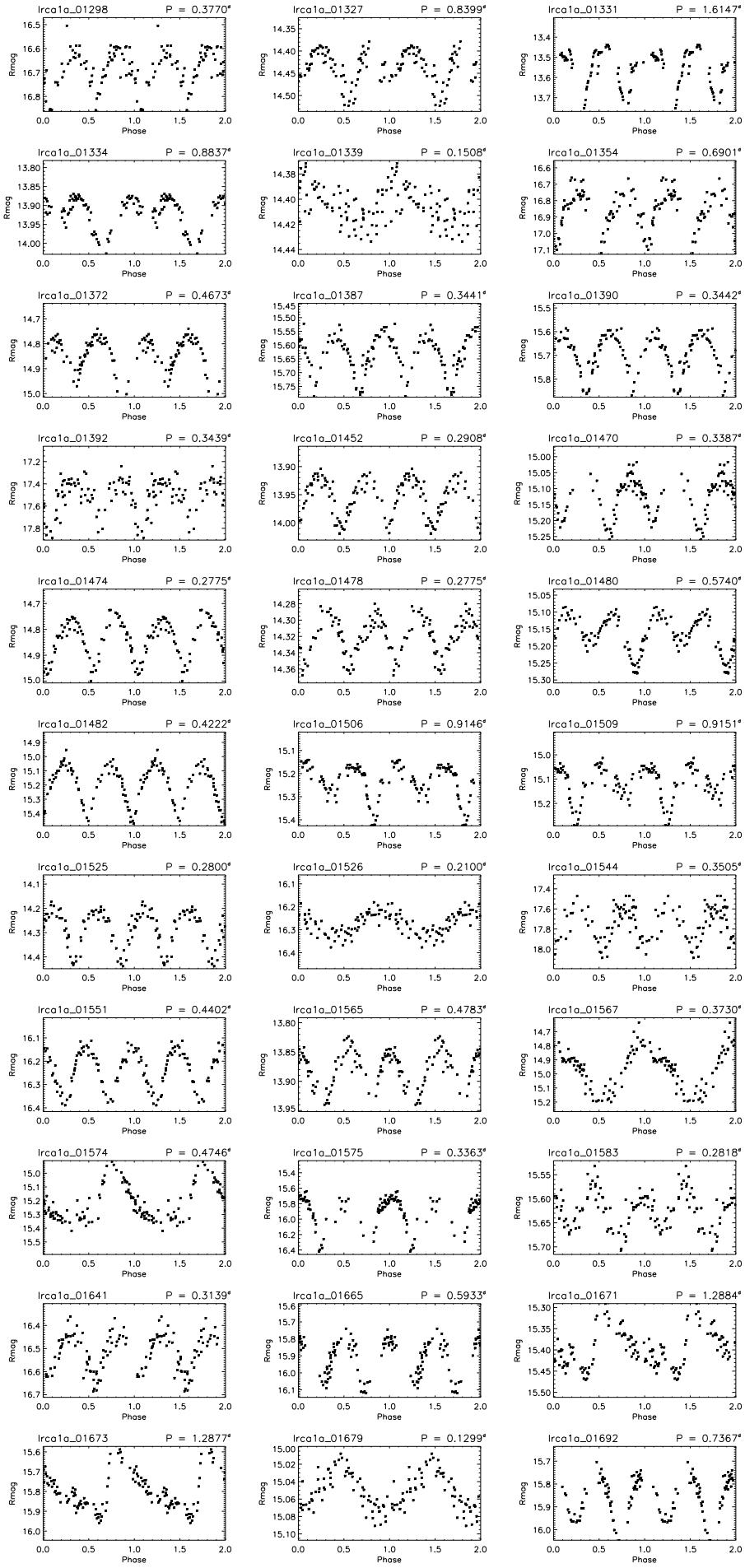
Ircа1a_01298 P = 0.3770d
Ircа1a_01327 P = 0.8399d
Ircа1a_01331 P = 1.6147d
Ircа1a_01334 P = 0.8837d
Ircа1a_01339 P = 0.1508d
Ircа1a_01354 P = 0.6901d
Ircа1a_01372 P = 0.4673d
Ircа1a_01387 P = 0.3441d
Ircа1a_01390 P = 0.3442d
Ircа1a_01392 P = 0.3439d
Ircа1a_01452 P = 0.2908d
Ircа1a_01470 P = 0.3387d
Ircа1a_01474 P = 0.2775d
Ircа1a_01478 P = 0.2775d
Ircа1a_01480 P = 0.5740d
Ircа1a_01482 P = 0.4222d
Ircа1a_01506 P = 0.9146d
Ircа1a_01509 P = 0.9151d
Ircа1a_01525 P = 0.2800d
Ircа1a_01526 P = 0.2100d
Ircа1a_01544 P = 0.3505d
Ircа1a_01551 P = 0.4402d
Ircа1a_01565 P = 0.4783d
Ircа1a_01567 P = 0.3730d
Ircа1a_01574 P = 0.4746d
Ircа1a_01575 P = 0.3363d
Ircа1a_01583 P = 0.2818d
Ircа1a_01641 P = 0.3139d
Ircа1a_01665 P = 0.5933d
Ircа1a_01671 P = 1.2884d
Ircа1a_01673 P = 1.2877d
Ircа1a_01679 P = 0.1299d
Ircа1a_01692 P = 0.7367d
Rmag
Phase

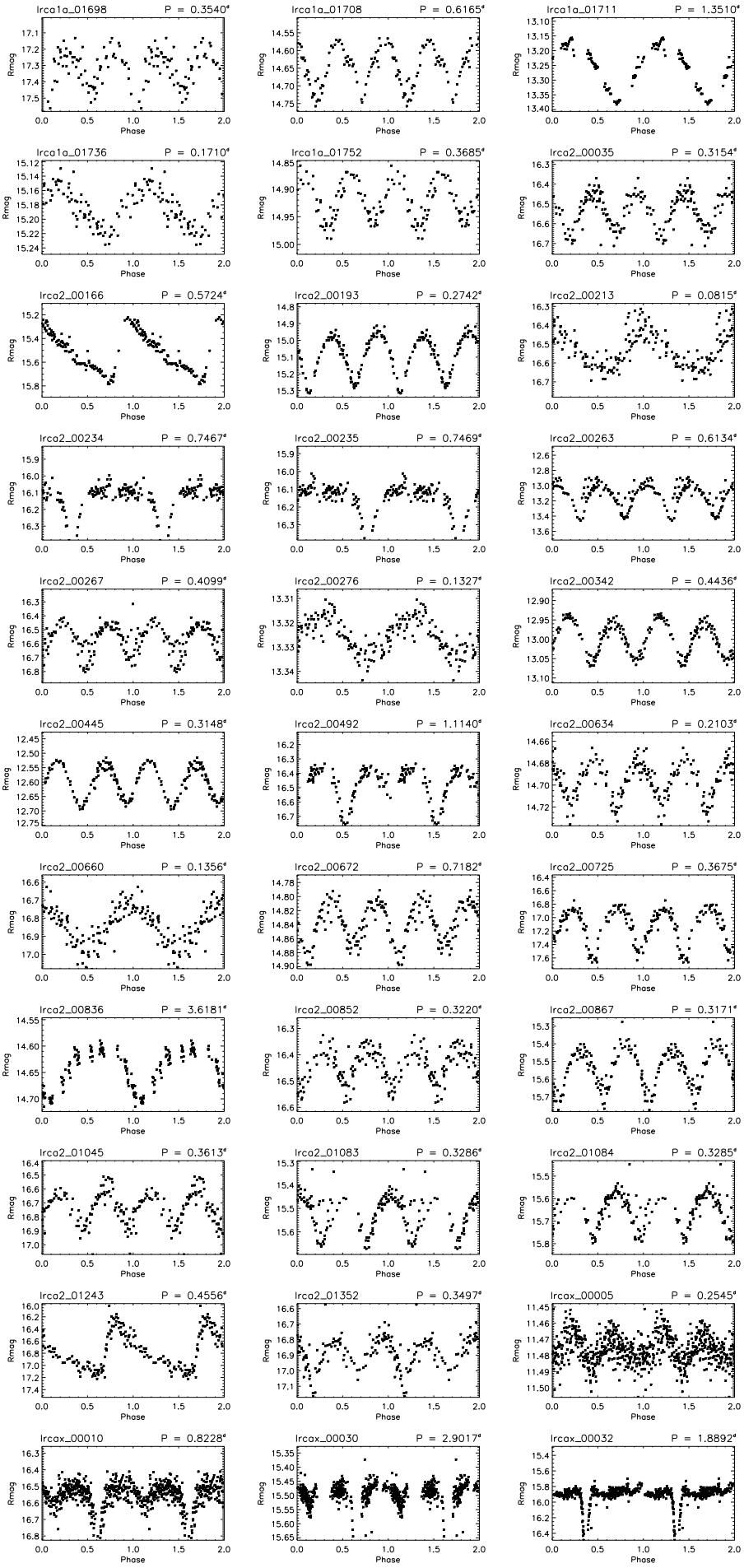
Irca1a_01698 P = 0.3540d
Irca1a_01708 P = 0.6165d
Irca1a_01711 P = 1.3510d
Irca1a_01736 P = 0.1710d
Irca1a_01752 P = 0.3685d
Irca2_00035 P = 0.3154d
Irca2_00166 P = 0.5724d
Irca2_00193 P = 0.2742d
Irca2_00213 P = 0.0815d
Irca2_00234 P = 0.7467d
Irca2_00235 P = 0.7469d
Irca2_00263 P = 0.6134d
Irca2_00267 P = 0.4099d
Irca2_00276 P = 0.1327d
Irca2_00342 P = 0.4436d
Irca2_00445 P = 0.3148d
Irca2_00492 P = 1.1140d
Irca2_00634 P = 0.2103d
Irca2_00660 P = 0.1356d
Irca2_00672 P = 0.7182d
Irca2_00725 P = 0.3675d
Irca2_00836 P = 3.6181d
Irca2_00852 P = 0.3220d
Irca2_00867 P = 0.3171d
Irca2_01045 P = 0.3613d
Irca2_01083 P = 0.3286d
Irca2_01084 P = 0.3285d
Irca2_01243 P = 0.4556d
Irca2_01352 P = 0.3497d
Ircax_00005 P = 0.2545d
Ircax_00010 P = 0.8228d
Ircax_00030 P = 2.9017d
Ircax_00032 P = 1.8892d
Rmag
Phase

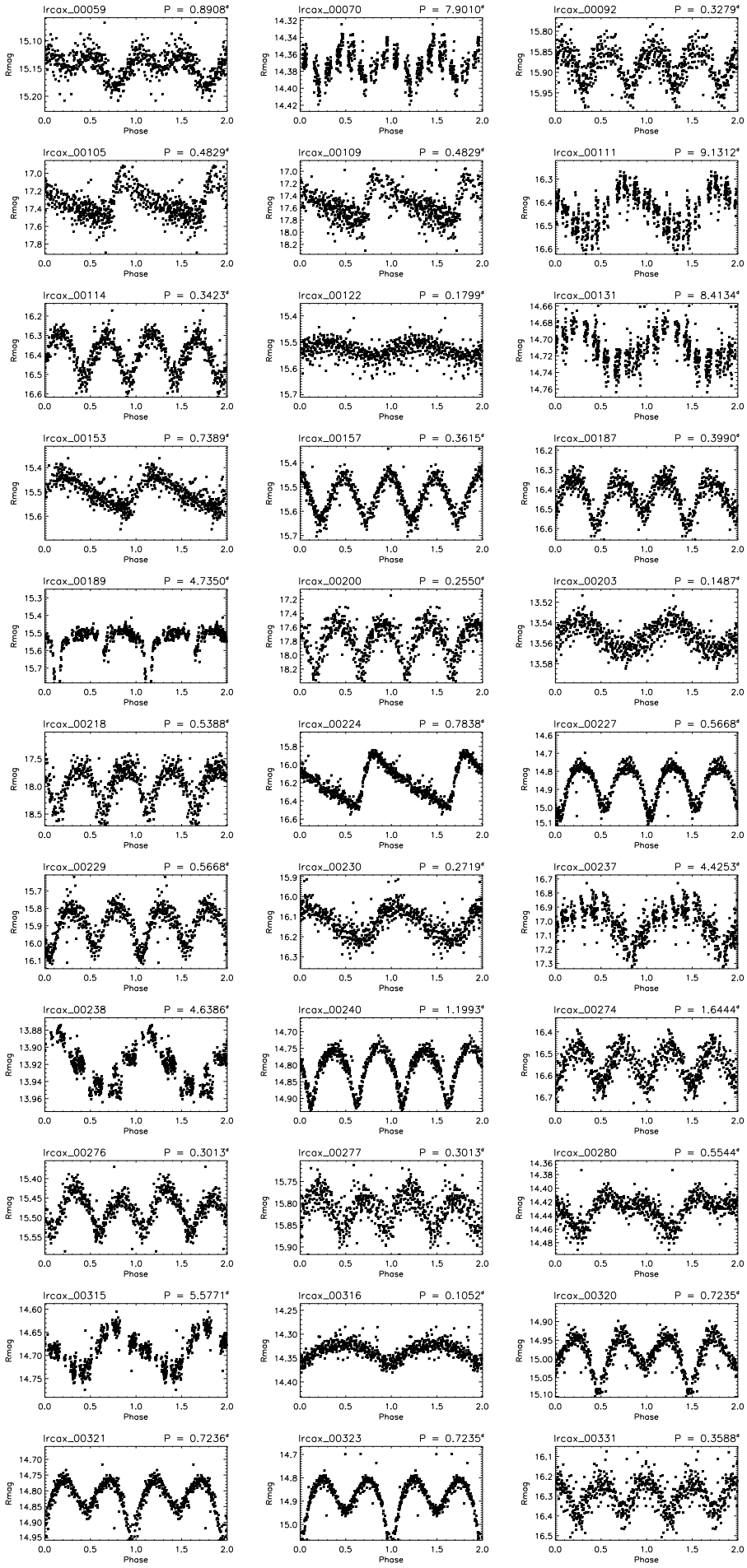
Ircax_00059 P = 0.8908d
Ircax_00070 P = 7.9010d
Ircax_00092 P = 0.3279d
Ircax_00105 P = 0.4829d
Ircax_00109 P = 0.4829d
Ircax_00111 P = 9.1312d
Ircax_00114 P = 0.3423d
Ircax_00122 P = 0.1799d
Ircax_00131 P = 8.4134d
Ircax_00153 P = 0.7389d
Ircax_00157 P = 0.3615d
Ircax_00187 P = 0.3990d
Ircax_00189 P = 4.7350d
Ircax_00200 P = 0.2550d
Ircax_00203 P = 0.1487d
Ircax_00218 P = 0.5388d
Ircax_00224 P = 0.7838d
Ircax_00227 P = 0.5668d
Ircax_00229 P = 0.5668d
Ircax_00230 P = 0.2719d
Ircax_00237 P = 4.4253d
Ircax_00238 P = 4.6386d
Ircax_00240 P = 1.1993d
Ircax_00274 P = 1.6444d
Ircax_00276 P = 0.3013d
Ircax_00277 P = 0.3013d
Ircax_00280 P = 0.5544d
Ircax_00315 P = 5.5771d
Ircax_00316 P = 0.1052d
Ircax_00320 P = 0.7235d
Ircax_00321 P = 0.7236d
Ircax_00323 P = 0.7235d
Ircax_00331 P = 0.3588d
Rmag
Phase

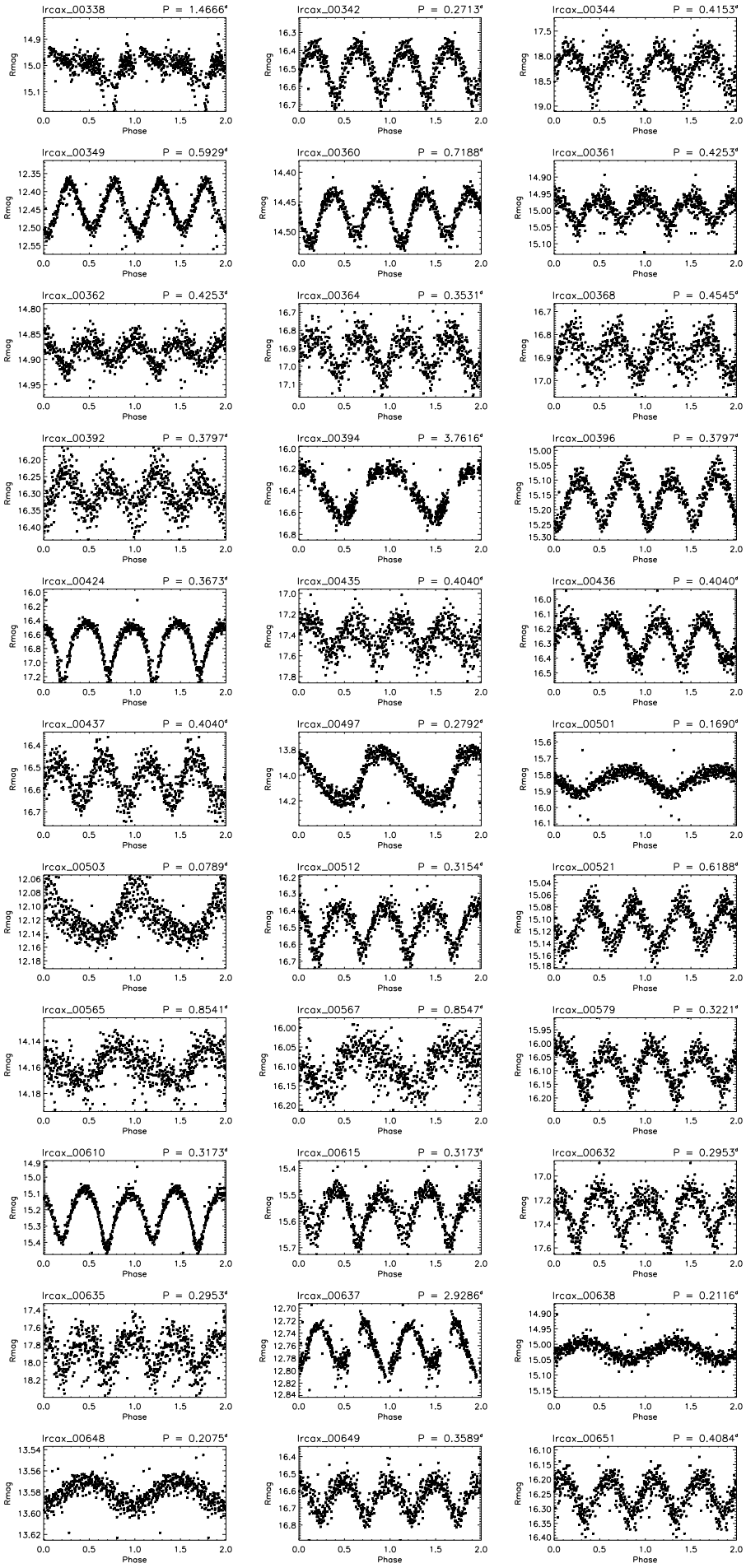
Ircax_00338 P = 1.4666ᵈ
Ircax_00342 P = 0.2713ᵈ
Ircax_00344 P = 0.4153ᵈ
Ircax_00349 P = 0.5929ᵈ
Ircax_00360 P = 0.7188ᵈ
Ircax_00361 P = 0.4253ᵈ
Ircax_00362 P = 0.4253ᵈ
Ircax_00364 P = 0.3531ᵈ
Ircax_00368 P = 0.4545ᵈ
Ircax_00392 P = 0.3797ᵈ
Ircax_00394 P = 3.7616ᵈ
Ircax_00396 P = 0.3797ᵈ
Ircax_00424 P = 0.3673ᵈ
Ircax_00435 P = 0.4040ᵈ
Ircax_00436 P = 0.4040ᵈ
Ircax_00437 P = 0.4040ᵈ
Ircax_00497 P = 0.2792ᵈ
Ircax_00501 P = 0.1690ᵈ
Ircax_00503 P = 0.0789ᵈ
Ircax_00512 P = 0.3154ᵈ
Ircax_00521 P = 0.6188ᵈ
Ircax_00565 P = 0.8541ᵈ
Ircax_00567 P = 0.8547ᵈ
Ircax_00579 P = 0.3221ᵈ
Ircax_00610 P = 0.3173ᵈ
Ircax_00615 P = 0.3173ᵈ
Ircax_00632 P = 0.2953ᵈ
Ircax_00635 P = 0.2953ᵈ
Ircax_00637 P = 2.9286ᵈ
Ircax_00638 P = 0.2116ᵈ
Ircax_00648 P = 0.2075ᵈ
Ircax_00649 P = 0.3589ᵈ
Ircax_00651 P = 0.4084ᵈ
Rmag
Phase

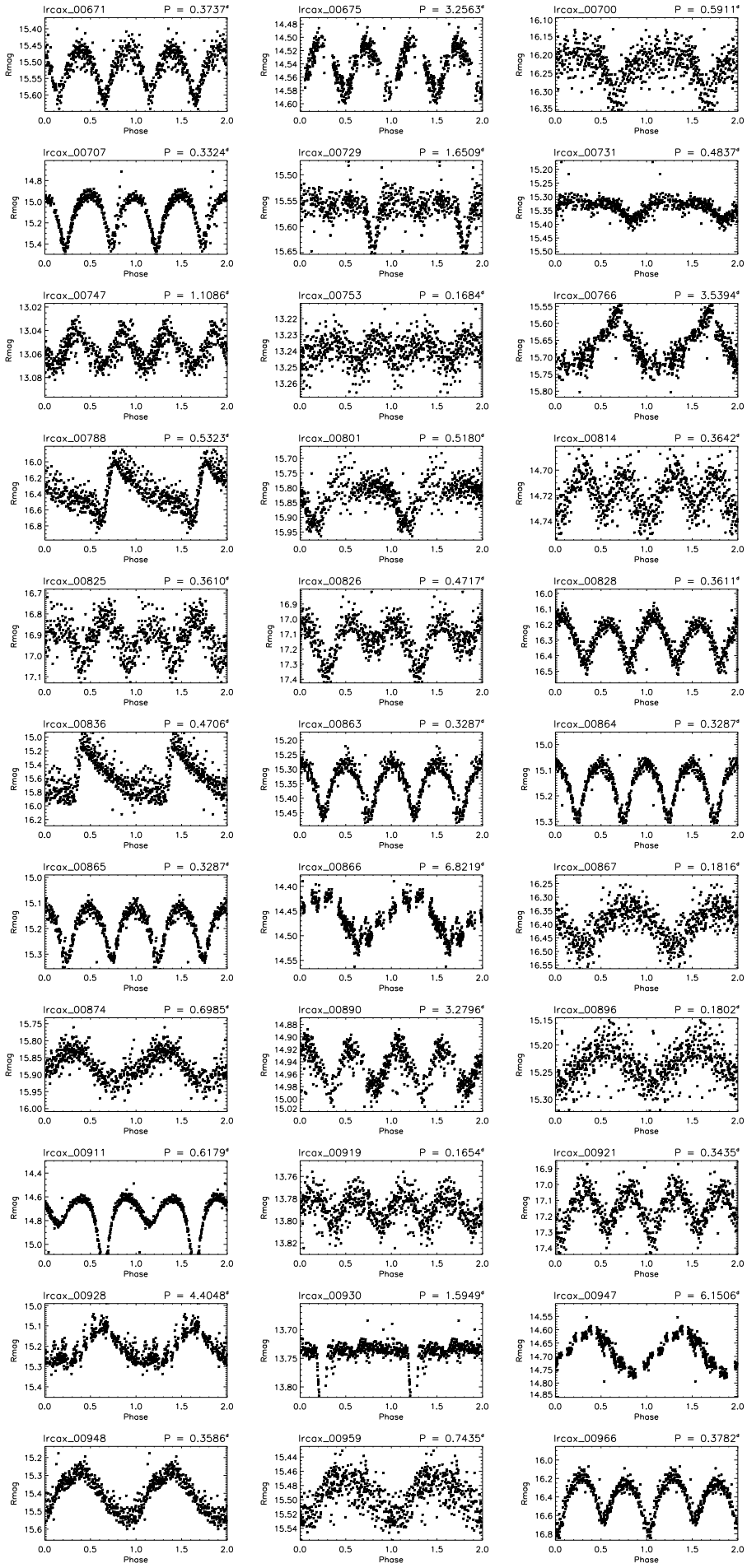
lrcax_00671 P = 0.3737d
lrcax_00675 P = 3.2563d
lrcax_00700 P = 0.5911d
lrcax_00707 P = 0.3324d
lrcax_00729 P = 1.6509d
lrcax_00731 P = 0.4837d
lrcax_00747 P = 1.1086d
lrcax_00753 P = 0.1684d
lrcax_00766 P = 3.5394d
lrcax_00788 P = 0.5323d
lrcax_00801 P = 0.5180d
lrcax_00814 P = 0.3642d
lrcax_00825 P = 0.3610d
lrcax_00826 P = 0.4717d
lrcax_00828 P = 0.3611d
lrcax_00836 P = 0.4706d
lrcax_00863 P = 0.3287d
lrcax_00864 P = 0.3287d
lrcax_00865 P = 0.3287d
lrcax_00866 P = 6.8219d
lrcax_00867 P = 0.1816d
lrcax_00874 P = 0.6985d
lrcax_00890 P = 3.2796d
lrcax_00896 P = 0.1802d
lrcax_00911 P = 0.6179d
lrcax_00919 P = 0.1654d
lrcax_00921 P = 0.3435d
lrcax_00928 P = 4.4048d
lrcax_00930 P = 1.5949d
lrcax_00947 P = 6.1506d
lrcax_00948 P = 0.3586d
lrcax_00959 P = 0.7435d
lrcax_00966 P = 0.3782d
Rmag
Phase

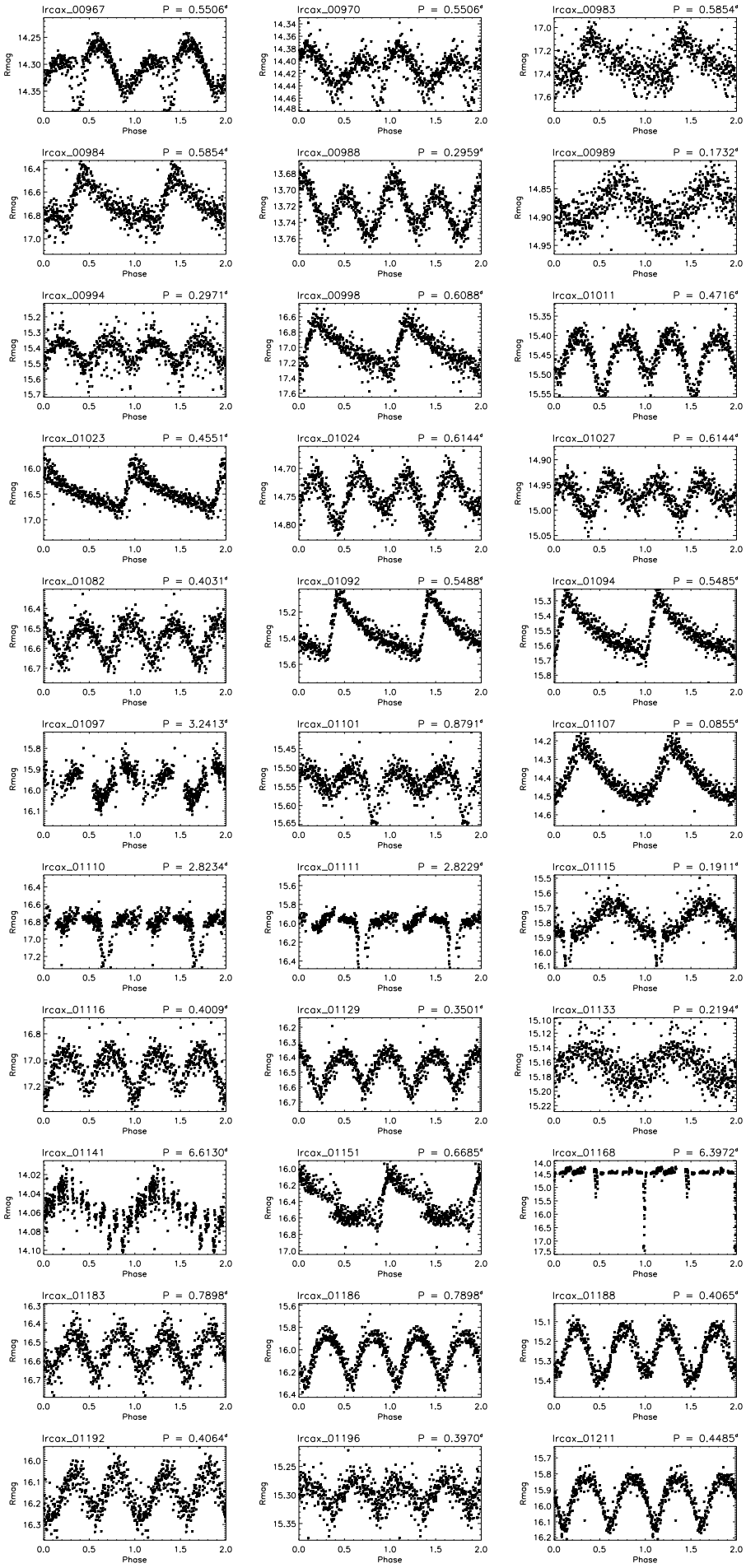
Ircax_00967 P = 0.5506d
Ircax_00970 P = 0.5506d
Ircax_00983 P = 0.5854d
Ircax_00984 P = 0.5854d
Ircax_00988 P = 0.2959d
Ircax_00989 P = 0.1732d
Ircax_00994 P = 0.2971d
Ircax_00998 P = 0.6088d
Ircax_01011 P = 0.4716d
Ircax_01023 P = 0.4551d
Ircax_01024 P = 0.6144d
Ircax_01027 P = 0.6144d
Ircax_01082 P = 0.4031d
Ircax_01092 P = 0.5488d
Ircax_01094 P = 0.5485d
Ircax_01097 P = 3.2413d
Ircax_01101 P = 0.8791d
Ircax_01107 P = 0.0855d
Ircax_01110 P = 2.8234d
Ircax_01111 P = 2.8229d
Ircax_01115 P = 0.1911d
Ircax_01116 P = 0.4009d
Ircax_01129 P = 0.3501d
Ircax_01133 P = 0.2194d
Ircax_01141 P = 6.6130d
Ircax_01151 P = 0.6685d
Ircax_01168 P = 6.3972d
Ircax_01183 P = 0.7898d
Ircax_01186 P = 0.7898d
Ircax_01188 P = 0.4065d
Ircax_01192 P = 0.4064d
Ircax_01196 P = 0.3970d
Ircax_01211 P = 0.4485d
Rmag
Phase

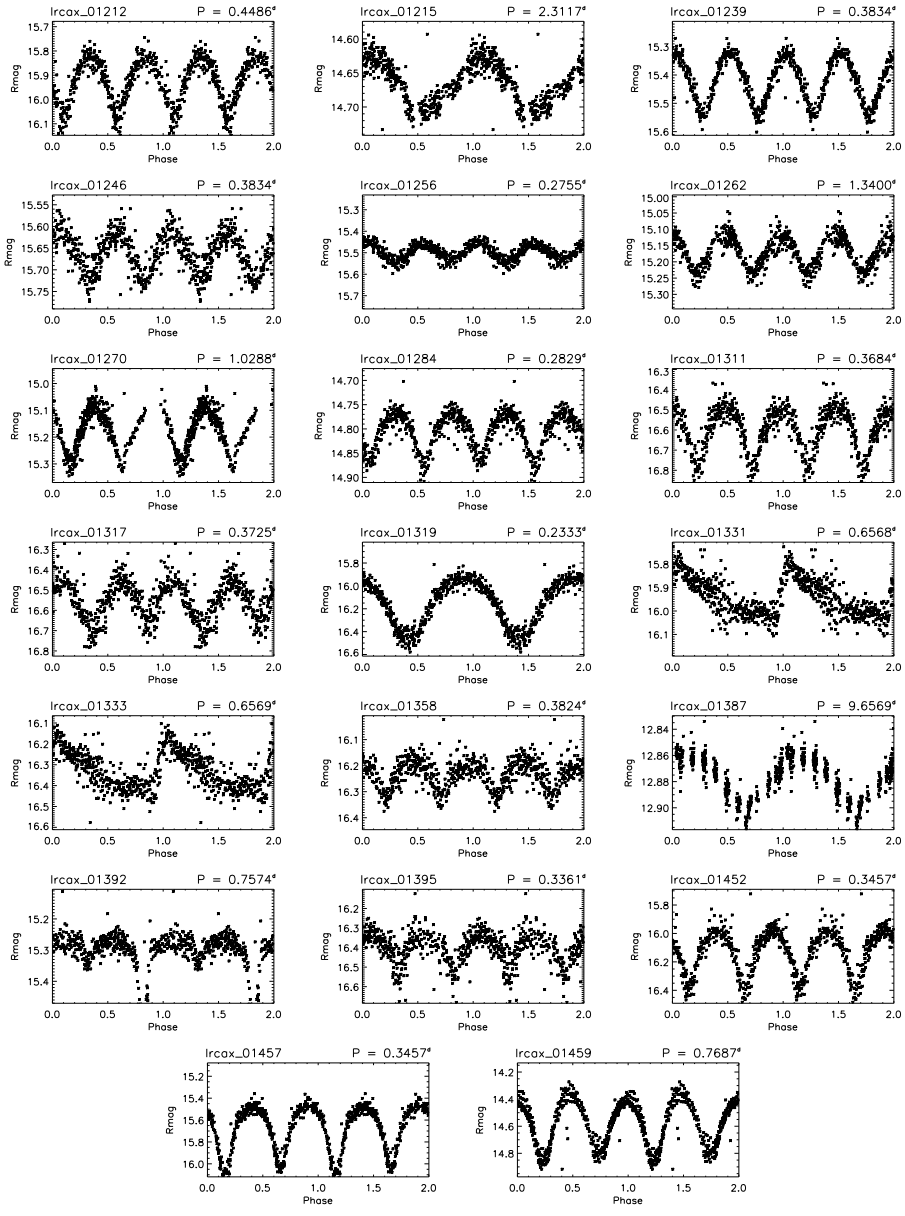

Figure A.22: *Variable stars in BEST II lrca(x1a2) fields with the second phase mirrored.*

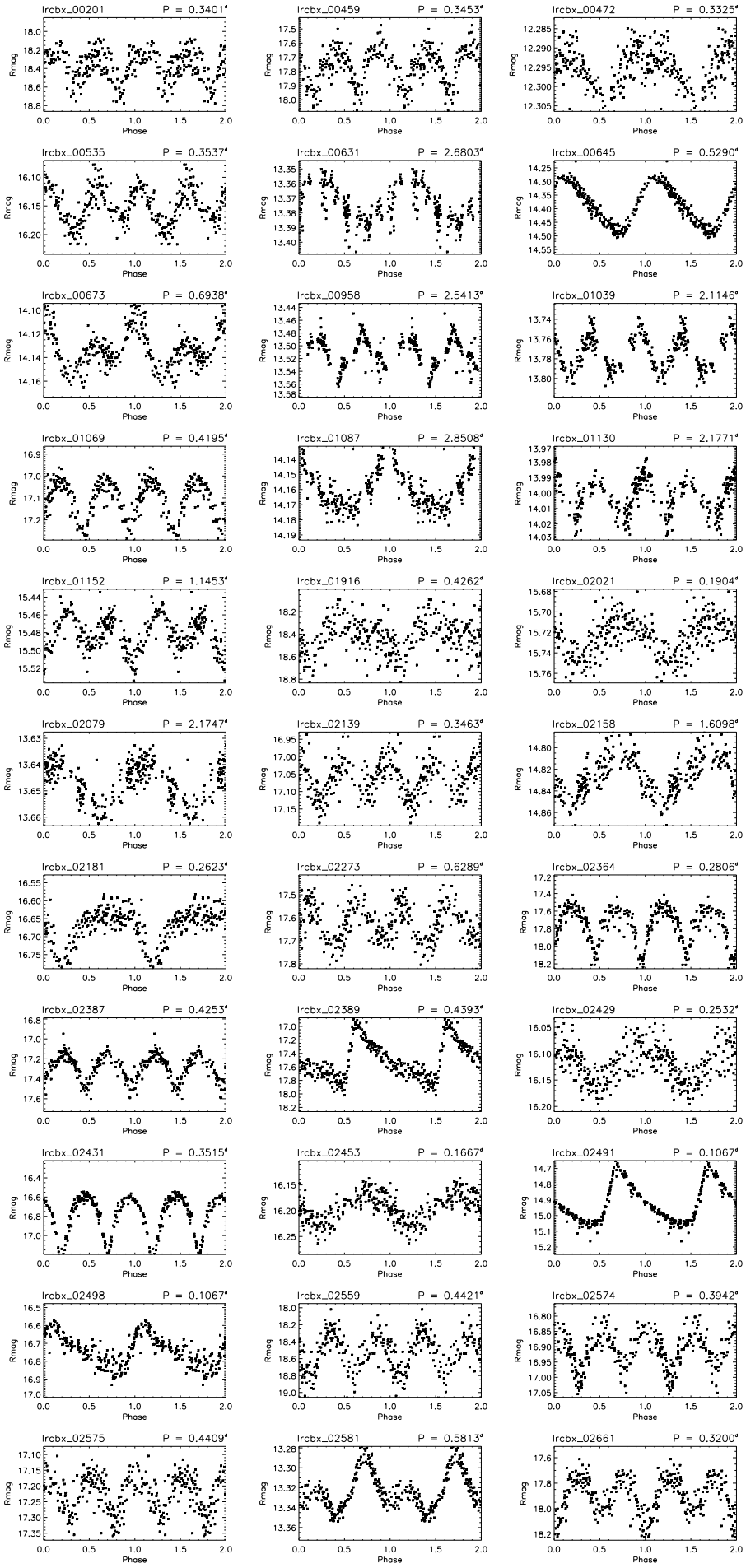
lrcbx_00201 P = 0.3401d
lrcbx_00459 P = 0.3453d
lrcbx_00472 P = 0.3325d
lrcbx_00535 P = 0.3537d
lrcbx_00631 P = 2.6803d
lrcbx_00645 P = 0.5290d
lrcbx_00673 P = 0.6938d
lrcbx_00958 P = 2.5413d
lrcbx_01039 P = 2.1146d
lrcbx_01069 P = 0.4195d
lrcbx_01087 P = 2.8508d
lrcbx_01130 P = 2.1771d
lrcbx_01152 P = 1.1453d
lrcbx_01916 P = 0.4262d
lrcbx_02021 P = 0.1904d
lrcbx_02079 P = 2.1747d
lrcbx_02139 P = 0.3463d
lrcbx_02158 P = 1.6098d
lrcbx_02181 P = 0.2623d
lrcbx_02273 P = 0.6289d
lrcbx_02364 P = 0.2806d
lrcbx_02387 P = 0.4253d
lrcbx_02389 P = 0.4393d
lrcbx_02429 P = 0.2532d
lrcbx_02431 P = 0.3515d
lrcbx_02453 P = 0.1667d
lrcbx_02491 P = 0.1067d
lrcbx_02498 P = 0.1067d
lrcbx_02559 P = 0.4421d
lrcbx_02574 P = 0.3942d
lrcbx_02575 P = 0.4409d
lrcbx_02581 P = 0.5813d
lrcbx_02661 P = 0.3200d
Rmag
Phase

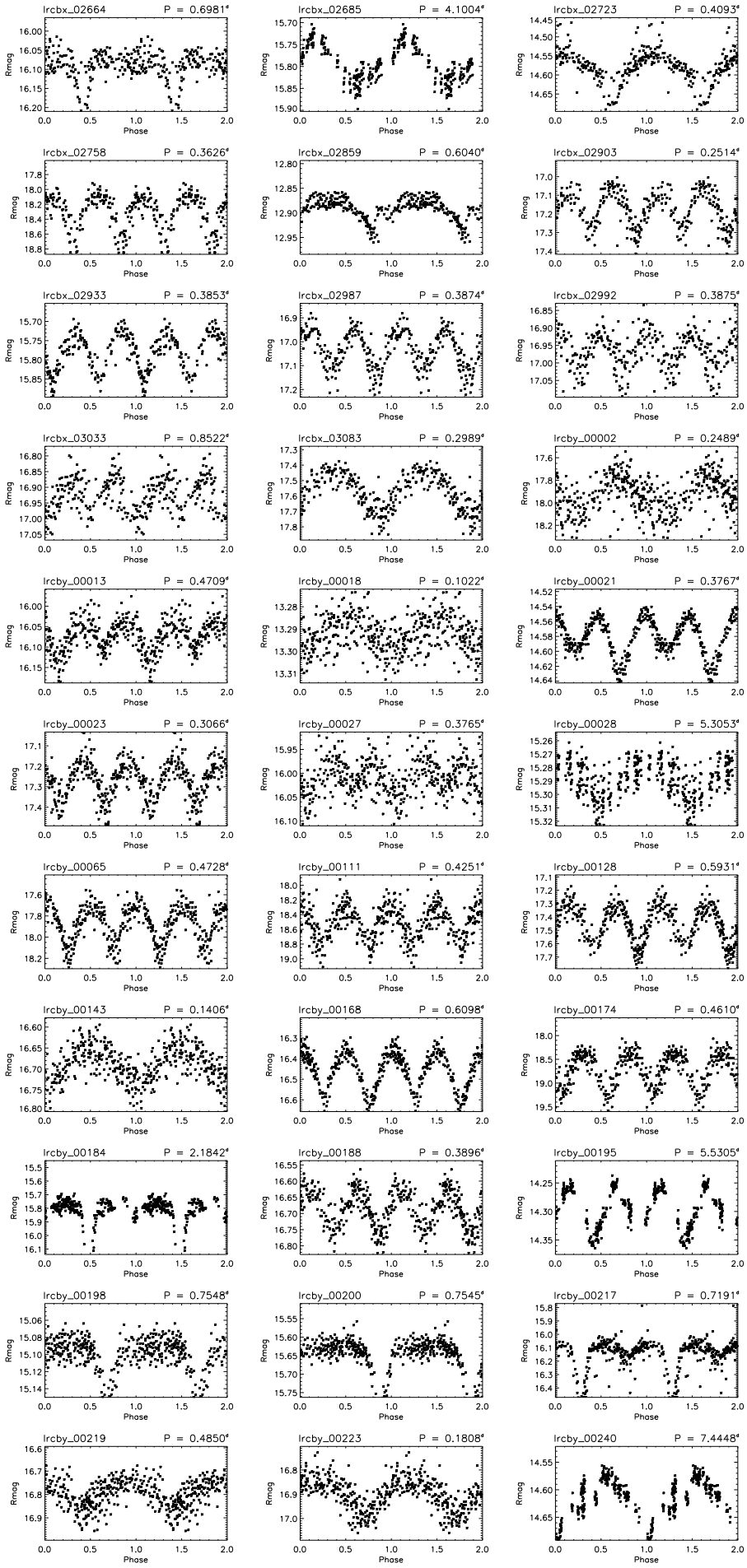
lrcbx_02664 P = 0.6981d
lrcbx_02685 P = 4.1004d
lrcbx_02723 P = 0.4093d
lrcbx_02758 P = 0.3626d
lrcbx_02859 P = 0.6040d
lrcbx_02903 P = 0.2514d
lrcbx_02933 P = 0.3853d
lrcbx_02987 P = 0.3874d
lrcbx_02992 P = 0.3875d
lrcbx_03033 P = 0.8522d
lrcbx_03083 P = 0.2989d
lrcby_00002 P = 0.2489d
lrcby_00013 P = 0.4709d
lrcby_00018 P = 0.1022d
lrcby_00021 P = 0.3767d
lrcby_00023 P = 0.3066d
lrcby_00027 P = 0.3765d
lrcby_00028 P = 5.3053d
lrcby_00065 P = 0.4728d
lrcby_00111 P = 0.4251d
lrcby_00128 P = 0.5931d
lrcby_00143 P = 0.1406d
lrcby_00168 P = 0.6098d
lrcby_00174 P = 0.4610d
lrcby_00184 P = 2.1842d
lrcby_00188 P = 0.3896d
lrcby_00195 P = 5.5305d
lrcby_00198 P = 0.7548d
lrcby_00200 P = 0.7545d
lrcby_00217 P = 0.7191d
lrcby_00219 P = 0.4850d
lrcby_00223 P = 0.1808d
lrcby_00240 P = 7.4448d
Rmag
Phase

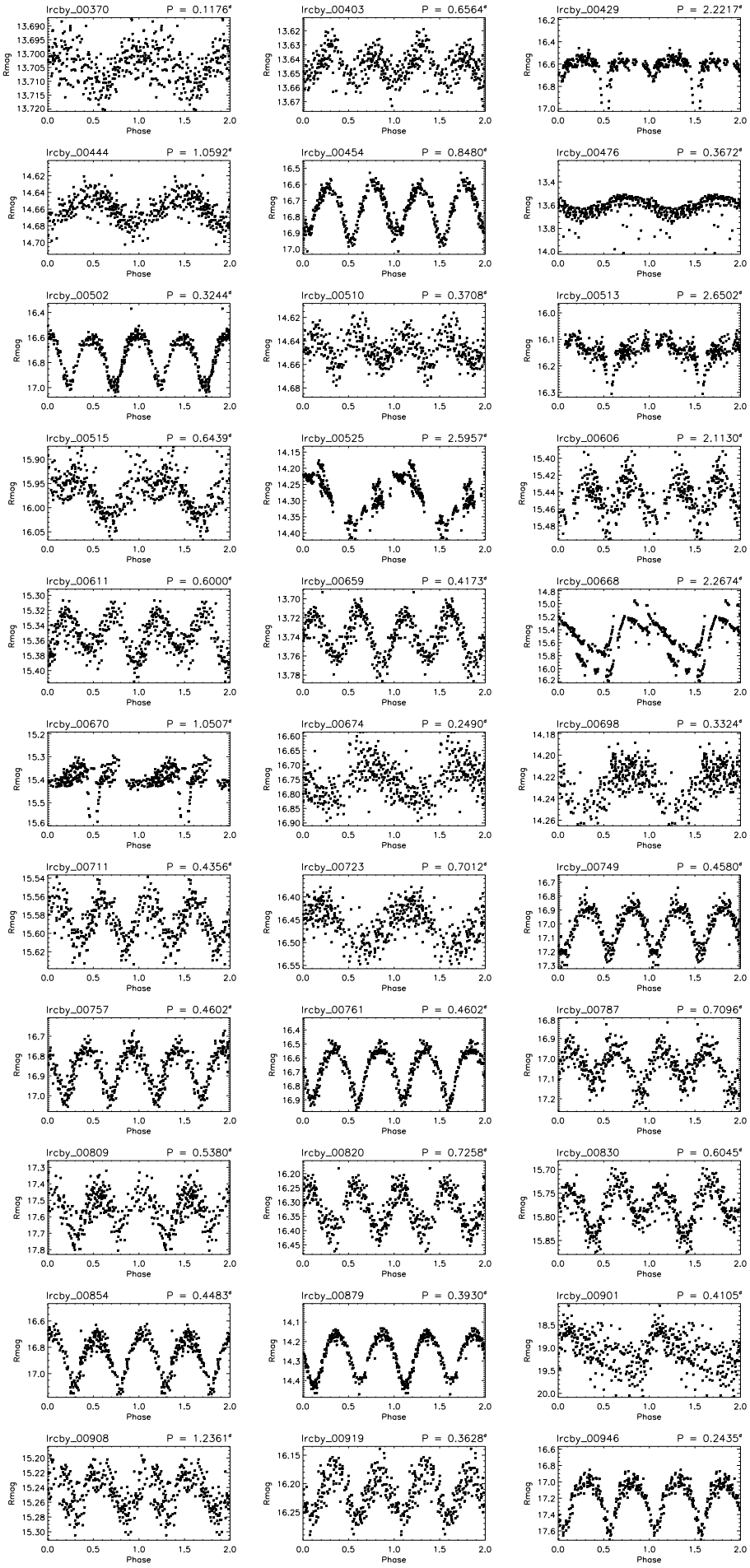
lrcby_00370 P = 0.1176d
lrcby_00403 P = 0.6564d
lrcby_00429 P = 2.2217d
lrcby_00444 P = 1.0592d
lrcby_00454 P = 0.8480d
lrcby_00476 P = 0.3672d
lrcby_00502 P = 0.3244d
lrcby_00510 P = 0.3708d
lrcby_00513 P = 2.6502d
lrcby_00515 P = 0.6439d
lrcby_00525 P = 2.5957d
lrcby_00606 P = 2.1130d
lrcby_00611 P = 0.6000d
lrcby_00659 P = 0.4173d
lrcby_00668 P = 2.2674d
lrcby_00670 P = 1.0507d
lrcby_00674 P = 0.2490d
lrcby_00698 P = 0.3324d
lrcby_00711 P = 0.4356d
lrcby_00723 P = 0.7012d
lrcby_00749 P = 0.4580d
lrcby_00757 P = 0.4602d
lrcby_00761 P = 0.4602d
lrcby_00787 P = 0.7096d
lrcby_00809 P = 0.5380d
lrcby_00820 P = 0.7258d
lrcby_00830 P = 0.6045d
lrcby_00854 P = 0.4483d
lrcby_00879 P = 0.3930d
lrcby_00901 P = 0.4105d
lrcby_00908 P = 1.2361d
lrcby_00919 P = 0.3628d
lrcby_00946 P = 0.2435d
Rmag
Phase

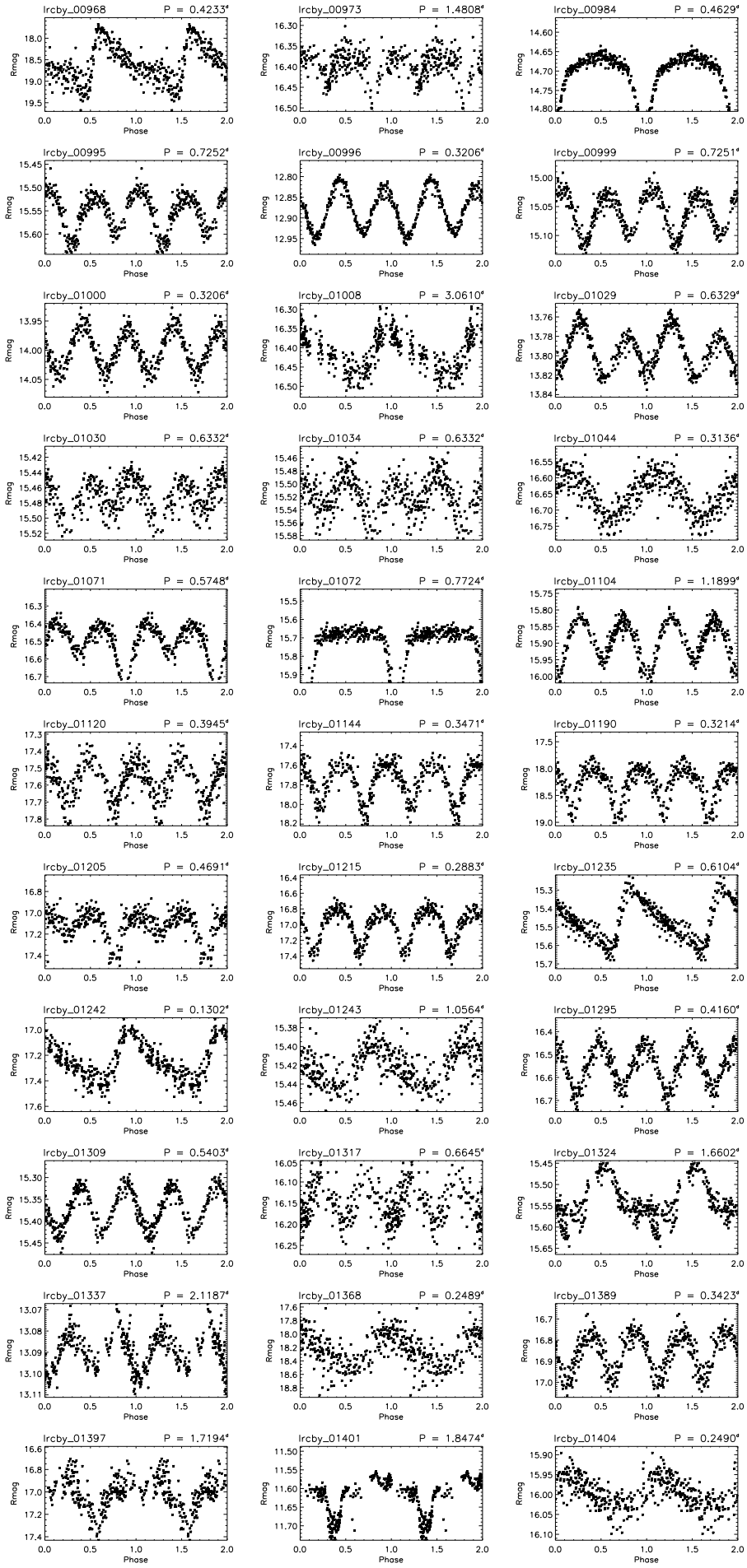
Ircby_00968 P = 0.4233d
Ircby_00973 P = 1.4808d
Ircby_00984 P = 0.4629d
Ircby_00995 P = 0.7252d
Ircby_00996 P = 0.3206d
Ircby_00999 P = 0.7251d
Ircby_01000 P = 0.3206d
Ircby_01008 P = 3.0610d
Ircby_01029 P = 0.6329d
Ircby_01030 P = 0.6332d
Ircby_01034 P = 0.6332d
Ircby_01044 P = 0.3136d
Ircby_01071 P = 0.5748d
Ircby_01072 P = 0.7724d
Ircby_01104 P = 1.1899d
Ircby_01120 P = 0.3945d
Ircby_01144 P = 0.3471d
Ircby_01190 P = 0.3214d
Ircby_01205 P = 0.4691d
Ircby_01215 P = 0.2883d
Ircby_01235 P = 0.6104d
Ircby_01242 P = 0.1302d
Ircby_01243 P = 1.0564d
Ircby_01295 P = 0.4160d
Ircby_01309 P = 0.5403d
Ircby_01317 P = 0.6645d
Ircby_01324 P = 1.6602d
Ircby_01337 P = 2.1187d
Ircby_01368 P = 0.2489d
Ircby_01389 P = 0.3423d
Ircby_01397 P = 1.7194d
Ircby_01401 P = 1.8474d
Ircby_01404 P = 0.2490d
Rmag
Phase

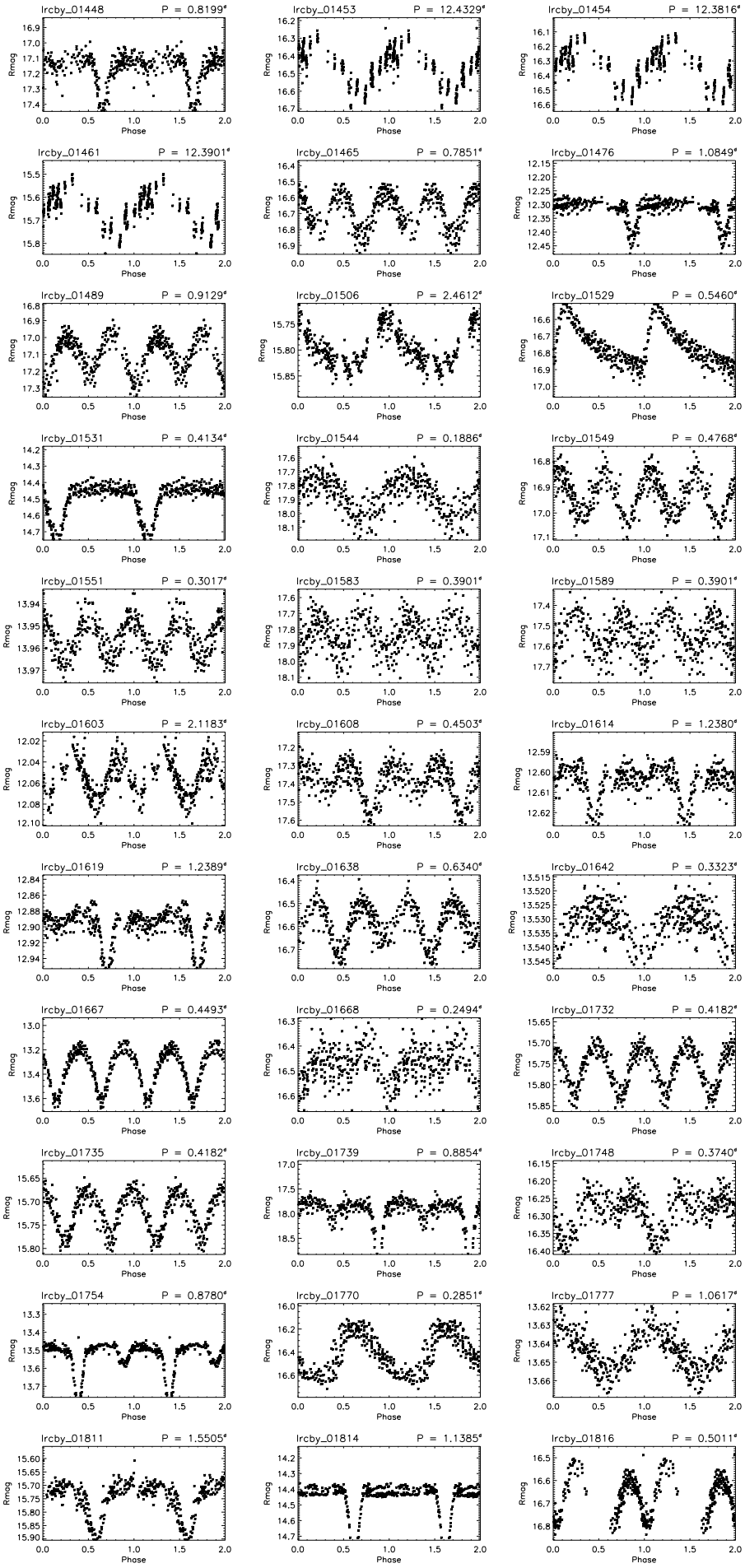
lrcby_01448 P = 0.8199d
lrcby_01453 P = 12.4329d
lrcby_01454 P = 12.3816d
lrcby_01461 P = 12.3901d
lrcby_01465 P = 0.7851d
lrcby_01476 P = 1.0849d
lrcby_01489 P = 0.9129d
lrcby_01506 P = 2.4612d
lrcby_01529 P = 0.5460d
lrcby_01531 P = 0.4134d
lrcby_01544 P = 0.1886d
lrcby_01549 P = 0.4768d
lrcby_01551 P = 0.3017d
lrcby_01583 P = 0.3901d
lrcby_01589 P = 0.3901d
lrcby_01603 P = 2.1183d
lrcby_01608 P = 0.4503d
lrcby_01614 P = 1.2380d
lrcby_01619 P = 1.2389d
lrcby_01638 P = 0.6340d
lrcby_01642 P = 0.3323d
lrcby_01667 P = 0.4493d
lrcby_01668 P = 0.2494d
lrcby_01732 P = 0.4182d
lrcby_01735 P = 0.4182d
lrcby_01739 P = 0.8854d
lrcby_01748 P = 0.3740d
lrcby_01754 P = 0.8780d
lrcby_01770 P = 0.2851d
lrcby_01777 P = 1.0617d
lrcby_01811 P = 1.5505d
lrcby_01814 P = 1.1385d
lrcby_01816 P = 0.5011d
Rmag
Phase

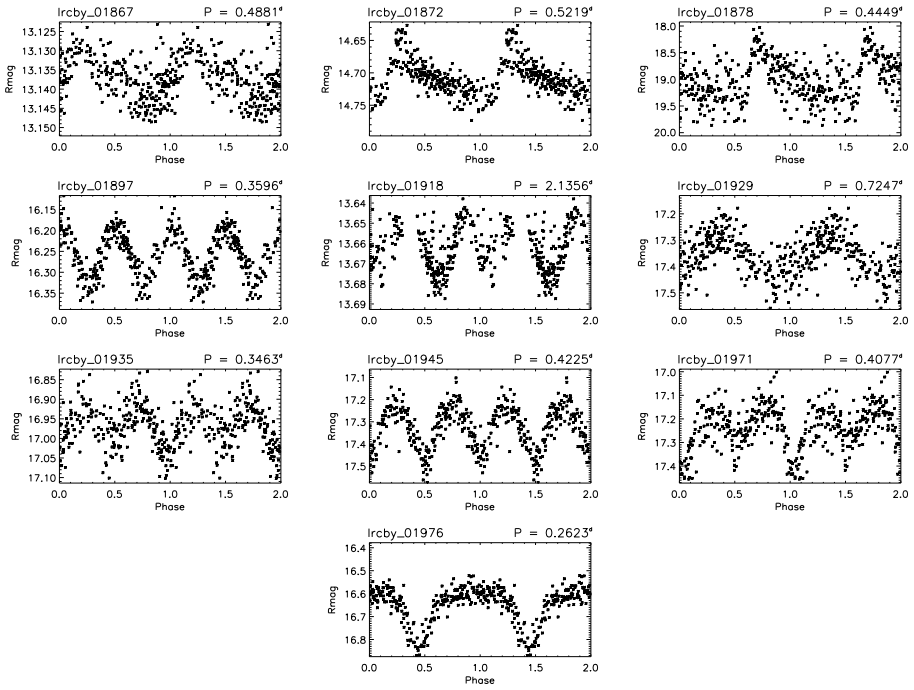

Figure A.23: *Variable stars detected in the BEST II lrcb(xy) field with the second phase mirrored*

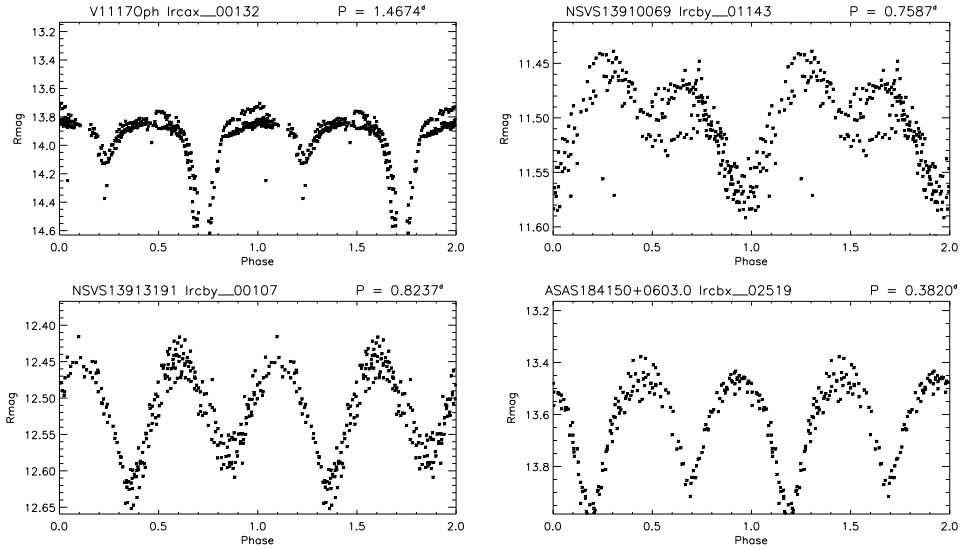

Figure A.24: *Light curves of known periodic variable stars in LRc2 field.*

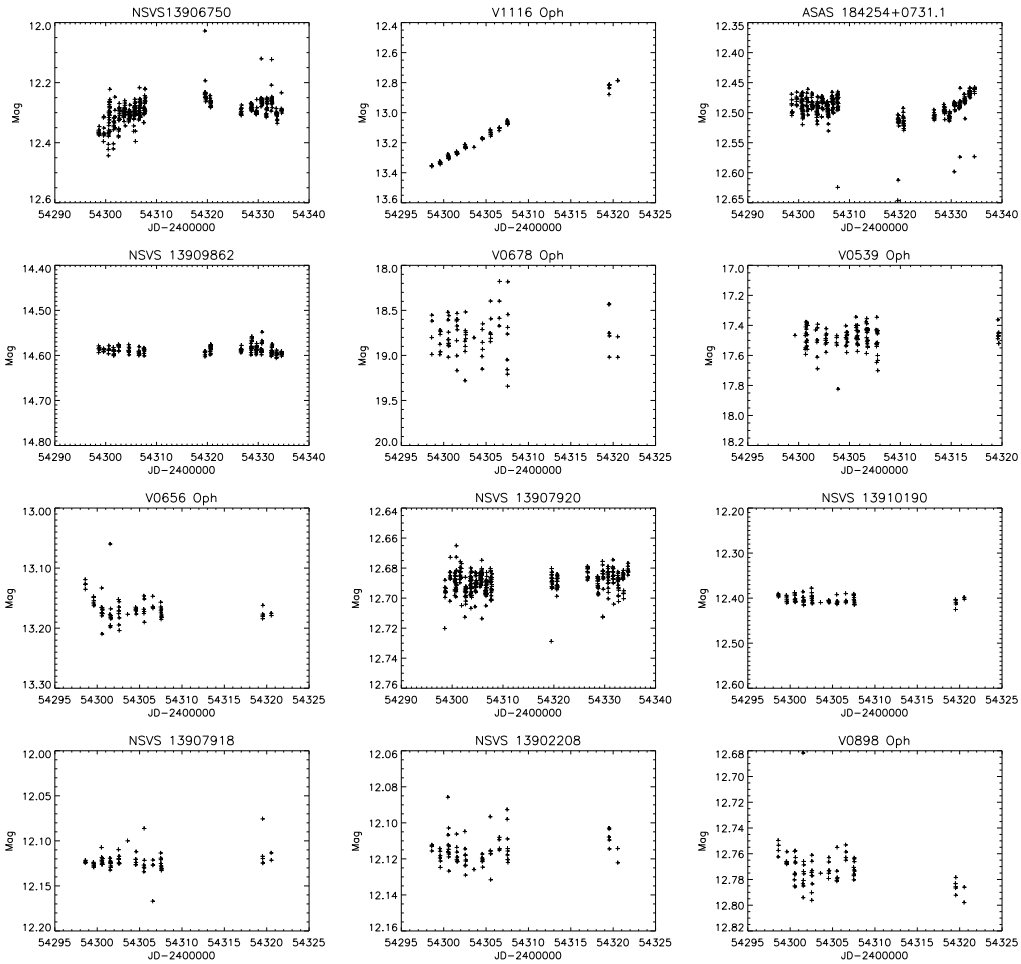

Figure A.25: *Light curves of known variable stars in the LRc2 fields with long periods or without clear periodicity.*

Target field LRa02

Target field parameters

LRa2a: $\alpha = 06^h\ 50^m\ 46.3^s$, $\delta = -03^\circ\ 59'\ 31.0"$
LRa2b: $\alpha = 06^h\ 51^m\ 13.9^s$, $\delta = -05^\circ\ 26'\ 16.0"$

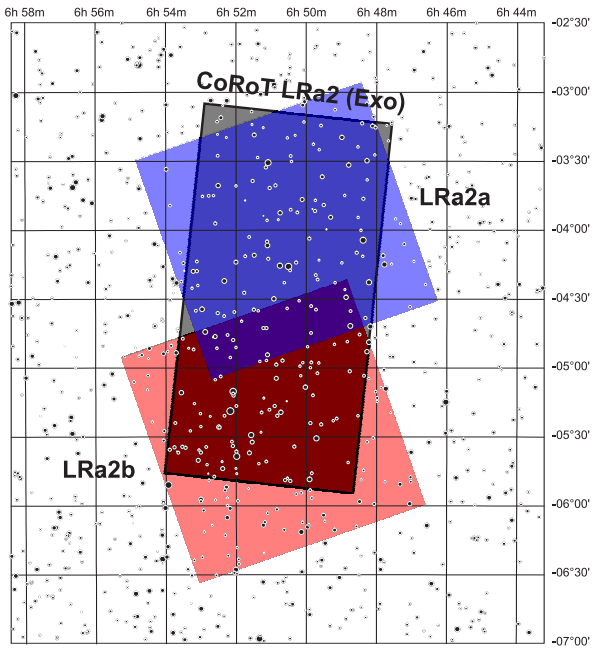

Figure A.26: *Orientation of LRa02 subfields with respect to CoRoT exoplanetary field.*

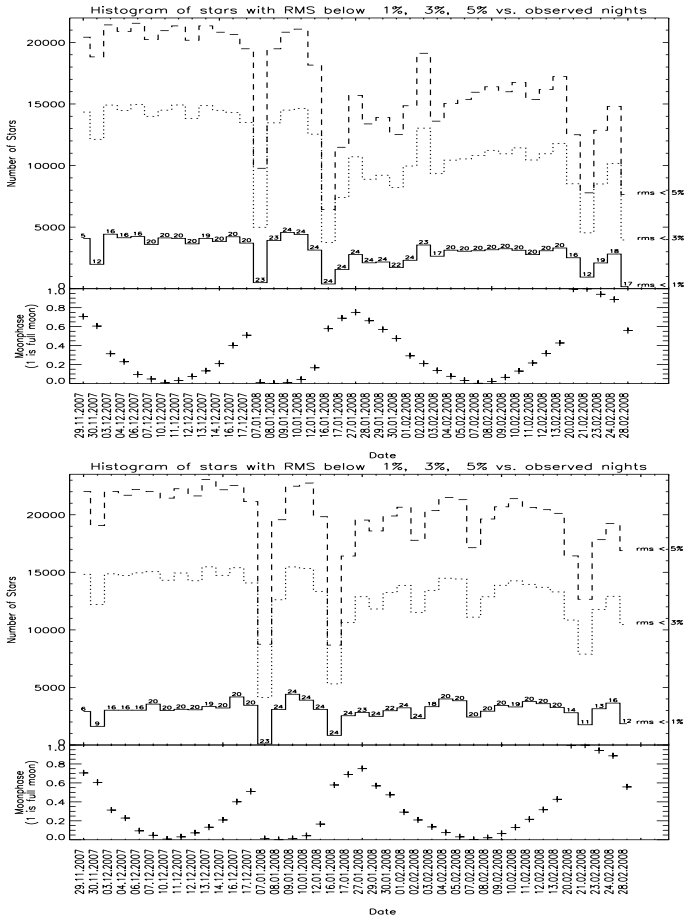

Figure A.27: *Upper panel presents a histogram of stars with RMS below* 1% *(solid line),* 3% *(shor dashed line) and* 5% *(long dashed line) for every night in BEST II LRa02a target field. Lower panel presents similar plot for a LRa02b subfield. In the lower box he corresponding Moon phase is shown.*

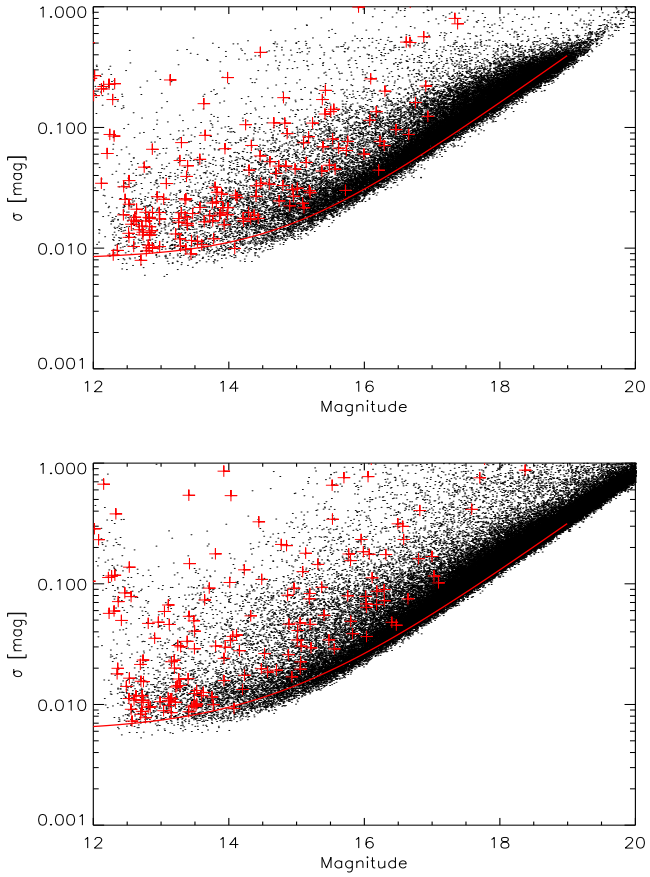

Figure A.28: *RMS plot for BEST II fields LRa02a (upper panel) and LRa02b (lower panel). Red line presents the limiting total noise and red crosses represent the detected variable stars.*

Periodic variable stars

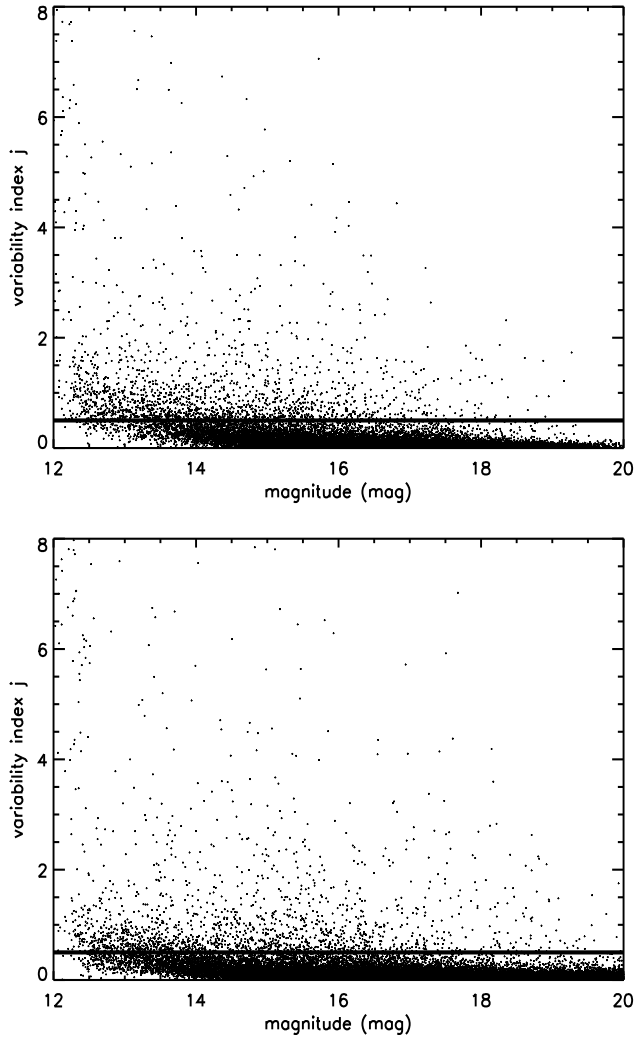

Figure A.29: *Variability index j against magnitude for stars in LRa02a (top) and LRa02b (bottom) target fields.*

Table A.8: *Periodic variable stars detected in LRa2a. Magnitudes are based on calibration against USNO catalog only. Stars with asterisk are located in the CoRoT's exoplanetary field-of-view. Potential stellar crowding affecting the light curve of stars is marked with c.*

BEST ID	2MASS ID	α(J2000)	δ(J2000)	$\overline{m}$(mag)	P(days)	Amp.(mag)	Type	Note
lra2a_00004*	06472576-0354198	6 47 25.8	-3 54 20.4	15.172	0.682	0.07	EW	
lra2a_00074*	06475959-0335092	6 47 59.6	-3 35 9.4	12.937	0.989	0.04	SP	
lra2a_00079*	06480297-0333011	6 48 3.0	-3 33 1.2	12.703	1.024	0.06	γDor	
lra2a_00092	06473486-0357256	6 47 34.9	-3 57 26.1	15.166	1.402	0.08	EB	
lra2a_00133*	06481854-0329035	6 48 18.6	-3 29 3.7	15.456	2.186	0.10	EA	
lra2a_00134	06474958-0352496	6 47 49.6	-3 52 50.0	12.344	2.310	0.20	EA	ASAS 064750-0352.8
lra2a_00138*	06481445-0333074	6 48 14.5	-3 33 7.7	15.398	3.449	0.10	SP	
lra2a_00143	06474412-0359120	6 47 44.1	-3 59 12.4	14.218	1.039	0.08	EA	
lra2a_00159	06474131-0404558	6 47 41.3	-4 4 56.1	16.121	0.436	0.15	EW	
lra2a_00186	06474594-0405436	6 47 46.0	-4 5 42.0	15.098	0.180	0.14	RRcLyr	
lra2a_00194*	06484004-0324130	6 48 40.0	-3 24 13.2	15.631	1.950	0.10	EA	
lra2a_00203	06473681-0417436	6 47 36.8	-4 17 43.8	15.899	20.470	0.20	VAR	
lra2a_00221*	06482041-0345317	6 48 20.4	-3 45 31.9	15.913	0.663	0.22	EA	
lra2a_00223*	06484348-0327173	6 48 43.5	-3 27 17.3	17.279	0.649	0.40	EA	
lra2a_00238	06475752-0407048	6 47 57.5	-4 7 5.1	14.618	6.398	0.19	SP	
lra2a_00244*	06480847-0359231	6 48 8.5	-3 59 23.3	12.308	3.678	0.04	EB	
lra2a_00245	06472906-0431527	6 47 29.0	-4 31 52.2	12.317	0.666	0.20	EW	
lra2a_00259*	06485379-0325069	6 48 53.8	-3 25 7.2	14.927	0.541	0.08	VAR	
lra2a_00269	06473121-0432567	6 47 31.1	-4 32 56.2	15.044	2.909	0.22	EA	
lra2a_00295	06473586-0432542	6 47 35.8	-4 32 53.7	16.204	0.8425	0.25	EA	
lra2a_00298*	06491310-0314030	6 49 13.1	-3 14 2.8	14.904	21.388	0.15	α^2CVn	
lra2a_00301*	06485712-0327249	6 48 57.1	-3 27 25.2	14.538	2.927	0.12	DCEP	
lra2a_00302*	06485993-0325275	6 48 59.9	-3 25 27.7	15.764	0.510	0.24	EB	
lra2a_00304*	06484317-0339351	6 48 43.2	-3 39 35.3	16.911	0.350	0.55	EW	
lra2a_00311	06484802-0336168	6 48 48.0	-3 36 16.8	12.564	1.652	0.45	DCEP	V0376 Mon
lra2a_00319	06474707-0427025	6 47 47.1	-4 27 2.4	14.440	0.955	0.06	SP	
lra2a_00325*	06484192-0343065	6 48 41.9	-3 43 6.6	15.860	11.773	0.00	LP	
lra2a_00342*	06480352-0416460	6 48 3.5	-4 16 46.2	15.741	3.474	0.55	DCEP	
lra2a_00343*	06492660-0309246	6 49 26.6	-3 9 24.8	14.884	0.474	0.34	EB	
lra2a_00346*	06482771-0357328	6 48 27.7	-3 57 33.1	12.631	2.375	0.05	ELL	
lra2a_00356*	06490979-0325538	6 49 9.8	-3 25 54.2	14.181	1.543	0.06	ELL/SP	
lra2a_00408*	06482880-0409053	6 48 28.8	-4 9 5.6	15.752	0.868	0.10	SP	
lra2a_00416*	06483188-0407577	6 48 31.9	-4 7 57.9	16.611	0.750	0.20	EA	
lra2a_00435*c	06492145-0332384	6 49 21.5	-3 32 39.2	16.091	0.265	0.50	EW	
lra2a_00438*c	06492144-0332442	6 49 21.4	-3 32 44.3	16.014	0.265	0.60	EW	
lra2a_00450*c	06491193-0342336	6 49 11.9	-3 42 33.7	16.162	0.272	0.48	EW	
lra2a_00459*	06481562-0430030	6 48 15.6	-4 30 3.1	16.825	0.784	0.35	EA	
lra2a_00466*	06490094-0354075	6 49 0.9	-3 54 7.6	12.957	12.878	0.15	ELL	
lra2a_00476*	06485459-0401340	6 48 54.6	-4 1 33.8	14.817	0.565	0.06	VAR	
lra2a_00477*	06482272-0427312	6 48 22.7	-4 27 31.4	14.601	10.863	0.10	VAR	
lra2a_00479*	06485491-0401291	6 48 54.9	-4 1 29.2	14.523	0.565	0.06	VAR	
lra2a_00485*	06485905-0359090	6 48 59.1	-3 59 9.1	15.334	3.964	0.11	VAR	
lra2a_00488*	06481978-0432424	6 48 19.8	-4 32 42.4	14.270	0.266	0.38	EW	
lra2a_00491*	06482534-0428360	6 48 25.3	-4 28 36.2	13.542	0.220	0.04	DSCT	
lra2a_00492*	06495531-0315442	6 49 55.3	-3 15 44.4	15.468	0.653	0.37	EA	
lra2a_00495*	06484754-0411406	6 48 47.6	-4 11 40.7	14.067	2.875	0.08	α^2CVn	
lra2a_00517*	06483463-0425378	6 48 34.6	-4 25 38.1	14.936	2.890	0.18	VAR	
lra2a_00524*	06484810-0416130	6 48 48.1	-4 16 13.3	13.309	33.768	0.00	LP	
lra2a_00529*	06492898-0343193	6 49 29.0	-3 43 19.4	14.924	5.533	0.08	α^2CVn	
lra2a_00531*	06500331-0315474	6 50 3.3	-3 15 47.5	16.466	0.674	0.30	EA	
lra2a_00533*	06484980-0416279	6 48 49.8	-4 16 28.0	13.193	35.176	0.17	LP	
lra2a_00549*	06493894-0339172	6 49 38.9	-3 39 17.3	12.738	0.055	0.03	DSCT	
lra2a_00551*	06492376-0351520	6 49 23.8	-3 51 52.0	14.829	3.735	0.04	α^2CVn	
lra2a_00559*	06490729-0406270	6 49 7.3	-4 6 27.2	13.936	1.780	0.09	ELL	
lra2a_00571*	06491929-0358586	6 49 19.3	-3 58 58.6	16.814	24.413	0.20	VAR	
lra2a_00579*	06494398-0340111	6 49 44.0	-3 40 11.3	12.369	1.018	0.04	EW	
lra2a_00586*	06491682-0403076	6 49 16.8	-4 3 7.8	13.180	0.990	0.01	VAR	
lra2a_00601*	06485506-0423379	6 48 55.1	-4 23 38.2	15.337	0.976	0.28	RRLyr	
lra2a_00603*	06483611-0440018	6 48 36.1	-4 40 2.0	13.204	1.024	0.01	γDor	
lra2a_00621*	06501378-0323200	6 50 13.8	-3 23 20.4	14.380	0.809	0.40	EB	
lra2a_00637*	06491871-0410214	6 49 18.7	-4 10 21.6	16.482	2.780	0.20	DCEP	
lra2a_00642*	06500981-0329026	6 50 9.8	-3 29 2.7	14.562	4.226	0.09	ELL/SP	
lra2a_00646*	06495951-0337371	6 49 59.5	-3 37 37.2	14.799	2.741	0.04	ELL/SP	
lra2a_00649*	06492236-0408156	6 49 22.4	-4 8 15.8	12.596	0.581	0.05	RRLyr	
lra2a_00652*	06494921-0346398	6 49 49.2	-3 46 40.0	13.579	0.185	0.04	SXPHE/DSCT	
lra2a_00656*	06493211-0401410	6 49 32.1	-4 1 41.1	14.579	14.616	0.06	α^2CVn	
lra2a_00662*	06502316-0321053	6 50 23.2	-3 21 5.7	14.607	0.820	0.09	EA	
lra2a_00663*	06495275-0346122	6 49 52.7	-3 46 12.4	14.219	16.178	0.04	LP	
lra2a_00673*	06490980-0424545	6 49 9.8	-4 24 54.6	13.997	1.893	0.60	EA	
lra2a_00683*	06492634-0413091	6 49 26.3	-4 13 9.3	13.181	0.317	0.08	EB	
lra2a_00721*	06504255-0319206	6 50 42.6	-3 19 21.0	12.861	0.905	0.11	ELL/SP	
lra2a_00732*	06494128-0411169	6 49 41.3	-4 11 16.9	14.161	3.074	0.07	ELL/SP	
lra2a_00742*	06504787-0318096	6 50 47.9	-3 18 10.1	11.962	1.448	0.07	VAR	
lra2a_00744*	06493211-0419598	6 49 32.1	-4 19 59.9	15.341	33.507	0.12	LP	
lra2a_00757*	06493592-0418296	6 49 35.9	-4 18 29.7	15.391	0.535	0.09	EA	
lra2a_00761*	06495752-0401401	6 49 57.5	-4 1 40.0	14.707	2.201	0.10	DCEP	
lra2a_00764*	06500411-0357205	6 50 4.1	-3 57 20.5	13.508	1.012	0.03	γDor	
lra2a_00771*	06491012-0442323	6 49 10.1	-4 42 32.5	16.383	28.418	0.00	LP	
lra2a_00788*	06495594-0410207	6 49 55.9	-4 10 20.7	12.630	1.539	0.20	EA	V0452 Mon
lra2a_00799*	06494455-0421312	6 49 44.6	-4 21 31.4	14.938	4.475	0.04	α^2CVn	
lra2a_00808*	06510307-0319432	6 51 3.1	-3 19 43.6	15.582	0.868	0.10	VAR	
lra2a_00809*	06503829-0340019	6 50 38.3	-3 40 2.0	13.759	31.362	0.00	LP	
lra2a_00811*	06503672-0341301	6 50 36.7	-3 41 30.3	13.226	1.816	0.06	EB	
lra2a_00817*	06492766-0439506	6 49 27.7	-4 39 50.7	12.093	0.357	0.10	DSCT	
lra2a_00820*	06501761-0359301	6 50 17.6	-3 59 29.9	15.028	0.669	0.40	EA	
lra2a_00822*	06495696-0416327	6 49 57.0	-4 16 32.7	14.880	0.886	0.06	VAR	
lra2a_00839*	06500179-0414283	6 50 1.8	-4 14 28.3	13.663	7.326	0.04	α^2CVn	
lra2a_00851*	06502424-0358373	6 50 24.2	-3 58 37.1	16.702	1.742	0.25	EA	
lra2a_00855*c	06505170-0336412	6 50 51.7	-3 36 41.3	15.114	0.929	0.08	RRLyr	
lra2a_00856*c	06505181-0336367	6 50 51.8	-3 36 37.6	15.109	0.929	0.08	RRLyr	
lra2a_00862*	06503880-0348144	6 50 38.8	-3 48 14.5	13.776	3.709	0.12	EA	

Table A.8: *continued.*

BEST ID	2MASS ID	α(J2000)	δ(J2000)	$\overline{m}$(mag)	P(days)	Amp.(mag)	Type	Note
lra2a_00863*	06500327-0417088	6 50 3.3	-4 17 8.8	13.287	0.967	0.03	RRLyr	
lra2a_00873*	06495873-0422291	6 49 58.7	-4 22 29.0	15.441	0.607	0.12	RRLyr	
lra2a_00876*	06501226-0411535	6 50 12.2	-4 11 53.3	13.892	0.666	0.04	VAR	
lra2a_00879*c	06511257-0323040	6 51 12.6	-3 23 4.7	15.722	1.416	0.13	EW	
lra2a_00880*c	06511248-0323088	6 51 12.5	-3 23 8.9	15.723	1.416	0.13	EW	
lra2a_00891*	06510465-0330432	6 51 4.7	-3 30 43.4	16.664	0.588	0.40	EB	
lra2a_00896*	06500785-0418300	6 50 7.8	-4 18 30.1	17.238	0.979	0.51	EA	
lra2a_00900*	06510525-0332513	6 51 5.3	-3 32 51.7	12.970	5.573	0.08	α^2CVn	
lra2a_00925*	06501489-0417160	6 50 14.9	-4 17 16.0	13.680	1.672	0.06	VAR	
lra2a_00926*	06500533-0425178	6 50 5.3	-4 25 17.8	14.211	13.305	0.06	VAR	
lra2a_00940*	06511871-0327416	6 51 18.7	-3 27 41.7	16.507	4.460	0.25	EA	
lra2a_00950*	06501612-0420369	6 50 16.1	-4 20 36.9	16.140	9.123	0.17	DCEP	
lra2a_00963*	06501580-0421518	6 50 15.8	-4 21 51.7	13.614	21.337	0.03	LP	
lra2a_00968*	06495042-0443181	6 49 50.4	-4 43 18.0	13.485	9.906	0.06	LP	
lra2a_01071*	06510707-0359092	6 51 7.1	-3 59 9.2	16.239	0.316	0.47	EW	
lra2a_01088*	06505503-0411143	6 50 55.0	-4 11 14.3	13.948	4.752	0.06	α^2CVn	
lra2a_01098*	06514793-0331527	6 51 47.9	-3 31 52.9	14.504	1.355	0.14	EA	
lra2a_01103*	06512209-0354038	6 51 22.1	-3 54 3.9	14.005	0.393	0.72	EW	
lra2a_01111*	06503162-0436431	6 50 31.6	-4 36 43.4	16.200	2.137	0.13	VAR	
lra2a_01123*	06511923-0359522	6 51 19.2	-3 59 52.2	13.974	4.202	0.10	DCEP	
lra2a_01125*	06511002-0407400	6 51 10.0	-4 7 39.9	18.003	1.452	1.00	EA	
lra2a_01126*	06520050-0326327	6 52 0.5	-3 26 32.9	13.676	2.711	0.20	EA	
lra2a_01127*	06520077-0326255	6 52 0.8	-3 26 25.8	14.311	1.694	0.10	EA	
lra2a_01137*	06514038-0344546	6 51 40.4	-3 44 54.9	14.954	8.149	0.08	α^2CVn	
lra2a_01163*	06511819-0407406	6 51 18.2	-4 7 40.4	15.243	0.530	0.08	RRLyr	
lra2a_01168*	06515875-0335435	6 51 58.8	-3 35 44.0	12.122	0.665	0.20	VAR	
lra2a_01169*	06515256-0340546	6 51 52.6	-3 40 54.9	15.197	3.941	0.10	VAR	
lra2a_01170*	06514139-0349581	6 51 41.4	-3 49 58.2	12.295	1.010	0.02	γDor	
lra2a_01184*	06512594-0406260	6 51 25.9	-4 6 25.8	15.992	1.723	0.15	VAR	
lra2a_01191*	06515385-0345415	6 51 53.9	-3 45 41.9	12.580	0.666	0.02	EW	
lra2a_01194c*	06503821-0447288	6 50 38.2	-4 47 29.0	15.913	32.136	0.00	LP/CV	
lra2a_01196c*	06503844-0447354	6 50 38.4	-4 47 35.6	15.777	32.159	0.00	LP/CV	
lra2a_01211*	06520334-0342160	6 52 3.4	-3 42 16.3	17.281	0.620	0.82	EB	
lra2a_01212*	06511753-0420239	6 51 17.5	-4 20 23.8	13.538	0.762	0.04	EW	
lra2a_01219*	06514910-0356440	6 51 49.1	-3 56 44.1	12.680	0.665	0.03	EW	
lra2a_01224*	06521674-0335553	6 52 16.8	-3 35 55.6	13.772	1.881	0.30	EB	
lra2a_01245*	06521143-0343311	6 52 11.4	-3 43 31.4	13.396	1.700	0.10	VAR	
lra2a_01246*	06514341-0406202	6 51 43.4	-4 6 20.2	16.212	2.271	0.15	EB	
lra2a_01253*	06505580-0446098	6 50 55.8	-4 46 9.9	13.632	6.817	0.06	ELL/SP	
lra2a_01265*	06512426-0425509	6 51 24.3	-4 25 50.8	15.637	3.394	0.13	DCEP	
lra2a_01269*	06521408-0346014	6 52 14.1	-3 46 1.7	12.845	0.628	0.08	RRLyr	
lra2a_01293*	06522569-0340401	6 52 25.7	-3 40 40.4	15.697	0.704	0.20	RRLyr	
lra2a_01297*	06513157-0425357	6 51 31.6	-4 25 35.7	13.383	0.846	0.14	EW	
lra2a_01298*	06521428-0351005	6 52 14.3	-3 51 0.3	16.919	0.650	0.38	RRLyr	
lra2a_01310*	06522283-0347013	6 52 22.8	-3 47 1.5	14.390	5.341	0.05	VAR	
lra2a_01314*	06524208-0332543	6 52 42.1	-3 32 54.5	14.454	0.661	0.50	EB	
lra2a_01338	06524845-0332472	6 52 48.4	-3 32 47.3	13.972	5.896	0.08	DCEP	
lra2a_01358*	06514548-0429172	6 51 45.5	-4 29 17.0	14.570	14.277	0.15	DCEP	
lra2a_01366	06525102-0336570	6 52 51.0	-3 36 57.2	14.840	9.298	0.04	α^2CVn	
lra2a_01372*	06522231-0401110	6 52 22.3	-4 1 11.2	15.020	0.485	0.35	EB	
lra2a_01381	06530018-0332288	6 53 0.2	-3 32 28.8	16.424	0.583	0.40	EB	
lra2a_01384*	06523144-0356300	6 52 31.4	-3 56 30.2	14.003	1.083	0.04	γDor	
lra2a_01394	06524198-0350201	6 52 42.0	-3 50 20.4	15.497	6.133	0.08	α^2CVn	
lra2a_01396	06530279-0333359	6 53 2.8	-3 33 35.8	14.063	2.754	0.05	VAR	
lra2a_01405*	06522763-0404042	6 52 27.6	-4 4 4.2	14.623	14.576	0.05	VAR	
lra2a_01427*	06520097-0428571	6 52 1.0	-4 28 57.0	15.200	1.589	0.06	ELL/SP	
lra2a_01429*	06515040-0437579	6 51 50.4	-4 37 57.8	14.641	17.165	0.08	α^2CVn	
lra2a_01441	06524826-0355267	6 52 48.3	-3 55 26.9	14.253	0.868	0.09	RRLyr	
lra2a_01456*	06515958-0438103	6 51 59.6	-4 38 10.2	14.604	2.091	0.20	EB	
lra2a_01462	06524744-0359531	6 52 47.4	-3 59 53.2	12.295	0.129	0.04	DSCT	
lra2a_01472	06532070-0335031	6 53 20.7	-3 35 2.9	15.667	4.634	0.10	VAR	
lra2a_01487	06524919-0405332	6 52 49.2	-4 5 33.4	15.009	1.724	0.15	DCEP/EW	
lra2a_01492*	06530180-0356043	6 53 1.8	-3 56 4.5	13.896	1.344	0.05	SP/ELL	
lra2a_01510*	06530390-0359478	6 53 3.9	-3 59 48.0	14.123	12.578	0.05	α^2CVn	
lra2a_01533*	06525598-0411048	6 52 56.0	-4 11 5.0	15.110	1.247	0.06	γDor	
lra2a_01550	06534316-0335545	6 53 43.1	-3 35 54.1	12.602	1.213	0.08	VAR	
lra2a_01551*	06525515-0415177	6 52 55.2	-4 15 17.9	14.796	1.849	0.10	VAR	
lra2a_01565	06534650-0337257	6 53 46.4	-3 37 25.3	16.391	3.229	0.25	DCEP	
lra2a_01573	06535554-0333262	6 53 55.4	-3 33 25.3	15.641	1.886	0.20	DCEP	
lra2a_01584*	06530293-0418533	6 53 3.0	-4 18 53.4	15.835	1.648	0.10	α^2CVn	
lra2a_01592	06534626-0345272	6 53 46.2	-3 45 27.2	14.126	2.276	0.08	α^2CVn	
lra2a_01593*	06525199-0429498	6 52 52.0	-4 29 49.8	16.380	0.964	0.60	EB	
lra2a_01595	06534626-0345435	6 53 46.2	-3 45 43.4	15.574	2.790	0.35	DCEP	
lra2a_01609*	06525078-0433067	6 52 50.8	-4 33 6.7	15.539	0.227	0.30	DSCT/EW	
lra2a_01627*	06525914-0429063	6 52 59.1	-4 29 6.3	16.564	0.253	0.56	EW	
lra2a_01686	06540969-0344074	6 54 9.7	-3 44 6.9	15.452	7.362	0.10	LP	
lra2a_01702	06533647-0413215	6 53 36.8	-4 13 15.6	14.357	0.876	1.00	EA	XZ Mon
lra2a_01739	06530708-0440366	6 53 7.1	-4 40 36.5	15.650	1.132	0.20	EA	
lra2a_01811	06535071-0412227	6 53 50.7	-4 12 23.0	17.030	0.255	0.65	EW	
lra2a_01820c	06535998-0405514	6 53 60.0	-4 5 51.7	13.866	0.498	0.06	VAR	
lra2a_01828c	06542227-0348393	6 54 22.2	-3 48 38.7	12.545	0.498	0.04	VAR	
lra2a_01858c	06540106-0408135	6 54 1.1	-4 8 13.8	13.896	0.498	0.08	VAR	

Table A.9: *Periodic variable stars detected in LRa2b. Magnitudes are based on calibration against USNO catalog only. Stars with asterisk are located in the CoRoT's exoplanetary field-of-view. Potential stellar crowding affecting the light curve of stars is marked with c.*

BEST ID	2MASS ID	α(J2000)	δ(J2000)	$\overline{m}$(mag)	P(days)	Amp.(mag)	Type	Note
lra2b_00049	06535497-0553063	6 53 55.0	-5 53 6.6	14.806	6.269	0.08	α^2CVn	
lra2b_00053	06545012-0507166	6 54 50.1	-5 7 16.8	16.934	0.280	0.54	EW	
lra2b_00116	06531502-0617280	6 53 15.0	-6 17 28.2	13.296	1.891	0.12	EW	
lra2b_00117	06533942-0557263	6 53 39.4	-5 57 26.7	14.116	0.886	0.15	RRLyr	
lra2b_00124	06531766-0614104	6 53 17.7	-6 14 10.6	15.493	8.936	0.15	VAR	
lra2b_00137	06533463-0558279	6 53 34.7	-5 58 28.2	17.231	0.708	0.60	EB	
lra2b_00179*	06533609-0551510	6 53 36.1	-5 51 51.2	16.139	2.568	0.15	VAR	
lra2b_00186	06530929-0612448	6 53 9.3	-6 12 44.9	12.294	0.690	0.10	EW	
lra2b_00190	06543360-0503138	6 54 33.7	-5 3 13.3	13.171	0.287	0.09	DSCT	
lra2b_00222	06531071-0605587	6 53 10.7	-6 5 58.9	16.008	4.290	0.15	VAR	
lra2b_00250	06532919-0547016	6 53 29.2	-5 47 1.9	13.527	1.022	0.15	γDor	
lra2b_00269	06535058-0524204	6 53 50.6	-5 24 20.3	16.148	3.600	0.40	EB	
lra2b_00295	06541558-0458539	6 54 15.6	-4 58 54.0	15.369	2.396	0.20	DCEP	
lra2b_00300	06540467-0506508	6 54 4.7	-5 6 51.1	16.351	0.251	0.40	EW	
lra2b_00323*	06531961-0540496	6 53 19.6	-5 40 49.6	15.383	0.373	0.70	EW	
lra2b_00331	06541082-0456551	6 54 10.8	-4 56 55.2	16.108	0.344	0.50	EB	
lra2b_00348	06524623-0601086	6 52 46.2	-6 1 8.8	15.318	1.209	0.15	DCEP	
lra2b_00376*	06530026-0542399	6 53 0.3	-5 42 40.1	12.489	0.898	0.05	VAR	
lra2b_00378*	06530722-0536314	6 53 7.2	-5 36 31.6	15.789	21.515	0.20	VAR	
lra2b_00389*	06534165-0502400	6 53 41.7	-5 2 40.1	16.581	2.254	0.40	EA	
lra2b_00396	06524244-0549140	6 52 42.4	-5 49 14.2	13.283	4.217	0.08	ELL/SP	
lra2b_00397	06520502-0619199	6 52 5.0	-6 19 19.9	15.069	1.101	0.10	ELL/SP	
lra2b_00402*	06524739-0544130	6 52 47.4	-5 44 13.2	13.247	4.449	0.10	ELL/SP	
lra2b_00411*	06533975-0458220	6 53 39.8	-4 58 22.2	14.255	2.196	0.07	EB	
lra2b_00412*	06530095-0529521	6 53 1.0	-5 29 52.2	13.485	2.130	0.05	ELL	
lra2b_00419*	06533531-0459416	6 53 35.3	-4 59 41.7	14.017	1.368	0.06	α^2CVn	
lra2b_00421*	06533499-0459421	6 53 35.0	-4 59 42.2	13.998	1.369	0.06	α^2CVn	
lra2b_00429	06523176-0550078	6 52 31.8	-5 50 8.0	14.256	2.117	0.08	VAR	
lra2b_00430*	06524238-0541250	6 52 42.4	-5 41 25.1	14.927	0.352	0.70	EW	
lra2b_00443	06520504-0608578	6 52 5.0	-6 8 57.9	15.792	0.991	0.60	EW	
lra2b_00446	06520464-0608504	6 52 4.7	-6 8 50.9	17.155	0.991	1.00	VAR	
lra2b_00465	06521691-0554377	6 52 16.9	-5 54 37.7	14.306	14.355	0.06	LP	
lra2b_00466	06520721-0602299	6 52 7.2	-6 2 30.1	15.829	1.429	0.40	EA	
lra2b_00468	06522936-0544153	6 52 29.4	-5 44 15.4	14.252	0.561	0.20	EW	
lra2b_00469	06522734-0545516	6 52 27.3	-5 45 51.8	13.481	0.911	0.40	EA	EI Mon
lra2b_00490	06520377-0601463	6 52 3.8	-6 1 46.4	14.639	0.778	0.10	RRLyr	
lra2b_00493*	06524754-0525438	6 52 47.5	-5 25 43.8	13.142	2.138	0.08	α^2CVn	
lra2b_00506*	06522377-0542400	6 52 23.8	-5 42 40.2	14.371	2.674	0.04	α^2CVn	
lra2b_00511*	06525612-0515414	6 52 56.1	-5 15 41.6	14.302	0.620	0.08	EW	
lra2b_00513*	06524744-0522276	6 52 47.4	-5 22 27.6	14.758	5.042	0.05	VAR	
lra2b_00514	06515497-0605171	6 51 55.0	-6 5 17.1	14.513	0.582	0.38	EB	
lra2b_00518	06524748-0521590	6 52 47.5	-5 21 59.1	14.069	0.528	0.15	EW	
lra2b_00527	06515947-0559171	6 51 59.5	-5 59 17.4	15.528	2.718	0.25	DCEP	
lra2b_00551	06520404-0551036	6 52 4.0	-5 51 3.6	15.499	0.354	0.66	EW	
lra2b_00566	06520099-0551089	6 52 1.0	-5 51 8.8	16.870	0.302	0.64	EW	
lra2b_00570*	06522020-0535137	6 52 20.2	-5 35 13.7	15.063	1.260	0.15	DCEP	
lra2b_00590*	06525605-0503355	6 52 56.1	-5 3 35.6	16.898	24.786	0.00	LP	
lra2b_00595*	06530906-0452194	6 53 9.1	-4 52 19.4	14.352	2.723	0.06	SP	
lra2b_00598*	06523900-0515585	6 52 39.0	-5 15 58.6	14.903	3.274	0.08	α^2CVn	
lra2b_00617	06512904-0609407	6 51 29.0	-6 9 40.9	16.923	0.311	0.53	EW	
lra2b_00620	06512696-0610504	6 51 27.0	-6 10 50.3	12.975	1.683	0.10	α^2CVn	
lra2b_00629*	06521553-0529554	6 52 15.5	-5 29 55.6	14.415	0.114	0.08	DSCT	
lra2b_00656	06512963-0602256	6 51 29.6	-6 2 25.6	14.434	0.493	0.08	SP	
lra2b_00674*	06522265-0516311	6 52 22.7	-5 16 31.3	13.419	0.217	0.05	SXPHE	
lra2b_00675*	06523346-0507400	6 52 33.5	-5 7 39.8	14.024	32.080	0.00	LP	
lra2b_00678	06511451-0610357	6 51 14.5	-6 10 35.9	12.724	18.657	0.07	α^2CVn	
lra2b_00681*	06520776-0526248	6 52 7.8	-5 26 24.8	14.339	2.047	0.30	EA	
lra2b_00687	06511964-0605018	6 51 19.7	-6 5 2.1	15.818	2.274	0.15	DCEP	
lra2b_00722*	06523066-0458166	6 52 30.7	-4 58 16.7	17.249	1.523	0.30	DCEP	
lra2b_00730*	06514351-0535028	6 51 43.5	-5 35 3.0	13.384	2.674	0.05	VAR	
lra2b_00733*		6 51 47.4	-5 30 42.7	15.918	0.973	0.14	RRLyr	
lra2b_00738	06512387-0549233	6 51 23.9	-5 49 23.6	13.585	1.014	0.12	SP	
lra2b_00742*	06513994-0535082	6 51 39.9	-5 35 8.3	14.805	1.662	0.06	SP	
lra2b_00743	06510486-0603305	6 51 4.9	-6 3 30.5	15.054	1.140	0.07	γDor	
lra2b_00745	06512019-0550241	6 51 20.2	-5 50 24.2	16.239	1.633	0.18	DCEP	
lra2b_00755*	06520507-0511481	6 52 5.1	-5 11 48.3	14.990	0.895	0.14	RRLyr	
lra2b_00761*	06515838-0515216	6 51 58.4	-5 15 21.7	15.134	14.554	0.30	DCEP	
lra2b_00772*	06514236-0525587	6 51 42.4	-5 25 58.9	13.694	1.011	0.03	γDor	
lra2b_00785	06505928-0557488	6 50 59.3	-5 57 49.0	13.949	1.051	0.06	VAR	
lra2b_00786*	06521123-0458477	6 52 11.2	-4 58 47.7	15.476	11.531	0.15	ELL	
lra2b_00800	06505581-0558198	6 50 55.8	-5 58 20.0	14.887	0.946	0.15	EA	
lra2b_00803	06504824-0604034	6 50 48.2	-6 4 3.4	13.564	0.300	0.05	EW	
lra2b_00807*	06515425-0509363	6 51 54.3	-5 9 36.6	15.881	2.923	0.16	DCEP	
lra2b_00821*	06513340-0524050	6 51 33.4	-5 24 5.0	15.484	1.723	0.15	EA	
lra2b_00843	06510251-0546453	6 51 2.5	-5 46 45.5	17.573	0.737	0.90	EB	
lra2b_00844	06505996-0548080	6 50 60.0	-5 48 8.1	16.407	2.323	0.17	SP	
lra2b_00855*	06514089-0513051	6 51 40.9	-5 13 5.3	13.155	2.208	0.06	α^2CVn	
lra2b_00865	06504363-0557114	6 50 43.6	-5 57 11.7	14.758	35.685	0.00	LP	
lra2b_00884*	06512729-0517154	6 51 27.3	-5 17 15.6	14.332	0.897	0.06	SP	
lra2b_00915	06514570-0457314	6 51 45.7	-4 57 31.7	15.885	0.326	0.40	EW	
lra2b_00928	06514146-0459244	6 51 41.5	-4 59 24.8	15.133	0.656	0.18	EA	
lra2b_00949*	06505007-0536311	6 50 50.1	-5 36 31.3	13.904	1.862	0.06	VAR	
lra2b_00951*	06514300-0453055	6 51 43.0	-4 53 5.7	13.707	10.812	0.08	VAR	
lra2b_00958*	06505816-0526537	6 50 58.2	-5 26 53.9	16.071	0.644	0.30	EW	
lra2b_00962*	06513913-0452228	6 51 39.2	-4 52 22.8	14.773	0.118	0.06	DSCT	
lra2b_00963*	06505216-0530253	6 50 52.2	-5 30 25.5	16.299	0.281	0.30	EW	
lra2b_00968*	06505364-0527405	6 50 53.6	-5 27 40.8	12.419	0.975	0.22	VAR	
lra2b_00973*	06504607-0532038	6 50 46.1	-5 32 3.8	16.684	1.218	0.20	EA	
lra2b_00977*	06504580-0531555	6 50 45.8	-5 31 55.6	15.448	1.218	0.19	EA	
lra2b_00980*	06510243-0517248	6 51 2.4	-5 17 25.1	15.037	3.724	0.06	α^2CVn	

Table A.9: *continued.*

BEST ID	2MASS ID	α(J2000)	δ(J2000)	$\overline{m}$(mag)	P(days)	Amp.(mag)	Type	Note
lra2b_00981	06501663-0554437	6 50 16.6	-5 54 43.9	14.572	7.399	0.06	VAR	
lra2b_00988*	06502912-0542443	6 50 29.1	-5 42 44.5	13.337	4.746	0.13	DCEP	
lra2b_00992*	06504360-0530168	6 50 43.6	-5 30 16.9	14.879	3.240	0.12	α^2CVn	
lra2b_01014*	06512189-0455005	6 51 21.9	-4 55 0.5	16.412	1.223	0.21	EW	
lra2b_01032*	06504096-0525512	6 50 41.0	-5 25 51.3	13.817	1.266	0.08	ELL	
lra2b_01041	06494574-0607317	6 49 45.7	-6 7 31.5	13.593	13.050	0.06	VAR	
lra2b_01044c	06501028-0547043	6 50 10.3	-5 47 4.5	14.918	0.464	0.07	RRLyr/SP	
lra2b_01045c	06500991-0547067	6 50 9.9	-5 47 6.9	14.702	0.464	0.08	RRLyr/SP	
lra2b_01046*	06501652-0541335	6 50 16.5	-5 41 33.7	13.596	2.385	0.05	VAR	
lra2b_01047	06500958-0547029	6 50 9.6	-5 47 3.5	15.212	0.929	0.14	VAR	
lra2b_01052*	06503814-0521479	6 50 38.1	-5 21 48.0	15.736	21.404	0.17	DCEP	
lra2b_01074*	06504774-0508275	6 50 47.8	-5 8 27.7	13.844	0.634	0.08	SP	
lra2b_01075*	06503217-0521030	6 50 32.2	-5 21 2.9	17.094	1.551	0.40	EW	
lra2b_01076	06494076-0602507	6 49 40.7	-6 2 50.7	16.192	0.647	0.31	EB	
lra2b_01080*		6 50 23.9	-5 26 29.5	15.488	0.746	0.18	EA	
lra2b_01081*	06510815-0449172	6 51 8.2	-4 49 17.3	13.373	8.074	0.10	α^2CVn	
lra2b_01082	06495929-0545296	6 49 59.3	-5 45 29.7	16.376	0.671	0.60	EA	
lra2b_01087	06495406-0549242	6 49 54.1	-5 49 24.3	16.489	0.532	0.40	EW	
lra2b_01088	06495901-0545215	6 49 59.0	-5 45 21.7	16.034	0.671	0.10	EA	
lra2b_01098	06493916-0600049	6 49 39.1	-6 0 5.1	14.808	9.771	0.20	DCEP/CV	
lra2b_01100	06495722-0544422	6 49 57.2	-5 44 42.3	15.000	7.347	0.19	DCEP	
lra2b_01113*	06501060-0531341	6 50 10.6	-5 31 34.3	13.444	0.719	0.05	RRLyr	
lra2b_01126*c	06501813-0523164	6 50 18.1	-5 23 16.4	16.336	1.287	0.15	DCEP	
lra2b_01127*c	06501791-0523109	6 50 18.0	-5 23 10.5	16.474	1.287	0.15	DCEP	
lra2b_01139	06494359-0549498	6 49 43.6	-5 49 49.8	13.666	2.656	0.08	SP	
lra2b_01144*	06504492-0459068	6 50 44.9	-4 59 7.1	13.625	0.586	0.20	EB	
lra2b_01149*	06500103-0534332	6 50 1.0	-5 34 33.3	15.151	0.906	0.10	EW	
lra2b_01151*	06503379-0507263	6 50 33.8	-5 7 26.4	14.743	2.184	0.12	DCEP	
lra2b_01172*	06500956-0524553	6 50 9.6	-5 24 55.4	13.846	0.618	0.08	RRLyr	
lra2b_01192*	06504495-0453327	6 50 45.0	-4 53 32.7	14.736	3.878	0.10	EA	
lra2b_01202*	06500738-0521515	6 50 7.4	-5 21 51.6	15.698	11.039	0.14	DCEP	
lra2b_01205	06494101-0542384	6 49 41.0	-5 42 38.7	13.920	0.413	0.15	EB	
lra2b_01207*	06500183-0524501	6 50 1.8	-5 24 50.2	14.341	1.958	0.05	SP	
lra2b_01208*	06500867-0518563	6 50 8.7	-5 18 56.4	15.807	9.226	0.20	VAR	
lra2b_01221*	06495556-0527141	6 49 55.6	-5 27 14.2	15.767	0.832	0.16	EA	
lra2b_01225*	06503112-0457068	6 50 31.1	-4 57 7.0	14.154	1.659	0.08	VAR	
lra2b_01227	06492270-0552235	6 49 22.7	-5 52 23.8	16.377	27.914	0.00	LP	
lra2b_01248*	06495338-0522213	6 49 53.4	-5 22 21.4	16.321	2.889	0.25	DCEP	
lra2b_01256*	06493107-0538073	6 49 31.1	-5 38 7.3	16.366	3.036	0.23	DCEP	
lra2b_01257	06491567-0550387	6 49 15.7	-5 50 38.9	14.070	1.486	0.08	EA	
lra2b_01264	06491528-0548185	6 49 15.3	-5 48 18.6	16.182	0.265	0.30	DSCT	
lra2b_01265	06502464-0450471	6 50 24.7	-4 50 47.3	15.058	1.294	0.06	SP	
lra2b_01274*	06493709-0525568	6 49 37.1	-5 25 56.5	14.714	6.168	0.08	α^2CVn	
lra2b_01275c	06491749-0541441	6 49 17.5	-5 41 44.2	15.400	0.260	0.30	EW	
lra2b_01277c	06491712-0541423	6 49 17.1	-5 41 42.6	15.395	0.260	0.30	EW	
lra2b_01285*	06500301-0502506	6 50 3.0	-5 2 50.7	16.109	1.541	0.33	EB	
lra2b_01286*	06493048-0529167	6 49 30.5	-5 29 16.7	15.190	3.194	0.17	DCEP	
lra2b_01287c	06490818-0546524	6 49 8.2	-5 46 52.8	15.826	1.021	0.10	γDor	
lra2b_01288c		6 49 8.3	-5 46 48.5	16.031	1.021	0.15	γDor	
lra2b_01292*c	06501084-0455094	6 50 10.8	-4 55 9.4	14.300	2.959	0.12	SP	
lra2b_01293*c	06501055-0455148	6 50 10.6	-4 55 14.2	14.527	2.956	0.12	SP	
lra2b_01296		6 49 30.9	-5 27 16.1	15.472	7.616	0.08	VAR	
lra2b_01303*	06503162-0436431	6 50 31.6	-4 36 42.7	16.194	2.135	0.18	DCEP	
lra2b_01307*	06494075-0518003	6 49 40.7	-5 18 0.3	15.074	4.091	0.10	DCEP	
lra2b_01309*	06494036-0518019	6 49 40.4	-5 18 2.0	15.138	4.094	0.10	DCEP	
lra2b_01316*	06494150-0515029	6 49 41.5	-5 15 3.0	15.147	4.197	0.06	VAR	
lra2b_01330	06490566-0540459	6 49 5.7	-5 40 46.0	14.815	1.412	0.08	EB	
lra2b_01334*	06495851-0456485	6 49 58.5	-4 56 48.7	16.261	0.303	0.60	EW	
lra2b_01340*	06492045-0526540	6 49 20.5	-5 26 54.1	14.049	1.266	0.30	EB	
lra2b_01352*	06492382-0521252	6 49 23.8	-5 21 25.3	15.384	1.584	0.12	VAR	
lra2b_01364*	06493845-0508114	6 49 38.4	-5 8 11.4	14.225	4.751	0.15	DCEP	
lra2b_01368*	06500269-0447453	6 50 2.7	-4 47 45.5	14.586	1.190	0.10	SP	
lra2b_01369	06484618-0549328	6 48 46.2	-5 49 32.9	12.352	0.117	0.06	SXPHE	
lra2b_01371*	06493408-0510099	6 49 34.1	-5 10 9.9	14.500	2.853	0.08	EA	
lra2b_01372*		6 49 34.3	-5 10 4.4	15.016	2.856	0.12	EA	
lra2b_01384	06484661-0545492	6 48 46.6	-5 45 49.5	14.932	0.470	0.40	EW	
lra2b_01387		6 48 46.2	-5 45 45.9	15.928	0.470	0.80	VAR	
lra2b_01394	06483196-0556002	6 48 31.9	-5 56 0.6	15.239	4.075	0.10	VAR	
lra2b_01396	06484147-0547398	6 48 41.5	-5 47 40.0	17.123	1.526	0.48	DCEP	
lra2b_01404	06482945-0556226	6 48 29.4	-5 56 22.9	15.166	0.943	0.15	EB	
lra2b_01405	06483132-0554408	6 48 31.3	-5 54 41.0	13.455	20.097	0.04	LP	
lra2b_01437	06484069-0537534	6 48 40.7	-5 37 53.5	14.378	0.418	0.40	EW	
lra2b_01458*c		6 49 15.5	-5 3 23.4	14.816	0.291	0.60	EW	
lra2b_01459*c	06491524-0503301	6 49 15.2	-5 3 30.4	13.860	0.291	0.60	EW	
lra2b_01463*	06485685-0518103	6 48 56.9	-5 18 10.4	14.986	1.110	0.14	EA	
lra2b_01482*	06482851-0535595	6 48 28.5	-5 35 59.7	13.055	1.918	0.06	ELL	
lra2b_01485	06480100-0557326	6 48 1.0	-5 57 33.0	12.295	0.497	0.40	EB	
lra2b_01511*	06485620-0507196	6 48 56.2	-5 7 19.7	14.946	1.020	0.08	SP	
lra2b_01549	06475182-0552172	6 47 51.8	-5 52 17.7	14.762	1.588	0.07	ELL	
lra2b_01552*	06483819-0513562	6 48 38.2	-5 13 56.1	16.363	0.280	0.40	EB	
lra2b_01554*	06481923-0528506	6 48 19.2	-5 28 50.6	14.868	18.604	0.10	VAR	
lra2b_01561*	06490490-0449310	6 49 4.9	-4 49 31.2	16.145	0.363	0.60	EW	
lra2b_01600*	06484535-0458261	6 48 45.3	-4 58 26.2	15.709	0.387	0.30	EA	
lra2b_01630*	06484143-0456395	6 48 41.4	-4 56 39.6	15.547	5.893	0.60	EA	
lra2b_01648	06474385-0541125	6 47 43.8	-5 41 12.8	12.560	1.952	0.12	ELL	
lra2b_01660	06472622-0554256	6 47 26.2	-5 54 26.1	13.948	0.894	0.06	SP	
lra2b_01691	06474781-0534160	6 47 47.8	-5 34 16.2	16.389	2.230	0.20	DCEP	

Figure A.30: *Detected variable stars in LRa2a subfield.*

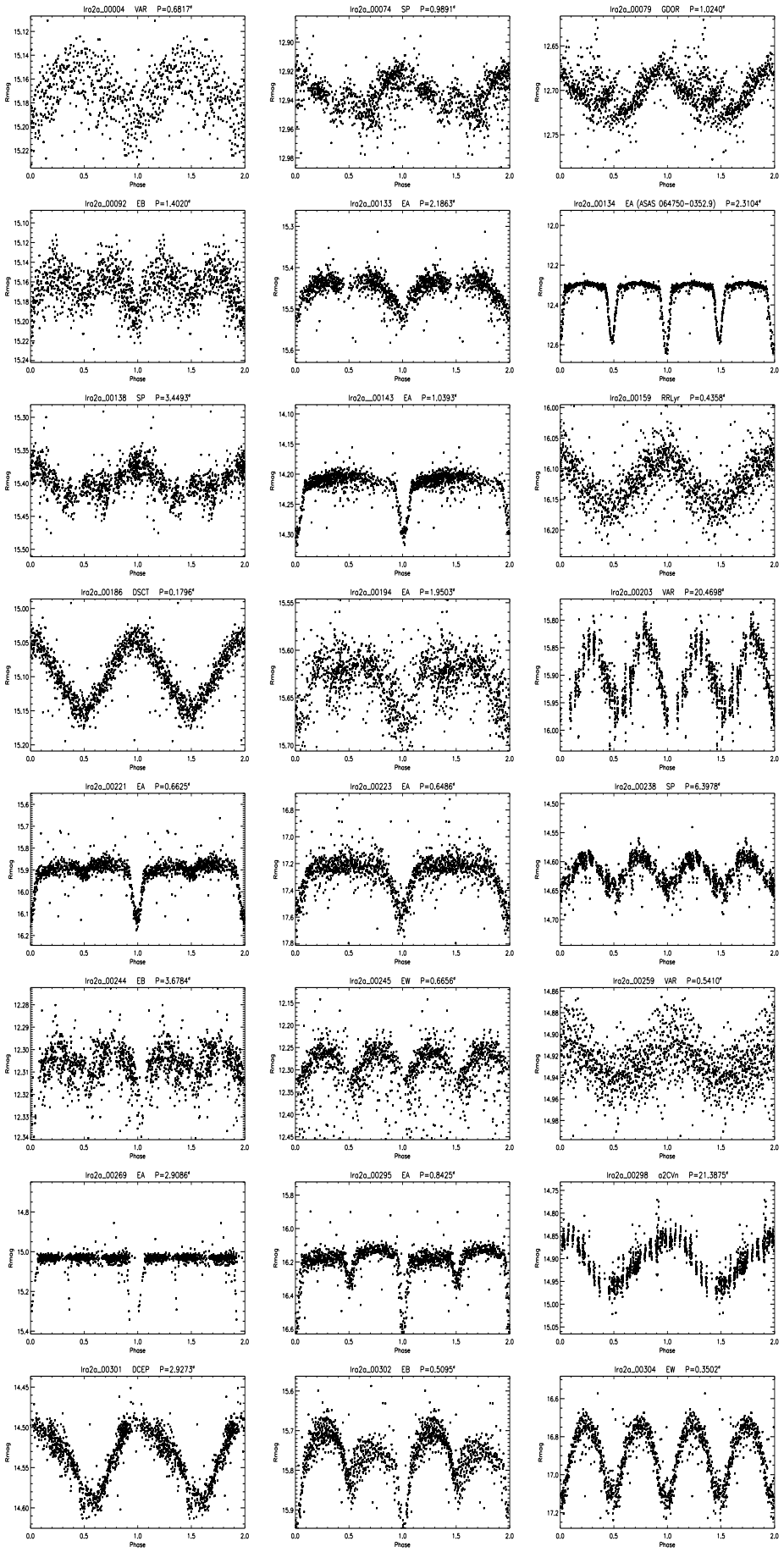

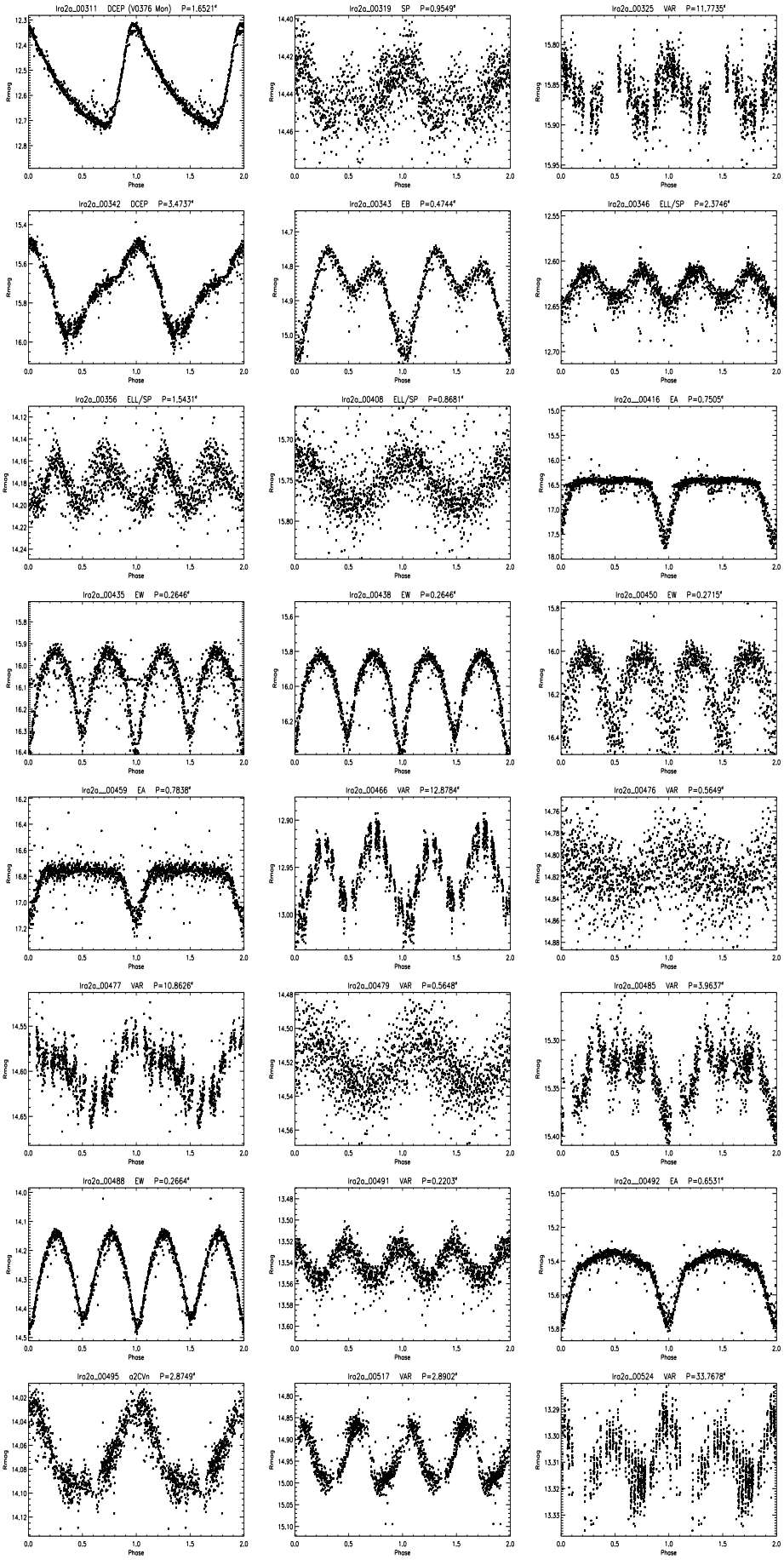
lra2a_00311 DCEP (V0376 Mon) P=1.6521d
lra2a_00319 SP P=0.9549d
lra2a_00325 VAR P=11.7735d
lra2a_00342 DCEP P=3.4737d
lra2a_00343 EB P=0.4744d
lra2a_00346 ELL/SP P=2.3746d
lra2a_00356 ELL/SP P=1.5431d
lra2a_00408 ELL/SP P=0.8681d
lra2a__00416 EA P=0.7505d
lra2a_00435 EW P=0.2646d
lra2a_00438 EW P=0.2646d
lra2a_00450 EW P=0.2715d
lra2a__00459 EA P=0.7838d
lra2a_00466 VAR P=12.8784d
lra2a_00476 VAR P=0.5649d
lra2a_00477 VAR P=10.8626d
lra2a_00479 VAR P=0.5648d
lra2a_00485 VAR P=3.9637d
lra2a_00488 EW P=0.2664d
lra2a_00491 VAR P=0.2203d
lra2a__00492 EA P=0.6531d
lra2a_00495 a2CVn P=2.8749d
lra2a_00517 VAR P=2.8902d
lra2a_00524 VAR P=33.7678d
Rmag
Phase

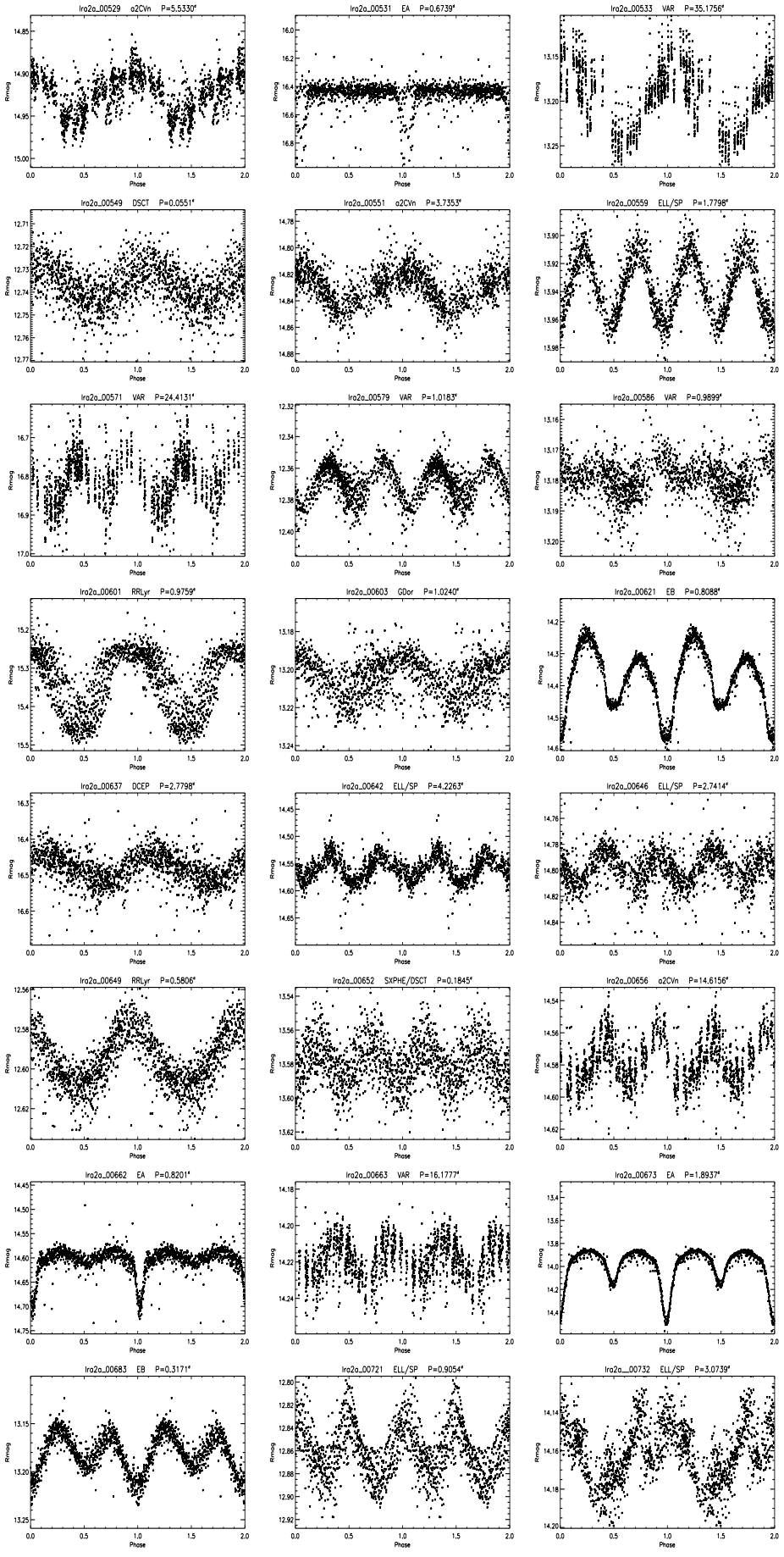
lra2a_00529 a2CVn P=5.5330d
lra2a_00531 EA P=0.6739d
lra2a_00533 VAR P=35.1756d
lra2a_00549 DSCT P=0.0551d
lra2a_00551 a2CVn P=3.7353d
lra2a_00559 ELL/SP P=1.7798d
lra2a_00571 VAR P=24.4131d
lra2a_00579 VAR P=1.0183d
lra2a_00586 VAR P=0.9899d
lra2a_00601 RRLyr P=0.9759d
lra2a_00603 GDor P=1.0240d
lra2a_00621 EB P=0.8088d
lra2a_00637 DCEP P=2.7798d
lra2a_00642 ELL/SP P=4.2263d
lra2a_00646 ELL/SP P=2.7414d
lra2a_00649 RRLyr P=0.5806d
lra2a_00652 SXPHE/DSCT P=0.1845d
lra2a_00656 a2CVn P=14.6156d
lra2a_00662 EA P=0.8201d
lra2a_00663 VAR P=16.1777d
lra2a_00673 EA P=1.8937d
lra2a_00683 EB P=0.3171d
lra2a_00721 ELL/SP P=0.9054d
lra2a_00732 ELL/SP P=3.0739d
Rmag
Phase

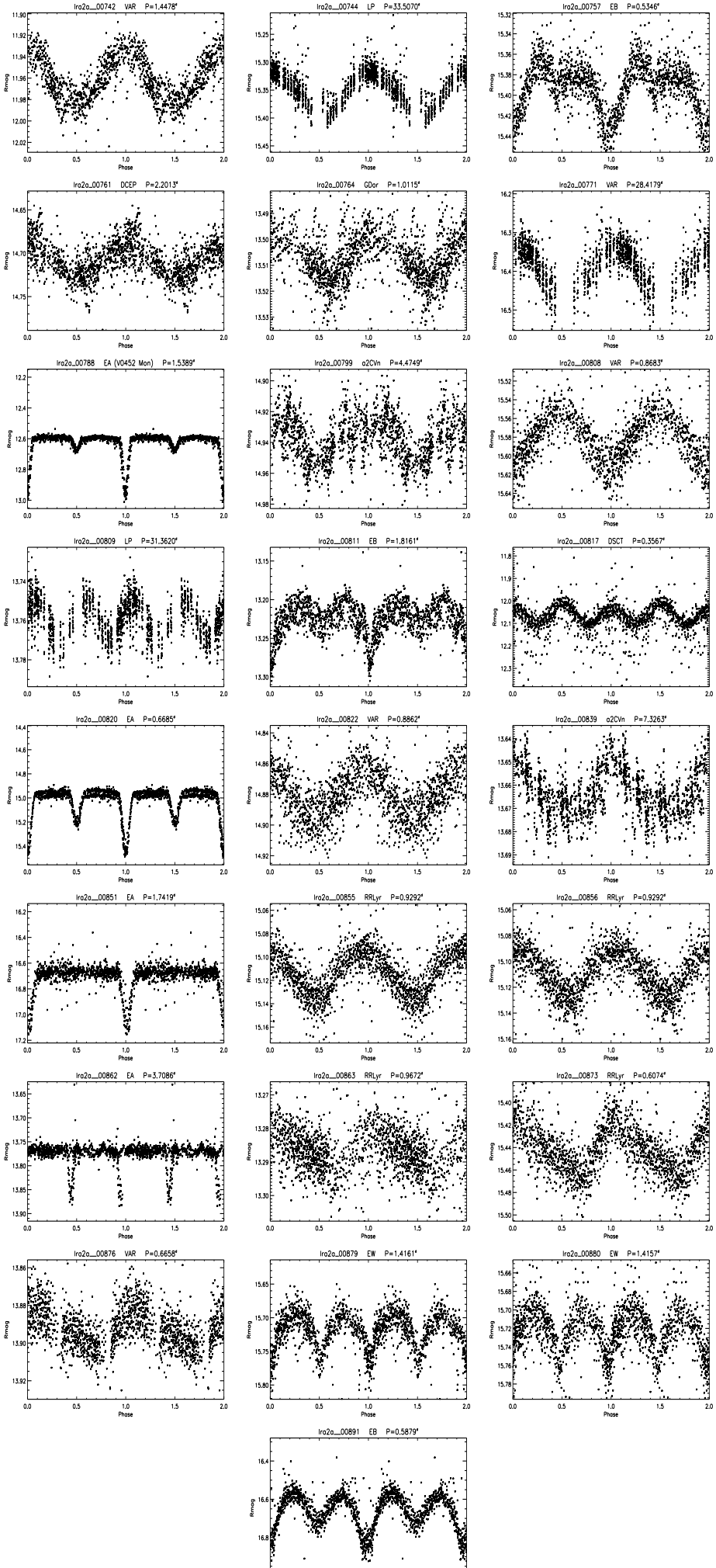
Ira2a__00742 VAR P=1.4478ᵈ
Ira2a__00744 LP P=33.5070ᵈ
Ira2a__00757 EB P=0.5346ᵈ
Ira2a__00761 DCEP P=2.2013ᵈ
Ira2a__00764 GDor P=1.0115ᵈ
Ira2a__00771 VAR P=28.4179ᵈ
Ira2a__00788 EA (V0452 Mon) P=1.5389ᵈ
Ira2a__00799 a2CVn P=4.4749ᵈ
Ira2a__00808 VAR P=0.8683ᵈ
Ira2a__00809 LP P=31.3620ᵈ
Ira2a__00811 EB P=1.8161ᵈ
Ira2a__00817 DSCT P=0.3567ᵈ
Ira2a__00820 EA P=0.6685ᵈ
Ira2a__00822 VAR P=0.8862ᵈ
Ira2a__00839 a2CVn P=7.3263ᵈ
Ira2a__00851 EA P=1.7419ᵈ
Ira2a__00855 RRLyr P=0.9292ᵈ
Ira2a__00856 RRLyr P=0.9292ᵈ
Ira2a__00862 EA P=3.7086ᵈ
Ira2a__00863 RRLyr P=0.9672ᵈ
Ira2a__00873 RRLyr P=0.6074ᵈ
Ira2a__00876 VAR P=0.6658ᵈ
Ira2a__00879 EW P=1.4161ᵈ
Ira2a__00880 EW P=1.4157ᵈ
Ira2a__00891 EB P=0.5879ᵈ
Rmag
Phase

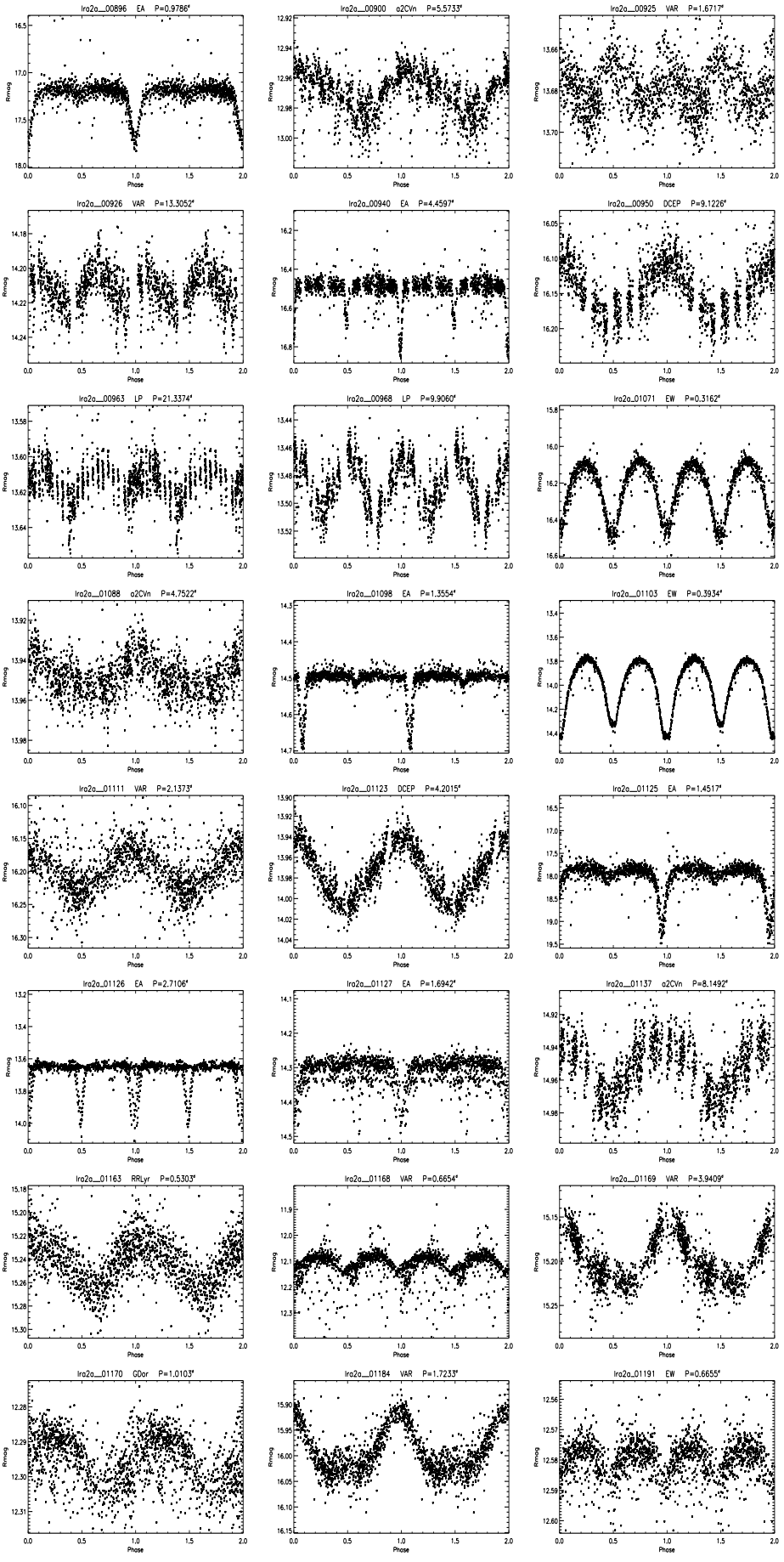
lra2a__00896 EA P=0.9786ᵈ
lra2a__00900 a2CVn P=5.5733ᵈ
lra2a__00925 VAR P=1.6717ᵈ
lra2a__00926 VAR P=13.3052ᵈ
lra2a__00940 EA P=4.4597ᵈ
lra2a__00950 DCEP P=9.1226ᵈ
lra2a__00963 LP P=21.3374ᵈ
lra2a__00968 LP P=9.9060ᵈ
lra2a__01071 EW P=0.3162ᵈ
lra2a__01088 a2CVn P=4.7522ᵈ
lra2a__01098 EA P=1.3554ᵈ
lra2a__01103 EW P=0.3934ᵈ
lra2a__01111 VAR P=2.1373ᵈ
lra2a__01123 DCEP P=4.2015ᵈ
lra2a__01125 EA P=1.4517ᵈ
lra2a__01126 EA P=2.7106ᵈ
lra2a__01127 EA P=1.6942ᵈ
lra2a__01137 a2CVn P=8.1492ᵈ
lra2a__01163 RRLyr P=0.5303ᵈ
lra2a__01168 VAR P=0.6654ᵈ
lra2a__01169 VAR P=3.9409ᵈ
lra2a__01170 GDor P=1.0103ᵈ
lra2a__01184 VAR P=1.7233ᵈ
lra2a__01191 EW P=0.6655ᵈ
Rmag
Phase

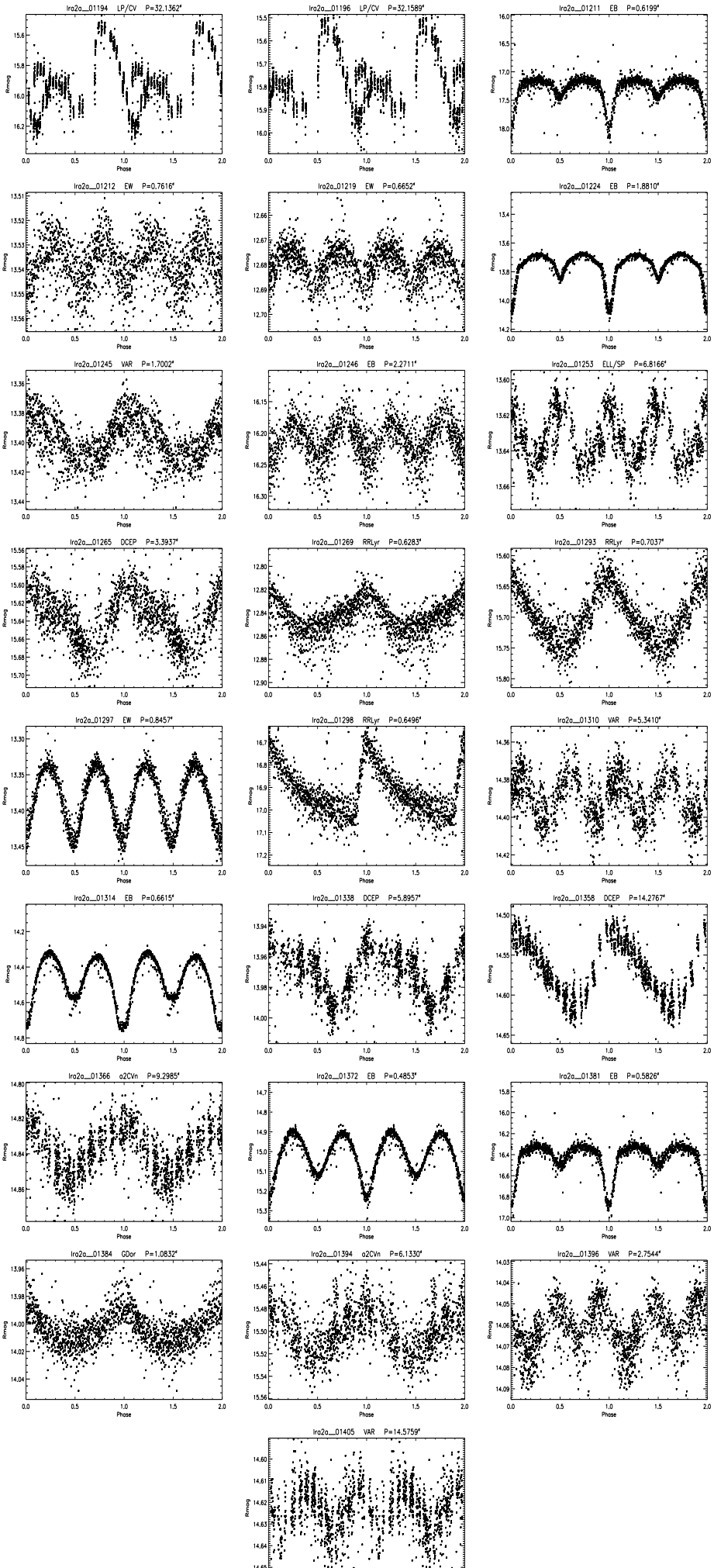
lra2a_01194 LP/CV P=32.1362*
lra2a_01196 LP/CV P=32.1589*
lra2a_01211 EB P=0.6199*
lra2a_01212 EW P=0.7616*
lra2a_01219 EW P=0.6652*
lra2a_01224 EB P=1.8810*
lra2a_01245 VAR P=1.7002*
lra2a_01246 EB P=2.2711*
lra2a_01253 ELL/SP P=6.8166*
lra2a_01265 DCEP P=3.3937*
lra2a_01269 RRLyr P=0.6283*
lra2a_01293 RRLyr P=0.7037*
lra2a_01297 EW P=0.8457*
lra2a_01298 RRLyr P=0.6496*
lra2a_01310 VAR P=5.3410*
lra2a_01314 EB P=0.6615*
lra2a_01338 DCEP P=5.8957*
lra2a_01358 DCEP P=14.2767*
lra2a_01366 a2CVn P=9.2985*
lra2a_01372 EB P=0.4853*
lra2a_01381 EB P=0.5826*
lra2a_01384 GDor P=1.0832*
lra2a_01394 a2CVn P=6.1330*
lra2a_01396 VAR P=2.7544*
lra2a_01405 VAR P=14.5759*
Rmag
Phase

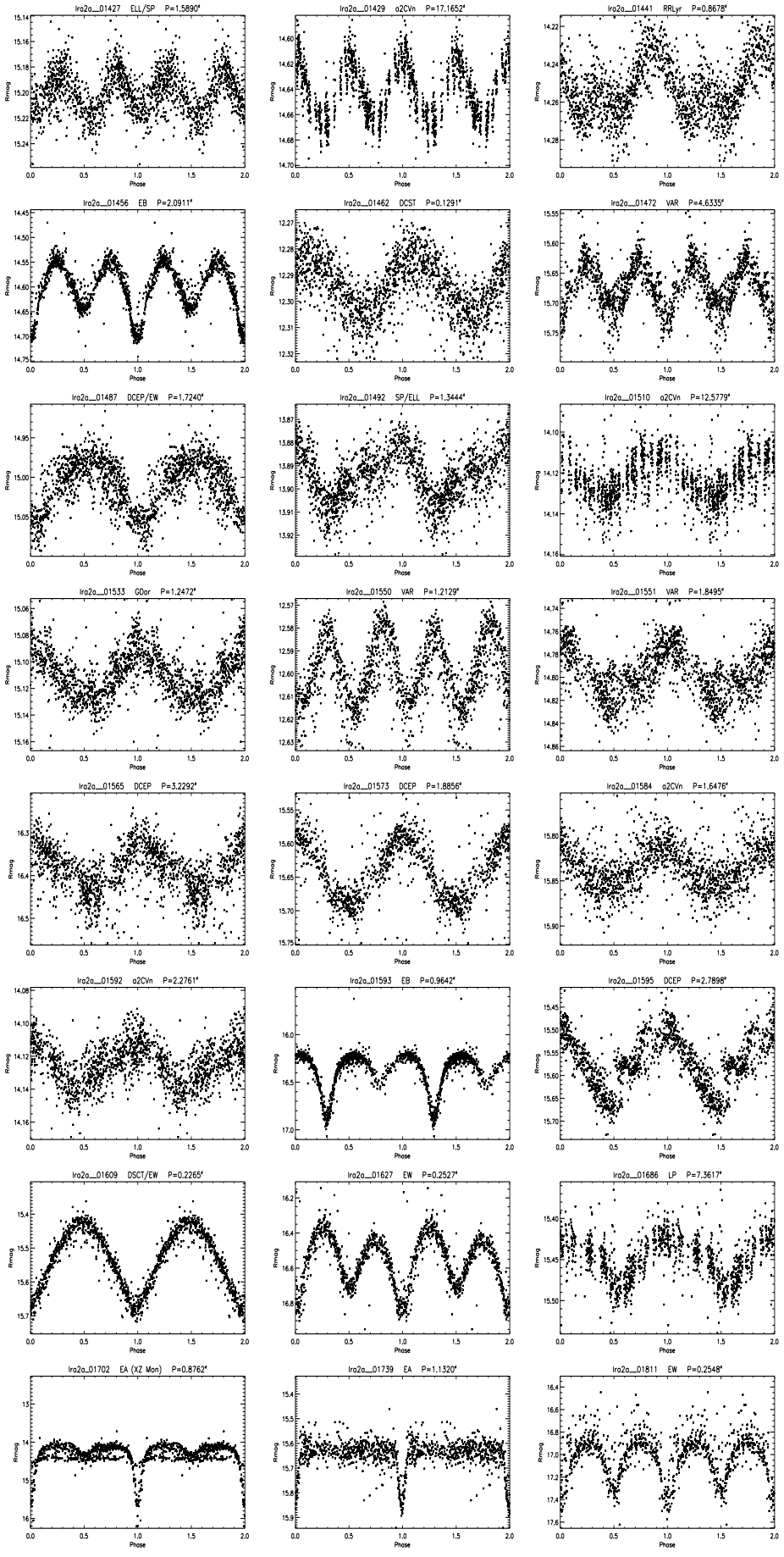
lra2a__01427 ELL/SP P=1.5890ᵈ
lra2a__01429 a2CVn P=17.1652ᵈ
lra2a__01441 RRLyr P=0.8678ᵈ
lra2a__01456 EB P=2.0911ᵈ
lra2a__01462 DCST P=0.1291ᵈ
lra2a__01472 VAR P=4.6335ᵈ
lra2a__01487 DCEP/EW P=1.7240ᵈ
lra2a__01492 SP/ELL P=1.3444ᵈ
lra2a__01510 a2CVn P=12.5779ᵈ
lra2a__01533 GDor P=1.2472ᵈ
lra2a__01550 VAR P=1.2129ᵈ
lra2a__01551 VAR P=1.8495ᵈ
lra2a__01565 DCEP P=3.2292ᵈ
lra2a__01573 DCEP P=1.8856ᵈ
lra2a__01584 a2CVn P=1.6476ᵈ
lra2a__01592 a2CVn P=2.2761ᵈ
lra2a__01593 EB P=0.9642ᵈ
lra2a__01595 DCEP P=2.7898ᵈ
lra2a__01609 DSCT/EW P=0.2265ᵈ
lra2a__01627 EW P=0.2527ᵈ
lra2a__01686 LP P=7.3617ᵈ
lra2a__01702 EA (XZ Mon) P=0.8762ᵈ
lra2a__01739 EA P=1.1320ᵈ
lra2a__01811 EW P=0.2548ᵈ
Rmag
Phase

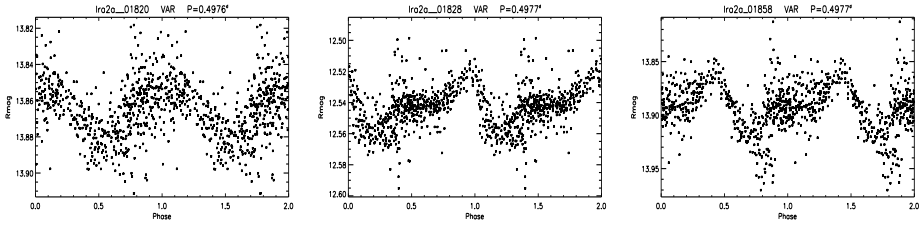
lro2a__01820 VAR P=0.4976*
lro2a__01828 VAR P=0.4977*
lro2a_01858 VAR P=0.4977*
Rmmag
Phase

Figure A.31: *Detected variable stars in LRa2b subfield.*

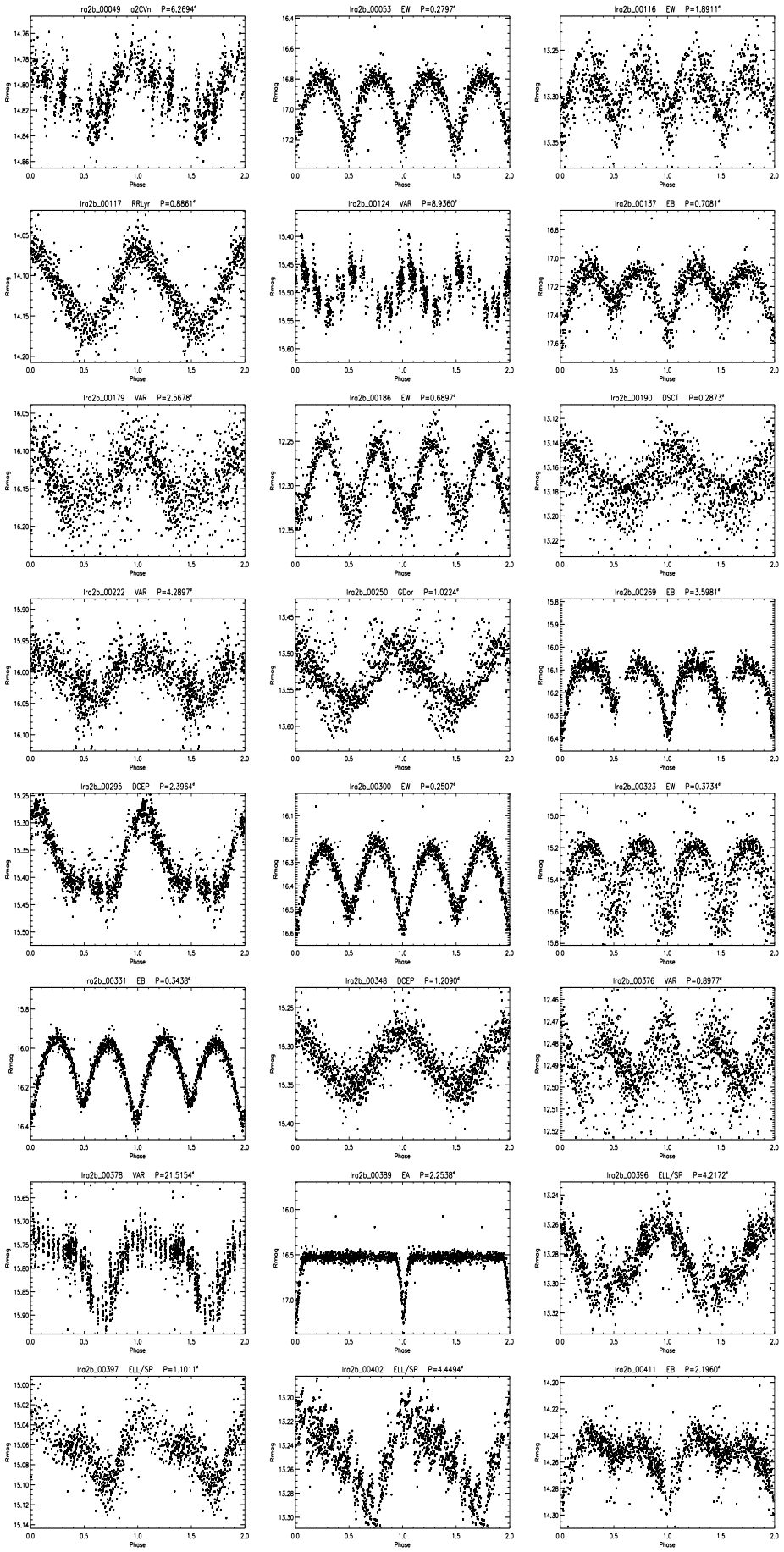

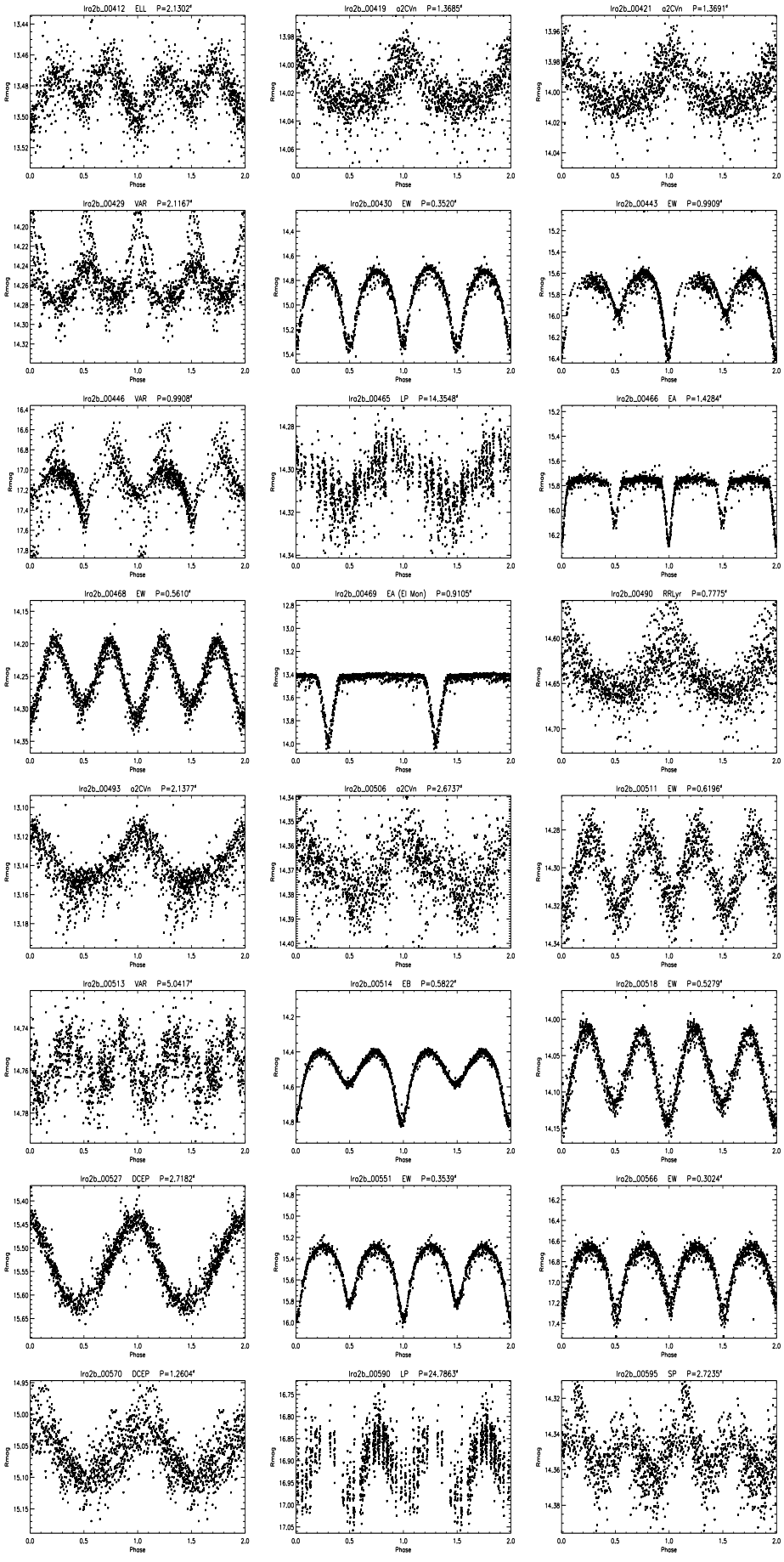
lra2b_00412 ELL P=2.1302ª
lra2b_00419 a2CVn P=1.3685ª
lra2b_00421 a2CVn P=1.3691ª
lra2b_00429 VAR P=2.1167ª
lra2b_00430 EW P=0.3520ª
lra2b_00443 EW P=0.9909ª
lra2b_00446 VAR P=0.9908ª
lra2b_00465 LP P=14.3548ª
lra2b_00466 EA P=1.4284ª
lra2b_00468 EW P=0.5610ª
lra2b_00469 EA (El Mon) P=0.9105ª
lra2b_00490 RRLyr P=0.7775ª
lra2b_00493 a2CVn P=2.1377ª
lra2b_00506 a2CVn P=2.6737ª
lra2b_00511 EW P=0.6196ª
lra2b_00513 VAR P=5.0417ª
lra2b_00514 EB P=0.5822ª
lra2b_00518 EW P=0.5279ª
lra2b_00527 DCEP P=2.7182ª
lra2b_00551 EW P=0.3539ª
lra2b_00566 EW P=0.3024ª
lra2b_00570 DCEP P=1.2604ª
lra2b_00590 LP P=24.7863ª
lra2b_00595 SP P=2.7235ª
Rmag
Phase

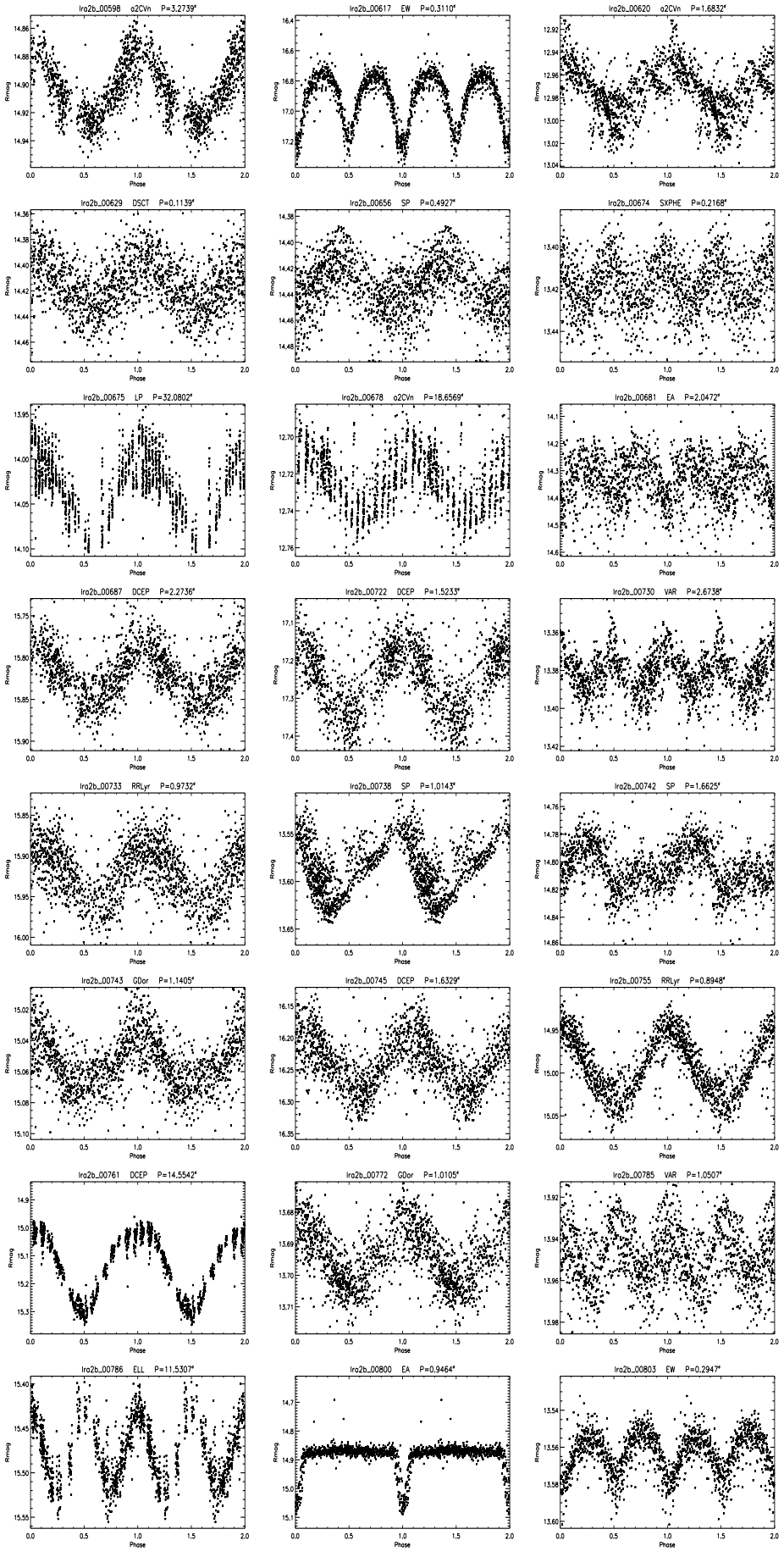
lra2b_00598 a2CVn P=3.2739ª
lra2b_00617 EW P=0.3110ª
lra2b_00620 a2CVn P=1.6832ª
lra2b_00629 DSCT P=0.1139ª
lra2b_00656 SP P=0.4927ª
lra2b_00674 SXPHE P=0.2168ª
lra2b_00675 LP P=32.0802ª
lra2b_00678 a2CVn P=18.6569ª
lra2b_00681 EA P=2.0472ª
lra2b_00687 DCEP P=2.2736ª
lra2b_00722 DCEP P=1.5233ª
lra2b_00730 VAR P=2.6738ª
lra2b_00733 RRLyr P=0.9732ª
lra2b_00738 SP P=1.0143ª
lra2b_00742 SP P=1.6625ª
lra2b_00743 GDor P=1.1405ª
lra2b_00745 DCEP P=1.6329ª
lra2b_00755 RRLyr P=0.8948ª
lra2b_00761 DCEP P=14.5542ª
lra2b_00772 GDor P=1.0105ª
lra2b_00785 VAR P=1.0507ª
lra2b_00786 ELL P=11.5307ª
lra2b_00800 EA P=0.9464ª
lra2b_00803 EW P=0.2947ª
Rmag
Phase

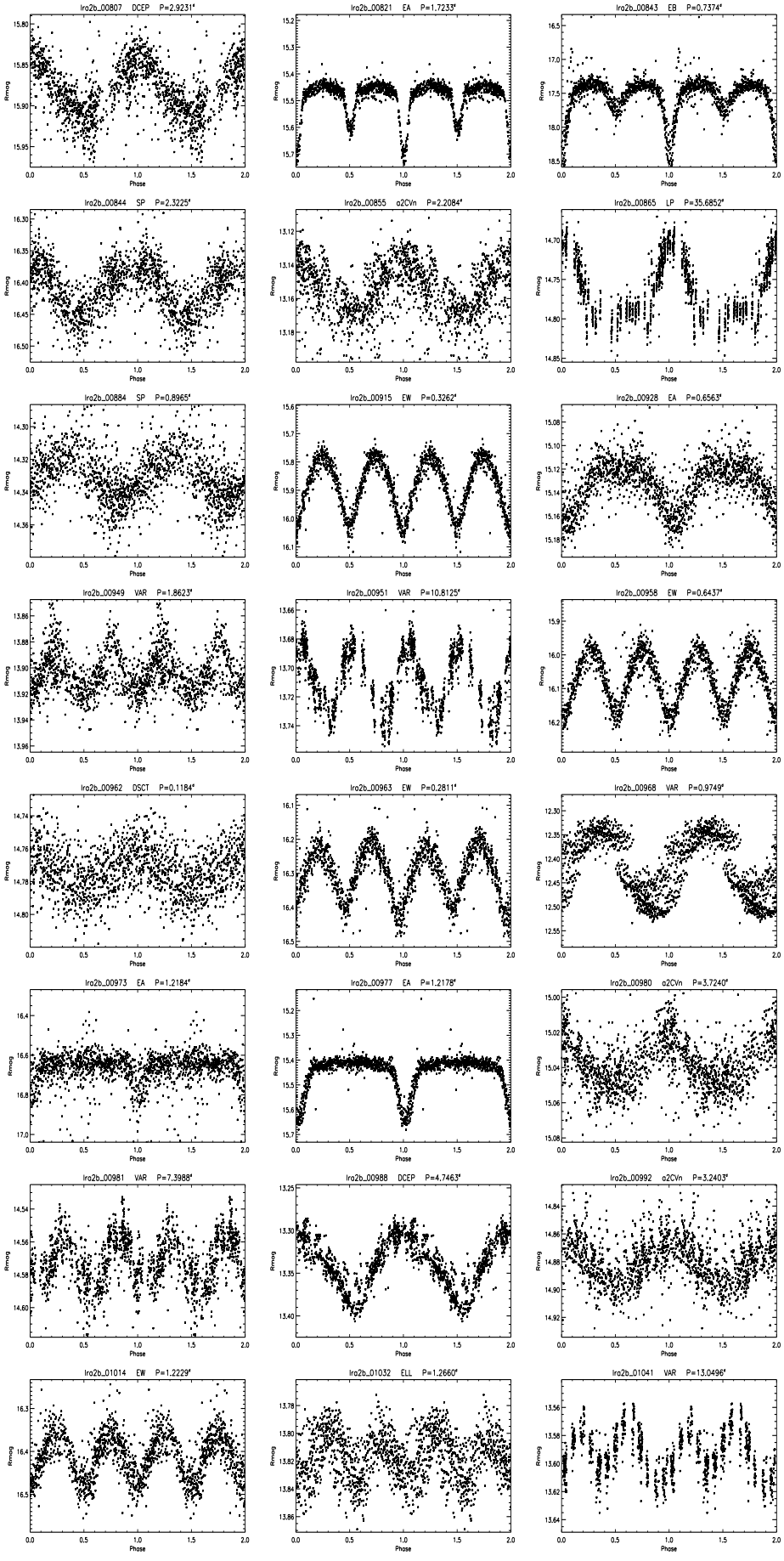
lra2b_00807 DCEP P=2.9231d
lra2b_00821 EA P=1.7233d
lra2b_00843 EB P=0.7374d
lra2b_00844 SP P=2.3225d
lra2b_00855 a2CVn P=2.2084d
lra2b_00865 LP P=35.6852d
lra2b_00884 SP P=0.8965d
lra2b_00915 EW P=0.3262d
lra2b_00928 EA P=0.6563d
lra2b_00949 VAR P=1.8623d
lra2b_00951 VAR P=10.8125d
lra2b_00958 EW P=0.6437d
lra2b_00962 DSCT P=0.1184d
lra2b_00963 EW P=0.2811d
lra2b_00968 VAR P=0.9749d
lra2b_00973 EA P=1.2184d
lra2b_00977 EA P=1.2178d
lra2b_00980 a2CVn P=3.7240d
lra2b_00981 VAR P=7.3988d
lra2b_00988 DCEP P=4.7463d
lra2b_00992 a2CVn P=3.2403d
lra2b_01014 EW P=1.2229d
lra2b_01032 ELL P=1.2660d
lra2b_01041 VAR P=13.0496d
Rmag
Phase

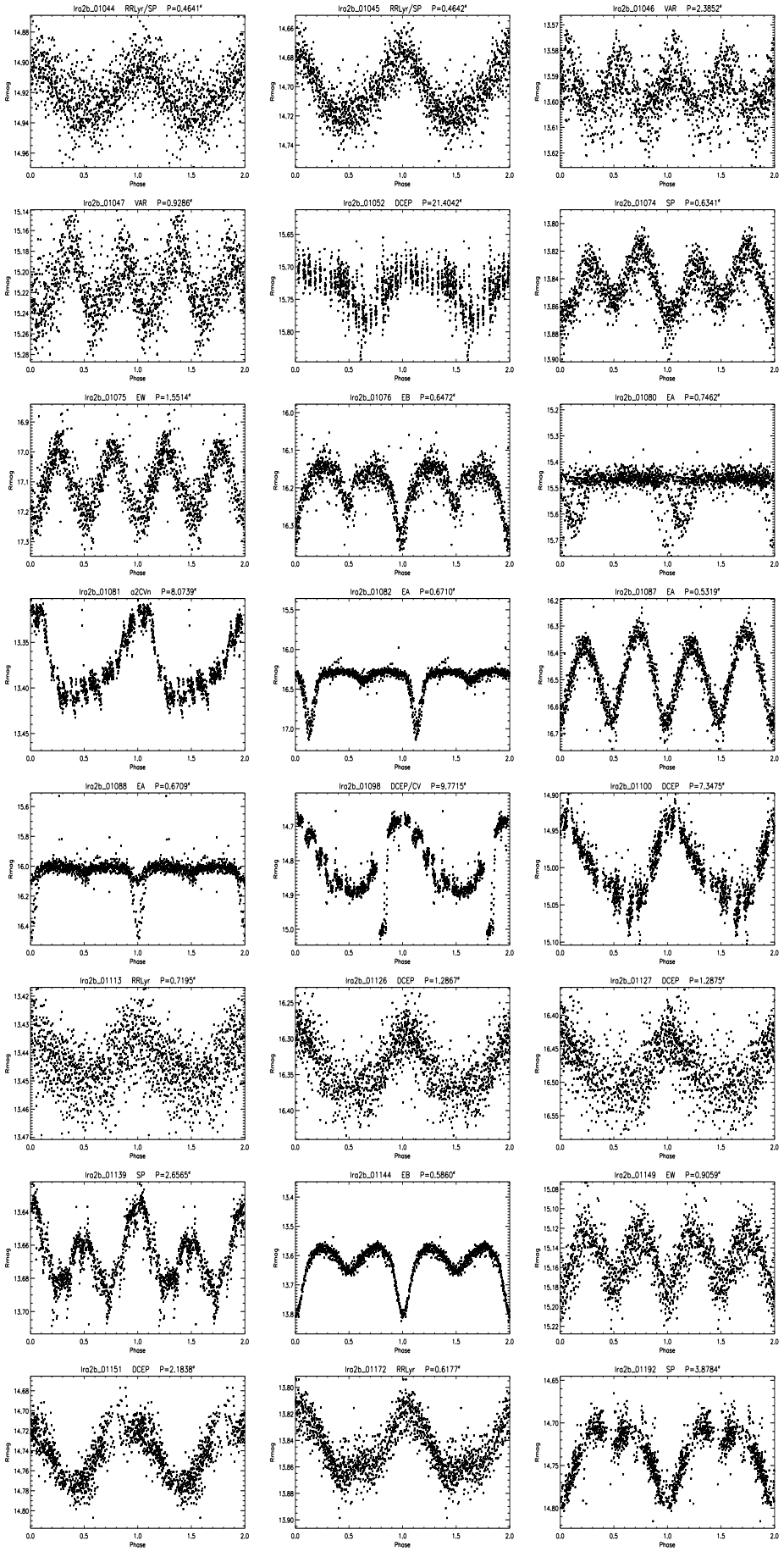
lra2b_01044 RRLyr/SP P=0.4641*
lra2b_01045 RRLyr/SP P=0.4642*
lra2b_01046 VAR P=2.3852*
lra2b_01047 VAR P=0.9286*
lra2b_01052 DCEP P=21.4042*
lra2b_01074 SP P=0.6341*
lra2b_01075 EW P=1.5514*
lra2b_01076 EB P=0.6472*
lra2b_01080 EA P=0.7462*
lra2b_01081 a2CVn P=8.0739*
lra2b_01082 EA P=0.6710*
lra2b_01087 EA P=0.5319*
lra2b_01088 EA P=0.6709*
lra2b_01098 DCEP/CV P=9.7715*
lra2b_01100 DCEP P=7.3475*
lra2b_01113 RRLyr P=0.7195*
lra2b_01126 DCEP P=1.2867*
lra2b_01127 DCEP P=1.2875*
lra2b_01139 SP P=2.6565*
lra2b_01144 EB P=0.5860*
lra2b_01149 EW P=0.9059*
lra2b_01151 DCEP P=2.1838*
lra2b_01172 RRLyr P=0.6177*
lra2b_01192 SP P=3.8784*
Rmag
Phase

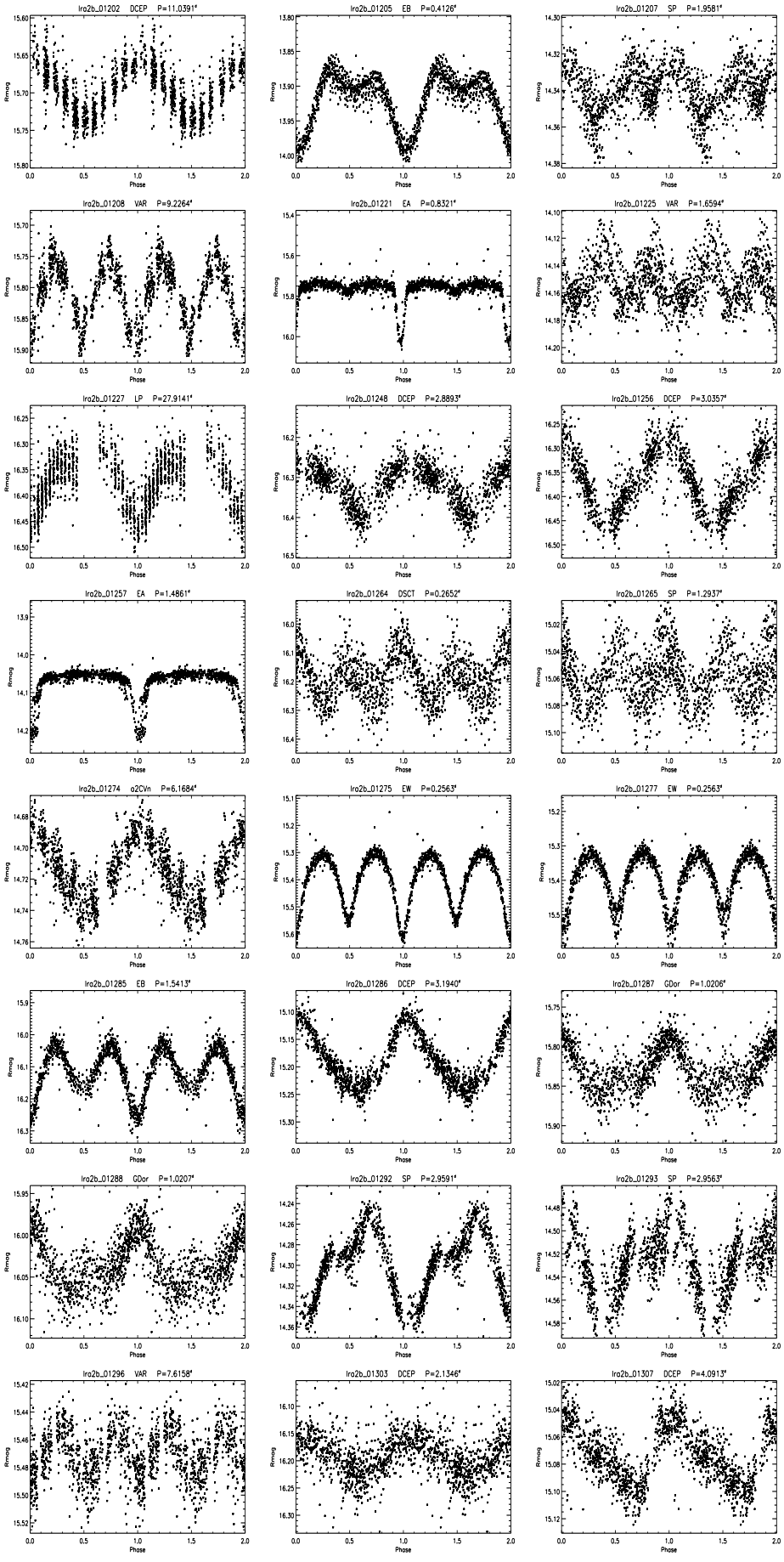
lra2b_01202 DCEP P=11.0391d
lra2b_01205 EB P=0.4126d
lra2b_01207 SP P=1.9581d
lra2b_01208 VAR P=9.2264d
lra2b_01221 EA P=0.8321d
lra2b_01225 VAR P=1.6594d
lra2b_01227 LP P=27.9141d
lra2b_01248 DCEP P=2.8893d
lra2b_01256 DCEP P=3.0357d
lra2b_01257 EA P=1.4861d
lra2b_01264 DSCT P=0.2652d
lra2b_01265 SP P=1.2937d
lra2b_01274 α2CVn P=6.1684d
lra2b_01275 EW P=0.2563d
lra2b_01277 EW P=0.2563d
lra2b_01285 EB P=1.5413d
lra2b_01286 DCEP P=3.1940d
lra2b_01287 GDor P=1.0206d
lra2b_01288 GDor P=1.0207d
lra2b_01292 SP P=2.9591d
lra2b_01293 SP P=2.9563d
lra2b_01296 VAR P=7.6158d
lra2b_01303 DCEP P=2.1346d
lra2b_01307 DCEP P=4.0913d
Rmag
Phase

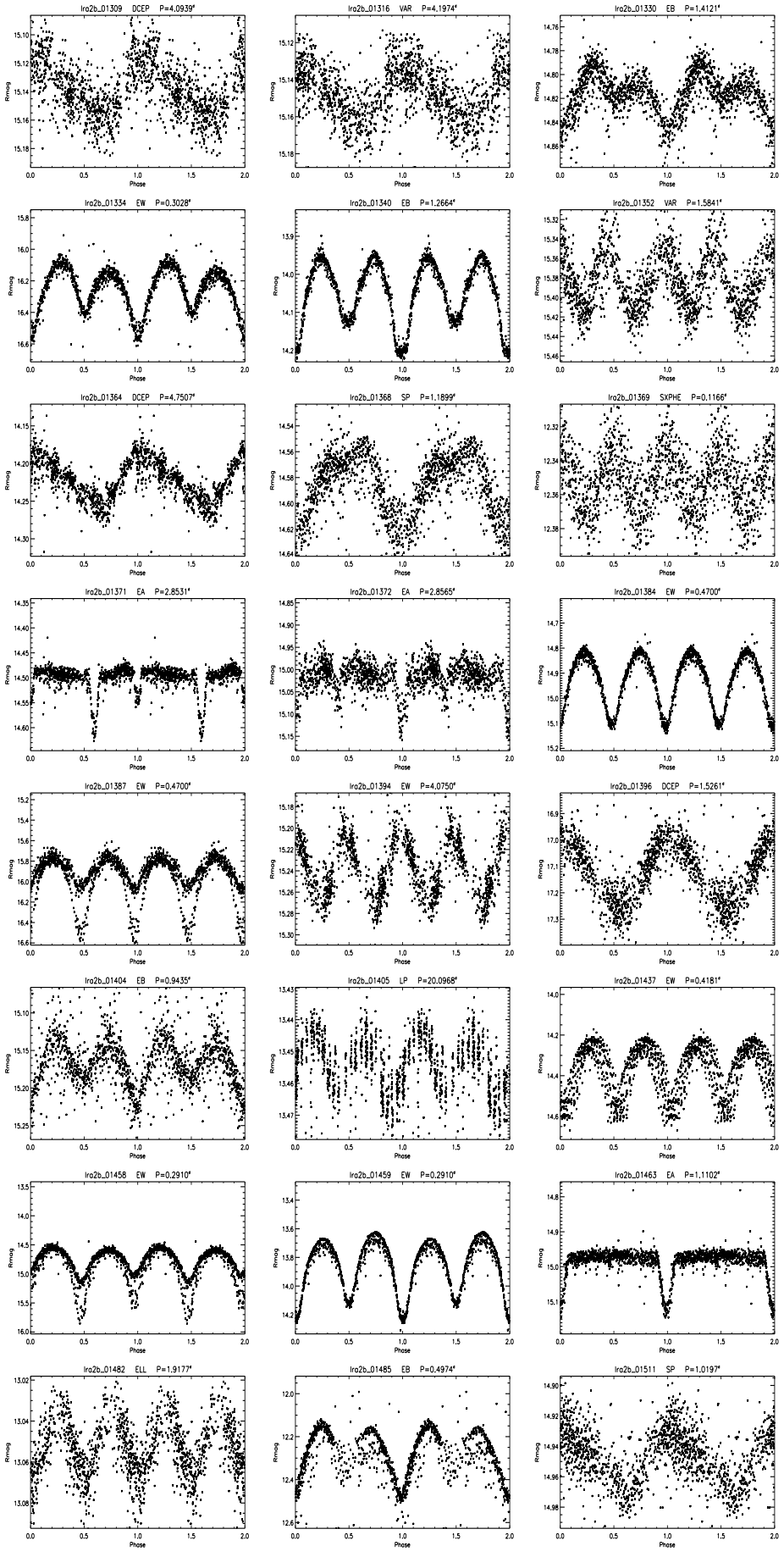
lra2b_01309 DCEP P=4.0939*
lra2b_01316 VAR P=4.1974*
lra2b_01330 EB P=1.4121*
lra2b_01334 EW P=0.3028*
lra2b_01340 EB P=1.2664*
lra2b_01352 VAR P=1.5841*
lra2b_01364 DCEP P=4.7507*
lra2b_01368 SP P=1.1899*
lra2b_01369 SXPHE P=0.1166*
lra2b_01371 EA P=2.8531*
lra2b_01372 EA P=2.8565*
lra2b_01384 EW P=0.4700*
lra2b_01387 EW P=0.4700*
lra2b_01394 EW P=4.0750*
lra2b_01396 DCEP P=1.5261*
lra2b_01404 EB P=0.9435*
lra2b_01405 LP P=20.0968*
lra2b_01437 EW P=0.4181*
lra2b_01458 EW P=0.2910*
lra2b_01459 EW P=0.2910*
lra2b_01463 EA P=1.1102*
lra2b_01482 ELL P=1.9177*
lra2b_01485 EB P=0.4974*
lra2b_01511 SP P=1.0197*
Rmag
Phase

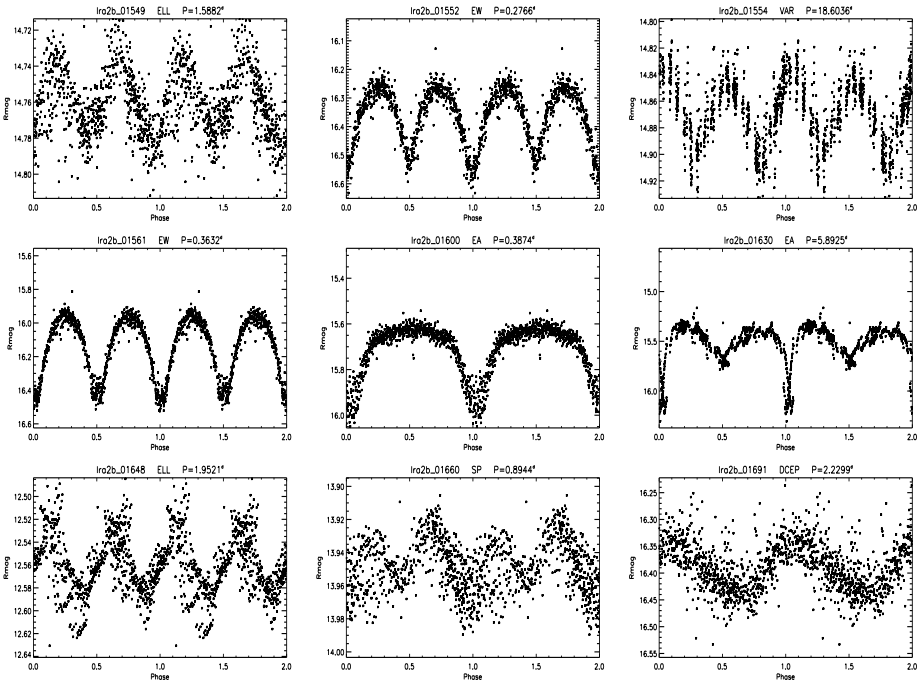
lra2b_01549 ELL P=1.5882ᵈ
lra2b_01552 EW P=0.2766ᵈ
lra2b_01554 VAR P=18.6036ᵈ
lra2b_01561 EW P=0.3632ᵈ
lra2b_01600 EA P=0.3874ᵈ
lra2b_01630 EA P=5.8925ᵈ
lra2b_01648 ELL P=1.9521ᵈ
lra2b_01660 SP P=0.8944ᵈ
lra2b_01691 DCEP P=2.2299ᵈ
Rmag
Phase

Bibliography

[1] Parrot, A. *The History, book VII translated by David Grene* (University of Chicago Press, 1987).

[2] Espenak, F. Http://eclipse.gsfc.nasa.gov/eclipse.html.

[3] Http://www.iau.org/public_press/news/release/iau0601/.

[4] (2006). IAU Press Releases iau603.

[5] Marcy, G. Http://exoplanets.org/newsframe.html.

[6] Http://exoplanet.eu/.

[7] Sagan, C. *Cosmos (Czech translation)* (TOK, 1996).

[8] Kant, I. *Kritik der reinen Vernünft* (1755).

[9] Herschel, W. On the diameter and magnitude of the georgium sidus; with a description of the dark and lucid disk and periphery micrometers. by william herschel, esq. f. r. s. *RSPT* **73**, 4 (1783).

[10] Herschel, W. On the remarkable appearances at the polar rgions of the planet mars, the inclination of its axis, the position of its poles, and its spheroidical figure; with a few hints relating to its real diameter and atmosphere. by william herschel, esq. f. r. s. *RSPT* **74**, 233 (1784).

[11] Herschel, W. Observations on the planet venus. by william herschel, ll. d. f. r. s. *RSPT* **83**, 201 (1793).

[12] Struve, O. Proposal for a project of high-precision stellar radial velocity work. *Obs.* **72**, 199 (1952).

[13] Wolszczan, A. & Frail, D. A. tr. *Nature* **355**, 145 (1991).

[14] Mayor, M. & Queloz, D. A jupiter mass companion to a solar-type star. *Nature* **378**, 355 (1995).

[15] Baranne, A. *et al.* Elodie: A spectrograph for accurate radial velocity measurements. *A&A Suppl. Ser.* **119**, 373 (1996).

[16] Perruchot, S. *et al.* The sophie spectrograph: design and technical key-points for high throughput and high stability. *SPIE Proceedings* **7014**, 17 (2008).

[17] Pepe, F. *et al.* "harps, a new high-resolution spectrograph for the serach of extra-solar planets," in optical and ir telescope instrumentation and detectors. *SPIE Proceedings* **4008**, 582 (2000).

[18] Charbonneau, D., Brown, M. T., Latham, W. D. & Mayor, M. Detection of planetary transits across a sun-like star. *ApJ* **529**, 45 (2000).

[19] Baglin, A. *et al.* Corot: asteroseismology and planet finding. *ESA SP-485: Stellar Structure and Habitable Planet Finding* **485**, 17 (2002).

[20] Lagrange, A.-M. *et al.* A probable giant planet imaged in the β pictoris disk. vlt/naco deep l'-band imaging. *A&A* **493**, 21 (2009).

[21] Fischer, D. & Valenti, J. The planet-metallicity correlation. *ApJ* **622**, 1102 (2005).

[22] Rauer, H. e. a. Statistical distributions of planets (group discussions) **in preparation** (2009).

[23] Hatzes, A. P. *et al.* A giant planet around the massive giant star hd 13189. *A&A* **437**, 743 (2005).

[24] Guenther, E. W. & Wuchterl, G. Companions of old brown dwarfs, and very low mass stars. *A&A* **401**, 677 (2003).

[25] Http://www.esa.int/esaCP/index.html.

[26] Alonso, R. *et al.* Tres-1: The transiting planet of a bright k0 v star. *ApJ* **613**, 153 (2004).

[27] Deleuil, M. *et al.* Transiting exoplanets from the corot space mission . vi. corot-exo-3b: the first secure inhabitant of the brown-dwarf desert. *A&A* **491**, 889 (2008).

[28] Bonfils, X. *et al.* The harps search for southern extra-solar planets. vi. a neptune-mass planet around the nearby m dwarf gl 581. *A&A* **443**, 15 (2005).

[29] Léger, A. & et al. Transiting exoplanets from the corot space mission viii. corot-7b: the first super-earth with measured radius. *A&A* **submitted** (2009).

[30] Hoffmeister, C. *Veränderliche Sterne* (Johann Ambrosius Barthel, 1984).

[31] Fernie, J. D. In search of better skies:harvard in peru, ii. *American Scientist* **3** (2001).

[32] Shapley, H. On the nature and cause of cepheid variation. *ApJ* **40**, 448 (1914).

[33] Eddington, A. S. Stars, gaseous, on the pulsations of a gaseous star. *Mon. Not. R. Astron. Soc.* **79**, 2 (1918).

[34] Kazarovets, E. V., Samus, N. N., Durlevich, O. V., Kireeva, N. N. & Pastukhova, E. N. The 79th name-list of variable stars. *IBVS* **5863**, 1 (2008).

[35] Http://outreach.atnf.csiro.au/education/senior/astrophysics/.

[36] Hertzsprung, E. On the relation between period and form of the lightcurve of variable stars of the δ cep type. *BAN* **3**, 115 (1926).

[37] Ribas, I. Binaries as astrophysical laboratories: Open questions. *ASPC* **349**, 55 (2006).

[38] Http://hubblesite.org/.

[39] Http://www.aavso.org/.

[40] Http://csep10.phys.utk.edu/astr162/lect/binaries/algol.html.

[41] Goodricke, J. On the periods of the changes of light in the star algol. *Philosophical Transactions of the Royal Society of London* **74**, 287 (1784).

[42] Markwick, E. E. ϵ, note on the variation of. *MNRAS* **65**, 83 (1904).

[43] Http://jbworld.jbs.st-louis.mo.us/science/astromet/NAAP/ebs/animations/ebs.swf.

[44] Vincent, A., Piskunov, N. E. & Tuominen, I. Surface imaging of eclipsing binary stars. 1: Techniques. *A&A* **278**, 523 (1993).

[45] Samus, N. N., Durlevich, O. V. & et al. Combined general catalogue of variable stars (samus+ 2004). *SIMBAD* (2004).

[46] Henry, T. J., Kirkpatrick, J. D. & Simons, D. A. The solar neighborhood, 1: Standard spectral types (k5-m8) for northern dwarfs within eight parsecs. *AJ* **108**, 1437 (1994).

[47] Saumon, D., Bergeron, P., Luine, J. I. & Hubbard, W. B. Cool zero-metallicity stellar atmospheres. *ApJ* **424**, 333 (1994).

[48] Saumon, D. *et al.* A theory of extrasolar giant planets. *ApJ* **460**, 993 (1996).

[49] Kirkpatrick, J. D. Outstanding issues in our understanding of l, t, and y dwarfs. *ASPC* **384**, 85 (2008).

[50] Nakajima, T. *et al.* Discovery of a cool brown dwarf. *Nature* **378**, 463 (1995).

[51] Rebolo, R. & Zapatero-Osorio, R., M. Discovery of a brown dwarf in the pleiades star cluster. *Nature* **377**, 129 (1995).

[52] Martín, E. L., Brandner, W. & Basri, G. A search for companions to nearby brown dwarfs: The binary denis-p j1228.2-1547. *Science* **238**, 1718 (1999).

[53] Koerner, D. W., Kirkpatrick, J. D., McElwain, M. W. & Bonaventura, N. R. Keck imaging of binary l dwarfs. *ApJ* **526**, 25 (1999).

[54] Butler, R. P., Marcy, G. W., Williams, E., Hauser, H. & Shirts, P. Three new "51 pegasi–type" planets. *ApJ* **474**, 115 (1997).

[55] Bouchy, F. *et al.* Two new "very hot jupiters" among the ogle transiting candidates. *A&A* **421**, 13 (2004).

[56] Mandushev, G. *et al.* Tres-4: A transiting hot jupiter of very low density. *ApJ* **667**, 195 (2007).

[57] Marcy, G. W. & Butler, P. R. A planetary companion to 70 virginis. *ApJ* **464**, 147 (1996).

[58] Butler, R. P. & Marcy, G. W. A planet orbiting 47 ursae majoris. *Ap.J.Lett* **464**, 153 (1996).

[59] Fischer, D. A. *et al.* Planetary companions to hd 12661, hd 92788, and hd 38529 and variations in keplerian residuals of extrasolar planets. *ApJ* **551**, 1107 (2001).

[60] Udry, S. *et al.* The harps search for southern extra-solar planets. xi. super-earths (5 and 8 $m_{\oplus}$) in a 3-planet system. *A&A* **469**, 43 (2007).

[61] Mayor, M. *et al.* The harps search for southern extra-solar planets. xiii. a planetary system with 3 super-earths (4.2, 6.9, and 9.2 $m_{\oplus}$. *A&A* **493**, 639 (2009).

[62] Guillot, T., Burrows, A., Hubbard, W. B., Lunine, J. I. & Saumon, D. Giant planets at small orbital distances. *ApJ* **459**, 35 (1996).

[63] Vidal-Madjar, A. *et al.* An extended upper atmosphere around the extrasolar planet hd209458b. *Nature* **422**, 143 (2003).

[64] Vidal-Madjar, A. *et al.* Detection of oxygen and carbon in the hydrodynamically escaping atmosphere of the extrasolar planet hd 209458b. *ApJ* **604**, 69 (2004).

[65] Barman, T. Identification of absorption features in an extrasolar planet atmosphere. *ApJ* **661**, 191 (2007).

[66] Pätzold, M., Carone, L. & Rauer, H. Tidal interactions of close-in extrasolar planets: The ogle cases. *A&A* **427**, 1075 (2004).

[67] Vidal-Madjar, A. *et al.* Exoplanet hd 209458b (osiris): Evaporation strengthened. *ApJ* **676**, 57 (2008).

[68] Lecavelier des Etangs, A., Vidal-Madjar, A., McConnell, J. C. & Hébrard, G. Diagram to determine the evaporation status of extrasolar planets. *A&A* **418**, 1 (2004).

[69] Lecavelier des Etangs, A. Diagram to determine the evaporation status of extrasolar planets. *A&A* **461**, 1185 (2007).

[70] Butler, P. R. *et al.* A neptune-mass planet orbiting the nearby m dwarf gj 436. *ApJ* **617**, 580 (2004).

[71] Valencia, D., Sasselov, D. D. & O'Connel, R. J. Detailed models of super-earths: How well can we infer bulk properties? *ApJ* **665**, 1413 (2007).

[72] Fortney, J. J., Marley, M. S. & Barnes, J. W. Planetary radii across five orders of magnitude in mass and stellar insolation: Applications to transits. *ApJ* **659**, 1661 (2007).

[73] Kasting, J. F. Earth's early atmosphere. *Nature* **259**, 920 (1993).

[74] Woolf, N. J., Smith, P. S., Traub, W. A. & Jucks, K. W. The spectrum of earthshine: A pale blue dot observed from the ground. *ApJ* **574**, 430 (2002).

[75] Beaulieu, J.-P. e. a. Discovery of a cool planet of 5.5 earth masses through gravitational microlensing. *Nature* **439**, 437 (2006).

[76] Selsis, F. *et al.* Habitable planets around the star gliese 581. *A&A* **476**, 1373 (2007).

[77] von Paris, P. *et al.* Extrasolar planets in the gliese 581 system - model atmospheres and implications for habitability. *A&A* **submitted** (2009).

[78] Marcy, G. *et al.* Observed properties of exoplanets: Masses, orbits, and metallicities. *Progress of Theoretical Physics Supplement* **158**, 24 (2005).

[79] Greaves, J. S., Fischer, D. A., Wyatt, M. C., Beichman, C. A. & Bryden, G. Predicting the frequencies of diverse exo-planetary systems. *MNRAS* **378**, 1 (2007).

[80] Lineweaver, C. & D., G. What fraction of sun-like stars have planets. *ApJ* **598**, 1350 (2003).

[81] Perryman, M. Review: Extra-solar planets. *Rep. Prog. Phys.* **63**, 1209 (2000).

[82] Dvorak, R. e. *Extrasolar Planets Formation, Detection and Dynamics* (Wiley-VCH, Berlin, 2007).

[83] Kane, S. R. & von Braun, K. Constraining orbital parameters through planetary transit monitoring. *ApJ* **689**, 492 (2008).

[84] Sullivan, D. J. & Sullivan, T. Mauna kea high speed photometry of transits of the extrasolar planet hd 209458 b. *Baltic Astronomy* **12**, 145 (2003).

[85] Mandel, K. & Agol, E. Analytic light curves for planetary transit searches. *ApJ* **580**, 171 (2002).

[86] Voss, H. *Developing a ground-based search system for transits of extrasolar planets* (PhD thesis Technische Universität Berlin, 2006).

[87] Claret, A. A new non-linear limb-darkening law for lte stellar atmosphere models. calculations for $-5.0 <= \log[m/h] <= +1$, 2000 k <= teff <= 50000 k at several surface gravities. *A&A* **363**, 1081 (2000).

[88] Tingley, B. & Sackett, P. D. A photometric diagnostics to aid in the identification of transiting planets. *ApJ* **627**, 1011 (2005).

[89] Seager, S. & Mallén-Ornelas, G. A unique solution of planet and star parameters from an extrasolar planet transit light curve. *ApJ* **585**, 1038 (2003).

[90] Agol, E., Steffen, J., Sari, R. & Clarkson, W. On detecting terestrial planets with timing of giant planet transits. *MNRAS* **359**, 567 (2005).

[91] Steffen, J. *Detecting new planets in transiting systems* (PhD thesis University of Washington, 2006).

[92] Kirste, S. *Prospects for transit timing analysis of extrasolar planets* (Batchelor thesis Humboldt Universität Berlin, 2008).

[93] Miller-Ricci, E. *et al.* Most space-based photometry of the transiting exoplanet system hd 209458: Transit timing to search for additional planets. *ApJ* **682**, 586 (2008).

[94] Charbonneau, D. *et al.* Detection of thermal emission from an extrasolar planet. *ApJ* **626**, 523 (2005).

[95] Http://obswww.unige.ch/ udry/planet/method.html.

[96] Hatzes, A. Simulations of stellar radial-velocity and spectral line bisector variations. i. nonradial pulsations. *PASP* **108**, 839 (1996).

[97] Henry, G. W., Baliunas, S. L., Donahue, R. A., Fekel, F. C. & Soon, W. Photometric and ca_{II} and h and k spectroscopic variations in nearby sun-like stars with planets. iii. *ApJ* **531**, 415 (2000).

[98] Cumming, A., Marcy, G. W. & Butler, R. P. The lick planet search: Detectability and mass thresholds. *ApJ* **526**, 890 (1999).

[99] Einstein, A. Lens-like action of a star by the deviation in the gravitational field. *Science* **84**, 506 (1936).

[100] Paczynski, B. Gravitational microlensing by the galactic halo. *ApJ* **304**, 1 (1986).

[101] Horne, K. Gravitational lensing brings extrasolar planets into focus. *Physics World* **10 June** (2004).

[102] Docobo, J. A. *et al.* A methodology for studying physical and dynamical properties of multiple stars. application to the system of red dwarfs gl 22. *A&A* **478**, 187 (2008).

[103] Perryman, M. A. C. *et al.* Gaia: Composition, formation and evolution of the galaxy. *A&A* **369**, 339 (2001).

[104] Helminiak, K. & Konacki, M. Precise astrometry of visual binaries with adaptive optics. a way for finding exoplanets? *2008arXiv0807.4139H* (2008).

[105] Guyon, O., Pluzhnik, E. A., Kuchner, M. J., Collins, B. & Ridgway, S. T. Theoretical limits on extrasolar terrestrial planet detection with coronagraphs. *ApJS* **167**, 81 (2006).

[106] Marois, C. *et al.* Direct imaging of multiple planets orbiting the star hr 8799. *Science* **322**, 1348 (2008).

[107] Mazeh, T. *et al.* The spectroscopic orbit of the planetary companion transiting hd 209458. *ApJ* **532**, 55 (2000).

[108] Deeg, H. J. *et al.* Ground-based photometry of space-based transit detections: Photometric follow-up of the corot mission. *A&A* **accepted** (2009).

[109] Bouchy, F., Moutou, C., Queloz, D. & the CoRoT Exoplanet Science Team. Radial velocity follow-up for confirmation and characterization of transiting exoplanets. *IAUS* **253**, 129 (2009).

[110] Deleuil, M. *et al.* Complemetary observations for the corot exoplanet program. *ESA SP-1306: The CoRoT Mission* **1306**, 341 (2006).

[111] Deming, D., Sara, S., Richardson, J. L. & Harrington, J. Infrared radiation from an extrasolar planet. *Nature* **434**, 740 (2005).

[112] Sing, D. K. & López-Morales, M. Ground-based secondary eclipse detection of the very-hot jupiter ogle-tr-56b. *A&A* **493**, 31 (2009).

[113] de Mooij, E. J. W. & Snellen, I. A. G. Ground-based k-band detection of thermal emission from the exoplanet tres-3b. *A&A* **493**, 35 (2009).

[114] Alonso, R., Deeg, H. J., Kabath, P. & M., R. Ground-based observations of the secondary eclipse of corot-2b. *MNRAS* **submitted** (2009).

[115] Brown, T. M., Charbonneau, D., Gilliland, R. L., Noyes, R. W. & Burrows, A. Hubble space telescope time-series photometry of the transiting planet of hd 209458. *ApJ* **552**, 699 (2001).

[116] Sahu, K. C. *et al.* Transiting extrasolar planetary candidates in the galactic bulge. *Nature* **443**, 534 (2006).

[117] Auvergne, M. *et al.* The corot satellite in flight : description and performance. *A&A accepted* **IAUS** (2009).

[118] Llebaria, A. (2005). CoRoT templates, how robust they are? (CoRoT Week-8).

[119] Boisnard, L. & Avergne, M. Corot in brief. *ESA SP-1306: The CoRoT Mission* **1306**, 19 (2006).

[120] Barge, P. *et al.* The corot mission. *ESA SP-1306: The CoRoT Mission* **1306**, 83 (2006).

[121] Http://smsc.cnes.fr/COROT/.

[122] Kovcs, G., Zucker, S. & Mazeh, T. A box-fitting algorithm in the search for periodic transits. *A&A* **391**, 369 (2002).

[123] Renner, S. *et al.* The bast algorithm for transit detection. *A&A* **492**, 617 (2008).

[124] Alonso, R. *et al.* Transiting exoplanets from the corot space mission. ii. corot-exo-2b: a transiting planet around an active g star. *A&A* **482**, 21 (2008).

[125] Barge, P. *et al.* Transiting exoplanets from the corot space mission. i. corot-exo-1b: a low-density short-period planet around a g0v star. *A&A* **482**, 17 (2008).

[126] Alonso, R., Aigrain, S., Pont, T., Frdric an Mazeh & Team, T. C. E. S. Searching for the secondary eclipse of corot-exo-2b and its transit timing variations. *IAUS* **253**, 91 (2009).

[127] Aigrain, S. *et al.* Transiting exoplanets from the corot space mission. iv. corot-exo-4b: a transiting planet in a 9.2 day synchronous orbit. *A&A* **488**, 43 (2008).

[128] Moutou, C. *et al.* Transiting exoplanets from the corot space mission. v. corot-exo-4b: stellar and planetary parameters. *A&A* **488**, 47 (2008).

[129] Rauer, H. *et al.* Transiting exoplanets from the corot space mission vii. the "hot-jupiter"-type planet corot-5b. *A&A* **accepted** (2009).

[130] Fridlund, M. e. a. Corot 6b (tbc). *A&A* **in prep.** (2009).

[131] Koch, D. *et al.* Kepler: a space mission to detect earth-class exoplanets. *Space Telescopes and Instruments V, SPIE Conference 3356* **3356**, 599 (1998).

[132] Koch, D. *et al.* The kepler mission design overview, a decade of extrasolar planets around normal stars. *http://kepler.nasa.gov/pdf_files/Koch_STScI_2005.pdf* (2005).

[133] Catala & consortium, P. Detection of planetary transits across a sun-like star. *J. Phys.: Conf. Ser.* **118**, 2040 (2008).

[134] Udalski, A., Kubiak, M. & Szymanski, M. Optical gravitational lensing experiment. ogle-2 – the second phase of the ogle project. *AcA* **47**, 319 (1997).

[135] Borucki, W. J., Caldwell, D., Koch, D. G. & Webster, L. D. The vulcan photometer: A dedicated photometer for extrasolar planet searches. *PASP* **113**, 439 (2001).

[136] Rauer, H. *et al.* The berlin exoplanet search telescope system. *PASP* **116**, 38 (2004).

[137] Rauer, H. *et al.* Pre-discovery observations of corot-1b and corot-2b with best survey. *AJ* **submitted** (2009).

[138] McCullogh, P. R. *et al.* The xo project to find transiting hot jupiters: The first year's data. *AAS* **36**, 1566 (2004).

[139] Shporer, A. *et al.* The what project. *arXiv:astro-ph/0510766v1* .

[140] Hartman, J. D., Bakos, G., Stanek, K. Z. & Noyes, R. W. Hatnet variability survey in the high stellar density "kepler field" with millimagnitude image subtraction photometry. *AJ* **128**, 1761 (2004).

[141] O'Donovan, F. T., Charbonneau, D. & Kotredes, L. First results from sleuth: The palomar planet finder. *arXiv:astro-ph/0312289v1* (2003).

[142] Dunham, E. W., Mandushev, G. I., Tylor, B. W. & Oetiker, B. Psst: The planet search telescope. *PASP* **116**, 1072 (2004).

[143] Eigmüller, P. & Eislöffel, J. Test - the tautenburg exoplanet search telescope. *arXiv:0807.4844v1* (2008).

[144] Deeg, H. J. *et al.* Pass: An all sky survey for the detection of transiting extrasolar planets and for permanent variable star tracking. *PASP* **116**, 985 (2004).

[145] Cameron, A. C. *et al.* Wasp-1b and wasp-2b: two new transiting exoplanets detected with superwasp and sophie. *MNRAS* **375**, 951 (2007).

[146] Bakos, G. *et al.* Wide-field millimagnitude photometry with the hat: A tool for extrasolar planet detection. *PASP* **116**, 266 (2004).

[147] Bakos, G. A. *et al.* Hat-p-1b: A large-radius, low-density exoplanet transiting one member of a stellar binary. *ApJ* **656**, 552 (2007).

[148] Irwin, J., Charbonneau, D., Nutzman, P. & Falco, E. The mearth project: searching for transiting habitable super-earths around nearby m-dwarfs. *arXiv:0807.1316v1* (2008).

[149] Udalski, A. *et al.* The optical gravitational lensing experiment. search for planetary and low-luminosity object transits in the galactic disk. results of 2001 campaign. *AcA* **52**, 1 (2002).

[150] Erikson, A., Rauer, H., Kabath, P. & team, B. Best ii paper. *AJ* **in preparation** (2009).

[151] Konacki, M., Torres, G., Jha, S. & Sasselov, D. D. An extrasolar planet that transits the disk of its parent star. *Nature* **421**, 507 (2003).

[152] Afonso, C. & Henning, T. The pan-planets project. *ASPC* **366**, 326 (2007).

[153] Crouzet, N. *et al.* Astep south: An antarctic search for transiting planets around the celestial south pole. *arXiv:0809.4391v1* (2008).

[154] Lawrence, J. S., Ashley, M. C. B., Tokovinin, A. & Travouillon, T. Exceptional astronomical seeing conditions above dome c in antarctica. *Nature* **431**, 278 (2004).

[155] Http://obswww.unige.ch/udry/planet/planet.html.

[156] Fischer, D. A. *et al.* The n2k consortium. i. a hot saturn planet orbiting hd 88133. *ApJ* **620**, 481 (2005).

[157] Butler, P. R. *et al.* Two new planets from the anglo-australian planet search. *ApJ* **555**, 410 (2001).

[158] Http://www.cfa.harvard.edu/harps/.

[159] Http://obswww.unige.ch/Instruments/harps_north/home/home.html.

[160] Http://www.eso.org/blog/20080624/astronomers-are-thirstyae/#more-19.

[161] Guenther, E. W., Martín, E. L., Barrado y Navascués, D. & Laux, U. Nahual: A cool spectrograph for planets of ultra-cool objects. *arXiv:astro-ph* **0509387v1** (2005).

[162] Berry, R. & Burnell, J. *The handbook of astronomical image processing* (Willmann-Bell Inc., 2006).

[163] Www.kodak.com.

[164] Deiries, S. Http://www.eso.org/s̃deiries/CCD/ccd_opendoor.html.

[165] Landolt, A. U. Ubvri photometric standard stars in the magnitude range 11.5-16.0 around the celestial equator. *AJ* **104**, 340 (1992).

[166] Hardie, R. H. *Photoelectric reductions* (University of Chicago Press, 1964).

[167] Beckers, J. M. Adaptive optics for astronomy: Principles, performance, and applications. *Ann. Rev. Astron. Astrophys.* **31**, 13 (1993).

[168] Fruth, T. *Perspektiven für die Transitsuche: Vergleich des Standortes Dome C (Antarktis) mit Standorten gemäßigter Breite* (Freie Universität Berlin - Diploma thesis, 2008).

[169] Geissler, K. & Masciadri, E. Meteorological parameter analysis above dome c using data from the european centre for medium-range weather forecasts. *PASP* **118**, 1048 (2006).

[170] Kenyon, S. L. *et al.* Atmospheric scintillation at dome c, antarctica; implications for photometry and astrometry. *PASP* **118**, 924 (2006).

[171] Karoff, C. *et al.* Identification of variable stars in corot's first main observing field (lrc1). *AJ* **134**, 766 (2007).

[172] Kabath, P. *et al.* Characterization of corot target fields with best: Identification of periodic variable stars in the ir01 field. *AJ* **134**, 1560 (2007).

[173] Kabath, P. *et al.* Characterization of corot target fields with the berlin exoplanet search telescope: Identification of periodic variable stars in the lra1 field. *AJ* **136**, 654 (2008).

[174] Http://www.obs-hp.fr/welcome.shtml.

[175] Http://www.eso.org/sci/facilities/paranal/site/paranal-figs.html#seeing.

[176] Rauer, H., Fruth, T. & Erikson, A. Prospects of long-time-series observations from dome c for transit search. *PASP* **120**, 542 (2008).

[177] Denny, B. Http://acp.dc3.com/images/ACPLayers.png.

[178] Kabath, P. *et al.* Characterization of corot target fields with berlin exoplanet search telescope. ii. identification of periodic variable stars in the lrc2 field. *AJ* **137**, 391 (2009).

[179] Kabath, P. *et al.* Characterization of corot target fields with berlin exoplanet search telescope. ii. identification of periodic variable stars in the lra02 field. *A&A* **accepted** (2009b).

[180] Michel, E., Deleuil, M. & Baglin, A. The observing programme, present status. *ESA-SP* **1306**, 473 (2006).

[181] Udalski, A. *et al.* The optical gravitational lensing experiment. planetary and low-luminosity object transits in the carina fields of the galactic disc. *AcA* **52**, 317 (2002).

[182] Wiese, T. *Analyse von stellaren Lichtkurven zur Suche nach Transits extrasolarer Planeten* (Diploma thesis Freie Universität Berlin, 2007).

[183] Fressin, F., Guillot, T., Morello, V. & Pont, F. Interpreting and predicting the yield of transit surveys: giant planets in the ogle fields. *A&A* **475**, 729 (2007).

[184] Alard, C. Image subtraction using a space-varying kernel. *A&AS* **144**, 363 (2000).

[185] Pasternacki, T. *Optimierte photometrische Datenauswertung zur Suche variabler Sterne und Planetentransits in BEST-Daten* (Freie Universität Berlin, 2009).

[186] Pál, A. & Bakos, G. A. Astrometry in wide-field surveys. *ASPC* **366**, 340 (2007).

[187] Stetson, P. B. Daophot - a computer program for crowded-field stellar photometry. *PASP* **99**, 191 (1987).

[188] Alard, C. & Lupton, R. H. A method for optimal image subtraction. *ApJ* **503**, 325 (1998).

[189] Monet, D. G. The 526,280,881 objects in the usno-a2.0 catalog. *AAS* **30**, 1427 (1998).

[190] Tamuz, O., Mazeh, T. & Zucker, S. Correcting systematic effects in a large set of photometric light curves. *MNRAS* **1466**, 199 (356).

[191] Newberry, M. V. Signal-to-noise considerations for sky-subtracted ccd data. *PASP* **103**, 122 (1991).

[192] Pont, F., Zucker, S. & Queloz, D. The effect of red noise on planetary transit detection. *MNRAS* **373**, 217 (2006).

[193] Stetson, P. B. On the automatic determination of light-curve parameters for cepheid variables. *PASP* **108**, 851 (1996).

[194] Zhang, X.-B., Deng, L.-C., Xin, Y. & Zhou, X. Searching for variable stars in the field of ngc 7789. *Chinese Journal of Astronomy and Astrophysics* **3**, 151 (2003).

[195] Schwarzenberg-Czerny, A. Fast and statistically optimal period search in uneven sampled observations. *ApJ* **460**, 107 (1996).

[196] Skrutskie, M. *et al.* The two micron all sky survey (2mass). *AJ* **131**, 1163 (2006).

[197] Sterken, C. & Jaschek, C. *Light curves of variable stars* (Cambridge University press, 1996).

[198] Kaye, B. A., Handler, G., Krisciunas, K., Poretti, E. & Zerbi, M. F. Gamma doradus stars: Defining a new class of pulsating variables. *PASP* **111**, 840 (1999).

[199] Blažko, S. Mitteilung über veränderliche sterne. *AN* **175**, 325 (1907).

[200] Kolenberg, K. *et al.* The blazhko effect of rr lyrae in 2003-2004. *A&A* **459**, 577 (2006).

[201] La Cluyzeé, A. *et al.* The changing blazhko effect of xz cygni. *AJ* **127**, 1653 (2004).

[202] Szczygieł, D. M. & Fabrycky, D. C. Multiperiodic galactic field rr lyrae stars in the asas catalogue. *MNRAS* **377**, 1263 (2007).

[203] Vaz, L. P. R. The reflection effect in eclipsing binary systems. *Ap&SS* **113**, 349 (1985).

[204] Peraiah, A. & Srinivasa Rao, M. A series of theoretical line profiles formed in the irradiated expanding atmospheres of close binary components. *A&AS* **132**, 45 (1998).

[205] Maceroni, C. & van't Veer, F. The uniqueness of photometric solutions for spotted w ursae majoris binaries. *A&A* **277**, 515 (1993).

[206] Fernandez-Figueroa, M., Montes, D., De Castro, E. & Cornide, M. Ca ii h and k and h alpha emissions in chromospherically active binary systems (rs canum venaticorum and by draconis). *ApJS* **90**, 433 (1994).

[207] Benko, J. M. & Csurby, Z. Variable star census in corot "eyes". *AcA* **57**, 73 (2007).

[208] Hoffmeister, C. Mitteilungen über neuentdeckte veränderliche sterne (s 1927-s 10152). *AN* **290**, 43 (1967).

[209] Ahnert, P. Katalog und efemeriden veränderlicher sterne für 1942. *KVBB* **N28** (1943).

[210] Pojmanski, G. The all sky automated survey catalog of variable stars i. 0 h - 6 h quarter of the southern hemisphere. *AcA* **52**, 397 (2002).

[211] Ahnert, P. *VSS* **N3** (1949).

[212] Cabrera, J. *et al.* Planetary transit candidates in corot-lrc01 field. *A&A* **accepted** (2009).

[213] Carpano, S. *et al.* Planetary transit candidates in the corot initial run. *A&A* **accepted** (2009).

[214] Udalski, A., Szymanski, M., Kaluzny, J., Kubiak, M. & Mateo, M. The optical gravitational lensing experiment. *AcA* **42**, 253 (1992).

[215] Eyer, L. & Mowlavi, N. Variable stars across the observational hr diagramm. *Journal of Physics: Conf. Series* **118**, 012010 (2008).

[216] Titz, R. (2009). Status of the CoRoT candidates checked with BEST data sets, private communication.

[217] Csizmadia, S. (2009). Transit fitting package, private communication.

[218] Croll, B. Markov chain monte carlo methods applied to photometric spot modeling. *PASP* **118**, 1351 (2006).

[219] Vereš, P., Budaj, J., Világi, J., Galád, A. & Kornoš, L. Relative photometry of transiting exoplanet corot-exo-2b. *Contributions of the Astronomical Observatory Skalnaté Pleso* **39**, 34 (2009).

[220] Gandolfi, D. (2009). Private communication.

[221] Güenther, E. (2009). Private communication.

[222] Http://www.aao.gov.au/local/www/aaomega/.

[223] Habets, G. M. H. J. & Heintze, J. R. W. Empirical bolometric corrections for the main-sequence. *Astron. Astrophys. Suppl. Ser.* **193**, 1302 (1981).

[224] Halbwachs, J. L., Mayor, M., Udry, S. & Arenou, F. Multiplicity among solar-type stars. iii. statistical properties of the f7-k binaries with periods up to 10 years. *A&A* **397**, 159 (2003).

[225] Mazeh, T., Simon, M., Prato, L., Markus, B. & Zucker, S. The mass ratio distribution in main-sequence spectroscopic binaries measured by infrared spectroscopy. *ApJ* **599**, 1344 (2003).

[226] Sderhjelm, S. & Dischler, J. Eclipsing binary statistics theory and observation. *A&A* **442**, 1003 (2005).

[227] Beatty, T. G. & Gaudi, B. S. Predicting the yields of photometric surveys for transiting extrasolar planets. *ApJ* **686**, 1302 (2008).

[228] Brown, T. M. Expected detection and false alarm rates for transiting jovian planets. *ApJ* **593**, 125 (2003).

[229] Cox, A. N. *Allen's astrophysical quantities* (4^{th} ed.; New York: Springer, 2000).

Acknowledgments

It is a pleasure to thank the many people who made this thesis possible.

First of all I would like to express my sincere gratitude to Prof. Heike Rauer, Head of the Department of Extrasolar Planets and Atmospheres at the German Aerospace Center Berlin, who has been my supervisor since the beginning of my studies. She has always provided me with many constructive suggestions, motivation, immense knowledge and most importantly who has given me the unique opportunity to work on the world-class transit survey project, the BEST.

I also wish to express my deep appreciation to Prof. Erwin Sedlmayr for reading the thesis and for writing of the second referee report. I want to express my deeply-felt thanks to Anders Erikson who was patiently resisting my furiously persistent questioning and who has always helped me throughout the compilation of this thesis. His pragmatic suggestions certainly increased the readability and reduced the ambiguity of this thesis.

I am indebted to Thomas Fruth for the numerous inspirational discussions and for the preparation of some figures in Chapter 7 and for further contributions to this paper. I am also very delighted that he has been selected to take over the BEST II work. Furthermore, I appreciate the help of Thomas Pasternacki who rescued the variable stars paper on the BEST II LRa02 data and who has also prepared some figures in Chapter 8 of this thesis. Thanks goes also to Szilard Csizmadia for the patient modeling of our transit candidates and to Davide Gandolfi for help with spectral classification of host stars.

Furthermore, I am very thankful for the proof-reading of this thesis to Heike Rauer, Anders Erikson, Juan Cabrera, Ruth Titz, Stefan Renner and my wife Martina who all provided refreshing insight, critical questions and common sense that was exhilarating.

Many others at DLR and elsewhere have also been involved and deserve recognition. It is, however, not possible to list them all here. Their support in this effort is, however, greatly appreciated.

Lastly and most importantly I would like to thank my family. My warmest thanks are reserved for my and my wife's parents and especially for my wife Martina. I need to thank her for the patience which she had with me during the compiling of this thesis. She helped me to concentrate on completing this dissertation and supported me mentally during the course of this work. Without her help and encouragement, this study would not have been completed. Thank you, Martina, and I am looking forward to starting a new chapter of our life in Chile.

About the author - Observing experience

- 01.01.06-12.01.06 - observing campaign with BEST az OHP
- 01.03.06-12.03.06 - observing campaign with BEST at OHP
- 24.05.06-09.06.06 - observing campaign with BEST at OHP
- 10.08.06-22.08.06 - observing campaign with BEST at OHP
- 02.02.07-18.02.07 - installation of BEST II at OCA
- 09.04.07-25.04.07 - alignment of the BEST II+first light
- 07.06.07-28.06.07 - test phase and first observations at OCA
- 14.07.07-05.08.07 - observing campaign on LRc02 with BEST II at OCA
- 01.08.07-30.08.07 - observing campaign on LRc02 with BEST II at OCA
- 09.10.07-26.10.07 - maintenance trip to BEST II
- 28.03.08-11.04.08 - maintenance trip to BEST II
- 10.07.08-24.07.08 - 4.2-m WHT observations, La Palma, Spain
- 15.10.08-28.10.08 - maintenance trip to BEST II
- 10.06.08-22.06.08 - maintenance trip to BEST II

Conferences visited

- 29.08.06-09.09.06 ESO NEON Archiving Summer School, Garching, Germany
- 24.09.06-28.09.06 Transit Workshop Heidelberg, Germany (20 min. talk)
- 24.03.07-30.03.07 ARENA workshop Tenerife, Spain (20 min. talk)
- 17.09.07-21.09.07 ARENA conference Potsdam, Germany (organizer)
- 24.09.07-28.09.07 CoRoT CEST Meeting Paris, France (short presentation)
- 20.11.07-23.11.07 CoRoT CEST Meeting Paris, France (shport presentation)
- 03.03.08-07.03.08 DPG meeting, Freiburg, Germany (20 min. talk)
- 19.05.08-26.05.08 IAU colloquium Transiting Planets, Boston, USA (20 min. talk)
- 01.12.08-02.12.08 German CoRoT Co-I meeting, Köln, Germany (short presentation)